Advances in Mechanical Engineering

Marine Energy Conversion

Guest Editors: Fabrizio Marignetti, Haitao Yu, and Luigi Cappelli

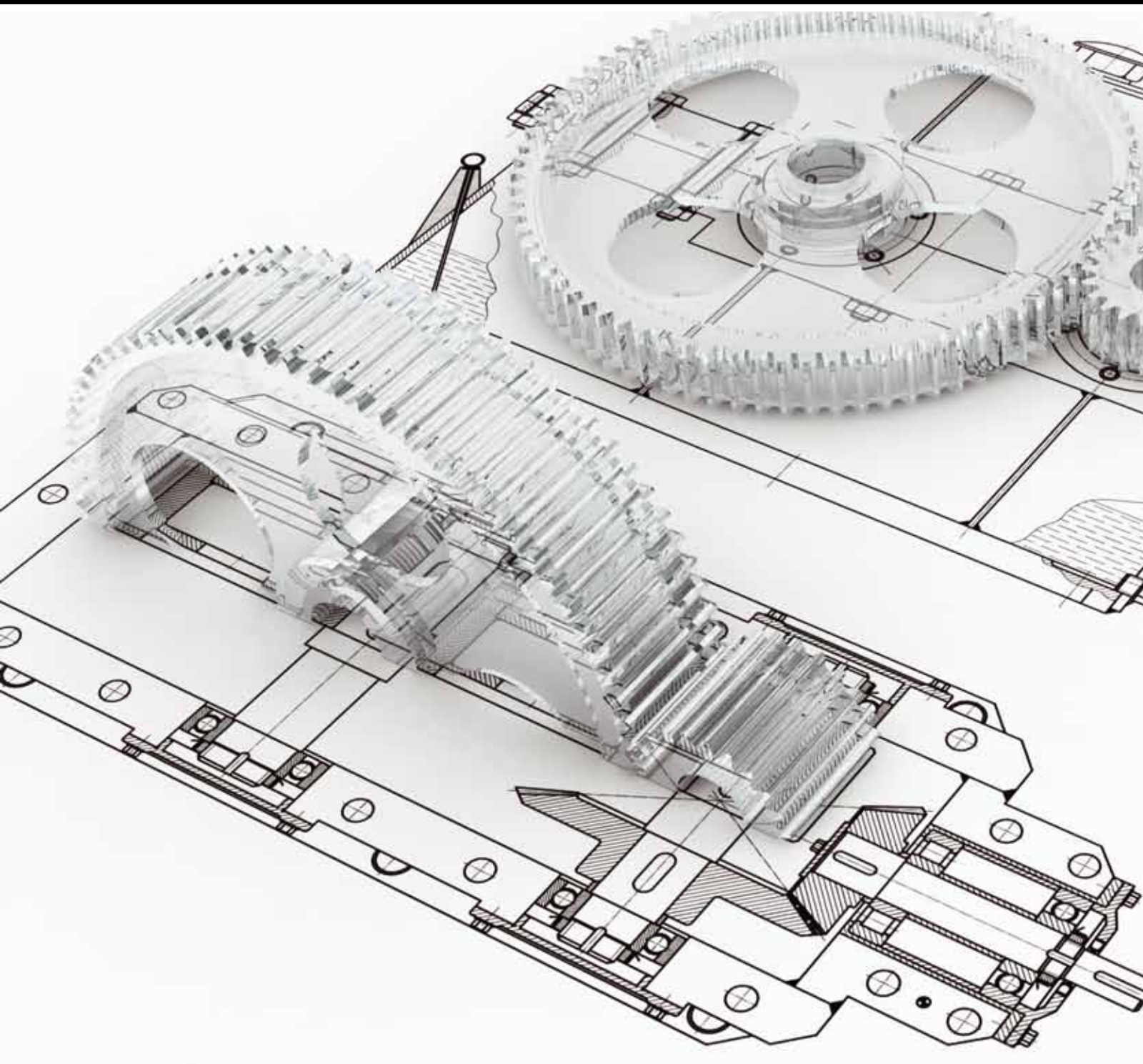

Marine Energy Conversion

Advances in Mechanical Engineering

Marine Energy Conversion

Guest Editors: Fabrizio Marignetti, Haitao Yu, and Luigi Cappelli

Copyright © 2013 Hindawi Publishing Corporation. All rights reserved.

This is a special issue published in "Advances in Mechanical Engineering." All articles are open access articles distributed under the Creative Commons Attribution License, which permits unrestricted use, distribution, and reproduction in any medium, provided the original work is properly cited.

Editorial Board

Koshi Adachi, Japan
Mehdi Ahmadian, USA
Rehan Ahmed, UK
Muhammad T. Akhtar, Japan
Nacim Alilat, France
M. Affan Badar, USA
Luis Baeza, Spain
R. Balachandran, UK
Claude Bathias, France
Adib Becker, UK
Leonardo Bertini, Italy
L. A. Blunt, UK
Noël Brunetière, France
Marco Ceccarelli, Italy
Fakher Chaari, Tunisia
Chin-Lung Chin, Taiwan
H. Hee Cho, Republic of Korea
Seung-Bok Choi, Korea
Kangyao Deng, China
Francisco D. Denia, Spain
T.S. Dhanasekaran, USA
Nihad Dukhan, USA
Farzad Ebrahimi, Iran
Ali El Wahed, UK
Bogdan I. Epureanu, USA
M. R. Eslami, Iran
Ali Fatemi, USA
Mario L. Ferrari, Italy
Siegfried Fouvry, France
Ian Frigaard, Canada
Mergen H. Ghayesh, Canada
Lus Godinho, Portugal
Tian Han, China
F. J. Huera-Huarte, Spain
D. Jalali-Vahid, Iran
Jiin Yuh Jang, Taiwan
Zhongmin Jin, UK
Xiaodong Jing, China
S.-W. Kang, Republic of Korea
Xianwen Kong, UK
Michal Kuciej, Poland
Yaguo Lei, China
Zili Li, The Netherlands
Jaw-Ren Lin, Taiwan
Cheng-Xian Lin, USA
S. Nima Mahmoodi, USA
Oronzio Manca, Italy
Ramiro Martins, Portugal
Aristide F. Massardo, Italy
Francesco Massi, Italy
T.H. New, Singapore
Kim Choon Ng, Singapore
C. T. Nguyen, Canada
Hirosi Noguchi, Japan
Hakan F. Oztop, Turkey
Duc Truong Pham, UK
Jurij Prezelj, Slovenia
Xiaotun Qiu, USA
Pascal Ray, France
Robert L. Reuben, UK
Pedro A.R. Rosa, Portugal
Elsa de Sá Caetano, Portugal
D.R. Salgado, Spain
Mohammad R. Salimpour, Iran
Sunetra Sarkar, India
Pietro Scandura, Italy
A. Seshadri Sekhar, India
Ahmet Selim Dalkılıç, Turkey
Liyuan Sheng, China
Xi Shi, China
Seiichi Shiga, Japan
C. S. Shin, Taiwan
Ray W. Snidle, UK
Margaret M. Stack, UK
Neil Stephen, UK
Kumar K. Tamma, USA
Yaya Tan, China
Anand Thite, UK
Cho W. Solomon To, USA
Yoshihiro Tomita, Japan
Shan-Tung Tu, China
Sandra Velarde-Surez, Spain
Moran Wang, China
Junwu Wang, China
Jia-Jang Wu, Taiwan
Fengfeng Xi, Canada
Gongnan Xie, China
Wei Mon Yan, Taiwan
Jianqiao Ye, UK
Byeng D. Youn, USA
Bo Yu, China
Jianbo Yu, China
Zhongrong Zhou, China

Contents

Marine Energy Conversion, Fabrizio Marignetti, Haitao Yu, and Luigi Cappelli
Volume 2013, Article ID 457083, 2 pages

Optimization Study of Shaft Tubular Turbine in a Bidirectional Tidal Power Station, Xinfeng Ge, Yuan Feng, Ye Zhou, Yuan Zheng, and Chunxia Yang
Volume 2013, Article ID 731384, 9 pages

Numerical Simulation of Section Systems in the Pelamis Wave Energy Converter, Hongzhou He, Quanyou Qu, and Juyue Li
Volume 2013, Article ID 186056, 8 pages

Buoy-Rope-Drum Wave Power System, Linsen Zhu, Yangang Wang, Ze Yang, and Yanming Qu
Volume 2013, Article ID 609464, 5 pages

New Concept for Assessment of Tidal Current Energy in Jiangsu Coast, China, Ji-Sheng Zhang, Jun Wang, Ai-Feng Tao, Jin-Hai Zheng, and Hui Li
Volume 2013, Article ID 340501, 9 pages

Analysis of Floating Buoy of a Wave Power Generating Jack-Up Platform *Haiyuan 1*, Date Li, Detang Li, Fei Li, Jingxin Shi, and Wei Zhang
Volume 2013, Article ID 105072, 7 pages

Comparison of Structural Properties between Monopile and Tripod Offshore Wind-Turbine Support Structures, Da Chen, Kai Huang, Valentin Bretel, and Lijun Hou
Volume 2013, Article ID 175684, 9 pages

Modeling, Simulation, and Experiment of Switched Reluctance Ocean Current Generator System, Hao Chen, Xiaoxiao Zhang, and Yang Xu
Volume 2013, Article ID 261241, 14 pages

Development of Ocean Energy Technologies: A Case Study of China, Qin Guodong, Lou Ping, and Wu Xianglian
Volume 2013, Article ID 941781, 6 pages

Design and Analysis of a Linear Hybrid Excitation Flux-Switching Generator for Direct Drive Wave Energy Converters, Lei Huang, Minqiang Hu, Jing Liu, Chunyuan Liu, and Weibo Zhong
Volume 2013, Article ID 963093, 11 pages

Performance Analysis of a Completely Sealed Double Oscillating Structure Applied in Wave Energy Extraction, Zhenchuan Shi, Haitao Yu, and Fabrizio Marignetti
Volume 2013, Article ID 297803, 6 pages

Efficiency of a Directly Driven Generator for Hydrokinetic Energy Conversion, Mårten Grabbe, Katarina Yuen, Senad Apelfröjd, and Mats Leijon
Volume 2013, Article ID 978140, 8 pages

Bidirectional Power Performance of a Tidal Unit with Unilateral and Double Guide Vanes,
Chunxia Yang, Yuan Zheng, Daqing Zhou, Xinfeng Ge, and Lingyu Li
Volume 2013, Article ID 835051, 11 pages

A Review of Offshore Wave Energy Extraction System, Zhongxian Chen, Haitao Yu, Minqiang Hu, Gaojun Meng, and Cheng Wen
Volume 2013, Article ID 623020, 9 pages

Numerical Analysis of Impulse Turbine for Isolated Pilot OWC System, Zhen Liu, Jiyuan Jin, Ying Cui, and Haiwen Fan
Volume 2013, Article ID 416109, 11 pages

Hindawi Publishing Corporation
Advances in Mechanical Engineering
Volume 2013, Article ID 457083, 2 pages
http://dx.doi.org/10.1155/2013/457083

Editorial
Marine Energy Conversion

Fabrizio Marignetti,[1] Haitao Yu,[2] and Luigi Cappelli[1]

[1] *Department of Electrical and Information Engineering (DIEI), University of Cassino and Southern Latium, Via Di Biasio, 03043 Cassino, Italy*
[2] *School of Electrical Engineering, Southeast University, Si Pai Lou 2, Nanjing 210096, China*

Correspondence should be addressed to Fabrizio Marignetti; marignetti@unicas.it

Received 4 December 2013; Accepted 4 December 2013

Copyright © 2013 Fabrizio Marignetti et al. This is an open access article distributed under the Creative Commons Attribution License, which permits unrestricted use, distribution, and reproduction in any medium, provided the original work is properly cited.

As the Earth's surface is mostly covered by water, the sea represents an enormous source of clean energy. This source is so far minimally exploited, but its potential is much larger than the entire global energy demand.

This energy can be converted from different forms as tidal, wave, marine current, temperature variation, and salinity, representing an effective resource for most of the planet. Conversion strategies and technologies developed so far have demonstrated the feasibility and the interest in such a large issue, showing the way forward to big challenges to match with. Recent advances in engineering and technology led to more efficient and cost-effective solutions.

Different governments have provided funding to research activities regarding the exploitation of marine energy, most notably UK, China, USA, Canada, Sweden, Portugal, Ireland, Spain, Australia, Korea, Nigeria, New Zealand, Mexico, and Japan.

As a result of this interest, a large number of devices, exploiting different marine energy components, have been proposed. Many marine energy converters have been patented, while some have already been considered mature for application. The extraordinary variety of the proposed technologies testifies both the vitality of the field and the ingenuity of the researchers in the field.

In this special issue authors submitted their original contributions and review articles that cover the main important aspects related to ocean technologies, mainly focusing on wave, ocean current, and tidal energy harvesting. Numerical simulations and experimental validation have been carried out. Several devices have already been built and performance is reported. Efficiency is a key point for this kind of application; thus, a strong effort has been made in order to develop control algorithms and mechanical solutions which improve the performance of the energy conversion.

It is now a common opinion that marine energy conversion will be one of the leading research fields at least in the next 15 years.

Overview of the Articles of the Special Issue. Marine energy conversion is a multidisciplinary topic, requiring the expertises of sectors ranging from ocean engineering to electrical engineering. The scope of this Special Session is accordingly wide, helping to build a global and complete overview of the topic.

This special session comprises the work of some of the leading institutions working in the field. The contributions are relevant to four main areas.

In the field of wave energy conversion, Z. Liu et al. investigate the operating performance of a designed impulse turbine for the pilot oscillating water column (OWC) system which is under the construction on Jeju Island, Korea; D. Li et al. focus on the performance of floating buoys of a wave power generating jack-up platform, called Haiyuan 1; Lei Huang et al. propose a novel hybrid excitation flux-switching generator for direct drive wave energy converters; Z. Shi et al. propose a wave energy extracting structure which can be completely sealed and works under the principle of double oscillation. L. Zhu et al. propose a new type of floating oscillating buoy wave power device, a buoy-rope-drum wave power system, and

H. He et al. carried out simulations on the expected performance of the Pelamis wave energy converter in China.

Concerning water current harvesting, H. Chen et al. present a nonlinear simulation model of a switched reluctance (SR) ocean current generator system on MATLAB/simulink which described the structure of generator system, while M. Grabbe et al. studied the efficiency of a directly driven generator for hydrokinetic energy conversion.

The tidal energy field is explored by C. Yang et al. who present a bidirectional power performance of a tidal unit with unilateral and double guide vanes; A. F. Tao et al. studied a two-dimensional hydrodynamic model in order to predict the distribution of mean density of tidal current energy and X. Ge et al. introduce and study the optimization of a form of tidal power station, which can satisfy bidirectional power.

Finally, two review articles are presented in this special issue: Z. Chen et al. made a review of offshore wave energy extraction system in order to provide some useful guidelines for future studies in this field; Q. Guodong et al. carried out a review of development of ocean energy in China giving recommendations for the future development of ocean energy.

Acknowledgments

We hope that the readers will find in these articles a useful support for their research projects and a motivating incentive for further investigations. We would like to express our gratitude to all the contributing authors for sharing their research work through this special issue and to all the reviewers for their serious effort, which improved the quality of this special issue. It has been a pleasure and an interesting experience for us to work on this special issue.

Fabrizio Marignetti
Haitao Yu
Luigi Cappelli

Hindawi Publishing Corporation
Advances in Mechanical Engineering
Volume 2013, Article ID 731384, 9 pages
http://dx.doi.org/10.1155/2013/731384

Research Article

Optimization Study of Shaft Tubular Turbine in a Bidirectional Tidal Power Station

Xinfeng Ge,[1,2] Yuan Feng,[3] Ye Zhou,[4] Yuan Zheng,[2] and Chunxia Yang[1]

[1] *College of Water Conservancy and Hydropower Engineering, Hohai University, Nanjing 210098, China*
[2] *College of Energy and Electrical Engineering, Hohai University, Nanjing 210098, China*
[3] *Yunnan Electric Power Test & Research Institute (Group) Limited Company, Electric Power Research Institute, Kunming 650217, China*
[4] *China Institute of Water Resources and Hydropower Research (IWHR), Beijing 100048, China*

Correspondence should be addressed to Xinfeng Ge; endless9452@163.com

Received 28 June 2013; Accepted 3 October 2013

Academic Editor: Haitao Yu

Copyright © 2013 Xinfeng Ge et al. This is an open access article distributed under the Creative Commons Attribution License, which permits unrestricted use, distribution, and reproduction in any medium, provided the original work is properly cited.

The shaft tubular turbine is a form of tidal power station which can provide bidirectional power. Efficiency is an important turbine performance indicator. To study the influence of runner design parameters on efficiency, a complete 3D flow-channel model of a shaft tubular turbine was developed, which contains the turbine runner, guide vanes, and flow passage and was integrated with hybrid grids calculated by steady-state calculation methods. Three aspects of the core component (turbine runner) were optimized by numerical simulation. All the results were then verified by experiments. It was shown that curved-edge blades are much better than straight-edge blades; the optimal blade twist angle is 7°, and the optimal distance between the runner and the blades is 0.75–1.25 times the diameter of the runner. Moreover, the numerical simulation results matched the experimental data very well, which also verified the correctness of the optimal results.

1. Introduction

Tidal power generated by falling and rising water, which is a kind of potential energy [1], can transform mechanical energy into electricity. More specifically, a dam is built to back up the water located adjacent to bays or estuaries which are separate from the ocean and therefore form a reservoir. A hydroelectric generating set is then installed in the dam, and the pressure of the water from all tidal states turns the wheel, a motion which can be used to make electric power. The tubular turbine is applicable to tidal power stations because it can provide power from low water levels. The tubular turbine offers good technical and economic feasibility, which has contributed to its wide use and rapid development since its advent in the 1930s. In hydropower developments below 25 m level power, the tubular turbine has largely displaced the axial turbine, and therefore it is typically used for tidal power. Currently, the largest per unit installed capacity is 65.8 MW (bulb turbine in Japan only), the largest runner diameter has reached 8.2 m (shaft-well tubular turbine in America), and the highest power level is 22.45 m (bulb turbine in Japan) [2–4]. Since the 1960s, research and application of tubular turbines has been well developed in China, and the largest runner diameter of an operating bulb tubular turbine is now 7.5 m. Tubular-turbine hydropower stations have been planned and constructed all over the country. The hydropower station constructed in Changzhou Guangxi includes 15 turbine installations and 621.3 MW installed capacity [5].

Shaft-extension type tubular turbines and shaft tubular turbines have almost the same advantages of technical and economic feasibility as bulb tubular turbines for low-water-level power stations. However, shaft tubular turbines have been used only in a few stations with relatively low capacity in China. The main reason for this is that the key technologies of flow-passage design, integrated turbine structure, corrosion-resistant blades, methods of connecting the speed-increase gearbox, and arrangement of the oil head in a double adjustable structure are still unsupported by thorough research and design, with the result that the shaft tubular turbine is still undeveloped and underutilized, although it

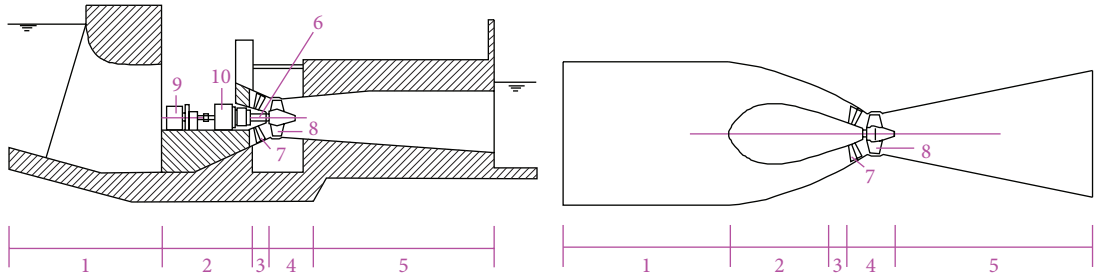

Figure 1: 2D view of the flow channel in a bidirectional shaft tubular turbine; (b) is the top view of (a). 1 indicates the inlet section, 2 is the shaft section, 3 is the guide-vane section, 4 is the movable guide-vane section, 5 is the draft tube section, 6 is the principal axis, 7 is the movable guide vane, 8 is the wheels, 9 is the generator, and 10 is the speed-change gearbox.

offers simple structure and good performance, is easy to install and maintain, and is from 20% to 60% cheaper than the bulb tubular turbine. Therefore, research into these new types of tubular turbines is a far-reaching, significant, and urgent task so that the costs of construction and operation can be reduced and the development of this turbine in tidal power plants can be promoted.

2. Working Principles

Figure 1 shows a profile view of a shaft tubular turbine in a tidal power plant. The 2D flow channel in the bidirectional shaft tubular turbine includes five parts: the inlet section, the shaft section, the guide-vane section, the wheels, and the draft tube section. The generator and the speed-change unit as described above are arranged on the shaft. The movable guide vane described above is arranged in the guide-vane section, which is installed before the inlet in the side of the turbine wheel. The principal axis described above is connected to the water turbine, speed-increase unit, and generator, which transmits the mechanical energy from the water turbine into the speed-increase unit and the generator. The water turbine described above is set in the runner chamber of the runner section. The runner described above is arranged at the end of the principal axis of the water turbine.

Working Principle [6, 7]. The turbine is installed as part of the bidirectional tidal power plant. After the tide starts to rise, the gate is closed when the tidal water level and the water level in the plant are close to equal. As the tide level continues to rise, a situation with internal low and external high water levels is created. The water turbine goes into operation and starts to generate electricity when the water head is higher than the minimum allowable working head. At the same time, water from the open ocean flows into the reservoir, raising the water level in the reservoir. The tide continues to rise rapidly, as well as the working head level, until high tide. When the tide starts to fall, the water level in the reservoir becomes high. The water turbine is shut down when the water head is lower than the minimum allowable working head. The main advantage of this type of tidal power plant is that it can generate electricity during both rising and falling tides except when the water levels in the internal and external reservoirs are equal. Therefore, the generation operating time and generation capacity are greater than those of a one-way tidal power station, making full use of tidal energy. The flow is in opposite directions at different times, and the turbine operates bidirectionally. In addition, the turbine has good energy conversion performance in both operating modes. Consequently, this turbine can extract as much tidal energy as possible, improve energy usage, and increase the benefits of tidal power.

3. Numerical Simulation [8–12]

3.1. Basic Equations. The continuity equations (incompressible viscous flow continuity equations) are

$$\frac{\partial u_i}{\partial x_i} = 0, \tag{1}$$

where u_i represents the instantaneous velocity in flow direction I and x_i represents the coordinates.

The Reynolds average model, which is widely applied in engineering, was used in this research. The Reynolds-averaged Navier model is obtained through the Navier-Stokes equations, which were averaged with the Reynolds-averaged equations. Averaged turbulence equations will contain pulsating second-order correlation measurements. For the closed equation, the corresponding equation turbulence model was introduced.

For the N-S Reynolds-averaged equations, it is possible to state that

$$\frac{\partial (u_i)}{\partial t} + \left(u_j\right) \frac{\partial (u_i)}{\partial x_j} = -\frac{1}{\rho} \frac{\partial (p)}{\partial x_i} + \upsilon \frac{\partial^2 (u_i)}{\partial x_j \partial x_j} - \frac{\partial \left(u_i' u_j'\right)}{\partial x_j} + \langle f_i \rangle . \tag{2}$$

In the above formula, the Reynolds stress term represents the rate of change in the space $-\rho(u_i' u_j') = \mu_t((\partial u_i/\partial x_j) + (\partial u_j/\partial x_i)) - (2/3)(\rho k + \mu_t(\partial u_i/\partial x_i))\delta_{ij}$. The physical meaning of the Reynolds stress is the average momentum flux pulsation. In other words, in a turbulent flow field, this stress plays a role in controlling the average pressure on the body, the

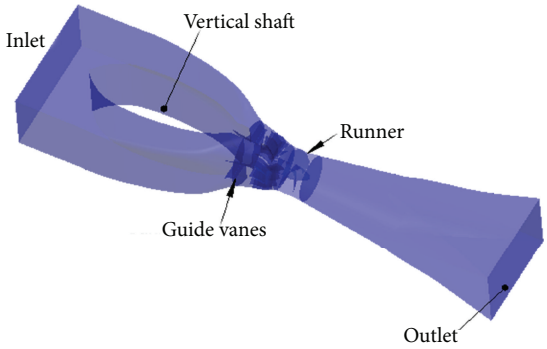

Figure 2: Overall calculation model.

viscous stress, and the average means molecular mass force, not only to provide an average amount of growth momentum but also to provide the average momentum flux pulsation. To make the equation closed, the Boussinesq approximation was used for analog Reynolds stress items. The Boussinesq approximation can be written as

$$-\rho\left(u_i'u_j'\right) = \mu_t\left(\frac{\partial u_i}{\partial x_j} + \frac{\partial u_j}{\partial x_i}\right) - \frac{2}{3}\left(\rho k + \mu_t\frac{\partial u_i}{\partial x_i}\right)\delta_{ij}, \quad (3)$$

where μ_t is the eddy viscosity coefficient and k is the turbulent kinetic energy. According to experimental calculations, the RNG $k-\varepsilon$ turbulence model was used.

3.2. Geometric Model and Boundary Conditions. Figure 2 shows the whole calculation model. The calculation area contains the turbine runner, guide vanes, and flow passage. Because the full-flow three-dimensional model is much more complex, the paper used a hybrid grid which was combined with the unstructured tetrahedral mesh and the structured hexahedral mesh to partition the model grid; the total number of grid cells was 931800.

The blade shape of the turbine runner played a decisive role in hydraulic performance. The turbine blades are a space warp face, as shown in Figure 3, which presents a geometric model of a turbine runner.

Near the Solid Wall Boundary. The velocity gradient of the viscous sublayer is high near the solid wall for turbulent flow. The high-Reynolds-number calculation model is no longer applicable. The gradient can be obtained using the wall function for flow near the wall.

Inlet Boundary. The inlet conduit imports the inlet boundary and uses the pressure-inlet boundary condition.

Outlet Boundary. The outlet conduit exports the outlet boundary and uses the pressure-outlet boundary condition.

3.3. Efficiency Calculation Method. Efficiency is an important parameter for measuring turbine energy performance.

Turbine output is the power output of the turbine shaft, commonly denoted by P and with kW for the units.

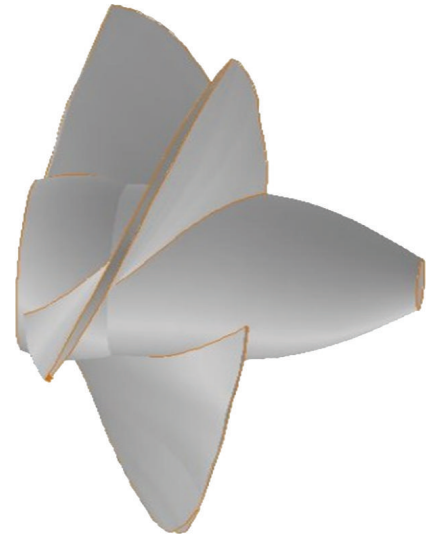

Figure 3: Runner model.

The turbine input power is the total energy flow through the turbine per unit time. The flow output is usually indicated by the symbol P_n:

$$P_n = \gamma QH = 9.81QH\,(\text{kW})\,. \quad (4)$$

A certain energy loss occurs as the water flows through the turbine. So the turbine output P is always smaller than the flow output P_n. The ratio of turbine output to water output is called the turbine efficiency and is indicated by η_t:

$$\eta_t = \frac{P}{P_n}. \quad (5)$$

4. Runner Optimization

Tubular-turbine blades have a 3D twisted leaf shape. In the work reported in this section, the flow component parameters were kept at the same values under the same calculation conditions to optimize the three aspects of the blade shape and to perform a CFD simulation using various models. The results obtained were analyzed for optimality.

4.1. Shape Optimization of Turbine Blade Edges. Figure 5 shows a schematic view of the modification; improved access to the turbine blade edge was achieved by changing the edge from straight to curved, as shown in Figure 4, which presents different single-blade diagrams for straight and curved edges.

Numerical simulations of the two blade-edge shapes were performed under the positive operating mode (H = 2.5 m, guide-vane opening speed = 65%, and speed = 200 rpm), with results listed in Table 1. It is apparent that different blade edges have an impact on performance, although the overall efficiency slightly decreased. However, the turbine discharge increased significantly, with a substantial increase in output torque, which contributes greatly to improved output.

Table 2 shows the head loss of various components for the two blade-edge shapes. It is clear that the hydraulic losses

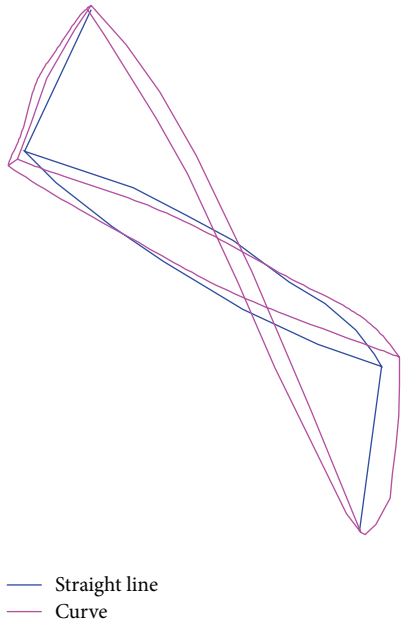

Figure 4: Turbine blade edge, schematic view.

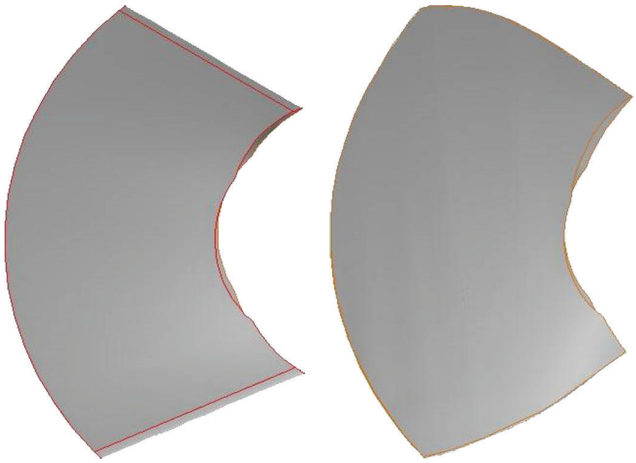

Figure 5: Single-blade diagram ((a) is a straight edge and (b) is a curved edge).

Table 1: Calculated results for two kinds of blade-edge shapes.

Blade-edge shapes	Discharge (m^3/s)	Torque (N M)	Efficiency (%)	Output (KW)
Straight edge	6.05	5909.23	83.36	123.74
Curved edge	9.38	9133.39	83.16	191.25

in the runner segment with the curved edge were greatly reduced, but this segment led to the inlet conduit section, where the guide-vane segments and the outlet conduit segment increased the hydraulic losses. The additional losses entailed by these components diminished slightly the reduced hydraulic losses in the runner segments, which corresponded to the efficiency change of the two blade-edge shapes shown in Table 1. However, the discharge was greatly improved, which directly increased unit output.

Table 2: Component hydraulic losses for different blade-edge shapes.

Blade-edge shape	Inlet conduit segment loss	Guide-vane segment loss	Runner segment loss	Outlet conduit segment loss
Straight	0.003	0.028	0.285	0.077
Curved	0.005	0.046	0.177	0.151

Table 3: Performance calculations for different blade twist angles under the positive power model.

Blade twist angle	Discharge (m^3/s)	Torque (N M)	Efficiency (%)	Output (KW)
3°	5.85	5529.77	80.71	115.79
5°	6.05	5909.23	83.36	123.74
7°	**9.38**	**9133.39**	**83.16**	**191.25**
9°	9.15	8537.45	79.67	178.78
11°	8.54	7453.39	74.52	156.07

Table 4: Performance calculations for different blade twist angles under the reverse power model.

Blade twist angle	Discharge (m^3/s)	Torque (N M)	Efficiency (%)	Output (KW)
3°	5.58	4529.77	69.31	94.85
5°	6.46	5609.23	74.14	117.46
7°	**8.39**	**8133.39**	**82.77**	**170.31**
9°	7.55	7037.45	79.59	147.37
11°	6.78	6053.39	76.23	126.76

4.2. Blade Twist Angle Optimization. The blade twist angle directly affects flow capacity and torque and has a significant impact on efficiency and unit output. Different blade twist angles were therefore investigated. Before retrofit design, the blade twist angle was 5°; a decrease to 3° and increases to 7°, 9°, and 11° were examined, giving five twist-angle cases. Numerical simulation was performed with the five models under the same operating conditions (H = 2.5 m, guide-vane opening speed = 65%, and speed = 200 rpm), and the calculated results are shown in Tables 3 and 4.

From Tables 3 and 4, when the blade twist angle = 7°, the efficiency and unit output have the largest values.

4.3. Optimization of the Distance between the Runner and the Guide Vanes. Figure 6 shows a three-dimensional model of the runner vanes and the runner. The distance between the two components, represented by the letter d, has a significant impact on efficiency and unit output. The runner diameter is denoted by r and has a fixed value. Simulated changes in d/r, which involve changing the distance between the guide vanes and the runner, were used to compare different blade

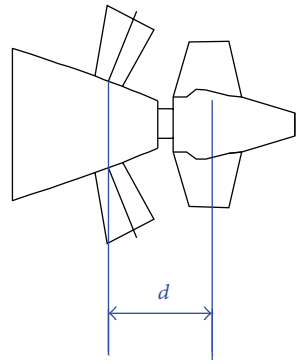

Figure 6: Three-dimensional model of runner vanes and runner.

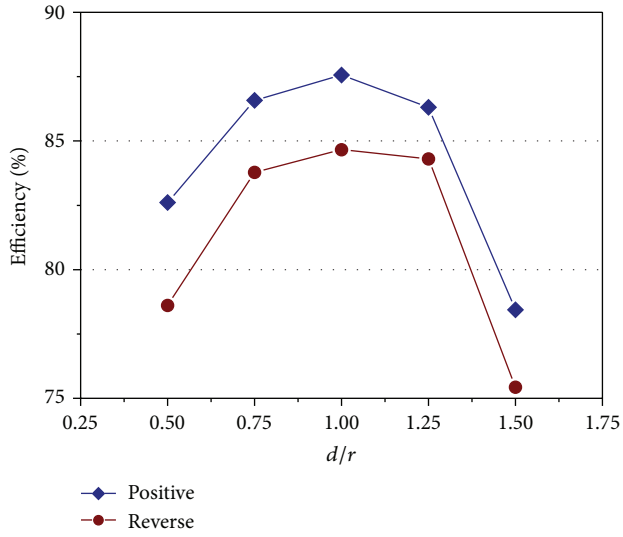

Figure 7: Efficiency versus d/r contribution plot for positive and reverse working conditions.

locations, where $d/r = 0.5, 0.75, 1.0, 1.25, 1.5$, and 2, giving five different positions. Numerical simulations were performed with the five models under the same operating conditions ($H = 2.5$ m, guide-vane opening speed = 65%, and speed = 200 rpm), with the calculated results shown in Figures 7 and 8.

From Figures 7 and 8, it can be seen that when $d/r = 0.75$, 1.0, and 1.25, the runner efficiency and the output had higher values, indicating that the distance between the guide vane and the runner must not be too large or too small. In this situation, $d/r = 0.75$ was taken as the optimal value.

4.4. Analysis of Flow Pattern before and after Optimization. In the previous sections, three optimization aspects were considered, and optimal parameter values were integrated to achieve optimization improvements. Specifically, the curved blade-edge shape was chosen, the optimal blade twist angle was 7°, and $d/r = 0.75$. Numerical simulations should be performed to analyze flow patterns before and after optimization.

4.4.1. Static Pressure Distribution of the Blade. Figures 9 and 10, respectively, show the static pressure distributions before and after modification of the blade. The pressures gradually decreased in the flow direction on the whole, with the positive pressure greater than the back pressure, which had some influence on the positive pressure, but the difference was small. After the blade was improved, the low pressure was localized mainly in the middle of the turbine wheel hub.

4.4.2. Surface Relative Velocity Distribution. Figures 11 and 12, respectively, show the front and back relative velocity distribution before and after modification. As is clear from the figure, both before and after blade retrofits, the water flow along the blade surface was smooth, with no turbulence, and the flow pattern was good.

5. Experiments

The hydraulic machinery multifunction test bench of Hohai University was used for the "211 Project" key construction

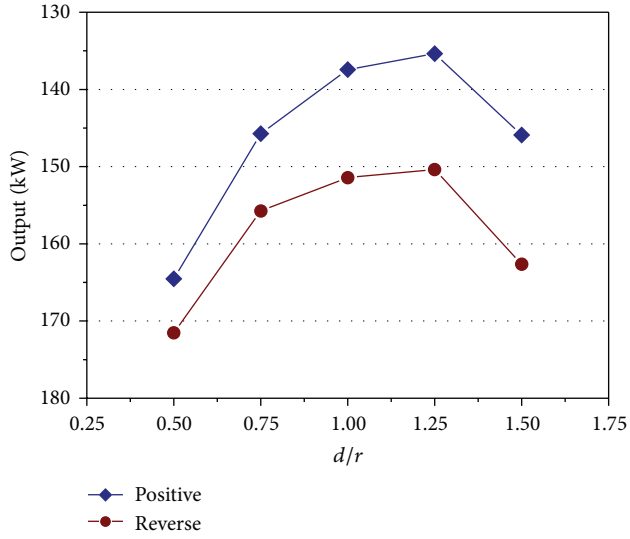

Figure 8: Output versus d/r contribution plot for positive and reverse working conditions.

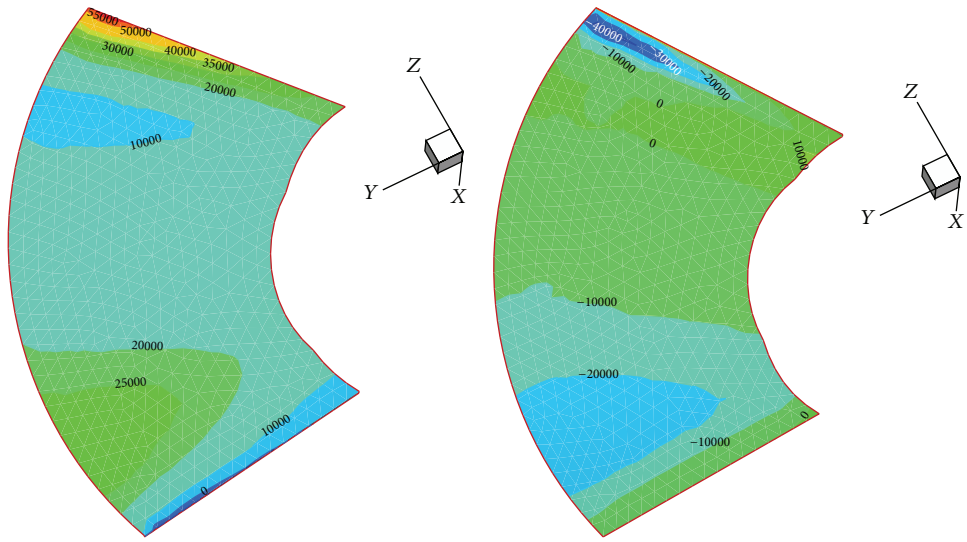

(a) (b)

Figure 9: Static pressure distribution of blade before modification ((a) is the front face and (b) is the back face).

projects. The test bench was designed and constructed according to standard DL446-91 "Turbine Model Acceptance Tests," with an integrated test error less than or equal to 4%. The test bed is a vertical closed-loop system with a total capacity of 50 m^3. The main equipment consists of the tail tank, pressure tank, electromagnetic water pump (or auxiliary pump), electric valve, manual butterfly valve, Φ500 pipes, and other components. The main parameters are as follows:

head: H = 0–20 m;

discharge: Q = 0–1 m^3/s;

torque: M = 0–200 N • M;

speed: n = 0–2000 rpm.

Figure 13 provides a photograph of a guide vane. The masses of water around the guide vanes are an important part of the turbine system, and the flow energy loss in the water guide vanes will affect the efficiency of the turbine. By adjusting the guide vanes, unit load changes can be compensated for. A photograph of the runner model is shown in Figure 14. Using the wheeled test bench, forward and reverse efficiency and performance experiments could be carried out. The model test head was kept stable at H = 2.5 m; by adjusting the guide vane in steps from 30° to 85°, each guide vane could be kept stable for five minutes in each position to collect data. Statistics of the collected data and efficiency data calculated by numerical simulation under the same conditions are shown in Figures 15–17.

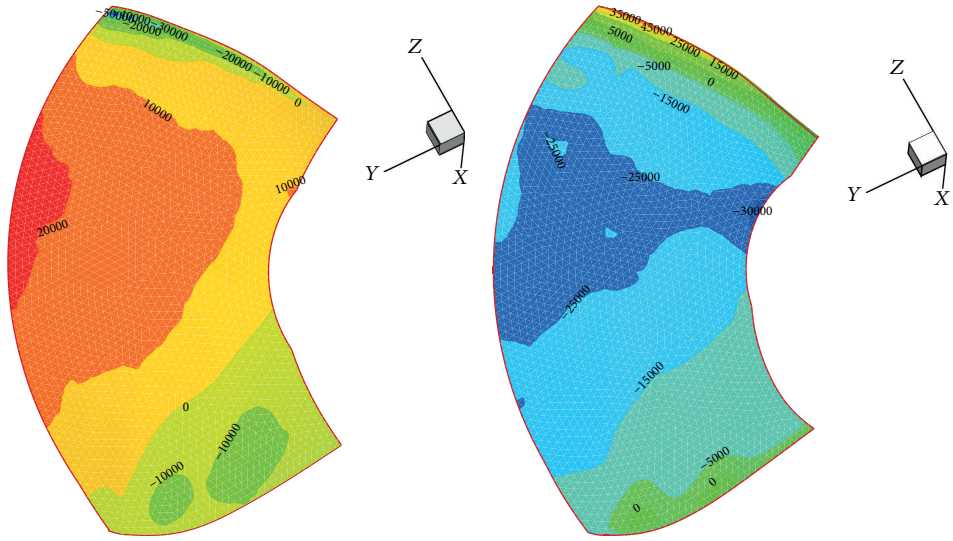

(a) (b)

Figure 10: Static pressure distribution of modified blade ((a) is the front face and (b) is the back face).

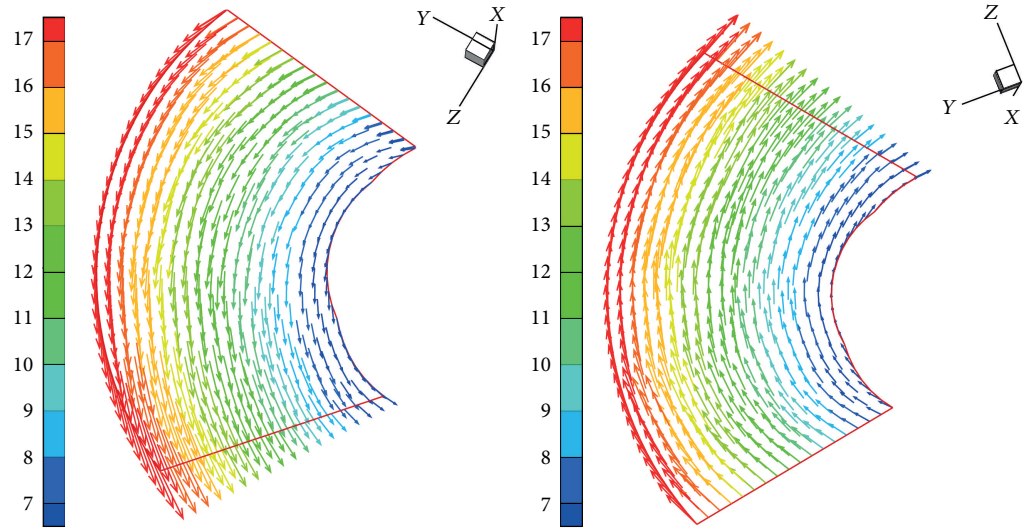

(a) (b)

Figure 11: Relative velocity distribution (front (a) and back (b)) of blade before modification.

As shown in Figure 15, the discharge increases with guide-vane opening flow for both positive and reverse generation cases. When the guide vane reaches 70% open, the discharge does not increase any more under the positive condition because with further opening of the guide vane, the hydraulic losses increase so much that further increases in discharge cannot be achieved.

Figures 16 and 17 show that

(1) numerical simulation results matched with experimental data very well;

(2) the efficiency of the positive generation condition is slightly greater than that of the reverse condition;

(3) the highest efficiency for positive generation was achieved at guide-vane opening = 60%, discharge = 8.5 m^3/s, efficiency = 86.4%, and output = 186.5 kW. The highest efficiency for reverse generation was achieved at guide-vane opening = 75%, discharge = 7.87 m^3/s, efficiency = 84.08%, and output = 163.5 kW.

6. Conclusion

The shaft tubular turbine is a form of tidal power station turbine which can provide bidirectional power with high efficiency. The turbine runner is the core component which converts water energy into mechanical energy. This paper

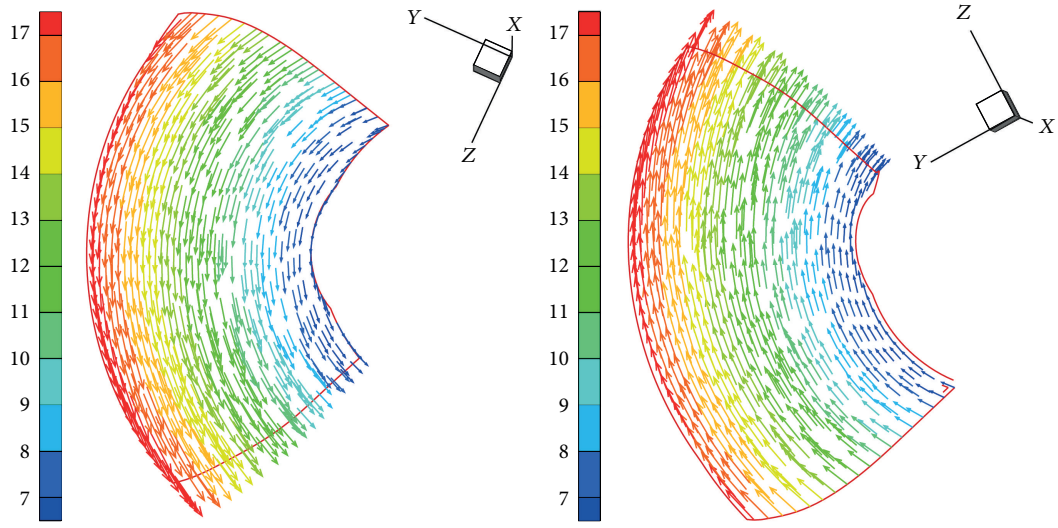

Figure 12: Relative velocity distribution (front (a) and back (b)) of modified blade.

Figure 13: Photograph of guide vane.

Figure 14: Photograph of turbine runner model.

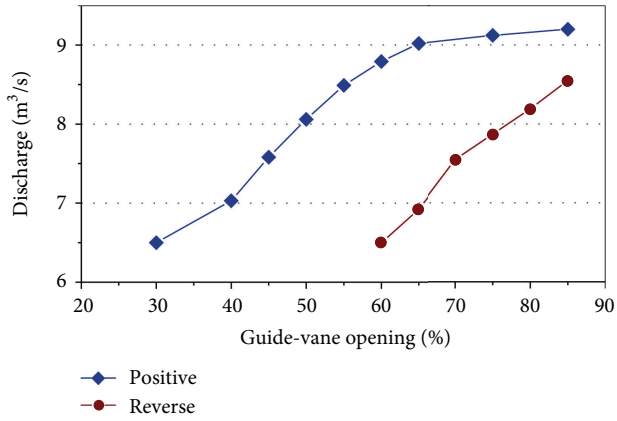

Figure 15: Discharge versus guide-vane opening curve.

has optimized the runner from three aspects using numerical simulation methods and verified the optimized runner design. From the hydraulic machinery multifunctional tests, the main conclusions are as follows.

(1) Comparing the curved-edge and straight-edge blades under the same operating conditions, the efficiency changes a little, but the curved-edge blade can directly increase discharge capacity and output, meaning that the curved-edge blade is much better than the straight-edge blade.

(2) Blade twist angle directly affects flow capacity and torque and has a significant impact on efficiency and unit output. According to the model used in this paper, when the blade twist angle = 7°, the bidirectional efficiency and unit output have the best values.

(3) The optimized ratio d/r of the guide vanes and runner distances is (0.75–1.25) because when the ratio is too large or too small, the flow patterns between guide vane and runner are relatively poor.

(4) When model tests of the optimized runner were carried out, by comparing the model test and numerical simulation results, it was found that the numerical simulation results matched the experimental data

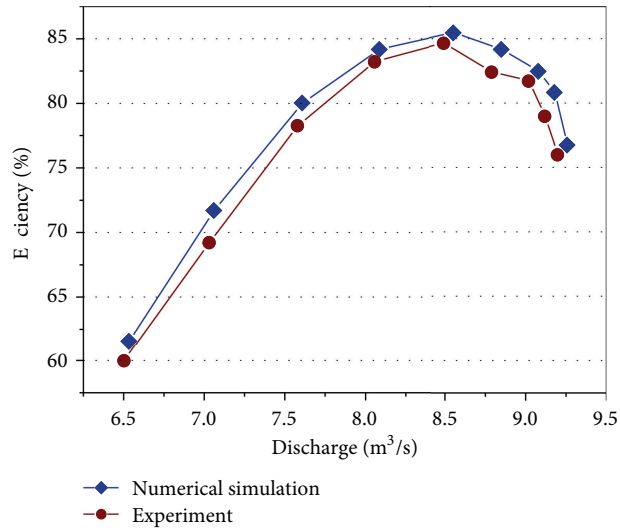

Figure 16: Efficiency versus discharge curve for the positive generation case.

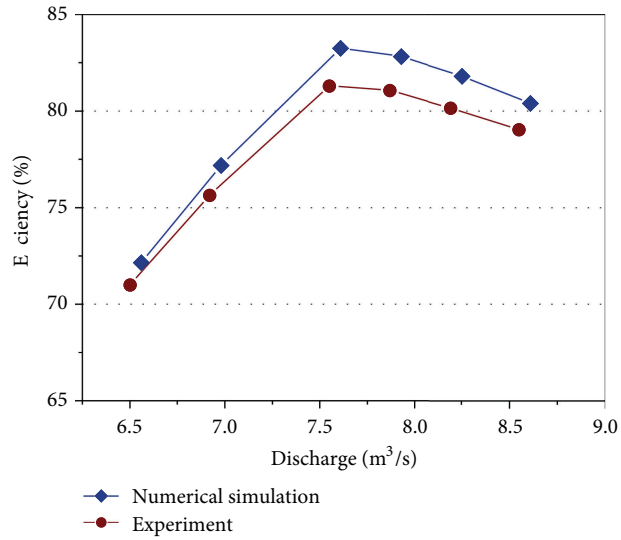

Figure 17: Efficiency versus discharge curve for the reverse generation case.

very well, which verified the correctness of the optimal results.

Acknowledgment

This work is supported by Special Funds for MRE: GHME2011CX02.

References

[1] C. Yang, Y. Zheng, and J. Yan, "Inlet passage's development and calculation of new tidal unit-shaft tubular turbine," in *Proceedings of the International Conference on Materials for Renewable Energy & Environment*, 2012.

[2] Y. Chunxia, Z. Yuan, and Z. Daqing, "Development and optimization design of shaf tubular turbine with super low-head," in *Proceedings of the 26th IAHR Symposium on Hydraulic Machinery and Systems*, 2012.

[3] Z. yuan and G. Zaiming, "Research on energy characteristics of bidirectional tubular turbine," in *Proceedings of the 5th Joint ASME/JSME Fluids Engineering (FEDSM '07)*, San Diego, Calif, USA, 2007.

[4] C. Nai-Xing and X. Yan-Ji, "Numerical computation of 3-D turbulent flow in turbine cascade," *Chinese Science Bulletin*, vol. 1, pp. 57–61, 2005.

[5] Z. yuan and Z. Zongyin, "Technique on flow measurement and its application in low head and large discharge pump stations," in *Proceedings of the 5th Joint ASME/JSME Fluids Engineering*, San Diego, Calif, USA, 2007.

[6] Y. Yang, L. Hao, J. Guo, and L. Zhang, "The research and design of vertical-shaft water turbine power generation device," in *Proceedings of the International Conference on Materials Science and Technology (ICMST '10)*, Trans Tech Publications, Jeju Island, Republic of Korea, December 2010.

[7] J. Feng-Mei, X. Gang, and X. Zhi-Min, "Calculation method of fluid and structure interaction in a vertical-axis tidal current turbine," *Zhendong Yu Chongji/Journal of Vibration and Shock*, vol. 32, no. 8, pp. 91–95, 104, 2013.

[8] S. Obara, Y. Morizane, and J. Morel, "Study on method of electricity and heat storage planning based on energy demand and tidal flow velocity forecasts for a tidal microgrid," *Applied Energy*, vol. 111, pp. 358–373, 2013.

[9] W. FuJun, *Computational Fluid Dynamics Analysis—CFD Software Principle and Application*, Tsinghua University Press, Beijing, China, 2004.

[10] G. Xinfeng, Z. yuan, G. Zhongxin, and S. Minghui, "Efficiency calculation and the vortex characteristics research of centrifugal pump," in *Proceedings of the 26th IAHR Symposium on Hydraulic Machinery*, Beijing, China, August 2012.

[11] X. Fan, L. Zhou, and X. Zhang, "Optimization of household mini tubularturbines of shaft extension," vol. 31, no. 5, pp. 260–265, 2012.

[12] L. Tan, S. Cao, and S. Gui, "Hydraulic design and pre-whirl regulation law of inlet guide vane for centrifugal pump," *Science China Technological Sciences*, vol. 53, no. 8, pp. 2142–2151, 2010.

Hindawi Publishing Corporation
Advances in Mechanical Engineering
Volume 2013, Article ID 186056, 8 pages
http://dx.doi.org/10.1155/2013/186056

Research Article

Numerical Simulation of Section Systems in the Pelamis Wave Energy Converter

Hongzhou He,[1,2] Quanyou Qu,[1] and Juyue Li[1]

[1] *Fujian Province Key Laboratory of Energy Cleaning Utilization and Development, Jimei University, Xiamen 361021, China*
[2] *Cleaning Combustion and Energy Utilization Research Center of Fujian Province, Jimei University, Xiamen 361021, China*

Correspondence should be addressed to Hongzhou He; hhe99@126.com

Received 28 June 2013; Revised 13 September 2013; Accepted 13 September 2013

Academic Editor: Fabrizio Marignetti

Copyright © 2013 Hongzhou He et al. This is an open access article distributed under the Creative Commons Attribution License, which permits unrestricted use, distribution, and reproduction in any medium, provided the original work is properly cited.

The working principle of the Pelamis wave energy converter is described in this paper. The sectional size suitable for the outside sea of Xiamen Bay is redesigned according to the Froude and Strouhal similarity criteria. The swing angles, hydrodynamic coefficients, and wave exciting forces are calculated based on the AQWA hydrodynamic software and the average outside sea condition of Xiamen Bay. It is concluded that the Pelamis after redesigned by the Froude and Strouhal similarity criteria can run better in the outside sea area of Xiamen Bay. The three sections indirectly contacted with the fixed axis have larger swing angles. The wave period and height affect the speed of the response of the section and its swing angle range, respectively. The larger the total forces, the larger the swing angles. The wave circular frequency has a greater effect on the added mass and the wave exciting force than on the radiation damping; the heave added mass and the heave wave exciting force will become smaller when the heave radiation damping becomes larger with the increase of the wave circular frequency.

1. Introduction

Power generation is the main wave utilization style. Many countries paid great attention to the wave utilization technologies. Britain has built oscillating-water column wave power station and Pelamis wave energy converter [1, 2]. Most of the oscillating-water column wave power stations are limited to be built off shore at the present stage. This technology is not stable enough to be utilized in deep sea conditions. Japan has focused on Mighty whale wave power boat and pendular type machines [3, 4]. Its Pendulum power generation device holds high energy conversion efficiency but low power efficiency. Meanwhile, it needs high initial investment and is easy to be damaged. Norway has studied Tapchan wave energy converter [5]. However, their device is highly related to the local geography. The Pelamis wave energy converter is of high stability and adapting to harsh environment and is concerned by many experts and scholars. Correspondingly, its generated electricity has been supplied to the grid network [6]. Pelamis wave energy converter has developed two generations of machines: the Pelamis P1 and the Pelamis P2. The Pelamis P2 is developed on the basis of the Pelamis P1. So a lot of significant design has been improved and it has higher efficiency than the Pelamis P1.

Considering the advantages mentioned above, it is of high significance to explore its performance in China's sea conditions. So the purpose of this paper is to analyze whether the Pelamis after redesigning by the Froude and Strouhal similarity criteria can achieve better performance in the outside sea condition of Xiamen Bay and to study the factors affecting its performance. The size of the sections based on the average sea condition of the outside sea area of Xiamen Bay is designed and the operating conditions of Pelamis wave energy converter are described. Meanwhile, the four-section swing angles, hydrodynamic coefficients, total forces, and wave exciting forces are calculated, respectively.

2. The Pelamis Wave Energy Converter

2.1. The Constitute of the Pelamis Wave Energy Converter. Although the Pelamis P2 has more outstanding feature than Pelamis P1 in Europe, no research has been done on their performance in China's sea conditions. The present research is based on the Pelamis P1 machine. The prototype was 120 m in length, 3.5 m in diameter, and comprised of four tubes

sections linked by three short power conversion modules [7]. The power conversion modules are joined to the tubes, which are used to convert wave energy into hydraulic energy.

Each machine requires its own individual mooring spread consisting of some main moorings and a yaw restraint line. The main moorings consist of a number of anchors connected to a central point. The yaw restrain line is a simple single anchor and mooring line configuration. The latter make the Pelamis always in the optimum orientation. There is scope for neighboring mooring spreads to share anchor points, depending on the anchoring techniques employed at the site. The Pelamis mooring spread has been designed to minimize its footprint area, allowing the highest concentration of MW capacity to seabed space and reducing infrastructure costs. The power take-off system includes hydraulic cylinders, motors, generators, reservoirs, accumulators, and associated piping and wiring, which are assembled in the tube section and have capability to isolate various parts of the system remotely.

2.2. Working Principle of the Pelamis Wave Energy Converter. The working principle of the Pelamis wave energy converter is shown in Figure 1. The longitudinal direction of Pelamis is perpendicular to the traveling direction of the waves, which will be ups and downs with the wave when they have effect on the section. This motion will cause the hydraulic cylinder to produce water pressure and to pass through the valve. Then it will push the hydraulic piston in hydraulic cylinder to produce a reciprocating motion. And finally, power generator is driven. In addition, Pelamis will dive into the sea when encountering high intensity wave.

The principle of energy transfer process of the Pelamis wave energy converter is described in Figure 2. It assumes that the hydraulic cylinder is double acting. Since double rod cylinder passes oil regardless of the motion direction, the upper and lower double rod cylinder can both transmit force. The section pushes the top double rod cylinder, simultaneously pulling the bottom double rod cylinder. So the energy transfer equation can be expressed as

$$E_1 = 2F_1 v = 2A_1 pr\omega = \frac{Q_1 p}{\eta_1}, \quad (1)$$

where E_1 is the input mechanical energy of two double rod cylinders, F_1 is the reaction, v is the velocity of double rod cylinders, A_1 is the piston area, p is the output pressure, r is the radius, ω is the angular frequency of wave, Q_1 is the total hydraulic flow of two double rod cylinders, and η_1 is the efficiency of the double rod cylinders.

The reaction force $-F_1$ generated by the bottom oil cylinder and the force F_1 generated by the top oil cylinder are equal in magnitude and opposite in direction. So the reaction force acting on O axis is

$$F_{c1} = F_1 - F_1 = 0. \quad (2)$$

3. Similarity Criteria

The designed wave height and period of Pelamis wave energy converter are 5.5 m and 8 s as described in the literature [7],

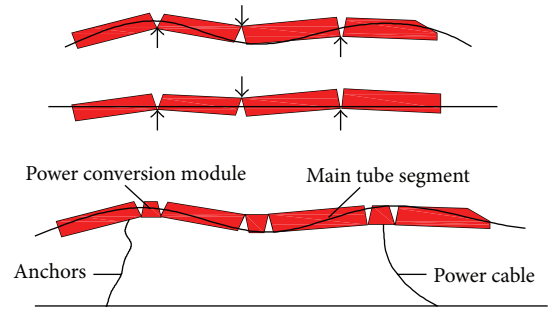

Figure 1: Working principle of the Pelamis wave energy converter.

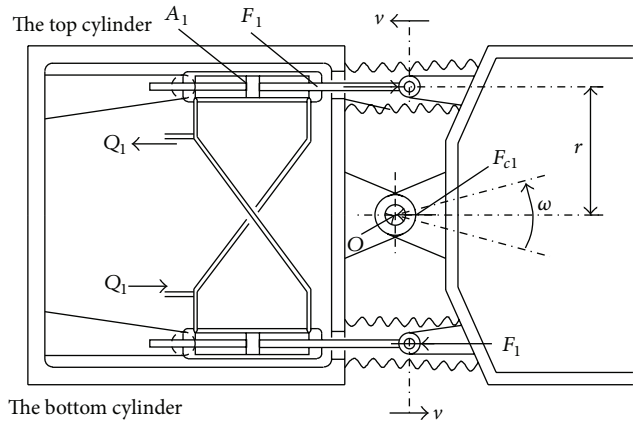

Figure 2: Schematic of the energy transfer process.

but the average wave height and period of the outside sea area of Xiamen Bay are 1 m and 3.8 s, respectively [8]. In order to analyze the performance of the converter based on the outside sea area of Xiamen Bay, the size of the Pelamis wave energy converter described in the literature needs to be adjusted by the Froude and Strouhal similarity criteria.

3.1. Froude Similarity Criteria. Froude similarity criteria ensure the correct relationship of the gravity and inertia force between the prototype and the studied model [9]. Froude number (Fr) is defined as

$$\mathrm{Fr} = \frac{v}{\sqrt{gL}}, \quad (3)$$

where g is the acceleration of gravity, L is the geometric length of the structure, and v is the characteristic velocity.

By assuming the subscript s represents the prototype and m represents the studied model and taking linear dimensions ratio (lamita) as $L_s/L_m = \lambda$, then the comprehensive equations can be described as

$$\frac{v_m}{\sqrt{gL_m}} = \frac{v_s}{\sqrt{gL_s}},$$
$$\frac{v_s}{v_m} = \sqrt{\frac{L_s}{L_m}} = \sqrt{\lambda}. \quad (4)$$

3.2. Strouhal Similarity Criteria. The Froude similarity criteria are applied to design the configuration model of the wave energy conversion device in [10, 11]. Reference [12] which indicates that the Strouhal number (St) is also an important similarity criteria number when considering the flow of having a frequency, and the rocking ship belongs to periodic motion. So the Strouhal similarity criteria must be considered when the device is redesigned. Strouhal number (St) is the ratio of the modification inertial force and the local inertial force; it ensures the period similarity of the motion and force between the prototype and the studied model [13]. Equal Strouhal number (St) of the prototype and the studied model can be expressed as

$$\frac{f_m L_m}{\nu_m} = \frac{f_s L_s}{\nu_s}, \qquad \frac{L_m}{T_m \nu_m} = \frac{L_s}{T_s \nu_s}. \tag{5}$$

So the comprehensive equation is

$$\frac{T_s}{T_m} = \sqrt{\lambda}, \tag{6}$$

where f is the wave frequency and T is the wave period.

As it is mentioned above, the prototype of pelamis can achieve better operation in Europe, but it may not be applied to China. Based on the outside sea condition of Xiamen Bay and according to the Froude similar criteria combined with Strouhal similarity criteria, the dimension of the Pelamis wave energy converter is redesigned and the length, diameter, and weight of each section of the Pelamis wave energy converter suitable for Xiamen sea conditions should be 6.8 m, 1 m, and 1102 kg, respectively.

In addition, the geometry shape of pelamis tube was also optimized. First, the section of four different tube shapes was selected according to the cylindrical shape, and then it was simulated and analyzed under the same sea condition. It seems from the simulation results that the quadrant has a better work performance than the three other tubes shapes. Therefore, the redesigned pelamis is studied on the basis of quadrant shape in this paper.

The shape and dimensions of the redesigned section are shown in Figure 3. The quadrant's two sides change into vertical planes because they are inclined planes which are not conducive to the converter's installation. Assuming the draft volumes and weights of the quadrant and the cylinder are equal, the draft depth, volume, and density can be calculated as 0.33 m, 6.95 m^3, and 158.6 kg/m^3, respectively.

4. Mathematical Model and Initial Conditions

4.1. Mathematical Model. In order to satisfy AQWA software's limitations, some assumptions are proposed as follows.

(1) Seawater is considered as the ideal fluid, the near-field solution method is used, and the four-section interactions are considered.

(2) The converter's three-dimensional model is built by the Design Modeler based on Workbench platform. Meanwhile, surface unit is applied to the quadrant's section.

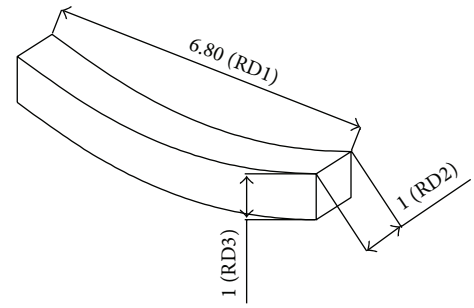

Figure 3: Schematic of the redesigned section (unit: m).

(3) The pelamis prototype is a mooring system consisting of some main moorings and a yaw restraint line. So it can not adjust itself with the winds and waves. Generally, the pelamis is arranged based on the local average wave direction. So the Pelamis device can be simplified to a fixed system, assuming the entire system is around a fixed axis, and there is no torque in axis. The simplified section model is shown in Figure 4; from left to right, the sections are named structure 1, structure 2, structure 3, and structure 4, respectively.

4.2. Initial Conditions. The limitations of AQWA software and the operation conditions of the Pelamis are described below.

(1) The quadrant section needs to meet the conditions

$$D > 0.5 r_f, \tag{7}$$

where D is the distance between the underside of device and the sea bed, r_f is the radius of the grid cell ($r_f = \sqrt{A/\pi}$), and A is the area of the grid cell.

(2) The minimum input circular frequency of the AQWA software can be calculated according to the following equation:

$$\omega_{\min} = 0.05\sqrt{\frac{g}{d}}, \tag{8}$$

where g is the acceleration of gravity and d is the water depth. Because the water depths of most outside sea area of Xiamen Bay are from 5 m to 20 m, we assume that the average water depth is 10 m in simulation. According to (8), the minimum input circular frequency can be calculated as 0.0495 rad/s.

(3) Assuming the wave is regular (the second order Stokes wave as standard), the sectional motion response under the outside sea wave condition of Xiamen Bay is analyzed by the AQWA software. Assuming the default wave direction is 0°, namely, the wave is perpendicular to the longitudinal direction of the pelamis. The sea condition parameters of the outside sea area of Xiamen Bay are shown in Table 1.

(4) Each sectional inertias moment is equal:

$$I_{xx} = 227.39\,\text{kg}\cdot\text{m}^2, \qquad I_{yy} = 4463.43\,\text{kg}\cdot\text{m}^2, \qquad I_{zz} = 4419.88\,\text{kg}\cdot\text{m}^2. \tag{9}$$

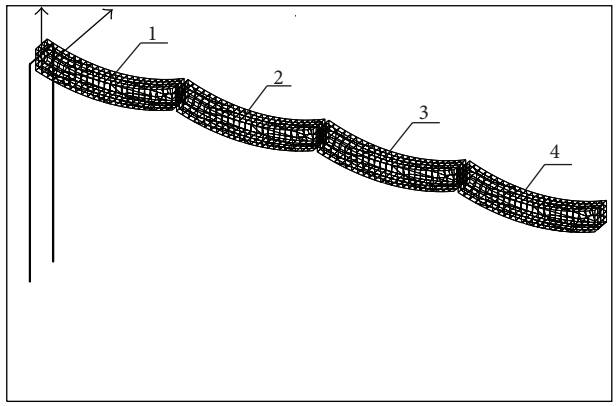

Figure 4: The section model after meshing.

Table 1: Parameters of the sea conditions [8].

	Wave height/m	Wave period/s
Spring	0.9	3.7
Summer	0.9	3.8
Autumn	1.2	4
Winter	1.1	4

5. Results and Discussion

5.1. The Swing Angle of Four Sections. Figures 5 and 6 show the four-section swing angles in spring and summer. It can be seen from Figures 5 and 6 that the swing angle ranges of structure 2, structure 3, and structure 4 are greater than that of structure 1, which indicates that the work capacity of structure 2, structure 3, and structure 4 is better than that of structure 1. It is concluded that fixed shaft limits the swing angle of structure 1. The swing angle ranges of structure 2 and structure 3 are the biggest, which indicates that the work capacities of the two section in the middle area are the strongest. Each sectional positive swing angle range is not equal to its negative swing angle range, which means that the work capacity of upper and lower hydraulic cylinder is different. The wave peaks of swing angle curve of the structure 4 vibrate with the time, which indicates that it is not conducive to achieve stable acting.

Figures 7 and 8 show the four-section swing angles in winter and autumn season. It can be seen from Figures 7 and 8 that only the swing angle curve of the structure 1 is in a steady swinging case, while the wave peaks of swing angle curve of the remaining three structures have a vibrating situation, which reveals that the swing becomes unstable with the wave period increasing. Different from Figures 5 and 6, the swing angle ranges of structure 3, and structure 4 are the greatest as it is shown in Figures 7 and 8; this means that the farther away from the fixed shaft, the greater the sectional swing angle range with the increasing of wave parameters. Meanwhile, it indicates that the work capacity of structure 3 and structure 4 is the strongest in autumn and winter season. The swing angles of structure 2, structure 3 and structure 4 are greater than that of structure 1 in Figures 7 and 8, and the ranges of the positive and negative swing angles of each swing angle curve are different.

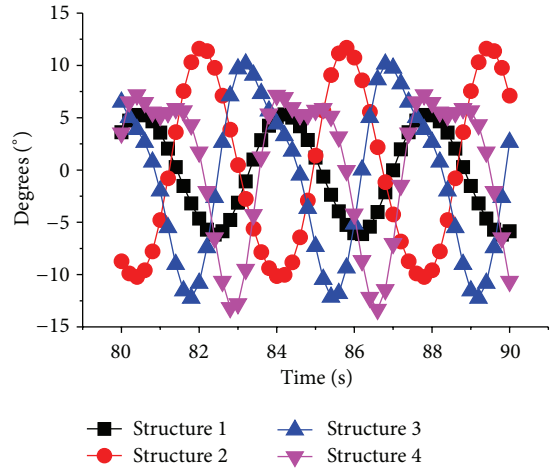

Figure 5: The four-section swing angles in spring.

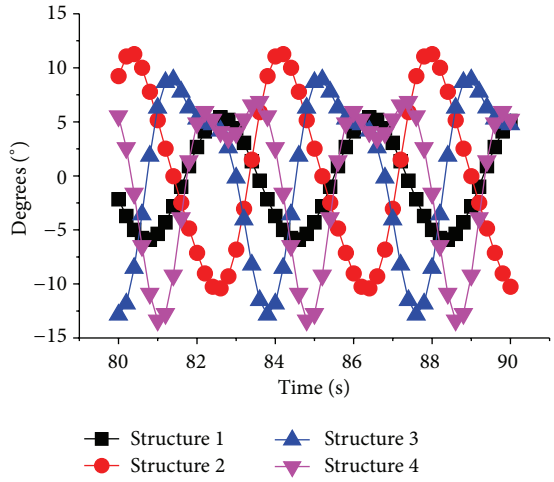

Figure 6: The four-section swing angles in summer.

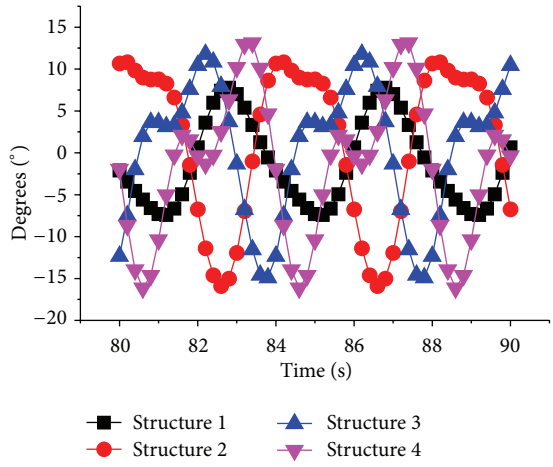

Figure 7: The four-section swing angles in autumn.

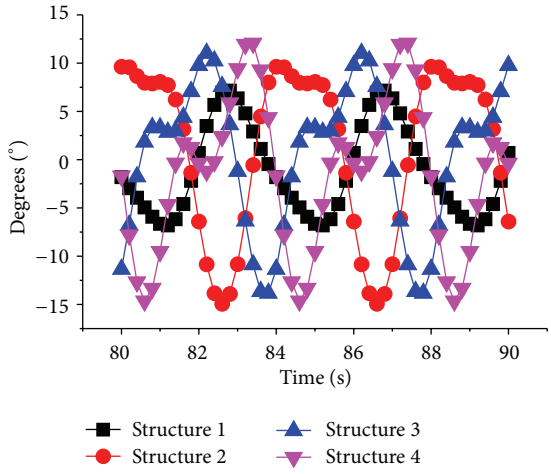

FIGURE 8: The four-section swing angles in winter.

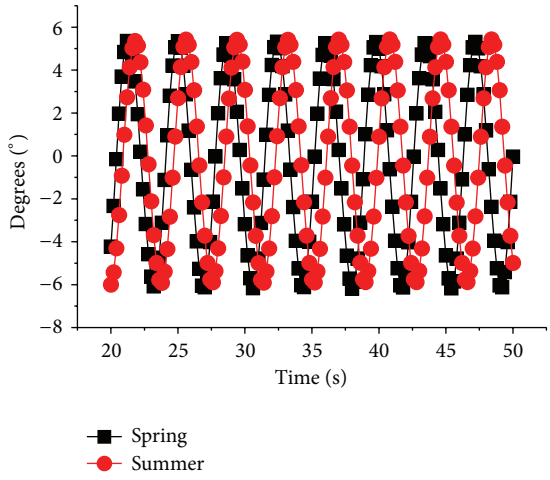

FIGURE 9: The sectional swing angles of structure 1 in spring and summer.

Figure 9 describes the swing angles of structure 1 in spring and summer season. As shown in Figure 9, the swing angles of structure 1 are from −6.1° to 5.2° and from −5.8° to 5.4°, respectively, which indicates that the wave period has little impact on the sectional swing angle in these two seasons. In addition, the swing angle's curve in summer lags behind that in spring, indicating that the wave period has some effect on the sectional swing speed.

Figure 10 shows the swing angles of structure 1 in autumn and winter season. As it is shown in Figure 10, the swing angles in structure 1 are from −7.3° to 7.7° and from −6.7° to 7.1° in autumn and winter season, respectively, which indicates that the wave height has some effect on the swing angle. The greater the wave height is, the greater the swing angle will be. The wave height has no evident effect on the speed of sectional response, because both the heave curves have no leading or lagging phenomena with the extension of the time.

5.2. The Total Force on Sections. The total forces on sections are the main factors that affect the swing angle. Figures 11 and 12, respectively represents the vertical forces on four sections

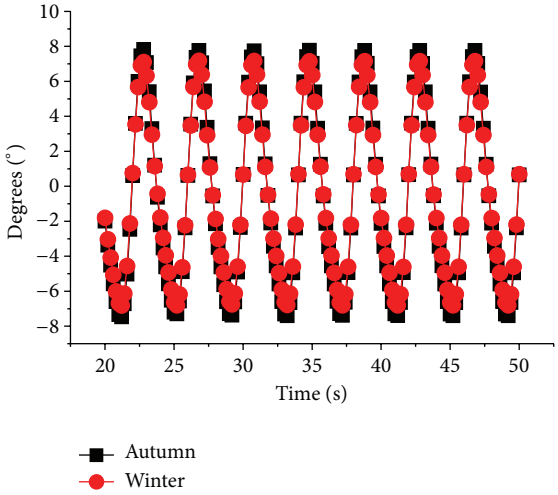

FIGURE 10: The sectional swing angles of structure 1 in winter and autumn.

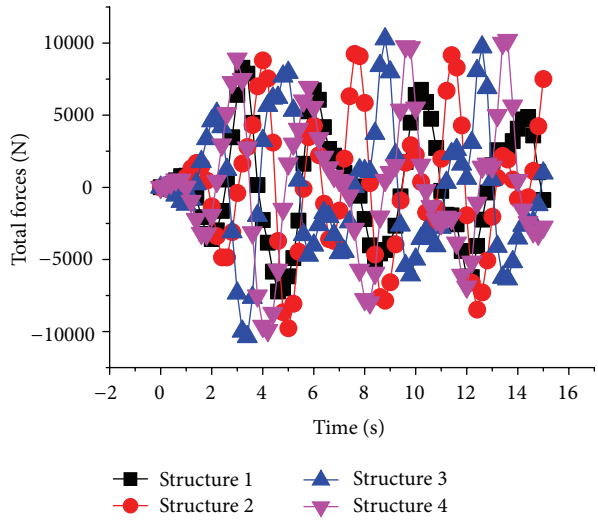

FIGURE 11: The total force on four sections in spring.

in the spring sea condition and the vertical forces on structure 1 in the four seasons' sea condition. As it is shown in Figure 11, the force on structure 1 is smaller than that of the other three situations. Considering Figure 5, it could be found that the greater the force on section is the greater the swing angle is. The force on structure 1 is smaller due to the offsetting effect of the fixed shaft. The forces on the remaining three structures are almost equal, indicating that the front section has a smaller wave-killing influence; the front section has a pulling force to the rear section and enhances the motion of the rear section. As shown in Figure 12, the forces on structure 1 are almost equal in spring and summer and also almost equal in autumn and winter. This indicates that the higher the sea level, the greater the force on section, and the more the work performance.

5.3. Hydrodynamic Coefficients and Wave Exciting Force of the Section. The purpose of this part is to investigate the

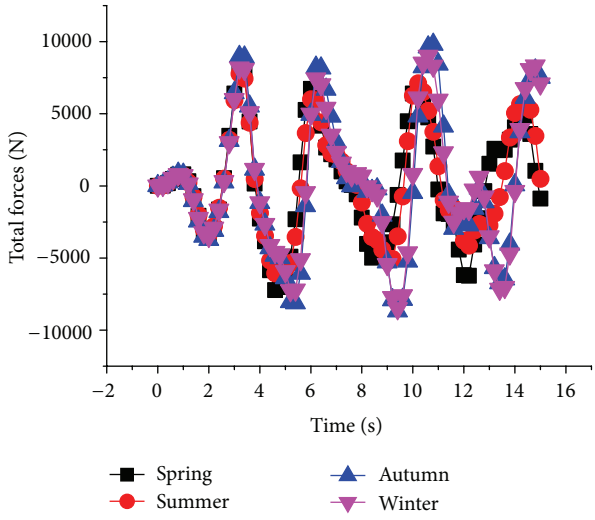

Figure 12: The total force on structure 1.

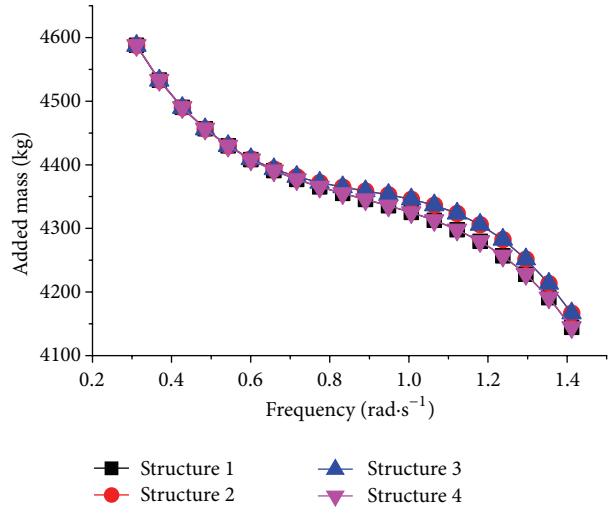

Figure 13: Added mass of four sections.

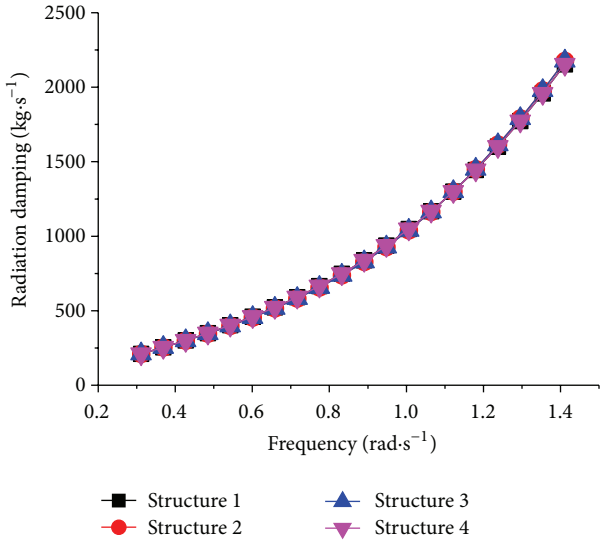

Figure 14: Radiation damping of four sections.

hydrodynamic parameters and wave exciting force on the swing angle of section, which will illustrate both values when acting on the work performance of section. When the section is acted under the wave loads, it will cause the movement of the surrounding fluid which produces radiation that generates reaction force (torque). Depending on the wave phase, the reaction force can be decomposed into corresponding modal oscillating movement velocity and acceleration, respectively, called radiation damping force and additional mass force. And their proportional coefficients are called radiation damping and added mass, respectively. The added mass and radiation damping can be described as follows under simple harmonic motion mode [14, 15]:

$$F_k = -A_{kj}\frac{d^2\eta_j}{dt^2} - B_{kj}\frac{d\eta_j}{dt}, \quad k = 1, 2, \ldots, 6, \tag{10}$$

where F_1, F_2, and F_3 represent the component force of x, y, and z directions, respectively; F_4, F_5, and F_6 are the component torque of rotating the x, y, and z directions A_{kj} and B_{kj} are the added mass and radiation damping which both have 36 parts and usually expressed as a form of matrix with $6 * 6$.

The calculation results of hydrodynamic coefficients in the vertical direction are shown in Figures 13 and 14. It can be seen from Figure 13 that the added four-section mass is almost equal when the wave frequency is less than 0.6 rad/s. The added mass of structure 2 and structure 3 differs greatly from that of structure 1 and structure 4 when the wave frequency is greater than 0.6 rad/s, which indicates that the wave circular frequency will affect the added mass under the same section geometry. The added mass decreases with the increase in the wave circular frequency while the changing rate differs greatly with different frequency band. Figure 14 shows that the heave radiation damping increases with the increasing of the wave circular frequency. The four-section heave radiation damping is almost equal, indicating that the wave condition has almost no effect on the heave radiation damping under the same section geometry. All of these show that the added mass has a great influence while the radiation damping has little influence on the swing angle of section.

For the regular wave, the unsteady fluid pressure can be divided into two parts: one is the unsteady pressure caused by undisturbed wave and the other part is diffraction force generated by changing fluid pressure spaces which are affected by the structure's existence. The sum of both parts is the wave exciting force which acts on the buoy in regular wave [16, 17]:

$$F_{\mathrm{EXi}} = \mathrm{Re}\left[-\rho A e^{i\omega t}\iint_{S_b} n_i\left(\phi_I + \phi_D\right) dS\right], \quad i = 1, 2, 3, \tag{11}$$

where Re is the Reynolds number, ρ is the density of sea water, A is the wave amplitude, ω is the wave circular frequency, n_i is the unit normal vector on S_b, and ϕ_I and ϕ_D represent the wave incident velocity potential and diffraction velocity potential, respectively.

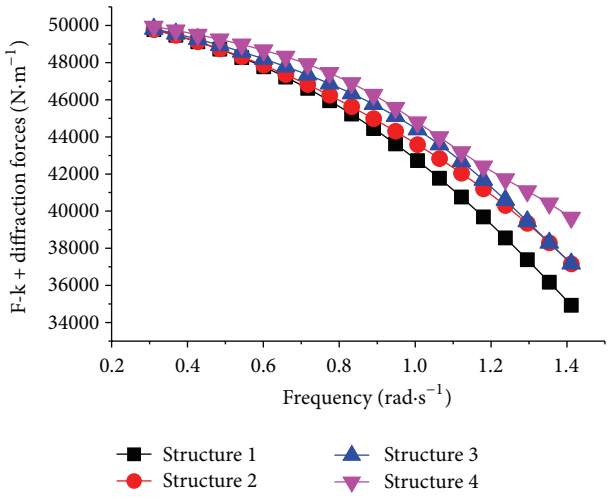

Figure 15: Wave exciting forces of four sections.

Figure 15 shows the amplitude of heave wave exciting force of the four sections under a unit wave height. It can be seen from Figure 15 that the heave wave exciting force of structure 1 is the minimum and that of structure 4 is the maximum. And the heave wave exciting forces of the other two structures are in the middle, which indicates that the swing angle increases with the increasing of heave wave exciting force, and also means that the wave exciting force has a great effect on the swing angle of section.

6. Conclusions

The characteristics of section system of a Pelamis wave energy converter were analyzed based on AQWA hydrodynamic software under four seasons' average sea condition of the outside sea area of Xiamen Bay, and the following conclusion can be drawn from this study.

(1) The pelamis after redesigned according to the Froude and Strouhal similarity criteria can run in the outside sea area of Xiamen Bay, and factors which affect its performance include the total force, the added mass, and the wave exciting force.

(2) The swing angle range of each section is different. The swing angle ranges of the three sections which are away from the fixed axis are greater than that of the section near the fixed axis.

(3) The larger the wave period, the slower the section response. And the larger the wave height, the greater the swing angle range of section.

(4) Different wave frequency will lead to different wave heave added mass and has little effect on radiation damping under the same geometry shape of section. With the increasing of wave circular frequency, the heave added mass and the exciting force decrease while the heave radiation damping increases.

(5) The produced power of the redesigned Pelamis wave energy converter in autumn and winter season is greater than that in spring and summer season.

Acknowledgments

This work was supported by the National Natural Science Foundation (no. 51209104) and Ocean Renewable Energy Development Foundation of the State Oceanic Administration (no. XMME2011BL02), which are gratefully acknowledged by the authors.

References

[1] C. Retzler, "Measurements of the slow drift dynamics of a model Pelamis wave energy converter," *Renewable Energy*, vol. 31, no. 2, pp. 257–269, 2006.

[2] S. Lindroth and M. Leijon, "Offshore wave power measurements—a review," *Renewable and Sustainable Energy Reviews*, vol. 15, no. 9, pp. 4274–4285, 2011.

[3] M. Imari, Y. Washio, and H. Osawa, "Development of an offshore floating type wave power energy converter system mighty whale," *Science & Technology in Japan*, vol. 60, no. 15, pp. 28–30, 1997.

[4] C. H. Retzler and D. J. Pizer, "The hydrodynamics of the pelamis wave energy device: experimental and numerical results," in *Proceedings of the 20th International Conference on Offshore Mechanics and Arctic Engineering; Ocean Space Utilization*, pp. 31–35, ASME, Rio de Janeiro, Brazil, June 2001.

[5] D. Vicinanza, L. Margheritini, P. Contestabile et al., "Sea wave slot-cone generator: an innovative caisson breakwater for energy production," in *Coastal Engineering 2008: Proceedings of the 31st International Conference. Hamburg, Germany*, J. M. Smith, Ed., pp. 3694–3705, World Scientific Publishing, Imperial College Press, 2008.

[6] G. J. Dalton, R. Alcorn, and T. Lewis, "Case study feasibility analysis of the Pelamis wave energy convertor in Ireland, Portugal and North America," *Renewable Energy*, vol. 35, no. 2, pp. 443–455, 2010.

[7] R. Henderson, "Design, simulation, and testing of a novel hydraulic power take-off system for the Pelamis wave energy converter," *Renewable Energy*, vol. 31, no. 2, pp. 271–283, 2006.

[8] Compilation Committee of China Bays, *China Bays*, Ocean Press, Beijing, China, 1993, (Chinese).

[9] W. Xu, *Fluid Mechanics*, National Defense Industry Press, Beijing, China, 1979.

[10] H. Zhou, *Experimental Study on the Pendulum Wave Energy Conversion Device*, South China University of Technology, Guangzhou, China, 2010, (Chinese).

[11] Y. Tian, *Numerical Simulations of Interactions Between Waves and Pendulum Wave Power Converter*, Tianjin University, Tianjin, China, 2010, (Chinese).

[12] Q. Xia, *Engineering Fluid Mechanics*, Shanghai Jiaotong University Press, Shanghai, China, 2006, (Chinese).

[13] K. Wang, X. Zhang, Z.-Q. Zhang, and W. Xu, "Numerical analysis of added mass and damping of floating production, Storage and off loading system," *Acta Mechanical Sinica*, vol. 28, no. 3, pp. 870–876, 2012.

[14] G. Yang, *TLP Research of Nonlinear Wave Force and Response*, Tianjin University, Tianjin, China, 2003, (Chinese).

[15] D. Tang, *Test Research of the Hydrodynamic Performance of Deep-Water Semi-Submersible Platform Under Wind and Waves*, Dalian University of Technology, Dalian, China, 2010, (Chinese).

[16] K. Liu, *Wave Induced Response Analysis and Heave Motion Control of a Semi-Submersible platform*, Harbin Institute of Technology, Harbin, China, 2010, (Chinese).

[17] O. M. Faltinsen, *Sea Loads on Ships and Offshore Structures*, Shanghai Jiao Tong University Press, Shanghai, China, 2008, (Chinese).

Hindawi Publishing Corporation
Advances in Mechanical Engineering
Volume 2013, Article ID 609464, 5 pages
http://dx.doi.org/10.1155/2013/609464

Research Article

Buoy-Rope-Drum Wave Power System

Linsen Zhu, Yangang Wang, Ze Yang, and Yanming Qu

Research Center of Mechanics and Mechatronic Equipment, Shandong University, Weihai 264209, China

Correspondence should be addressed to Linsen Zhu; zlinsen@sina.com

Received 28 June 2013; Revised 1 November 2013; Accepted 1 November 2013

Academic Editor: Fabrizio Marignetti

Copyright © 2013 Linsen Zhu et al. This is an open access article distributed under the Creative Commons Attribution License, which permits unrestricted use, distribution, and reproduction in any medium, provided the original work is properly cited.

A buoy-rope-drum wave power system is a new type of floating oscillating buoy wave power device, which absorbs energy from waves by buoy-rope-drum device. Based on the linear deep water wave theory and pure resistive load, with cylinder buoy as an example, the research sets up the theoretical model of direct-drive buoy-rope-drum wave power efficiency and analyzes the influence of the mass and load of the system on its generating efficiency. It points out the two main categories of the efficient buoy-rope-drum wave power system: light thin type and resonance type, and optimal designs of their major parameters are carried out on the basis of the above theoretical model of generating efficiency.

1. Introduction

As one of renewable clean energies, ocean wave energy is receiving more and more emphasis due to the double crisis of fossil energy and environment pollution [1–3]. Thousands of patents on wave power have been approved, while only a small proportion has been applied to commercial use on a large scale, the ultimate reasons for which are the great risk and high cost of wave power due to the complex and variable sea conditions [4, 5]. Therefore, the study of how to develop new type of wave power technology to enhance reliability and reduce the generating cost has become the focus of the wave power research [6–8].

A new type of floating wave power device is discussed in this paper based on the buoy-rope-drum system, which is simple in structure and costs less in laying and maintaining compared with the old oscillating buoy wave power device. The paper first introduces the working principles of buoy-rope-drum technology and studies the theoretical model and influential factors of the generating efficiency of direct-drive buoy-rope-drum wave power device on the basis of linear deep water theory and pure resistive load.

2. Buoy-Rope-Drum Wave Power System

2.1. Operating Principle of Buoy-Rope-Drum Wave Power. As shown in Figure 1, buoy-rope-drum wave power system consists of gravity anchor, rope, rope guider, generator, heating pipe, buoyant, and monitoring room. One respect of rope is tied to the gravity anchor on the bottom of the sea; the other respect is wound around the drum of the generator casing through the rope guide. When waves push the buoyant hull to rise, the rope will drag the drum to rotate, which will then drive the rotor (magnetic steel casing) of permanent magnet alternator to rotate around the stator winding so as to generate alternating current, which will supply power for the resistive load in the heating pipe after being monitored. When the buoyant hull falls with waves, the drum will collect the rope automatically under the action of the motor's built-in coiling spring. Because an overrunning clutch is installed between the drum and magnetic steel casing, the magnetic steel casing does not rotate when the drum rotates backward, and the buoyant hull does not generate power during falling.

2.2. Generating Features of Buoy-Rope-Drum Wave Power

(1) The device absorbs wave energy with the buoy-rope-drum device, which is simple in structure. The main component of the system is on the surface of the water, which hardly needs diving maintenance. Thus, the buoy-rope-drum wave power system costs less in manufacturing, laying, and maintenance compared to the current floating oscillating buoy wave power device.

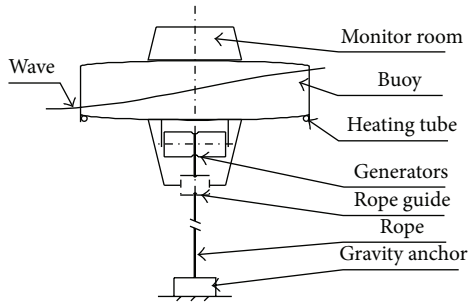

Figure 1: Schematic diagram of buoy-rope-drum wave power system.

(2) This device, which is water resistant, is equipped with low-speed permanent magnetic generator with no speed-up gearing, generator's casing adopted as drum, and built-in rope collecting coiling spring. The compact structure, light mass, and small moment of inertia all contribute to the small inertia load and strong ability of collecting wave energy.

3. The Theoretical Model of System's Generating Efficiency

3.1. Dynamic Analysis. Figure 2 shows the buoy in the rising process with still water level as reference level. X stands for the distance from reference level to static water level of the buoy, with upward direction as the positive direction, y stands for the vertical distance from reference level to surface level, with upward direction as the positive direction, and D stands for the static draft of the buoy.

With the whole device as the study object, because the buoy is floating on the sea, the whole time and the added mass of entrained water are so small that the added inertia force can be ignored, only the viscous force which formed at the bottom of the buoy when wave and buoy move at different speed. In vertical direction, based on Newton's second law, we have

$$F + Q - G - T = ma, \tag{1}$$

where F is the buoyancy of the device in N, Q is the viscous force in N, G is the gravity of the device in N, T is the tension of the rope in N, m is the mass of the device in kg, and a is the acceleration of the buoy in m/s^2.

With the roll wheel as the study object, because the moment of the coil spring is so small that it can be ignored, based on the axial rotation dynamics equation, we have

$$Tr = J\alpha + M_{\text{load}}, \tag{2}$$

where r is the radius of the roll wheel in m, J is the moment of inertia of the device in kg m^2, α is the angular acceleration in rad/s^2, and M_{load} is the resistance torque formed by load in Nm.

According to (1) and (2), we have

$$F + Q - G = ma + \frac{\left(J\alpha + M_{\text{load}}\right)}{r}, \tag{3}$$

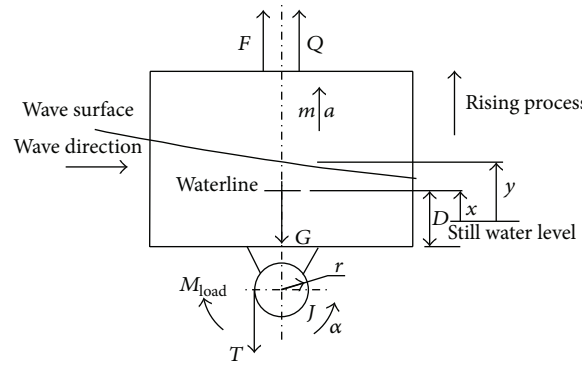

Figure 2: The dynamic analysis of buoy in rising process.

where F can be formulated as follows [9]:

$$F = \gamma A\left(ye^{-kD} - x + D\right) = \gamma A\left(ye^{-kD} - x\right) + G, \tag{4}$$

where γ is the specific gravity of the sea water with the value being set as 10094 N/m^3, A is the cross-sectional area of the buoy in m^2, D is the draft in m, k is the wave number, and

$$k = \frac{2\pi}{\lambda}, \tag{5}$$

where λ is the wave length in m. Q can be formulated as follows [9]:

$$Q = C_1\left(\dot{y}e^{-kD} - \dot{x}\right), \tag{6}$$

where C_1 is the linear coefficient of friction of the sea water in Ns/m, $\dot{y}$ is the rising velocity of wave in m/s, $\dot{x}$ is the rising velocity of the buoy in m/s, and

$$a = \ddot{x}, \tag{7}$$

$$\alpha = \frac{\ddot{x}}{r}. \tag{8}$$

As the load is pure resistive, the generator can be simply modelled with a damping coefficient; then,

$$M_{\text{load}} = C_2\dot{x}, \tag{9}$$

where C_2 is the resistance coefficient of the electrical generator in Ns.

Substituting (4)~(9) into (3), we have

$$\left(m + \frac{J}{r^2}\right)\ddot{x} + \left(C_1 + \frac{C_2}{r}\right)\dot{x} + \gamma Ax = C_1e^{-kD}\dot{y} + \gamma Ae^{-kD}y. \tag{10}$$

Let

$$y = \frac{H}{2}\cos\omega t, \tag{11}$$

where H is wave height in m and ω is the wave angular frequency in rad/s.

Then

$$\begin{aligned} C_1 e^{-kD}\dot{y} + \gamma A e^{-kD} y &= \frac{H}{2} e^{-kD}\left(\gamma A \cos\omega t - C_1\omega \sin\omega t\right) \\ &= \frac{H}{2} e^{-kD}\sqrt{(\gamma A)^2 + (C_1\omega)^2}\cos(\omega t + \sigma), \end{aligned} \tag{12}$$

where σ can be calculated as follows:

$$\sigma = \tan^{-1}\frac{C_1\omega}{\gamma A}. \tag{13}$$

Substituting (12) into (10), then

$$\begin{aligned} \ddot{x} + \frac{C_1 + (C_2/r)}{m + (J/r^2)}\dot{x} + \frac{\gamma A}{m + (J/r^2)}x &= \frac{(H/2)\, e^{-kD}\sqrt{(\gamma A)^2 + (C_1\omega)^2}}{m + (J/r^2)}\cos(\omega t + \sigma). \end{aligned} \tag{14}$$

Let

$$\begin{aligned} 2n &= \frac{C_1 + (C_2/r)}{m + (J/r^2)}, \\ \omega_0^2 &= \frac{\gamma A}{m + (J/r^2)}, \\ h &= \frac{(H/2)\, e^{-kD}\sqrt{(\gamma A)^2 + (C_1\omega)^2}}{m + (J/r^2)}. \end{aligned} \tag{15}$$

Equation (14) is simplified as follows:

$$\ddot{x} + 2n\dot{x} + \omega_0^2 x = h\cos(\omega t + \sigma). \tag{16}$$

The solution of (16) is

$$\begin{aligned} x(t) = e^{-nt}\left[c_3 \sin\sqrt{\omega_0^2 - n^2}t + c_4\cos\sqrt{\omega_0^2 - n^2}t\right] + \frac{h\cos(\omega\cdot t + \varphi)}{\sqrt{(\omega_0^2 - \omega^2)^2 + 4n^2\omega^2}}, \end{aligned} \tag{17}$$

where c_3 and c_4 are the integration constants, determined by the initial conditions and φ is the lag angle of the buoy relative to wave in rad. The steady component of (17) is

$$\begin{aligned} x(t) &= \frac{h\cos(\omega\cdot t + \varphi)}{\sqrt{(\omega_0^2 - \omega^2)^2 + 4n^2\omega^2}} \\ &= \frac{He^{-kD}\sqrt{(\gamma A)^2 + (C_1\omega)^2}}{2\left(m + (J/r^2)\right)\sqrt{(\omega_0^2 - \omega^2)^2 + 4n^2\omega^2}} \\ &\quad \times \cos(\omega\cdot t + \varphi). \end{aligned} \tag{18}$$

Then

$$\dot{x}(t) = \frac{-He^{-kD}\omega\sqrt{(\gamma A)^2 + (C_1\omega)^2}}{2\left(m + (J/r^2)\right)\sqrt{(\omega_0^2 - \omega^2)^2 + 4n^2\omega^2}}\sin(\omega t + \varphi). \tag{19}$$

Let

$$C_5 = \frac{-He^{-kD}\omega\sqrt{(\gamma A)^2 + (C_1\omega)^2}}{2\left(m + (J/r^2)\right)\sqrt{(\omega_0^2 - \omega^2)^2 + 4n^2\omega^2}}. \tag{20}$$

Then

$$\dot{x}(t) = C_5\sin(\omega t + \varphi). \tag{21}$$

3.2. Generating Efficiency Derivation. With pure resistive load, the instantaneous power of load is

$$P = I^2 R = \frac{E^2 R}{(R + r_1)^2} = \frac{(C_6\dot{x})^2 R}{(R + r_1)^2} = \frac{C_6^2 R}{(R + r_1)^2}\dot{x}^2, \tag{22}$$

where P is the instantaneous power of load in W, I is the load current in A, R is the load resistance in Ω, E is the electromotive force of generator in V, r_1 is the resistance of generator winding in Ω, and C_6 is the electromotive force coefficient in Vs/m.

Substituting (21) into (22), then the instantaneous power of the load in the rising process is as follows

$$\begin{aligned} P &= \frac{C_5^2 C_6^2 R}{(R + r_1)^2}\sin^2(\omega\cdot t + \varphi) \\ &= \frac{C_5^2 C_6^2 R}{2(R + r_1)^2}\left[1 - \cos 2(\omega\cdot t + \varphi)\right]. \end{aligned} \tag{23}$$

The generation of the device E_e in a wave period is

$$\begin{aligned} E_e &= \int_{\pi}^{2\pi}\frac{C_5^2 C_6^2 R}{2(R + r_1)^2\omega}\left[1 - \cos 2(\omega\cdot t + \varphi)\right] d(\omega\cdot t + \varphi) \\ &= \frac{\pi C_5^2 C_6^2 R}{2(R + r_1)^2\omega}. \end{aligned} \tag{24}$$

Wave energy occupied by the buoy in a wave period is [9]

$$E_w = \frac{1}{32\pi}\gamma g H^2 T^2 D_{\text{buoy}}, \tag{25}$$

where T is the wave period in s and D_{buoy} is the buoy diameter in m; then, the generating efficiency of buoy-rope-drum wave power system is

$$\eta = \frac{E_e}{E_w} = \frac{16\pi^2 C_5^2 C_6^2 R}{(R + r_1)^2\omega\gamma g D_{\text{buoy}} H^2 T^2}. \tag{26}$$

4. The Influence Factors of System Generating Efficiency

4.1. Some Parameters of System. According to many years' observation data of the Yellow Sea, the rated sea conditions are shown in Table 1.

The major parameters of the buoy are shown in Table 2.

Based on the equivalence principle of dissipated energy within the wave period, the linear coefficient of friction of the sea water C_1 can be derived from the method based on nonlinear coefficient of friction of the sea water C_D [9]:

$$C_1 = \frac{4}{3\pi}\rho C_D A_0 X_0 \omega, \tag{27}$$

where ρ is the sea-water density with the value being set as 1030 kg/m^3; C_D is the nonlinear coefficient of friction of the sea water, with the value being set as 1.2 [10]; A_0 is the wave amplitude, with the value being set as 0.5 m; X_0 is the buoy amplitude, with the value being set as 0.4 m; and ω is the wave angular frequency, with the value being set as 2 rad/s.

Substituting the above parameters into (27), we have

$$C_1 = 210\ \text{Ns/m}. \tag{28}$$

4.2. The Influence of System Mass and Load on the Generating Efficiency [11]. With system mass and load as variables and on the basis of the values of the above parameters, the calculating formulas of correlation coefficient are as follows:

$$C_2 = \frac{RE_r^2/(R+r_1)^2}{(2\pi \cdot n_r/60)^2 r\eta_r} = 48634 \times \frac{R}{(R+r_1)^2}, \tag{29}$$

$$n = 0.5 \times \frac{C_1 + (C_2/r)}{m + (J/r^2)} = \frac{105 + 3.33C_2}{m + 222}, \tag{30}$$

$$\omega_0^2 = \frac{\gamma A}{m + (J/r^2)} = \frac{45665}{m + 222}, \tag{31}$$

$$D = \frac{mg}{\gamma A} = 2.15 \times 10^{-4}\, m, \tag{32}$$

$$C_5 = \frac{-He^{-kD}\omega\sqrt{(\gamma A)^2 + (C_1\omega)^2}}{2\,(m + (J/r^2))\,\sqrt{(\omega_0^2 - \omega^2)^2 + 4n^2\omega^2}} = \frac{-e^{-0.408D} \times 45667}{(m+222)\,\sqrt{(\omega_0^2 - 4)^2 + 16n^2}}, \tag{33}$$

$$C_6 = \frac{60E_r}{2\pi r n_r} = 509, \tag{34}$$

$$\eta = \frac{16\pi^2 C_5^2 C_6^2 R}{(R+r_1)^2 \omega\gamma g D_{\text{buoy}} H^2 T^2} = 8.73 \times \frac{R}{(R+r_1)^2} C_5^2. \tag{35}$$

According to (29)~(35), after setting the system correlation parameters, generating efficiency is the dual function of the system's mass and load, whose image can be obtained by Matlab as shown in Figure 3.

Table 1

Wave parameter	Symbol	Data	Unit
Wave height	H	1	m
Wave period	T	3.14	s
Wave angular frequency	ω	2	rad/s
Wavelength	λ	15.4	m
Wave number	k	0.408	

Table 2

Wave parameter	Symbol	Data	Unit
Diameter of the cylindrical buoy	D_{buoy}	2.4	m
Cross-sectional area of the buoy	A	4.524	m^2
Radius of the roll wheel	r	0.15	m
Moment of inertia of the device	J	5	kgm^2
Electromotive force of generator	E_r	360	V
Rated generator speed	n_r	45	rpm
Resistance of stator winding	r_1	1	Ω
Rated efficiency of generator	η_r	80%	

According to the distribution feature of the high efficiency points, the buoy-rope-drum wave system can be divided into two categories.

(1) Light Thin Type of System. Generating efficiency of the light thin system increases as the load resistance decreases. The power of the wave acting on the buoy mainly transforms to the tension of the rope because the small mass brings about the small inertial load of the system, then drives the generator, and outputs useful work through resistive load. Due to the light and thin buoy, the amplitudes of the buoy and the wave are approximately the same, making the average velocity of the buoy under the rated sea conditions nearly constant, which means that the average value of the output voltage is nearly constant. All the above conditions and the adaptation of the pure resistive load contribute to the outcome that the useful power increases as the load resistance decreases. This type of system is relatively stable, but the mass of the actual engineering prototype should be big enough to meet the demands of strength and stiffness. For example, when the diameter of the buoy is 2.4 m, the mass of the system should be at least 1 ton. As shown in Figure 3, when the value of load resistance is set as 14 Ω, the highest generating efficiency can reach approximately 21%.

(2) Resonance Type of System. As shown in Figure 3, when the system mass is 11 tons, its generating efficiency increases as the load resistance increases, because when the diameter of the buoy is 2.4 m and the system mass is 11 tons, the natural frequency of the system is 2 rad/s, which happens to be the frequency of the wave under the rated sea conditions, and then the system is in the resonance state. In the resonance state, the system can accumulate the power, so that the amplitude of the buoy will continue to increase, so will the generating efficiency, which will ultimately lead to the destruction of the system. Therefore, the resonance type of system has to be designed appropriately to adjust the damping

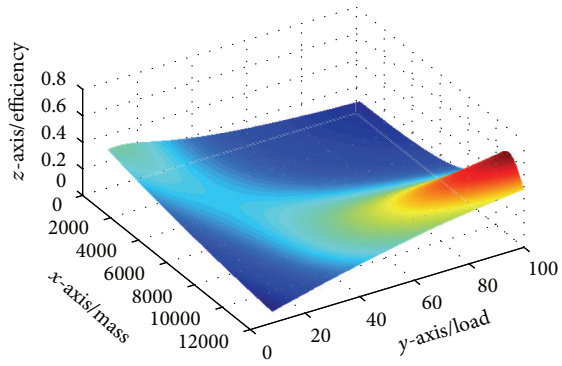

Figure 3: The influence of system's mass and load on generating efficiency.

and then adjust the amplitude of the buoy to control the system in stable resonance. For example, when the diameter of the buoy is 2.4 m, the mass of the system is 11 tons and the value of the system's amplitude is set as 0.5 m; then, the load resistance is 38 Ω, when the generating efficiency of the system is 22%.

5. Conclusion

Buoy-rope-drum wave power system is a new type of floating oscillating buoy wave power device, which absorbs energy from waves by buoy-rope-drum structure, simple in structure and cost efficient in laying and maintaining. By studying the generating efficiency of direct-drive buoy-rope-drum wave power system, this paper divides the high efficient buoy-rope-drum wave power system into two categories: the light thin type and the resonance type. The former is relatively stable while the latter needs to set reasonable load to make sure of the stability of the system. The conclusions above provide theoretical guidance for the research and development of the engineering prototype of the buoy-rope-drum wave power system for sea trials.

References

[1] M. Mccormick, *Ocean Wave Energy Conversion*, John Wiley & Sons, New York, NY, USA, 1981.

[2] J. P. Kofoed, P. Frigaard, E. Friis-Madsen, and H. C. Sørensen, "Prototype testing of the wave energy converter wave dragon," *Renewable Energy*, vol. 31, no. 2, pp. 181–189, 2006.

[3] M. Leijon, O. Danielsson, M. Eriksson et al., "An electrical approach to wave energy conversion," *Renewable Energy*, vol. 31, no. 9, pp. 1309–1319, 2006.

[4] Y. You, W. Li, W. Liu, X. Li, and F. Wu, "Development status and perspective of marine energy conversion systems," *Automation of Electric Power Systems*, vol. 34, no. 14, pp. 1–12, 2010.

[5] D.-X. Gao, F.-J. Wang, H.-D. Shi et al., "The research progress of foreign wave energy generation," *Ocean Development and Management*, vol. 11, pp. 21–26, 2012 (Chinese).

[6] D. Li, B. Bai, Q. Yu, and B. Zhu, "Research on sea wave power generation system by using bouy," *Acta Energiae Solaris Sinica*, vol. 32, no. 10, pp. 1566–1570, 2011.

[7] B.-W. Song, W.-J. Ding, and Z.-Y. Mao, "Conversion system of ocean buoys based on wave energy," *Journal of Mechanical Engineering*, vol. 48, no. 12, pp. 139–143, 2012.

[8] B.-J. Wu, X.-H. Diao, Y.-G. You et al., "10 kW floating point absorber direct drive wave energy device," *Ocean Technology*, vol. 31, no. 3, pp. 68–73, 2012.

[9] H. O. Beto, *Buoy Engineering*, Science Press, Beijing, China, 1980, (Chinese).

[10] Y.-F. Zeng, *Ocean Engineering Wave Mechanics*, Shanghai Jiaotong University Press, Shanghai, China, 2007, (Chinese).

[11] G.-P. Qiu and M. Qiu, *The Practical Design and Apply Technology of Permanent Magnet Dc Motor*, China Machine Press, Beijing, China, 2009, (Chinese).

Hindawi Publishing Corporation
Advances in Mechanical Engineering
Volume 2013, Article ID 340501, 9 pages
http://dx.doi.org/10.1155/2013/340501

Research Article

New Concept for Assessment of Tidal Current Energy in Jiangsu Coast, China

Ji-Sheng Zhang,[1] Jun Wang,[2] Ai-Feng Tao,[1] Jin-Hai Zheng,[1] and Hui Li[2]

[1] *State Key Laboratory of Hydrology-Water Resources and Hydraulic Engineering, Hohai University, Nanjing 210098, China*
[2] *College of Harbor, Coastal and Offshore Engineering, Hohai University, Nanjing 210098, China*

Correspondence should be addressed to Ai-Feng Tao; aftao@hhu.edu.cn

Received 29 June 2013; Revised 10 October 2013; Accepted 14 October 2013

Academic Editor: Luigi Cappelli

Copyright © 2013 Ji-Sheng Zhang et al. This is an open access article distributed under the Creative Commons Attribution License, which permits unrestricted use, distribution, and reproduction in any medium, provided the original work is properly cited.

Tidal current energy has attracted more and more attentions of coastal engineers in recent years, mainly due to its advantages of low environmental impact, long-term predictability, and large energy potential. In this study, a two-dimensional hydrodynamic model is applied to predict the distribution of mean density of tidal current energy and to determine a suitable site for energy exploitation in Jiangsu Coast. The simulation results including water elevation and tidal current (speed and direction) were validated with measured data, showing a reasonable agreement. Then, the model was used to evaluate the distribution of mean density of tidal current energy during springtide and neap tide in Jiangsu Coast. Considering the discontinuous performance of tidal current turbine, a new concept for assessing tidal current energy is introduced with three parameters: total operating time, dispersion of operating time, and mean operating time of tidal current turbine. The operating efficiency of tidal current turbine at three locations around radial submarine sand ridges was taken as examples for comparison, determining suitable sites for development of tidal current farm.

1. Introduction

The rapid development of economics and science technology has caused an enormous consumption of fossil fuel energy and environmental pollution. As marine renewable energies are clean and sustainable, they can offer a solution to relieve energy crisis and to reduce environmental impacts. It is well known that ocean covers nearly 71% of the earth's surface and holds a large amount of energy more than 2×10^3 TW [1]. Ocean energies can be exploited in many different forms, including tide, wave, tidal current, thermal, salinity gradients, and biomass [2]. Tidal current energy differs from tidal energy. Application of tidal current energy is to transform kinetic energy of tidal current to electricity, while application of tidal energy is about the usage of potential energy due to sea level variation [3]. Among all forms of ocean energies, tidal current energy is preferable mainly due to its advantages of the high energy density (approximately 832 times greater than wind) [2], long-time predictability, and potentially large resource [4]. For these reasons, tidal current energy draws more and more attentions from the public in recent years.

China has an excellent resource of tidal current energy with a huge capacity of approximate 13950 MW [5]. Exploitation of tidal current energy will be an important supply as a clean and reliable power in the near future. Jiangsu is a province on the eastern coast of China with a coastline of 954 Km. A radial submarine sand ridge was formed in the northern part of Jiangsu Coast due to strong tidal current and, undoubtedly, tidal current energy mainly concentrated in this area. Maximal current speeds in Huangshayang channel and Xiyang channel are over 2.5 m/s and 2.0 m/s, respectively. Therefore, assessment of tidal current energy in Jiangsu Coast is of great practical significance.

Assessment of tidal current energy is usually applied to identify location of greatest potential and to estimate level of energy production that can be achieved [6]. In the past ten years, some studies regarding assessment of tidal current energy in China have been conducted. For example, Li et al. investigated the distribution of tidal current energy and recommended some possible location for exploitation in China [7]. Liu et al. summarized distribution of tidal current energy in some several water channels around China and calculated

the theoretical value of tidal current power [8]. After reviewing previous two-dimensional model for evaluation of tidal currents energy, Chen implemented a three-dimensional, semi-implicit Euler-Lagrange finite element model (SELFE) to assess the potential tidal current energy of three locations around Kinmen Island in Taiwan and analyzed the impacts of energy extraction on hydrodynamics in Taiwan Strait [3, 6].

Previous assessment of tidal current energy mainly focused on simulation of specific coast, distribution of energy, and potential channel for future exploitation. Operating time of current turbine is acknowledged as an influencing factor on energy extraction, because frequently interrupted working condition will reduce efficiency of current turbine. Time-dependent magnitude of current velocity shows a process of periodic variation, and a current turbine has an upper limit and a lower limit to current speed within which it can transform energy properly. Therefore, operating time of current turbine is discontinuous and periodic. Period and interruption interval of current turbine during operation are mainly dependent on tidal cycle. Consequently, a water channel with more steady and consecutive tidal current is more suitable for transformation from tidal current energy to electricity.

Main objective of this study is to propose a new concept for assessment of tidal current energy in terms of total operating time, dispersion of operating time, and mean operating time. A two-dimensional hydrodynamic model is developed in Jiangsu Coast, which is based on the commercial software, MIKE 21 FM package, and the simulated results (water elevation and current velocity) are validated with the measurement data. Then, numerical results from validated model are used for assessment of tidal current energy. Density of tidal current energy, total operating time, dispersion of operating time, and mean operating time at three locations are compared to identify the most suitable site for deployment of tide current turbine.

2. Numerical Model

2.1. Governing Equations of Hydrodynamic Model. A two-dimensional model is built within the commercial MIKE 21 FM package to simulate tidal hydrodynamics in Jiangsu Coast. The two-dimensional incompressible Reynolds-Averaged Navier-Stokes (RANS) equations for describing tidal hydrodynamics can be written as

$$\frac{\partial h}{\partial t} + \frac{\partial h\overline{u}}{\partial x} + \frac{\partial h\overline{v}}{\partial y} = hS,$$

$$\frac{\partial h\overline{u}}{\partial t} + \frac{\partial h\overline{u}^2}{\partial x} + \frac{\partial h\overline{u}\overline{v}}{\partial y} = f\overline{v}h - gh\frac{\partial \eta}{\partial x} - \frac{h}{\rho_0}\frac{\partial p_a}{\partial x} - \frac{gh^2}{2\rho_0}\frac{\partial \rho}{\partial x} + \frac{\tau_{sx}}{\rho_0} - \frac{\tau_{bx}}{\rho_0} - \frac{1}{\rho_0}\left(\frac{\partial s_{xx}}{\partial x} + \frac{\partial s_{xy}}{\partial y}\right) + \frac{\partial}{\partial x}\left(hT_{xx}\right) + \frac{\partial}{\partial y}\left(hT_{xy}\right) + hu_sS,$$

$$\frac{\partial h\overline{v}}{\partial t} + \frac{\partial h\overline{v}^2}{\partial y} + \frac{\partial h\overline{u}\overline{v}}{\partial x} = -f\overline{u}h - gh\frac{\partial \eta}{\partial y} - \frac{h}{\rho_0}\frac{\partial p_a}{\partial y} - \frac{gh^2}{2\rho_0}\frac{\partial \rho}{\partial y} + \frac{\tau_{sy}}{\rho_0} - \frac{\tau_{by}}{\rho_0} - \frac{1}{\rho_0}\left(\frac{\partial s_{yx}}{\partial x} + \frac{\partial s_{yy}}{\partial y}\right) + \frac{\partial}{\partial x}\left(hT_{xy}\right) + \frac{\partial}{\partial y}\left(hT_{yy}\right) + hv_sS, \quad (1)$$

where (x, y) are horizontal Cartesian coordinates; t is time; η is surface elevation; d is still water depth; $h = \eta + d$ is total water depth; u and v are velocity components in x and y directions; $f = 2\Omega \sin\phi$ is Coriolis parameter (in which Ω is angular rate of revolution and ϕ is geographic latitude); g is gravitational acceleration; ρ is density of water; S_{xx}, S_{xy}, S_{yx}, and S_{yy} are components of radiation stress tensor; P_a is atmospheric pressure; ρ_0 is reference density of water; S is magnitude of discharge due to point sources; (u_s, v_s) is velocity by which water is discharged into the ambient water; T_{ij} are lateral stresses including viscous friction, turbulent friction, and differential advection; and overbar indicates a depth-averaged value.

2.2. Calculation Formulation of Tidal Current Energy. When tidal flow passes through a vertical cross-section of unit area perpendicular to the flow direction per unit time, the current energy extracted can be calculated by the method of kineticenergy density [9]:

$$P = \frac{1}{2}C_p\rho V^3, \quad (2)$$

where P is density of tidal current energy within unit area, C_p is turbine efficiency coefficient, and V is magnitude of flow velocity averaged over cross-section. Mean density of tidal current energy, P_m, over an arbitrary period T can be calculated by

$$P_m = \frac{1}{T}\int_0^T \frac{1}{2}C_p\rho V^3(t)\,dt. \quad (3)$$

2.3. Computational Domain and Boundary Conditions. The computational domain covers Jiangsu Coast and its adjacent ocean areas (Figures 1 and 2), with a distance of 246 Km in longitude from east (123°22′17″E) to west (120°23′36″E) and a distance of 300 Km in latitude from south (30°52′22″N) to north (35°56′43″N). As shown in Figure 3, this domain is divided into a series of unstructured triangular grids with 75882 nodes and 149926 elements. A small grid with a size of 200 m is used along coastal boundary, while a large grid with a size of 5000 m is applied at open-sea boundary.

Wind stress, surface net heat, and moisture flux can be imposed on model system via surface boundary, but they are not considered in this study. At sea bottom, bottom shear stress induced by bottom friction is specified. Time-dependent water elevation clamped open boundary condition is provided along open-sea boundary, while long-term averaged runoff from the Yangtze River is prescribed on

Figure 1: Regional map of study area in China (downloaded from Google map).

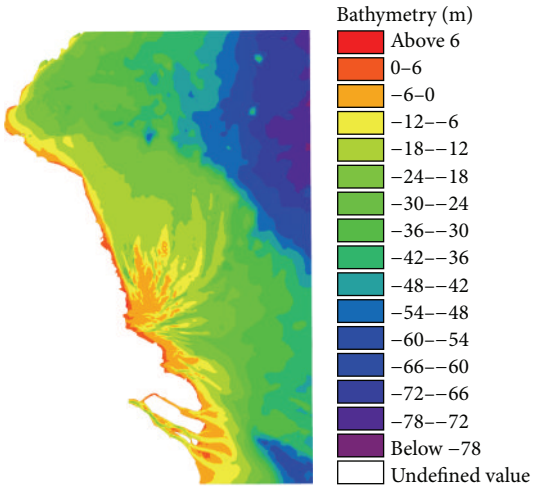

Figure 2: Map and bathymetry of study area.

Figure 3: Unstructured triangular grid of study area.

the land side. Initial surface elevation is set as 0 m with no velocity, and a spin-up period of 24 hours is adopted in the simulation to avoid the impact of initial condition.

3. Model Validation

To check/ensure accuracy of hydrodynamic model, the calculated results of water elevation and current velocity are compared with field measurement. During 22/August/2006–25/August/2006 (spring tide) and 29/August/2006–01/September/2006 (neap tide), a serial of field measurement including water elevation and current velocity was carried out in Jiangsu Coast. WFH-2 Absolute Machinery Coded water level meter is used for recording water elevation at *Dafeng* station (120°48′12″E, 33°16′55″N), while Acoustic Doppler Current Profiler (ADCP) is adopted for monitoring current velocity at stations t_1 (120°51′48″E, 33°10′18″N), t_2 (121°8′48″E, 32°34′60″N), and t_3 (121°29′42″E, 32°39′36″N) (see Figure 4).

Figure 5 shows the comparison of calculated water elevation and measured data during spring tide and neap tide, indicating a reasonable agreement between numerical model and field measurement. The values of mean absolute error (MAE) for spring tide and neap tide are 0.17 and 0.07, the values of root mean square error (RMSE) for spring tide and neap tide are 0.21 and 0.08, and the coefficients of determination (R^2) are 0.998 and 0.999.

A 24-hour spring tide from 08:00 24/August/2006 to 08:00 25/August/2006 and a 24-hour neap tide (12:00 31/August/2006 to 12:00 01/September/2006) are chosen for the comparison (Beijing time). Figure 6 demonstrates the comparison of current magnitude and current direction at stations t_1, t_2, and t_3, and Table 1 gives the values of MAE and RMSE between numerical simulation and field measurement. It can be seen that agreement between simulation and measurement at t_1 is much better than the others. However, some differences between the simulation and measurement are obvious, which may be ascribed to (i) complex bathymetry within the radial submarine sand ridges,

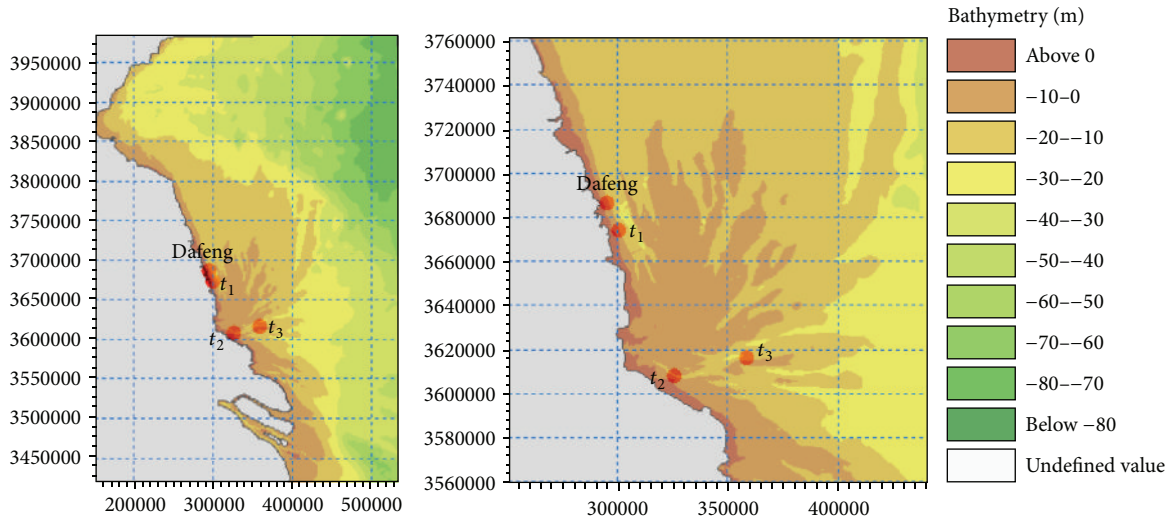

Figure 4: Locations of stations *Dafeng*, t_1, t_2, and t_3.

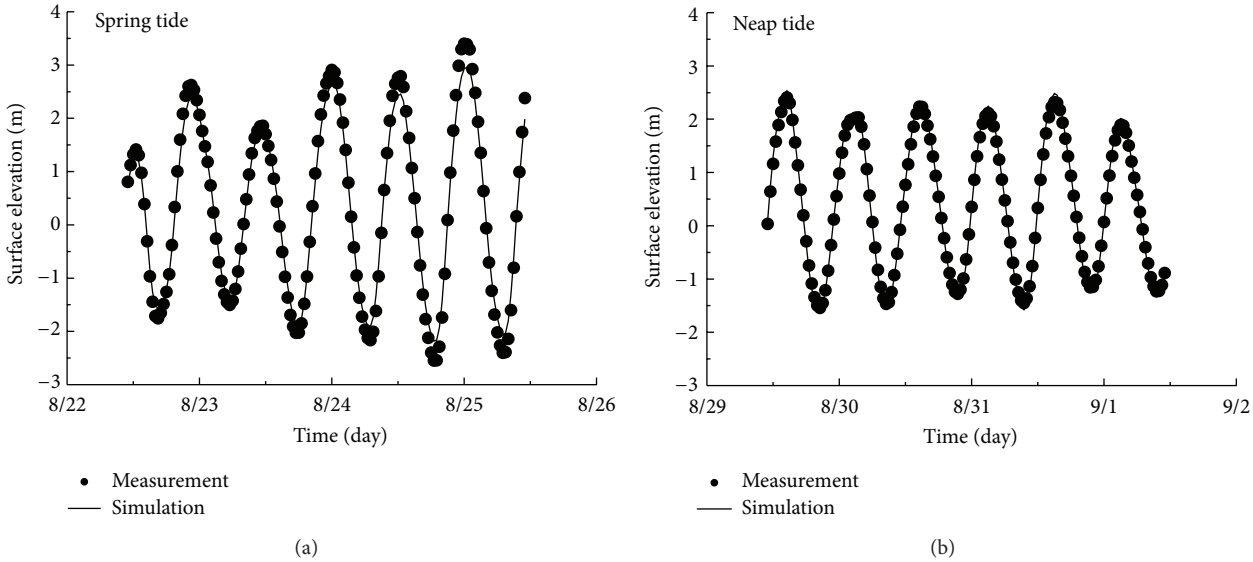

Figure 5: Comparison of calculated water elevation and measured data at *Dafeng* station.

(ii) various roughness coefficients during tidal cycle, and (iii) unsteady surface wind.

4. Assessment of Tidal Current Energy

Numerical results from validated model are used to evaluate distribution of tidal current energy in Jiangsu Coast. In addition to conventional method calculating mean density of tidal current energy within the domain, a new concept with three parameters, total operating time, dispersion of operating time, and mean operating time of tidal current turbine, is introduced to describe the total working condition of current turbine. With these three new indicators, three water channels are taken as examples to identify the most suitable site for exploitation of tidal current energy.

4.1. Mean Density of Tidal Current Energy. Mean density of tidal current energy is a concept indicating the ability of energy production over a given period. Density of current energy density is calculated by (2), and average of these values is taken as mean density of tidal current energy (3). It is noted that a typical value of 0.3 is adopted for the parameter C_p (the percentage of power that can be extracted from the tidal stream, taking into account the losses due to Betz' law and those assigned to internal mechanisms within the turbine) [6, 10]. Figure 7 shows the distribution of mean density of tidal current energy in spring tide and neap tide. It can be seen that tidal current energy concentrates around the radial submarine sand ridges with a highest value of 0.94 Kw/m^2 during spring tide and a highest value of 0.60 Kw/m^2 during neap tide.

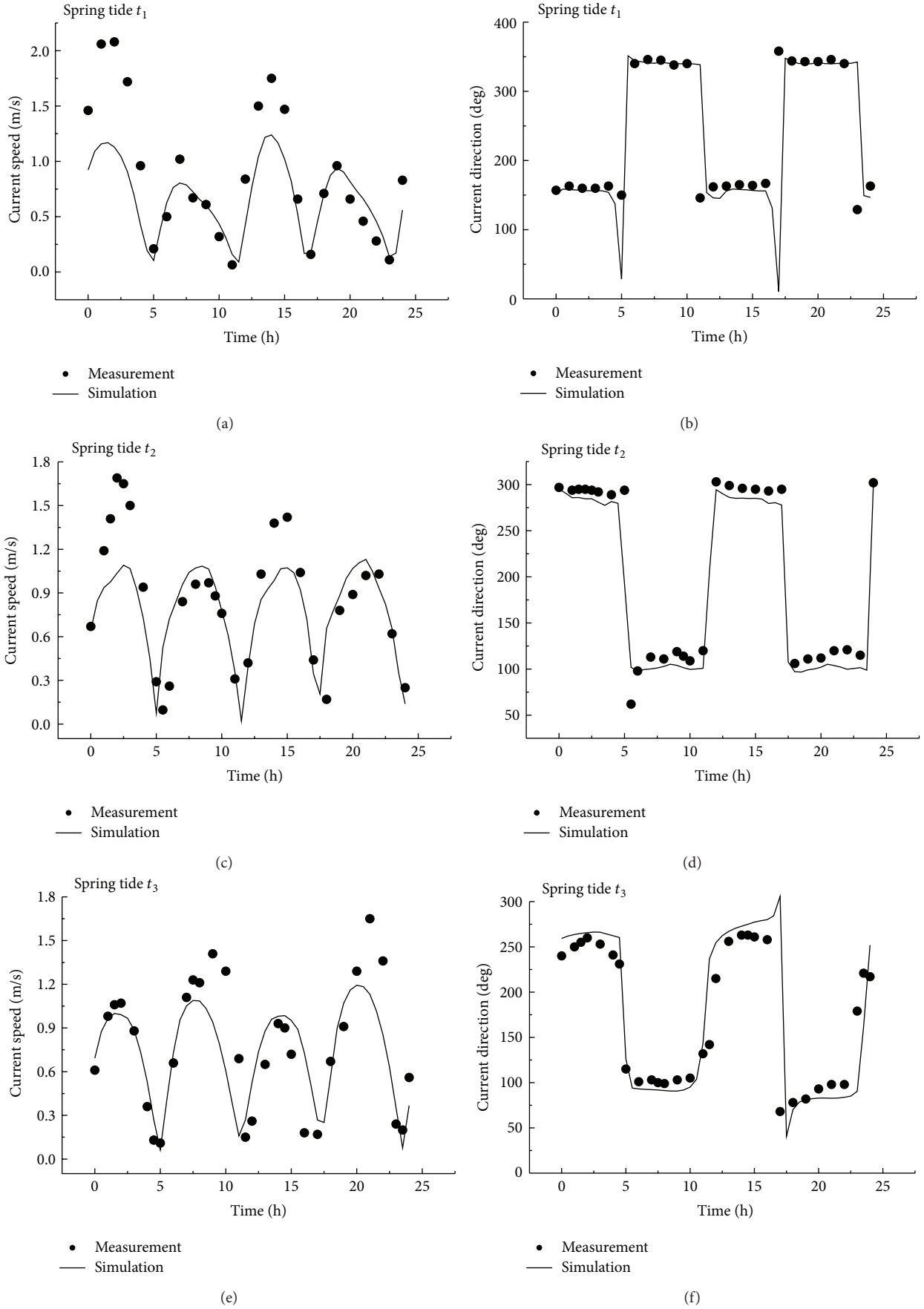

Figure 6: Continued.

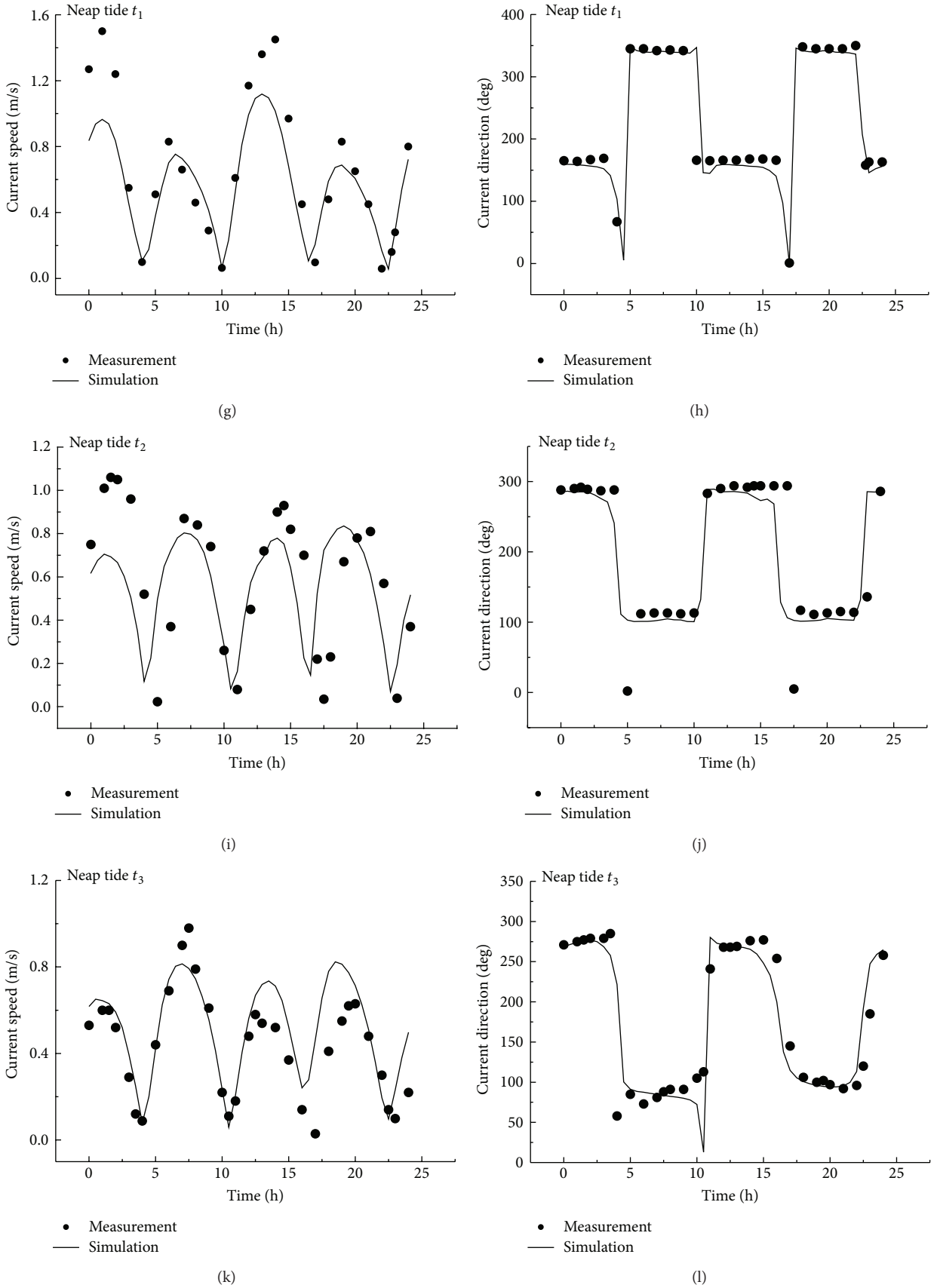

Figure 6: Comparisons of depth-averaged tidal current between numerical simulation and field measurement for ((a)–(f)) spring tide and ((g)–(l)) neap tide at stations t_1, t_2, and t_3.

Table 1: Values of MAE and RMSE between calculated and observed tidal current.

	t_1		t_2		t_3	
	Speed (m/s)	Direction (degree)	Speed (m/s)	Direction (degree)	Speed (m/s)	Direction (degree)
			Spring tide			
MAE	0.29	23	0.20	14	0.22	21
RMSE	0.40	51	0.26	23	0.29	34
R^2	0.89	0.91	0.79	0.98	0.74	0.93
			Neap tide			
MAE	0.16	17	0.22	27	0.12	21
RMSE	0.22	38	0.27	52	0.16	40
R^2	0.95	0.93	0.51	0.87	0.82	0.90

Note: MAE: mean absolute error, RMSE: root mean square error, R^2: coefficient of determination.

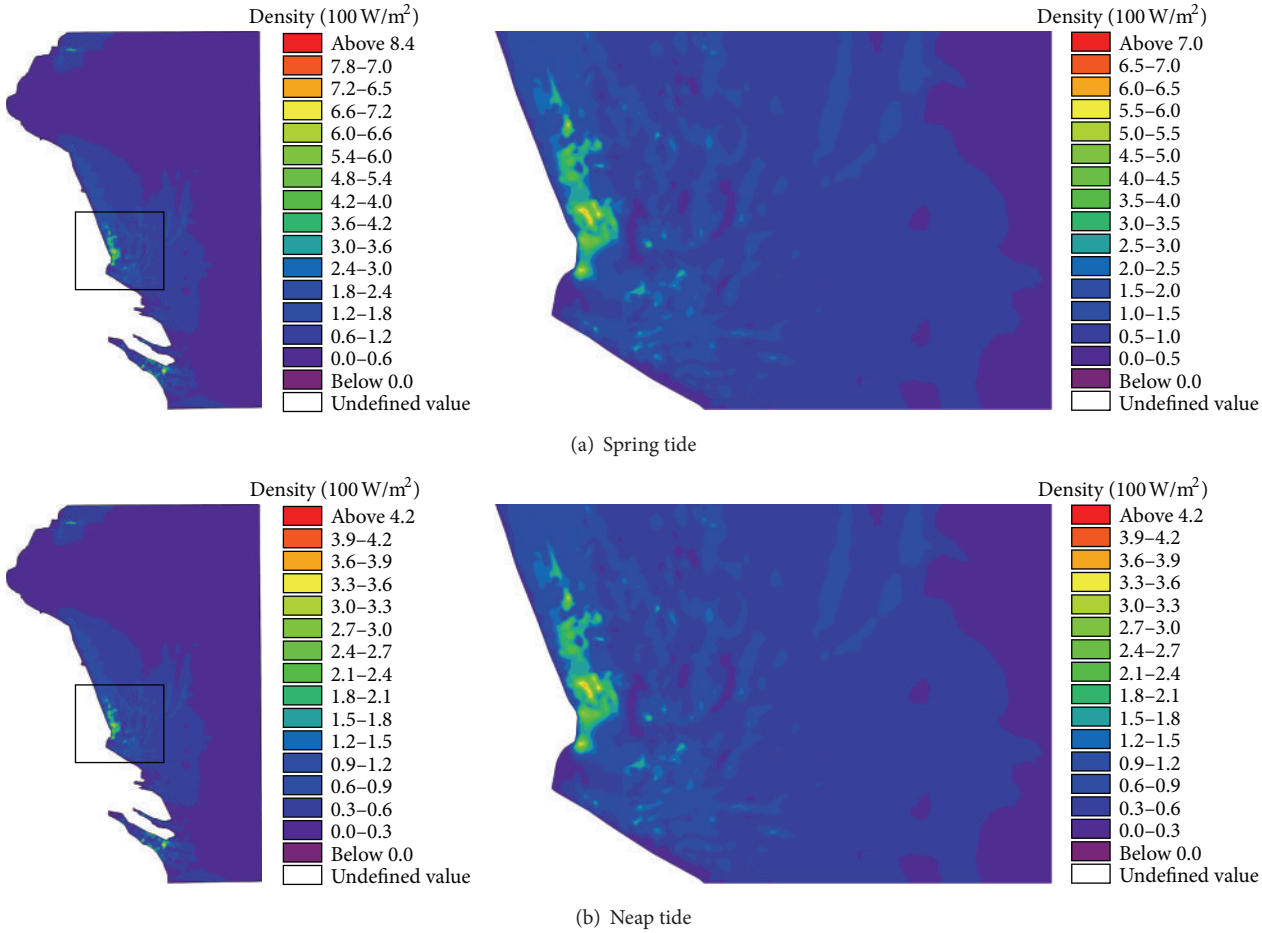

Figure 7: Distribution of mean density of tidal current energy during (a) spring tide and (b) neap tide (unit: 100 W/m^2).

The radial submarine sand ridges consist of many water channels that are ideal locations for exploitation of tidal current energy. According to long-term tidal measurement, three water channels (Xiyang, Huangshayang, and Lanshayang) with wide width and rapid current are considered in this study. After calculation of the potential mean density of energy, one representative point in each water channel is chosen for the comparison of tidal current energy to find a suitable site for tidal turbines. As displayed in Figure 8, locations t_4 (121°00′58″E, 33°00′06″N) in Xiyang, t_5 (121°26′51″E, 32°39′01″N) in Huangshayang, and t_6 (121°39′32″E, 32°34′04″N) in Lanshayang are around the radial submarine sand ridges. Table 2 gives values of mean density of tidal current energy at these three positions, showing that t_4 has a maximal value of mean density of tidal current energy among these three locations.

4.2. New Concept for Assessment of Tidal Current Energy. It is well known that tidal current turbine has a low limit of tidal current velocity for power generation. In 2010,

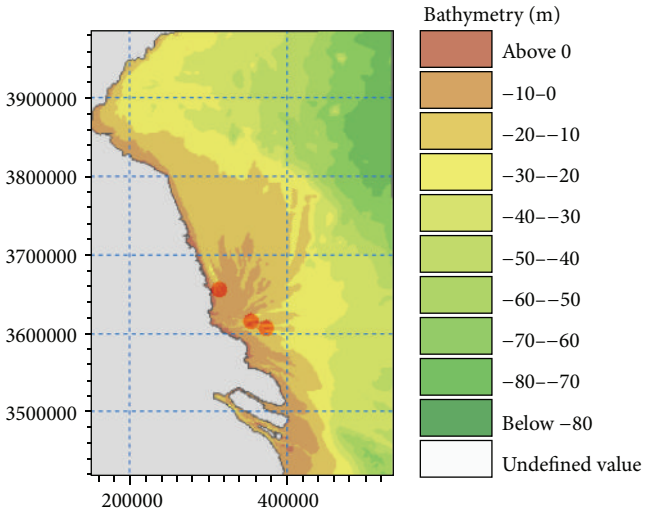

Figure 8: Locations of t_4, t_5, and t_6.

Table 2: Mean density of tidal current energy at t_4, t_5, and t_6.

Mean density of tidal current energy (100 w/m^2)			
	t_4	t_5	t_6
Spring tide	3.9	2.5	3.5
Neap tide	2.6	1.2	1.7

Benelghali et al. compared Doubly-Fed Induction Generator (DFIG) and Permanent Magnet Synchronous Generator (PMSG) for marine current turbine applications, and they found that DFIG is with a lower limit of 1.3 m/s [11]. In this study, the velocity of 1.3 m/s is taken as the lower limit of tidal current turbine. Due to the existence of the lower limit, tidal current turbine is with discontinuous operating in practical application. Total operating time, dispersion of operating time, and mean operating time consequently become three new important parameters in assessment of tidal current energy and evaluation of operating efficiency of tidal current turbine.

Total operating time is defined as the sum of operating times over a given period, indicating the duration of effective operation of tidal current turbine:

$$\text{Total Operating Time} = \int_0^T P(v_t)\,dt,$$
$$P(v_t) = \begin{cases} 0, & v < 1.3\ \text{m/s} \\ 1, & v \geq 1.3\ \text{m/s}, \end{cases} \tag{4}$$

where v_t is current velocity and T is a given period.

According to the low limit of 1.3 m/s of tidal current turbine, all the durations with a tidal current speed over 1.3 m/s are accumulated and their sum is considered as total operating time. As listed in Table 3, during 72-hour spring tide and neap tide, total operating time at locations t_4 and t_6 is longer than that at location t_5. For example, total operation time at location t_4 is 31.8 hours and 18.3 hours for spring tide and neap tide, respectively, indicating that tidal current turbine works in 44% of time in spring tide and 25% of time in neap tide.

Table 3: Total operating time during spring tide and neap tide at t_4, t_5, and t_6.

Total operating time (h) and proportion of 72 hours						
	t_4		t_5		t_6	
Spring tide	31.8	44%	26.5	37%	31.5	44%
Neap tide	18.3	25%	6	8%	13.3	18%

Table 4: Dispersion of operating time and mean operating time during spring tide and neap tide at t_4, t_5, and t_6.

	Spring tide			Neap tide		
	t_4	t_5	t_6	t_4	t_5	t_6
Dispersion of operating time (no unit)	12	11	12	7	3	6
Mean operating time (h)	2.65	2.41	2.63	2.61	2.00	2.22

Dispersion of operating time is defined as interruption number of turbine performance during a given period, which is calculated by counting the status shift from power-off (with a current velocity below 1.3 m/s) to power-on (with a current velocity over 1.3 m/s) of tidal current turbine:

$$\text{Dispersion of Operating Time} = \sum Q(v_t, t) \quad (0 \leq t \leq T),$$
$$Q(v,t) = \begin{cases} 1, & \lim_{\delta \to 0} P(v_{t-\delta}) < \lim_{\delta \to 0} P(v_{t+\delta}) \\ 0, & \text{others.} \end{cases} \tag{5}$$

Values of dispersion of operating time during spring tide and neap tide at t_4, t_5, and t_6 are given in Table 4, showing that interruption number of turbine performance is the largest. It is reasonable to have a larger interruption number when total operating time of tidal current turbine is longer. It is necessary to point out that, in these two indicators, total operating time of tidal current turbine is the main indicator for assessment of tidal current energy. In the case of similar amount of total operating time, a smaller value of dispersion of operating time is preferred.

It is also useful to define mean operation time of tidal current turbine as the ratio of total operating time to dispersion of operation time:

$$\text{Mean Operating Time} = \frac{\text{Total Operating Time}}{\text{Dispersion of Operating Time}}. \tag{6}$$

As listed in Table 4, mean operating time at stations t_4 and t_5 is obviously larger than that at t_6. It can be seen that a higher efficiency of turbine operation can be achieved at t_4 and t_5 (due to a higher value of total operating time) although interruption number of turbine operation is larger. Therefore, stations t_4 (Xiyang) and t_5 (Lanshayang) are more suitable sites for deployment of tidal current turbines among these three locations. However, the final decision on site selection for tidal current farm is also dependent on the large-scale ocean space-use plan along Jiangsu Coast.

5. Conclusion

A two-dimensional hydrodynamic model was developed with Mike 21 FM package to assess tidal current energy and seek for suitable sites for deployment of tidal current turbine. For model validation, calculated water elevation and current velocity are compared with field measurement, indicating a generally reasonable agreement. Then, simulation results were used to evaluate tidal current energy resources in Jiangsu Coast. In addition to traditional method calculating mean density of tidal current energy, a new concept in terms of total operating time, dispersion of operating time, and mean operating time of tidal current turbine was proposed for assessment. These three indicators were well defined in the study, and they were found to be very useful in determining suitable sites for deployment of tidal current turbine. It is noted that total operating time of tidal current turbine is the most important indicator for assessment of tidal current energy in this new concept. In the case of similar amount of total operating time, a smaller value of dispersion of operating time or a larger value of mean operating time is preferred. Based on this new concept, Xiyang and Lanshayang are the more suitable sites for deployment of tidal current turbine in Jiangsu Coast. However, the final decision on site selection for tidal current farm is also dependent on the large-scale ocean space-use plan along Jiangsu Coast.

Conflict of Interests

The authors declare that there is no conflict of interests regarding the publication of this paper.

Acknowledgments

This work was financially supported by the National Natural Science Foundation of China (51137002), Natural Science Foundation Project of Jiangsu Province (BK2011026), and the 111 project (B12032).

References

[1] K. Toshiaki, "Dream of marine-topia: new technologies to utilize effectivelyrenewable energies at offshore," *Current Applied Physics*, vol. 10, supplement 2, pp. S4–S8, 2010.

[2] C. W. Finkl and R. Charlier, "Electrical power generation from ocean currents in the Straits of Florida: some environmental considerations," *Renewable and Sustainable Energy Reviews*, vol. 13, no. 9, pp. 2597–2604, 2009.

[3] W. B. Chen, W. C. Liu, and M. H. Hsu, "Modeling evaluation of tidal stream energy and the impacts ofenergy extraction on hydrodynamics in the Taiwan Strait," *Energies*, vol. 6, no. 4, pp. 2191–2203, 2013.

[4] F. L. Ponta and P. M. Jacovkis, "Marine-current power generation by diffuser-augmented floating hydro-turbines," *Renewable Energy*, vol. 33, no. 4, pp. 665–673, 2008.

[5] C. K. Wang and W. Y. Shi, "The ocean resources and reserves evaluation in China," in *Proceedings of the 1st National Symposium on Ocean Energy in Hangzhou*, pp. 169–179, 2008.

[6] W. B. Chen, W. C. Liu, and M. H. Hsu, "Modeling assessment of tidal current energy at Kinmen Island, Taiwan," *Renewable Energy*, vol. 50, pp. 1073–1082, 2013.

[7] D. Li, S. Wang, and P. Yuan, "An overview of development of tidal current in China: energy resource, conversion technology and opportunities," *Renewable and Sustainable Energy Reviews*, vol. 14, no. 9, pp. 2896–2905, 2010.

[8] H. W. Liu, S. Ma, W. Li, H. G. Gu, Y. Lin, and X. Sun, "A review on the development of tidal current energy in China," *Renewable and Sustainable Energy Reviews*, vol. 15, no. 2, pp. 1141–1146, 2011.

[9] P. Michel, L. Véronique, and L. Denis, *Marine Renewable Energies Prospective Foresight Study for 2030*, QUAE edition, Paris, France, 2007.

[10] A. N. Gorban', A. M. Gorlov, and V. M. Silantyev, "Limits of the turbine efficiency for free fluid flow," *Journal of Energy Resources Technology*, vol. 123, no. 2–4, pp. 311–317, 2001.

[11] S. Benelghali, M. E. H. Benbouzid, and J. F. Charpentier, "Comparison of PMSG and DFIG for marine current turbine applications," in *Proceedings of the 19th International Conference on Electrical Machines (ICEM '10)*, Roma, Italy, September 2010.

Hindawi Publishing Corporation
Advances in Mechanical Engineering
Volume 2013, Article ID 105072, 7 pages
http://dx.doi.org/10.1155/2013/105072

Research Article

Analysis of Floating Buoy of a Wave Power Generating Jack-Up Platform *Haiyuan 1*

Date Li, Detang Li, Fei Li, Jingxin Shi, and Wei Zhang

Ship and Marine Engineering College of Zhejiang Ocean University, Zhoushan 316000, China

Correspondence should be addressed to Date Li; lidate@163.com

Received 16 June 2013; Revised 23 September 2013; Accepted 27 September 2013

Academic Editor: Luigi Cappelli

Copyright © 2013 Date Li et al. This is an open access article distributed under the Creative Commons Attribution License, which permits unrestricted use, distribution, and reproduction in any medium, provided the original work is properly cited.

The paper focuses on the performance of floating buoys of a wave power generating jack-up platform called *Haiyuan 1*, in order to work out the optimum designed draft and hydraulic pressure. The performance of the buoy, especially its delivered power, is an important issue in designing oscillating buoy wave energy converter. In this case, major factors affect the performance including incident wave, designed draft, and hydraulic pressure on the buoy. To find out the relationship among design draft, hydraulic pressure, and delivered power, the key point is to precisely estimate wave induced motion of the buoy. Three-dimensional theory and time domain method based on potential theory were adopted in the paper. Unlike ship and other floating structures, motion of wave energy converter (WEC) buoy in wave will be weakened because of energy take-off, which will cause significant draft changing with time. Thus, draft changing should be taken into consideration as well. In addition, green water problem occurs more frequently than that in ship and other floating structures and also might the reduce delivered power. Therefore, green water problem will also be taken into account when choosing the optimum designed draft and hydraulic pressure. The calculation indicates that the optimum designed draft is 0.935 m, while the optimum designed hydraulic pressure is 30 kN.

1. Introduction

The ocean reserves extremely huge wave energy, which is as high as 10^3 to 10^4 GW [1]. In addition, because energy density of wave is about 4 to 30 times larger than wind, smaller area is required in wave farm under the condition of the same generated power. Therefore, wave energy utilization has a promising prospect [2]. At present, great progress has been reached in the field of wave energy utilization; even some wave power generating stations had become commercialized. However, the cost of electricity from wave power is still very high, about 5~10 times higher than the price of traditional electricity. Therefore, in order to fulfill commercialized operation of wave power generating, further research is still required.

Oscillating buoy wave energy converter is one of the main types of wave energy converter; its wave energy absorbing system, the buoy, enables the transformation of wave energy into its kinetic energy and gravity potential energy by heaving in wave. Typical equipments such as *Wavestar* platform and *Powerbuoy* have shown competitive potential. The *Wavestar*, which is a wave generating platform built in Hanstholm, Denmark, had normally operated over two years. This *Wavestar* platform has two buoys, each of which has radius of 2.5 m, and its peak output power is 39 kW. *Powerbuoy* was invented by the *Ocean Power Technologies* (abbreviate as OPTs). OPTs built PB40 for a Spanish wave farm in 2008, which had jointed into the national grid of Spain. The wave farm is able to provide about 1.39 MW electric powers. This kind of WEC has the advantages of high generating efficiency and possesses commendable flexibility of scale of power generation. Hence, it will have a promising future.

The delivered power performance of the buoy is an important issue in designing an oscillating buoy wave energy converter. The delivered power of a WEC buoy refers to the work which the buoy has done to overcome the force produced by the system (such as hydraulic system) that connected to the buoy. In other words, it can be explained as the work the buoy transfers to the system. Obviously, its magnitude depends on the motion of the buoy and the force mentioned before.

Apparently, the motion of the buoy is induced by wave. In order to predict the wave induced motions, many methods and theories based on potential theory have been developed, such as two-dimensional strip theory, frequency and time domain method, and three-dimension theory [3–8]. Some are developed at first to solve the problem of ship or ocean platform motion in waves, then they are introduced to tackle with the wave energy extracting problem [9, 10]. Most authors usually deal with problems of motion of WEC buoy using time domain method because of the need of control, or because of strong nonlinear character of these problems. Although frequency domain method possesses advantages of simplicity and quickness, it cannot be adopted. In addition, 3D theory is more frequently adopted than 2D theory because most WEC buoys are designed to be rotators rather than slender bodies. For example, Ulvin et al. used time domain method and three-dimension theory to analyze power extraction capability of the BOLT [11]. Falcão et al. simulated the hydrodynamics of an oscillating buoy absorbing energy from sea waves also by using time domain method and three-dimension theory [12]. Generally, it seems that most of the authors calculated the related hydrodynamic coefficients at the mean draft and assumed that buoyance is always equal to gravity, instead of taking the effect of draft changing into consideration. However, draft changing might have an unnegligible effect on wave energy extracting problem. Because of energy delivered, the motion of the WEC buoy might greatly be attenuated, which will induce the draft of the buoy changing greatly, so the result is that hydrodynamic coefficients changing with time and unbalance of buoyance and gravity.

After motion of the buoy is calculated, deliver power of the WEC buoy can be obtained easily. However, because the problem of green water happens frequently in the process of energy extracting, green water need to be taken into consideration in order to judge the performance of the buoy.

The paper focuses on the performance of the buoy of a wave generating jack-up platform called *Haiyuan 1*, which was designed by Zhejiang Ocean University. Three-dimension theory, time domain method will be used in the paper, and besides, energy delivery induced draft changing will be taken into consideration as well. Following the Introduction, the platform will be introduced in Section 2. Section 3 is devoted to theoretical aspects about analyzing the performance of the buoy. Force on the buoy is analyzed; then the simplified force model is described, along with the motion equation of the buoy and computational formulas of wave forces. The numerical method to solve the motion equation is also presented. Finally, the results of computation and some conclusions are going to be revealed in Sections 4 and 5.

2. The Wave Power Generating Platform and the Buoys

The building of the wave power generating platform has been finished; now it is placed at Dongsha in Zhoushan, China. The *Haiyuan 1* prototype in Dongsha is shown in Figure 1. It mainly consists of a supporting jack-up platform,

Figure 1: *Haiyuan 1* wave power generating jack-up platform.

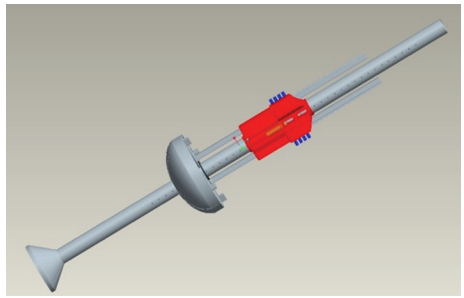

Figure 2: Wave energy collecting module.

three wave energy collecting modules, hydraulic system, and electricity take-off system. The supporting jack-up platform is made up of a platform body, three platform legs, and three pile shoes. It has the function of supporting, load bearing, and keeping core equipment away from seawater and preventing them from corrosion and damage. In addition, the platform legs can also be viewed as guiding poles, which can guide the floating buoys during vertical motion along the legs. The three floating buoys are settled on platform legs, each buoy conjoins with two tooth profile columns, which connect with a group of hydraulic cylinders. The buoys and the tooth profile columns compose the wave energy collecting modules (see Figure 2). The design can ensure the equipment working normally regardless of the sea level changes. The motion of the wave energy collecting modules drives the hydraulic system to work, finally propels the electric generator outputting electricity. The hydraulic system uses bidirectional hydraulic transmission form, which enables the buoys to drive the hydraulic system continuously by moving up or down. So, electricity can be continuously taken-off. Besides, hydraulic energy accumulators are stalled in the hydraulic system, which can store hydraulic energy and stabilize the fluctuate energy.

Designed wave of the WEC is a regular wave, which has wave height of 1.53 m and period of 6.2 s. The shape of the buoy is one of the important factors in designing. The buoy used in the *Haiyuan 1* is a rotator. Its projection on plane *XOZ* is shown in Figure 3. Its maximum diameter is 3.2 m, and its moulded depth is 1.465 m. Surface of the buoy consists of two parts, the upper part is a cylindrical surface, and the other

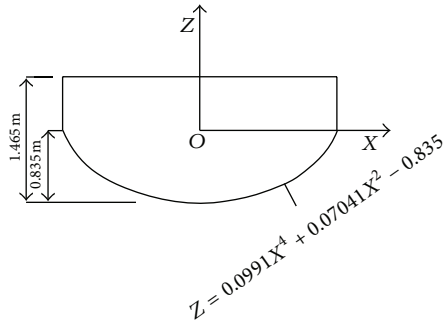

Figure 3: Shape and dimensions of the buoy.

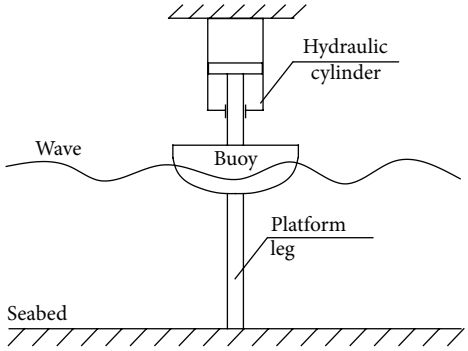

Figure 4: Simplified model for research

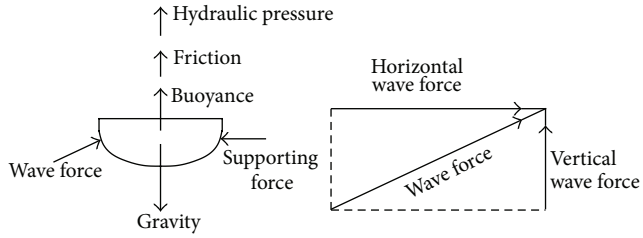

Figure 5: Forces acting on the buoy.

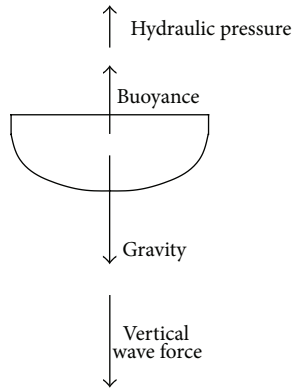

Figure 6: Simplified force model.

part is a rotated curve surface where the projection on plane XOZ can be described as the following function:

$$Z = 0.0991X^4 + 0.07041X^2 - 0.835 \quad (-1.6\,\text{m} \le X \le 1.6\,\text{m}). \tag{1}$$

3. Theoretical Analysis

In order to work out the optimum design draft and hydraulic pressure, wave induced motion of the buoy under different design drafts and different hydraulic pressures should be calculated first, and then delivered power of the buoy can be worked out; consequently, relationship among design draft, hydraulic pressure, and delivered power will be obtained. On the basis of the relationship, the optimum design parameters can be easily found out.

Cartesian coordinates x, y, and z are used with $z = 0$ and the plane of the equilibrium free surface and the $+z$-axis directed upwards.

3.1. Simplified Force Model. The interaction effect between the buoys is ignored; in this case, only the performance of a single buoy under the designed wave is concerned. A simplified model is used for describing the buoy and the surrounding conditions (as Figure 4 shows).

The forces acting on the buoy include vertical wave force, horizontal wave force, buoyance, supporting force by platform, and friction between buoy and platform leg, as well as hydraulic pressure (see as Figure 5). Because the forces are complex, a simplified force model for research is necessary. Obviously, the horizontal wave force and the supporting force have the same magnitude but in opposite direction; hence, these two forces can be canceled out. The friction between buoy and platform leg is rolling friction, so the friction coefficient is equal to 0.05, which plus the horizontal wave force usually will obtain a small value; thus, the friction between platform leg and the buoy can be ignored. Therefore, the remaining forces on the buoy are hydraulic pressure, buoyance, gravity, and vertical wave force. So, the simplified force model of the buoy can be described as Figure 6 shows.

3.2. General Motion Equation. To analyze the performance of the buoy, wave induced motion should be reckoned out first. Usually, to analyze the motion of a ship, buoyance and gravity are regarded as an equal [13, 14]. Therefore, in most situations, the motion equation do not contain the term of buoyance and gravity. However, unlike the motion of a ship or an ocean platform in wave, the motion of the buoy would be greatly weakened by hydraulic pressure when the *Haiyuan 1* is generated. On this occasion, buoyance and gravity contribute greatly to the motion; more importantly, they are always in the state of imbalance, so the buoyance and gravity of the buoy should be taken into consideration in the motion equation. In addition, hydrodynamic coefficients also vary with draft. A recent paper from Fang et al. provides a reasonable method considering the hydrodynamic coefficients changing with time when discussing the effect of added resistance from bow flare [15]. Because the effect of imbalance of buoyance and gravity in ship motion is unapparent, the authors did

not take it into account. In this paper, the method of Fang is improved, and the unbalance of buoyance and gravity is taken into consideration as well. Therefore, the following motion equation is used:

$$[M + m(t)]\ddot{z} + B(t)\dot{z} + C(t)z = F_f(t) - Mg + F_e(t) + F_{\mathrm{HP}}(t). \quad (2)$$

In the above equation, M, g, and F_f represent mass of the buoy, acceleration of gravity, and buoyance, respectively. Hydrodynamic coefficients such as added mass m, radiation damping coefficient B, and restoring spring coefficient C varied with time t because draft changes with the motion at any instant. F_{HP} denotes the hydraulic pressure on the buoy.

Assuming incident waves are unidirection regular waves, then wave elevation ξ can be described as the following cosine function:

$$\xi(t) = \xi_a \cos(\omega t - kx), \quad (3)$$

where ξ_a, ω, and k are the wave amplitude, wave frequency, and wave number, respectively.

Supposing sea water flow as a potential flow, incident velocity potential ϕ can be presented as follows [16]:

$$\phi = -\frac{\xi_a g}{\omega}\frac{\cosh[k(z+h)]}{\cosh(kh)}\sin(\omega t - kx), \quad (4)$$

where h refers to water depth.

Dynamic pressure P on the buoy is appropriated for the linearized Bernoulli equation according to [17]

$$P = -\rho\frac{\partial\phi}{\partial t} = -\rho g\xi_a\frac{\cosh[k(z+h)]}{\cosh(kh)}\cos(\omega t - kx). \quad (5)$$

Exciting force F_e can be approximated by the combination of incident wave force and diffraction force. If $D/\lambda < 0.2$ (where D is the characteristic dimension and λ refers to wave length), diffracted component can be neglected, only incident wave force will be concerned [18, 19]. This is known as Froude-Krylov Approximation. Based on Froude-Krylov Approximation, F_e can be express as

$$F_e(t) = \iint_{S(t)} P\frac{\partial z}{\partial n}dS, \quad (6)$$

in which n is an outward normal vector on surface dS. $S(t)$ is instantaneous wet surface at time t; it depends on the instantaneous draft of the buoy $d(t)$. The instantaneous draft of the buoy $d(t)$ can be described as

$$d(t) = d - [z(t) - \xi(t)], \quad (7)$$

where d represents the initial draft, which is a designed draft. And $z(t)$ represents the vertical displacement of the buoy.

Restoring spring coefficient is determined by the equation of $C(t) = \rho g A_{\mathrm{wp}}(t)$, where A_{wp} is the waterline plane area at instant t. Added mass and radiation damping coefficient can be solved by the source distribution method, and the concrete method can be obtained from [20, 21].

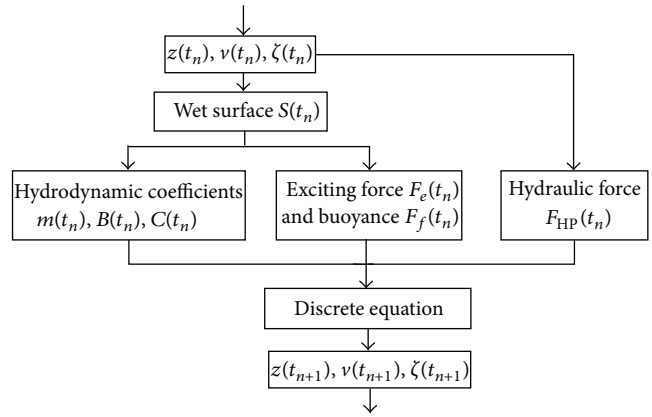

Figure 7: Progress of time marching process used in solving the motion equation.

The buoyance of the buoy can be calculated by the following equation:

$$F_f = \iint_{S(t)} \rho g z\frac{\partial z}{\partial n}dS. \quad (8)$$

Because of the hydraulic accumulators, the magnitude of hydraulic pressure acting on the buoy by hydraulic cylinder is approximately constant when the buoy is moving. Besides, its direction is always opposite to the velocity of the buoy. Thus, hydraulic pressure can be presented as follows:

$$F_{\mathrm{HP}} = \begin{cases} -K\dfrac{dz/dt}{|dz/dt|} & \dfrac{dz}{dt} \neq 0; \\ F_f - Mg + F_e(t) - C(t)z & \dfrac{dz}{dt} = 0, \end{cases} \quad (9)$$

where K is a constant.

3.3. Numerical Method for Solving the Motion Equation. Because of the complexity of the forces and the variation of hydrodynamic coefficients, we cannot get the analytical solution of the equation. To solve this motion equation, numerical method is necessary. Method of time marching process and explicit improved Euler method are adopted. The progress of time marching process has been used in solving the motion equation as Figure 7 shows.

3.4. Average Delivered Power of the Buoy. Direction of F_{HP} is always reverse to the velocity of the buoy, so the average delivered power of the buoy can be presented as follows:

$$\overline{P} = -\frac{\int_0^T F_{\mathrm{HP}}(dz/dt)\,dt}{T}, \quad (10)$$

where T is period of the incident wave.

If the magnitude of F_{HP} is a constant, and the motion of buoy is inline with Figure 8, then the average delivered power can be presented as follows:

$$\overline{P} = F_{\mathrm{HP}}\frac{Z_{\max} - Z_{\min}}{t}. \quad (11)$$

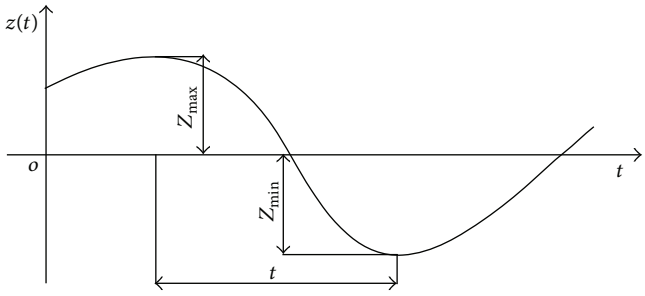

Figure 8: Periodic motion of sinusoidal form.

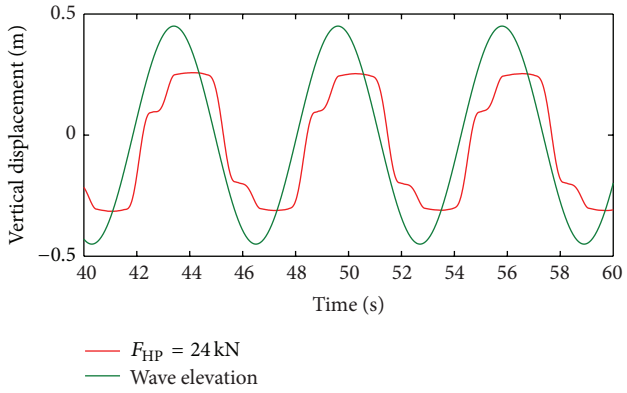

Figure 9: Computation result under the conditions of wave height of 0.9 m, initial draft of 0.835 m, and F_{HP} of 24 kN.

4. Result of Computation

First part of this section concerns the validation of the computation data by comparing to the real sea test. The other parts release the computation data under the condition of design wave.

4.1. Validation of the Computation Data. In order to verify the computation data, a comparison to test data from real sea state has been made. Figure 9 is the result from computation and Figure 10 is from the test. Both results are obtained under the conditions of wave height of 0.9 m, initial draft of 0.835 m, and F_{HP} of 24 kN. Both of the two figures have similar shape, and both have residence time on top and bottom of the curves. By comparing it to computation result, the test curve has less residence time on top and more on bottom. It is because the real incident wave is not sine-shaped; it is similar to the profile of Figure 11. The shape of the computational curve can also be verified by comparing it to reference [22]; both have similar shape as well. In addition, both have approximate amplitude. The amplitude of computation result is approximately 0.28 m and the amplitude of the test is 0.23 m. In general, though some differences exists, the approach to calculate the wave induced motion of the buoy is reliable.

4.2. Motion Characteristic of the Buoy. The situation when F_{HP} is larger than the gravity of the buoy is not taken into consideration. Because in this situation, the buoy could not move down; it would stop moving when incident waves could not have enough force to push it up.

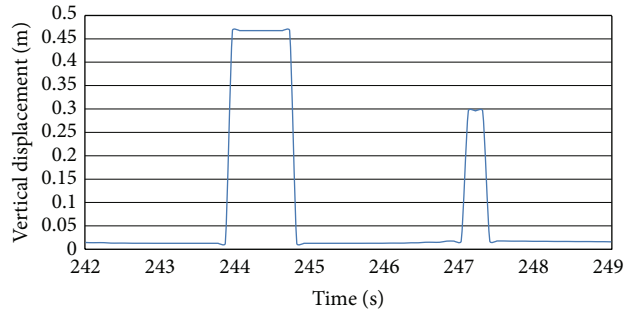

Figure 10: Test result under the conditions of wave height of 0.9 m, initial draft of 0.835 m, and F_{HP} of 24 kN.

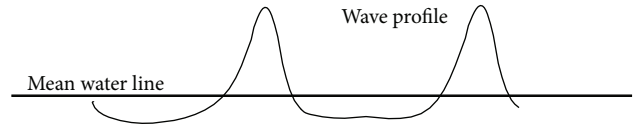

Figure 11: Shape of sea wave.

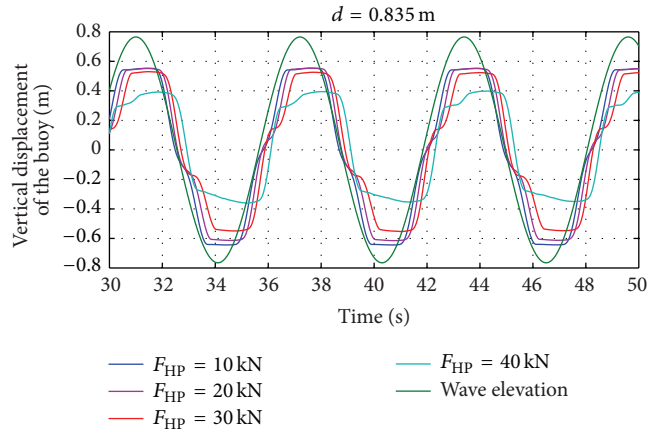

Figure 12: Vertical displacement of the buoy when d = 0.835 m.

Vertical displacement relative to the equilibrium free surface could be obtained after the motion equation being solved. Two groups of curves are presented when d = 0.835 and d = 1.035 m, and each group describes the changing vertical displacement of the buoy under different F_{HP}, as seen in Figures 12 and 13. Obviously, these groups of curves have distinct similarity. They share the following laws:

(a) period of motion is same as that of incident wave;

(b) phase lag increases with the rising F_{HP}, as well as residence time of the buoy at the place of maximum and minimum vertical displacement.

For comprehensive and richly detailed analysis, Figures 14, 15, and 16 were drawn according to the vertical displacement curves.

Figure 14 reflects the relationship between stroke length of the buoy and hydraulic pressure F_{HP} under different

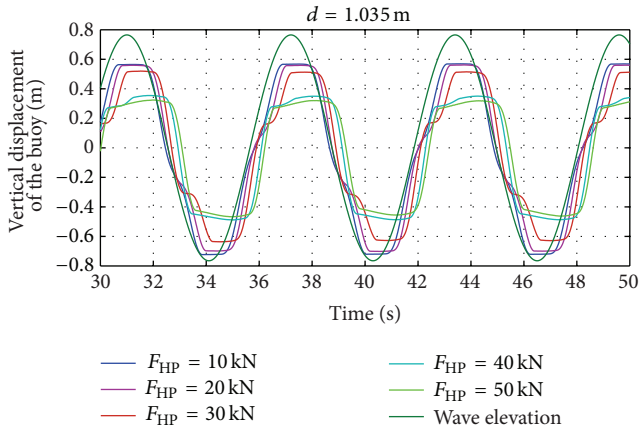

Figure 13: Vertical displacement of the buoy when $d = 1.035$ m.

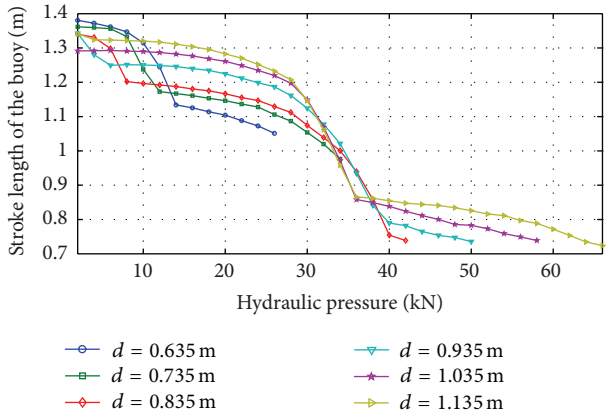

Figure 14: Stroke length of the buoy.

designed drafts. Stroke length of the buoy refers to the maximum vertical displacement minus the minimum vertical displacement of the buoy in a period. It is clearly shown in Figure 14 that the overall trend of the motion is attenuated with the increase of hydraulic pressure F_{HP}. The trend is nonlinearity. Take the curve of $d = 1.035$ as an example; stroke length decreases slowly from 1.3 m in 2 kN to 1.2 m in 28 kN, and then it drops sharply to 0.86 m in 36 kN. This is followed by a slowly attenuation trend until the end of the curve.

Figure 15 provides the relationship among maximum dynamic draft, designed draft, and F_{HP}. And Figure 16 provides the relationship among minimum dynamic draft, designed draft and F_{HP}. Maximum draft increases with the rising F_{HP}, while minimum draft decreases. The trend of these two groups of curves is almost near linear. In addition, slopes of curves in each group are approximately equal to each other. Every 10 kN increases of hydraulic pressure correspond to 0.1 m increases of maximum draft, while every 10 kN increases of hydraulic pressure correspond to 0.1 m decreases of minimum draft.

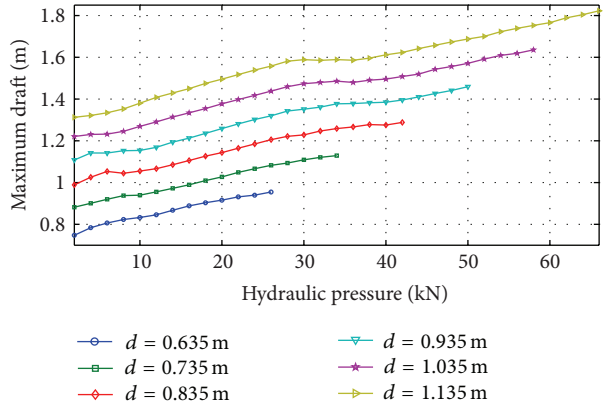

Figure 15: Maximum draft of the buoy.

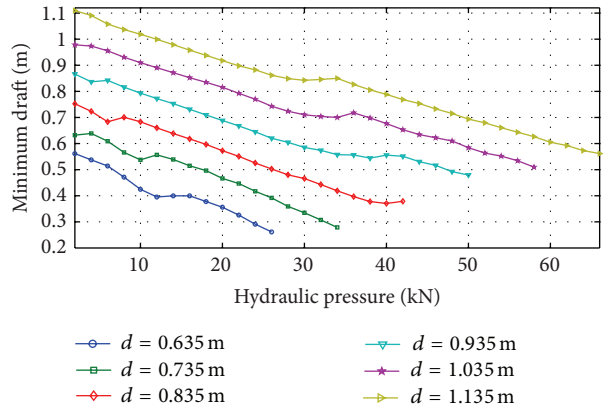

Figure 16: Minimum draft of the buoy.

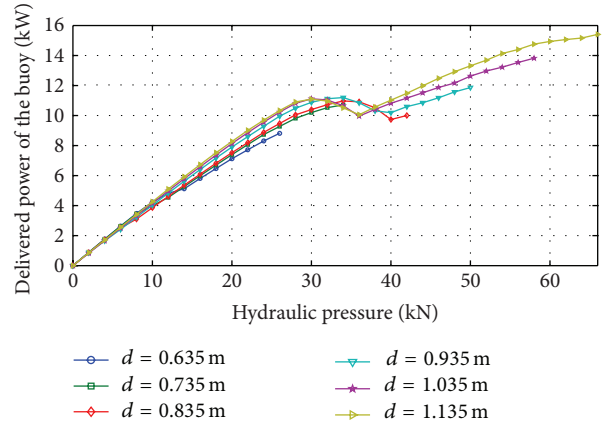

Figure 17: Delivered power of the buoy.

4.3. Rate of Work and Capture Width of the Buoy. Figure 17 shows the relationship between hydraulic pressure and delivered power of the buoy in different drafts. It is clearly shown in Figure 17 that delivered power increase with the rising designed draft when hydraulic pressure is lower than 30 kN. When designed draft is no more than 0.735 m, the delivered

Table 1: Delivered power and maximum draft under different designed drafts when $F_{HP} = 30$ kN.

Designed draft (m)	Delivered power (kW)	Maximum draft (m)
0.635	—	—
0.735	10.2	1.09
0.835	10.4	1.23
0.935	10.7	1.35
1.035	10.9	1.47
1.135	10.9	1.59

power of the buoy increases with the rising hydraulic pressure; while when designed draft is no less than 0.835 m, each curve will first climb to a peak value then will decrease little, after that it will continue increasing.

5. Conclusion

In the premise that the delivered power of the buoy ensured a high value, hydraulic pressure should be as small as possible. On one hand, if hydraulic pressure is too large, the buoy might hardly be driven when income wave is small. In this situation, the wave energy could not be absorbed. On the other hand, large designed hydraulic pressure would reduce the reliability of the hydraulic system and increase the cost and the building difficulty of the hydraulic system. Figure 17 shows that 30 kN is considered to be a suitable hydraulic pressure, because many curves reach a peak point near this value.

After hydraulic pressure is chosen to be equal to 30 kN, Table 1 can be obtained from Figure 17.

The moulded depth of the buoy should be larger than that of the maximum draft; otherwise, green water problem will occur, which will lead to practical delivered power less than the computational result. Therefore, because the moulded depth is 1.465 m, maximum draft should be smaller than 1.465 m. When hydraulic pressure is equal to 30 kN, delivered power and maximum draft increase with the rising designed draft (as seen in Table 1). When designed draft is no less than 1.035 m, the maximum draft of the buoy is larger than its moulded depth; thus, the best designed draft should be 0.935 m.

A conclusion that can be drawn from the above analysis is that the optimum designed draft is 0.935 m, while the optimum designed hydraulic pressure is 30 kN.

Acknowledgments

The authors would like to thank the State Oceanic Administration of China for financially supporting this research under Contract no. ZJME2011BL04. This work was also supported by the Research Foundation of the State Key Ocean Engineering Laboratory of Shanghai Jiao Tong University under Contract no. 1205 and the Zhejiang Provincial Natural Science Foundation of China under Contract no. Y5100180.

References

[1] J. Falnes, "A review of wave-energy extraction," *Marine Structures*, vol. 20, no. 4, pp. 185–201, 2007.

[2] Y. Zhang and Z. Lin, "Advances in ocean wave energy converters using piezoelectric materials," *Journal of Hydroelectric Engineering*, vol. 30, no. 5, pp. 145–169, 2011.

[3] B. V. Korvin-Kroukovsky, "Investigation of ship motions in regular waves," *Transactions of the SNAME*, vol. 63, pp. 386–435, 1995.

[4] M. C. Fang, M. L. Lee, and C. K. Lee, "Time simulation of water shipping for a ship advancing in large longitudinal waves," *Journal of Ship Research*, vol. 37, no. 2, pp. 126–137, 1993.

[5] B. E. Alexander and H. K. Josh, *Motions and Loads of a Trimaran Traveling in Regular Waves*, FAST, London, UK, 2001.

[6] N. Fonseca, C. Guedes Soares, and A. Incecik, "Numerical and experimental study of large amplitude motions of two-dimensional bodies in waves," *Applied Ocean Research*, vol. 19, no. 1, pp. 35–47, 1997.

[7] C. A. Brebbia and S. Walker, *Boundary Element Techniques in Engineering*, Butterworth, Dublin, Ireland, 1990.

[8] J. N. Newman, *The Approximation of Free-Surface Green Functions, Waves Asymptotics*, Cambridge University Press, Cambridge, UK, 1990.

[9] E. R. Jefferys, *Device Characterisation. Power from Sea Waves*, Academic Press, London, UK, 1980.

[10] J. N. Newman, "Absorption of wave energy by elongated bodies," *Applied Ocean Research*, vol. 1, no. 4, pp. 189–196, 1979.

[11] J. B. Ulvin, M. Molinas, and J. Sjolte, "Analysis of the power extraction capability for the wave energy converter BOLT," *Energy Procedia*, vol. 20, pp. 156–169, 2012.

[12] A. F. D. O. Falcão, P. E. R. Pereira, J. C. C. Henriques, and L. M. C. Gato, "Hydrodynamic simulation of a floating wave energy converter by a U-tube rig for power take-off testing," *Ocean Engineering*, vol. 37, no. 14-15, pp. 1253–1260, 2010.

[13] G. Van Oortmerssen, *The Motions of a Moored Ship in Waves*, 1979.

[14] J. V. Wehausen, "The motion of floating bodies," *Annual Review of Fluid Mechanics*, vol. 3, pp. 237–268, 1971.

[15] M.-C. Fang, Z.-Y. Lee, and K.-T. Huang, "A simple alternative approach to assess the effect of the above-water bow form on the ship added resistance," *Ocean Engineering*, vol. 57, pp. 34–48, 2013.

[16] O. M. Faltinsen, *Sea Loads on Ship and Offshore Structure*, Cambridge University Press, Cambridge, UK, 1990.

[17] J. M. J. Journée and W. W. Massie, *Offshore Hydromechanics*, Delft University of Technology, Delft, The Netherlands, 2001.

[18] T. Sarpkaya and M. Isaacson, *Mechanics of Wave Forces on Offshore Structures*, Van Nostrand Reinhold, New York, NY, USA, 1981.

[19] Y. Goda, *Random Seas and Design of Maritime Structures*, World Scientific Publishing, River Edge, NJ, USA, 2nd edition, 2000.

[20] J. N. Newman, *Marine Hydrodynamics*, MIT Press, Cambridge, Mass, USA, 1977.

[21] C. C. Mei, "Numerical methods in water wave diffraction and radiation," *Annual Review of Fluid Mechanics*, vol. 10, pp. 393–416, 1978.

[22] J. Cruz, *Ocean Wave Energy: Current Status and Future Prepectives*, Garrard Jassan and Partners Limited, Bristol, UK, 2008.

Hindawi Publishing Corporation
Advances in Mechanical Engineering
Volume 2013, Article ID 175684, 9 pages
http://dx.doi.org/10.1155/2013/175684

Research Article

Comparison of Structural Properties between Monopile and Tripod Offshore Wind-Turbine Support Structures

Da Chen,[1,2] Kai Huang,[1,2] Valentin Bretel,[1,2] and Lijun Hou[1,2]

[1] *Key Laboratory of Coastal Disaster and Defence, Ministry of Education, Hohai University, Nanjing 210098, China*
[2] *College of Harbor, Coastal, and Offshore Engineering, Hohai University, Nanjing 210098, China*

Correspondence should be addressed to Lijun Hou; ljhou_hhu@126.com

Received 28 June 2013; Revised 22 September 2013; Accepted 23 September 2013

Academic Editor: Luigi Cappelli

Copyright © 2013 Da Chen et al. This is an open access article distributed under the Creative Commons Attribution License, which permits unrestricted use, distribution, and reproduction in any medium, provided the original work is properly cited.

Offshore wind power provides a new kind of green energy. This paper presents a comparison study on the structural properties of monopile and tripod wind-turbine support structures, which are used extensively in offshore wind farms. Both structures have the same upper tower, but different lower structures, one with a monopile and the other with a tripod. Static, fatigue, and modal analyses indicate that both the tripod and monopile structures are feasible in the field, but that the tripod structure is superior to the monopile structure. Static analysis reveals that the location of maximum stress in the monopile structure is different from that in the tripod structure, and that the tripod structure shows higher stiffness and greater stress-control capacity than the monopile structure. Fatigue analysis indicates that the tripod structure has a longer lifetime than the monopile structure. Modal analysis indicates that the two structures exhibit large differences in their natural frequencies. Unlike the monopile structure, the third and first modes both have a substantial influence on the dynamic response of the tripod structure.

1. Introduction

In recent years, clean energy strategies have been given great importance in environment protection and durable development. In the case of electricity, offshore wind farms promise to become an important source of energy in the near future to decrease reliance on traditional coal-fired power. In the past three decades, nations around the world with wind energy have led the way in the development of offshore wind farms. Thirty to forty percent of all new installed power generation capacity in Europe and the United States is now associated with wind energy. It is expected that wind energy farms with a total of 80 GW will be installed in Europe and the United States by 2020 [1].

It is worth noting that the support structures of a wind-turbine system act as the main structural members of a wind electricity farm and are closely related to the structure's safety, stability, and durability. In general, the upper tower is composed of a conical steel pipe, whereas various types of substructures can be designed according to field conditions. The substructure is used to anchor the support structure to the seabed and typically belongs to one of six types: gravity, monopile, tripod, jacket, suction, and floating foundation [2, 3]. Based on current design philosophy, gravity-based structures are preferred for shallow waters (up to 5 m), whereas the monopile foundation is used for wind farms in water depths up to 20 m. For deeper water, tripod or jacket support structures are often considered. Floating support structures remain a challenge due to their high cost, but this challenge will need to be met for countries with fewer regions of shallow water [4]. However, Scharff and Siems [5] have explored the application of monopile foundations in water depths of up to 20–40 m and have provided two detailed discussions of design examples.

The support structures (tower and foundation) are subjected to a variety of combined static and dynamic loads such as gravity, wind, waves, tides, and earthquakes. The design and analysis of these support structures are key parts of the design of the whole wind-turbine system. A fatigue property analysis of a monopile structure by Mo et al. [6] indicated

that turbine-system vibration was a main source of load, resulting in structural fatigue damage. Torcinaro et al. [7] presented a structural optimization design for a tripod support structure through stress and stability analysis. Agbayani [8] reviewed damage to monopile structures subjected to high-cycle fatigue and proposed a series of repair measures. Bazeos et al. [9] investigated the static, seismic, and stability capabilities of the monopile support structure of a wind turbine and found that refined finite-element models were necessary at specific critical locations for a more accurate structural analysis.

However, few studies have yet been performed on the differences in structural properties among the different types of wind-turbine support structures. Moreover, a new planned wind-power installation in Donghai, China, is in the discussion stage, waiting for a decision on the type of foundation. In China, grouped pile foundations are used in most wind-turbine support structures. However, compared with monopile and tripod foundations, the grouped pile foundation involves more complex construction and higher cost. Given these points, to provide a reference for foundation-type selection, this paper presents a study on a support structure where the lower support structure is designed as a monopile or tripod structure, but the upper one remains the traditional tower structure. Results of static, fatigue, and modal analysis using the SOLIDWORKS2012 general FEM software were compared between monopile and tripod structures.

Table 1: Details of tubular shell pieces of the upper tower.

Piece	D_t (mm)	D_b (mm)	t (mm)
A	4800	5400	49
B	4200	4800	44
C	3600	4200	38
D	3000	3600	33

Note: D_t and D_b were the top and bottom diameters of different pieces; t was the thickness of steel shell concerning the bottom diameter D_b.

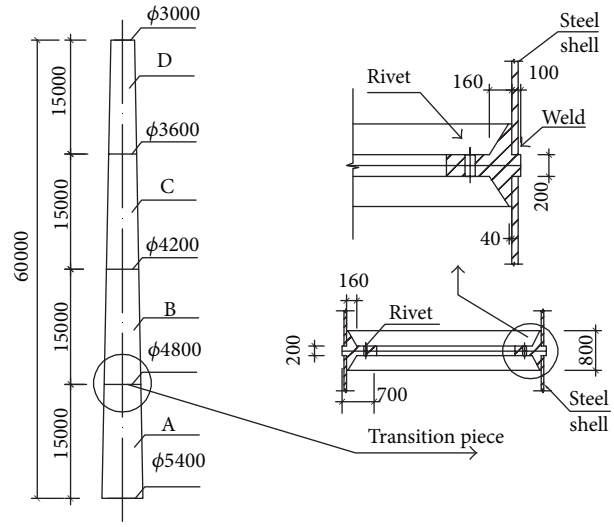

Figure 1: Configuration of the upper tower.

2. Description of Support Structures

In the present study, two types of offshore wind-turbine support structures were investigated. In these structures, the upper towers were the same, but the lower structures were different, one being a monopile and the other a tripod. Moreover, the support structure was made of high-strength steel S620M with a yield strength of 620 MPa.

2.1. Upper Tower Structure. Figure 1 shows a sketch of the upper tower. This upper tower consisted of four pieces of steel shell with diameters linearly varying along their height. The upper tower was 60 m in height, and each piece of shell had the same length, 15 m. The bottom diameter of the tower was designed as 5400 mm, which is identical to that of the upper tower in a similar wind-turbine system built in Donghai. The cross-sectional thickness of the tubular shell was designed based on design standard NORSOK N-004, where the ratio of diameter D to the thickness t of the tubular shell is required to be $D/t < 120$ [10]. Note that the thickness of steel tubular was determined according to the bottom diameter D_b of each piece and the D/t ratio of 110. These four pieces of tubular shell were labeled as A to D in sequence according to decreasing diameter. Details of all the pieces of tubular shell are summarized in Table 1.

Two steel transition pieces, as shown in Figure 1, were used as the end configuration of each steel shell and were welded onto the steel shell. The transition pieces of adjacent steel shells were connected together by rivets to make up the upper tower.

2.2. Lower Support Structures. Figure 2 shows details of the monopile and tripod substructures. Both types of substructures were 40 m long. The monopile structure had a constant diameter of 3600 mm, or in other words, the diameter decreased from 5400 mm in the upper tower to 3600 mm in the lower monopile. The thickness of the steel-pipe pile was 45 mm. The tripod structure consisted of a central column, three diagonal bracings, and three supporting pile sleeves. For the central column, the diameter of the top was 5.4 m and then decreased to 4.08 m. Each pile sleeve was 13 m high, was located at 12.5 m from the central column, and had a diameter of 2.4 m. The thickness of the pipes in the tripod substructure was constant at 40 mm. A diagonal transition member was used to connect the upper tower and the lower support structure together. All the joints between the steel shells were welded together.

Note that for the lower monopile support structure, its diameter is supposed to increase with water depth because of the increased bending moment and compressive force. However, it is also true that the wave loading on a pile, as one of the main loads considered in structural design, becomes larger with increasing pile diameter. Moreover, the pile-sinking construction of the monopile foundation is more difficult with the increasing diameter from the viewpoint of

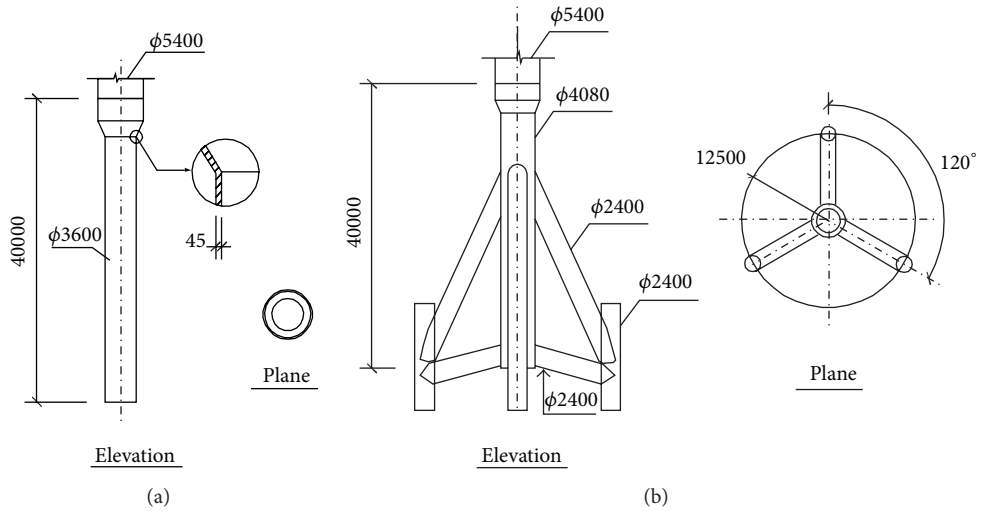

Figure 2: Detail of lower support structures: (a) monopole and (b) tripod.

the local stability. Given these two points, the authors used a monopile foundation as the lower support structure that was made of high-strength steel with a yield strength of 620 MPa, and thus a diameter (3600 mm), smaller than the 5400 mm bottom diameter of the upper tower, was utilized.

2.3. Applied Load. Offshore wind-turbine structures are not only exposed to highly corrosive environmental conditions, but are also subjected to various quasi-static, periodic, stochastic, and transient loads. For convenience in structural design, it is necessary to perform a reasonable load simplification. In this research, the main loads experienced, including horizontal wind load, wave load, and vertical gravity, were simplified as described below.

2.3.1. Wind Load. Wind conditions are important not only in defining the loads imposed on turbine structural components, but also in designing the support structures of the wind-turbine system. The measured on-site wind parameters strongly influence the design of wind-turbine support structures. The wind load can be obtained through a formula based on lift theory:

$$\xi = \frac{1}{2}\rho_{\text{air}} v_{\text{wind}}^2 S C_z, \tag{1}$$

where ξ is the force of the wind on the blades (kN), ρ_{air} is the density of air (1.225 kg/m^3), v_{wind} is the wind speed (m/s), S is the surface area of the blades (m^2), and C_z is the portance coefficient, assumed to be 0.8 for a classic blade.

According to observed data and information, the surface area of the blades was 50 m × 1.5 m × 3 blades = 225 m^2, and the maximum speed before installation of the wind farm was 34 m/s. Therefore, the wind load calculated by (1) was 127 kN. Furthermore, assuming a safety coefficient k of 1.35 (as recommended in DNV-OS-J101 [11]), the horizontal force applied on the structure by the wind would be 172 kN. In addition, according to the structural offshore wind-turbine optimization method, the wind exerted a pressure of 5 kN/m on one side of the upper tower.

2.3.2. Wave Load. In the ocean environment, wave force is also a major load imposed on the structure. The maximum horizontal wave force was calculated based on Airy's linear theory. In this theory, the horizontal and vertical water-particle velocity at coordinates (x, y) and time (t) can be expressed as [12]

$$\begin{aligned} u &= \frac{\omega H}{2}\frac{\cosh ky}{\sinh kd}\cos(kx - \omega t), \\ v &= \frac{\omega H}{2}\frac{\sinh ky}{\sinh kd}\sin(kx - \omega t), \end{aligned} \tag{2}$$

where u and v are the horizontal and vertical velocity of water, H denotes wave height, and k and ω represent the wave length and wave angular frequency. Based on Airy's linear theory, the correlation between k and ω is given by the dispersion equation

$$\omega^2 = gk\tanh kd. \tag{3}$$

Furthermore, the water-particle accelerations a_x and a_y can be obtained based on $a_x \approx du/dt$ and $a_y \approx dv/dt$ using the corresponding velocity (2):

$$\begin{aligned} a_x &= \frac{\omega^2 H}{2}\frac{\cosh ky}{\sinh kd}\sin(kx - \omega t), \\ a_y &= \frac{\omega^2 H}{2}\frac{\sinh ky}{\sinh kd}\cos(kx - \omega t), \end{aligned} \tag{4}$$

where y is the distance from the vertical position of the wave surface to the seabed and can be calculated as

$$y = \eta + d, \tag{5}$$

where d is the water depth, the distance from the seabed to the still-water level, and η is the distance from the vertical

position of the wave surface to the still-water level and can be obtained by [13]

$$\eta = \frac{H}{2}\cos(kx - \omega t). \quad (6)$$

For slender offshore structures such as monopiles, tripods, or offshore template structures, the Morison equation can be used to convert the velocity and acceleration terms into wave forces [14]. The Morison equation can be written as

$$F = \frac{1}{2}\rho C_D D|u|u + \rho C_I \frac{\pi D^2}{4} a_x, \quad (7)$$

where ρ denotes water density, C_D and C_I denote the drag and inertia coefficients, and D is the diameter of the structural member. The first term on the right-hand side of this equation is referred to as the drag term and is proportional to the square of the water velocity. The second term is referred to as the inertial term and is proportional to water acceleration. For the case under study, the parameters were taken as H = 10.66 m, C_D = 1.0, and C_I = 2.0. The predicted wave force was 357.46 kN. Assuming a safety factor of 1.04 (according to the DNV-OS-J101 standards), the horizontal wave force for the current case was 371.76 kN.

2.3.3. Blade and Rotor Loads. According to a real offshore wind farm such as M5000, the mass of the top structure (blades and rotor) is approximately 49.5 tons (or 493 kN). This load can be equivalently applied on the top of the tower in the vertical direction for calculating the wind-turbine support structure. Detailed data on the M5000 wind farm can be obtained on the AREAVA website [15].

2.3.4. Gravity Load of the Structure. The acceleration of gravity was assumed to be 9.81 m/s^2. The total load condition of the monopile structure is shown in Figure 3 and is identical to that of the tripod structure.

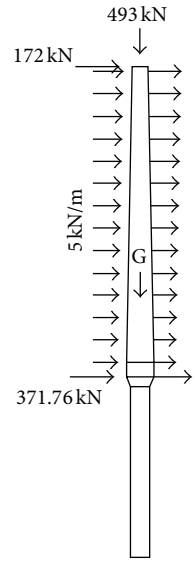

Figure 3: Load distribution on the monopile support structure.

3. Numerical Analysis and Discussion

3.1. Static Analysis

3.1.1. Stress Comparison. Figure 4 shows the calculated stress nephograms for the monopile and tripod support structures. Comparing the stress nephograms in Figures 4(a) and 4(b), it is apparent that the tripod structure shows the maximum stress at the transition junction from the lower support structure to the upper tower, whereas the monopile structure has its maximum stress value at the end of the lower pile. In addition, as shown in Figure 4, the maximum stress of the monopile structure is approximately 2.35 times greater than that of the tripod structure, but it is still far less than the yield strength of 620 MPa, and therefore these two structures remained in the elastic stage. For the monopile structure, the maximum tensile and compressive stresses were, respectively, 486.6 MPa and 499 MPa, while the corresponding values for the tripod structure were 279.2 MPa and 211.8 MPa. Given these points, the tripod structure was more effective than the monopile structure from a stress-control point of view.

Figure 5 shows the tensile and compressive stresses distribution along the longitudinal height of the two support structures. It is clear that the stress distributions in the upper tower are similar for the tripod and monopile foundations, whereas a large difference is apparent along the lower support structures. The stress was only 27 MPa at the foot of the tripod structure, where the maximum stress was observed for the monopile structure. Moreover, as the diameter increased from 4.08 m to 5.4 m, the stress rapidly dropped from the maximum value to 70 MPa for the tripod foundation structure. In addition, the maximum stress for the tripod foundation was observed in the transition section, a value close to the stress of 274 MPa at the same location in the monopile foundation. Judging from these points, the tripod structural system can be said to be superior to the monopile structural system from the structural stress distribution viewpoint.

As shown in Figure 5, note that the maximum stress in the tripod support structure and the tower structure was lower than the yield strength of 355 MPa for S355 steel. Therefore, the high-strength steel S620M can be replaced with the normal steel S355 to make full use of tensile strength of steel.

3.1.2. Deformation Comparison. Figure 6 shows the deformation nephogram for the monopile and tripod support structures. It is apparent that the deformation increased with the height above the seabed and that the maximum displacement occurred at the top of the structure in the lateral direction. The monopile structure showed a maximum deformation of 486 mm, whereas the tripod structure had a maximum displacement of 368 mm. In addition, the displacement of the tripod structure was less than that of the monopile structure at the same longitudinal location. In other words, the tripod structure had greater flexural stiffness than the monopile structure.

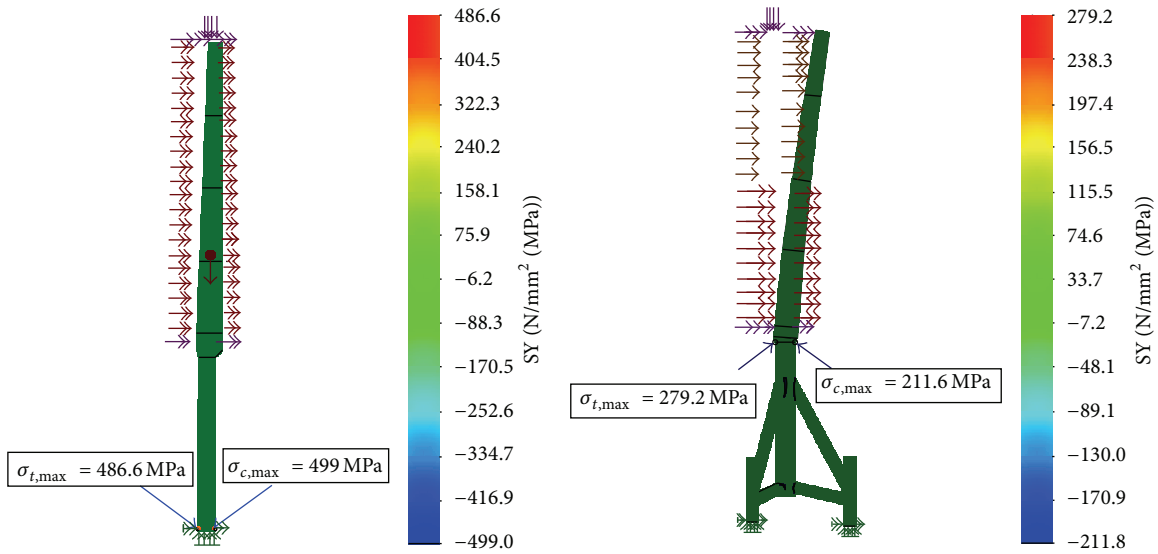

(a) Monopile (b) Tripod

FIGURE 4: Stress nephogram in the longitudinal direction.

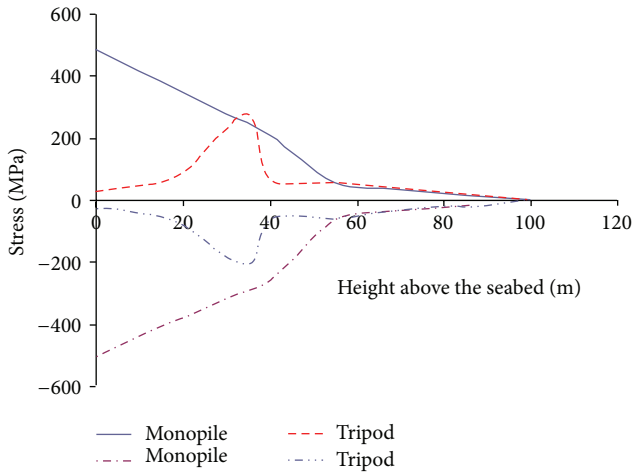

FIGURE 5: Comparison of stress distribution along the longitudinal height of the support structures.

With respect to the maximal lateral deformation h and the height of the structure H, the deflection factor a can be calculated based on DNV-OS-201J [11]:

$$a = \frac{H}{h}, \quad a > 200. \tag{8}$$

In the cases studied, when H = 100 m, the computed values of a for these two structures were 206 and 271.7, respectively, which both satisfied the requirements of DNV-OS-201J [11].

In summary, the tripod structure is clearly more stable and resistant to applied loads than the monopile structure.

3.2. Fatigue Analysis. Figure 7 shows the number of cyclic loads carried up to fatigue failure for the monopile and tripod structures. The most fatigue-affected locations still corresponded with the locations of the maximum tensile stress in the static analysis. However, the number of loading cycles carried by the tripod structure was far larger than that of the monopile structure. With respect to the most damaged structural position, the maximum number of load cycles was only 210,000 for the monopile structure, whereas the tripod structure was able to endure at least 410,000. In other words, the tripod support structure had a lifetime 48.5% greater than that of the monopile support structure. Judging from these points, the tripod structure is more resistant to fatigue than the monopile structure.

Both support structures satisfied the minimum cycle number of 1.0e + 05 recommended in DNV-OS-J101 [11]. However, it is also necessary to determine the lifetime of these two structures. The parameters were defined according to the study by Agbayani [8]. First, for these two structures, the number of loading cycles was estimated to be 40 per day. It should be highlighted that the stress on a structure subjected to different loading cycles varies between the minimum and maximum stresses, and some cycles must result in a stress lower than the maximum value. Indeed, all loads are not equal in intensity and always occur in a random time distribution. However, the forces and pressures applied in the present study have been set to their maximum values. Therefore, to perform a realistic calculation, the number of loading cycles has been assumed to be 40 per day.

Second, the working time ratio (proportion of working hours in each 24 hours) had to be determined for each structure. According to investigations of the structures under study, the maximum working time ratio was set to 0.85 for the tripod structure and 0.8 for the monopile structure [16]. Note that these ratios are defined in a conservative way because of safety considerations and that the actual ratios are probably less than these values.

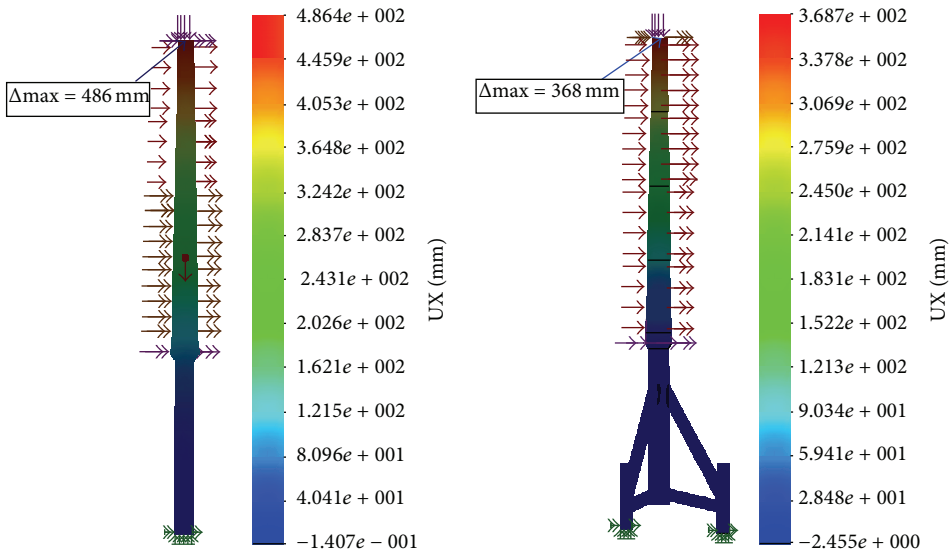

(a) Monopile (b) Tripod

Figure 6: Displacement nephogram in the lateral direction.

Knowing all these factors, the lifetime can be calculated for each structure. For the monopile structure, the number of load cycles is 11,680 per year considering the assumed working ratio. The lifetime durability can then be obtained as

$$T = \frac{N_{\min}}{N_{\text{py}}}, \tag{9}$$

where T is the lifetime (in years), $N_{\min}$ is the minimum number of loading cycles, and N_{py} is the loading cycles per year. For the case studied, the lifetime durability obtained by (9) was approximately 18 years. For the tripod support structure, the number of load cycles per year was 12,400 assuming a working ratio of 0.85. The lifetime durability calculated based on (9) was then approximately 33 years. From these results, it can be concluded that the tripod support structure can survive longer than the monopile structure, which is advantageous over the long term.

3.3. Modal Analysis. When a structure is subjected to dynamic loads, its natural structural frequencies should be adjusted to be far from the dynamic load frequency to avoid the resonance. If the natural structural frequency is close to the load frequency, even small driving forces can produce large-amplitude oscillations.

Modal analysis is the basis of dynamic analysis. A wind-turbine support structure is subjected to many periodic actions such as winds and waves. In general, these loads have progressive and changeable frequencies within a known and specific domain. Therefore, the risks of resonance can be estimated and eliminated through calculating and adjusting the natural frequencies of the structures.

Table 2 lists the natural frequency and period of the first three vibration modes for the monopile and tripod structures. The tripod structure was found to have higher natural frequencies and shorter periods than the monopile structure. To estimate whether resonance will occur, the dynamic load frequency must be established. In this research, only the main load (wind load) was taken into account to simplify the analysis. In fact, the vibration of structures subjected to wind load arises from rotary turbulences due to the impact of wind on the structure. The frequency of these rotations can be determined using the Strouhal number, a dimensionless number describing oscillating flow mechanisms.

Table 2: Results of modal analysis.

Series	*Nf#*	Frequency (Hz)	Period (s)	Maximum displacement (mm)
Monopile	1	0.389	2.570	3.267
	2	2.508	0.398	3.912
	3	6.401	0.156	4.674
Tripod	1	0.797	1.254	3.927
	2	4.188	0.238	4.663
	3	7.108	0.140	2.517

Note: *Nf#* denotes the number of each natural frequency.

Based on the theory for calculation of the Strouhal number, the turbulence frequencies can be obtained as

$$f_v = \frac{S_t v_w}{L_c}, \tag{10}$$

where f_v is the frequency of the vortex, v_w is the wind velocity, and L_c is the characteristic length of the structure. In the case under study, the Strouhal number (S_t) was in the range from 0.1 to 0.2. The minimum wind velocity for the structure was 11 m/s and the maximum 34 m/s. The characteristic length was taken as the length of the upper tower structure

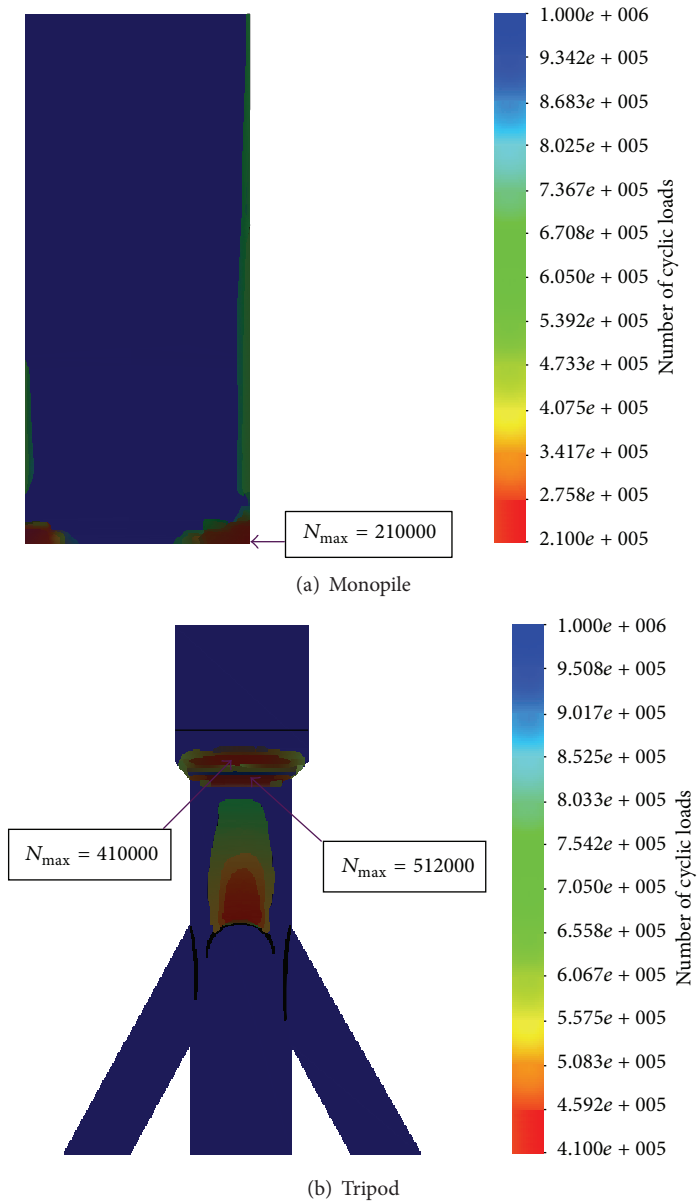

Figure 7: Number of load cycles carried by the structures.

(60 meters), and then the calculated vortex frequency (f_v) was in the range from 0.0183 Hz to 0.1130 Hz. As listed in Table 2, the lowest natural frequencies of the two structures were 0.390 Hz and 0.797 Hz. Therefore, resonance of these structures due to rotary turbulence can be eliminated.

Figures 8 and 9 show the first three mode shapes for the monopile and tripod structures. These mode shapes were similar for both structures, whereas the variance law of displacement coordinates showed a large difference. The maximum displacement coordinates are listed in Table 2. It is apparent that the maximum displacement gradually increased with increasing frequency for the monopile structure, whereas the tripod structure showed an increase first and then a drop with frequency.

Based on the mode shape, the mass participation factor M_j can be calculated as

$$M_j = \frac{\left[\sum_{k=1}^{n} \phi_{kj} m_k\right]^2}{\sum_{k=1}^{n} \phi_{kj}^2 m_k}, \tag{11}$$

where m_k is the mass of the kth mass particle and ϕ_{kj} is the displacement coordinate of this point for the jth mode. Figure 10 shows the mass participation factor of different modes for these two types of structures. For the monopile structure, the first mode shape, with a frequency of 0.390 Hz, has a maximum mass participation factor of 46%, approximately 3.5 times that of the second mode.

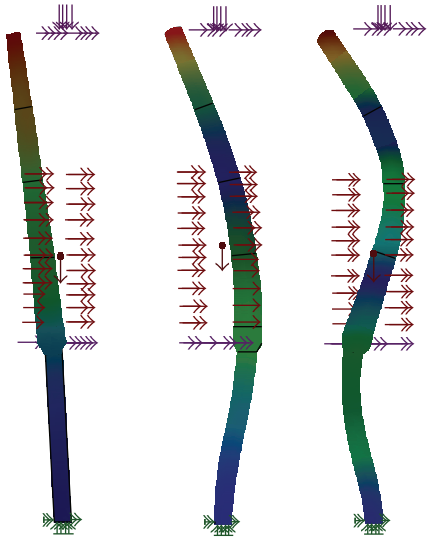

Figure 8: First three modes of the monopile structure.

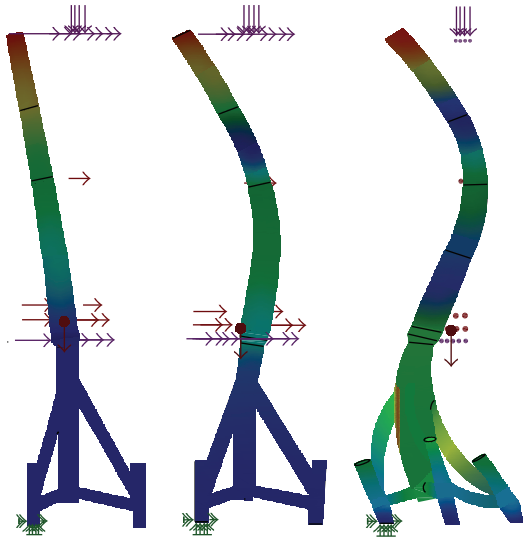

Figure 9: First three modes of the tripod structure.

This implies that the first mode plays a controlling role in the dynamic response of monopile structures. However, for the tripod structure, the third mode, with a frequency of 7.108 Hz, showed the maximum mass participation factor of 30.2%, slightly larger than the value of 24.5% for the first mode, but far greater than 9.6% for the second mode. It can be concluded that both the third and first modes play key roles in the dynamic response of tripod structures, which is clearly different from the response of monopile structures.

Moreover, the frequency separation can be further defined by the difference between any two adjacent frequencies. For the monopile structure, the first two modes presented the smallest frequency separation, 2.111 Hz, and the sum of the corresponding mass participation factors was 59%. In the tripod case, the smallest frequency separation was 2.920 Hz, between the second and third modes, and the total

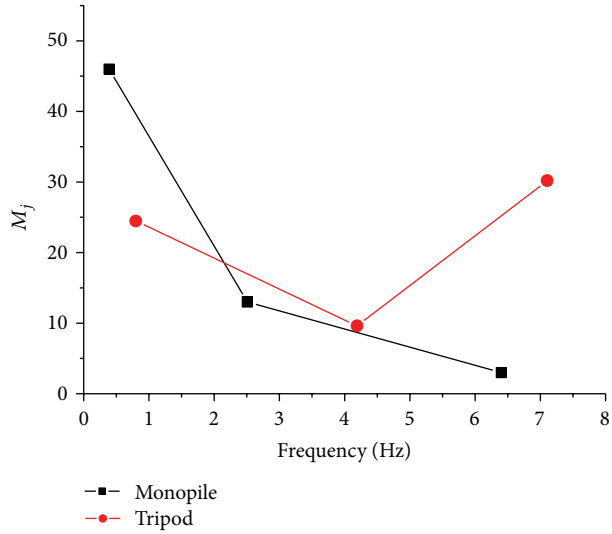

Figure 10: Comparison of the mass participation factor of different modes.

mass participation factor of these two modes was 39.8%. It can be concluded that the tripod is the safer structure because of its wider frequency separation and smaller mass participation factor.

The static, fatigue, and modal analyses of monopile and tripod support structures described above have demonstrated that both the monopile and tripod support structures are applicable under the field conditions considered. Note that the designed pile diameter and the use of high-strength steel are feasible for the support structures described in this paper. In contrast, a previous investigation by Scharff and Siems [5] indicated that for a wind-turbine system similar to those studied here, the pile diameter was increased to 7500 mm from 5500 mm of the upper tower for a water depth of 20–40 m. Comparing Scharff's study with the current one, several differences are evident. First, the type of steel used in Scharff's study was S355, with a yield strength of 355 MPa, whereas high-strength steel with a yield strength of 620 MPa was used in this study. High yield strength of steel is supposed to result in a smaller diameter based on the design of the ultimate limit state. Moreover, because the pile diameter was smaller than that in Scharff's study, the wave load applied to the pile was less in the current study, which is helpful to know when decreasing pile diameter.

4. Conclusions

This paper has presented an investigation into the structural properties of monopile and tripod wind-turbine support structures. Based on a comparison of the results of static, fatigue, and modal analyses results for these two structures, the following conclusions can be drawn.

(1) The maximum stress in the monopile structure was at the base, whereas the transition location from the lower central column to upper tower showed the maximum stress for the tripod structure. Moreover,

for the case under study, the maximum stress and displacement for the monopile structure were approximately 2.35 and 1.32 times greater than those of the tripod structure. The tripod showed greater stiffness and better stress-control capacity than the monopile structure.

(2) Under the same cyclic loading, the tripod structure has a longer lifetime than the monopile structure. This is beneficial for saving engineering cost in the long run.

(3) The modal analysis indicated that the first three natural frequencies of the tripod structure were higher than the corresponding frequencies of the monopile structure. The first mode played a controlling role in the dynamic response of the monopile structure, whereas both the third and first modes had a strong influence on the tripod structure. The results for frequency separation and mass participation factor indicated that the tripod structure was more reliable than the monopile structure.

(4) The analytical results indicated that both monopile and tripod structures can be used as wind-turbine support structures in the environment considered. However, comparison of structural responses using static, fatigue, and modal analyses revealed that the tripod structure is superior to the monopile structure. Moreover, it is effective to use high-strength steel in the monopile structure for optimizing the monopile diameter to be smaller than that of the upper tower bottom.

Acknowledgments

This research was supported by National Natural Science Foundation of China (51137002) and Natural Science Foundation of Jiangsu Province (BK2011026).

References

[1] A. R. Henderson, C. Morgan, B. Smith, H. C. Sørensen, R. J. Barthelmie, and B. Boesmans, "Offshore wind energy in Europe—a review of the state-of-the-art," *Wind Energy*, vol. 6, no. 1, pp. 35–52, 2003.

[2] S. Malhotra, "Selection, design and construction guidelines for offshore wind turbine foundations," in *Wind Turbines*, I. Al-Bahadly, Ed., pp. 231–264, InTech, Zagreb, Croatia, 2011.

[3] S. Malhotra, "Design and construction considerations for offshore wind turbine foundations in North America," in *GeoFlorida 2010: Advances in Analysis, Modeling and Design*, D. O. Fratta, A. J. Puppala, and B. Muhunthan, Eds., pp. 1533–1542, ASCE, West Palm Beach, Fla, USA, 2010.

[4] A. R. Henderson, R. Leutz, and T. Fujii, "Potential for floating offshore wind energy in Japanese waters," in *Proceedings of the 12th International Offshore and Polar Engineering Conference (ISOPE '02)*, Kitakyushu, Japan, May 2002.

[5] R. Scharff and M. Siems, "Monopile foundations for offshore wind turbines—solutions for greater water depths," *Steel Construction*, vol. 6, no. 1, pp. 47–53, 2013.

[6] J.-H. Mo, Y.-P. He, Y.-G. Li, and E.-H. Zhang, "Fatigue analysis of offshore wind turbine mono-pile support structure," *Journal of Shanghai Jiaotong University*, vol. 45, no. 4, pp. 565–569, 2011.

[7] M. Torcinaro, F. Petrini, and S. Arangio, "Structural offshore wind turbines optimization," in *Earth and Space 2010: Engineering, Science, Construction, and Operations in Challenging Environments*, G. Song and R. B. Malla, Eds., pp. 2130–2142, ASCE, Honolulu, Hawaii, USA, 2010.

[8] N. A. Agbayani, "Defects, damage, and repairs subject to high-cycle fatigue: examples from wind farm tower design," in *Forensic Engineering Congress 2009: Pathology of the Built Environment*, S. Chen, A. D. de Leon, A. M. Dolhon, M. J. Drerup, and M. K. Parfitt, Eds., pp. 546–555, ASCE, Washington, DC, USA, 2009.

[9] N. Bazeos, G. D. Hatzigeorgiou, I. D. Hondros, H. Karamaneas, D. L. Karabalis, and D. E. Beskos, "Static, seismic and stability analyses of a prototype wind turbine steel tower," *Engineering Structures*, vol. 24, no. 8, pp. 1015–1025, 2002.

[10] N. NORSOK-004, *NORSOK Standard for Design of Steel Structures*, Standards Norway, Lysaker, Norway, 2004.

[11] Dnv-Os-J101, *Offshore Standard- Design of Offshore Wind Turbine Structures*, Det Norske Veritas, Oslo, Norway, 2010.

[12] T. H. Dawson, *Offshore Structural Engineering*, Prentice Hall, New Jersey, NJ, USA, 1983.

[13] S. K. Charkrabarti, *Nonlinear Methods in Offshore Engineering: Developments in Marine Technology*, Elsevier, New York, NY, USA, 1990.

[14] A. R. Henderson, M. B. Zaaijer, and T. R. Camp, "Hydrodynamic loading on offshore wind turbines," in *Proceeding of the Offshore Windenergy in Mediterranean and Other European Seas*, Naples, Italy, 2003.

[15] The M5000 wind turbine (AREVA), http://www.areva.com/FR/activites-4430/l-eolienne-m5000.html.

[16] P. Schaumann, S. Lochte-Holtgreven, and S. Steppeler, "Special fatigue aspects in support structures of offshore wind turbines," *Materials Science and Engineering Technology*, vol. 42, no. 12, pp. 1075–1081, 2011.

Hindawi Publishing Corporation
Advances in Mechanical Engineering
Volume 2013, Article ID 261241, 14 pages
http://dx.doi.org/10.1155/2013/261241

Research Article

Modeling, Simulation, and Experiment of Switched Reluctance Ocean Current Generator System

Hao Chen, Xiaoxiao Zhang, and Yang Xu

School of Information and Electrical Engineering, China University of Mining and Technology, Xuzhou 221116, China

Correspondence should be addressed to Hao Chen; hchen@cumt.edu.cn

Received 13 June 2013; Revised 23 August 2013; Accepted 10 September 2013

Academic Editor: Luigi Cappelli

Copyright © 2013 Hao Chen et al. This is an open access article distributed under the Creative Commons Attribution License, which permits unrestricted use, distribution, and reproduction in any medium, provided the original work is properly cited.

This paper presents nonlinear simulation model of switched reluctance (SR) ocean current generator system on MATLAB/SIMULINK with describing the structure of generator system. The developed model is made up of main model, rotor position calculation module, controller module, gate module, power converter module, phase windings module, flux-linkage module, torque module, and power calculation module. The magnetization curves obtained by two-dimensional finite-element electromagnetic field calculation and the conjugated magnetic energy graphics obtained from the three-dimensional graphics of flux linkage are stored in the "Lookup Table" modules on MATLAB/SIMULINK. The hardware of the developed three-phase 12/8 structure SR ocean current generator system prototype with the experimental platform is presented. The simulation of the prototype is performed by the developed models, and the experiments have been carried out under the same condition with different output power, turn-off angle, and rotor speed. The simulated phase current waveforms agree well with the tested phase current waveforms experimentally. The simulated output voltage curves agree well with the tested output voltage curves experimentally. It is shown that the developed nonlinear simulation model of the three-phase 12/8 structure SR ocean current generator system is valid.

1. Introduction

DC generator, synchronous generator, and induction generator are used as ocean current generators now. DC generator has the armature with windings and drainage brushes. Its structure is complex, it has maintenance workload, and the life time is short because there exist the mechanical sliding mechanisms, such as the brushes and commutator. It is difficult for the rotor to manufacture the waterproof structure. There are two categories of synchronous generators, such as the electric excited synchronous generator and the permanent magnet synchronous generator. It is difficult for the electric excited synchronous generator to manufacture the waterproof structure because of the electric excited winding on the rotor. The structure and the power supply of the permanent magnet synchronous generator are more simple than those of the electric excited synchronous generator, but the permanent magnet materials are expensive due to the high overall cost of the permanent magnet synchronous generator system. The excitation of AC induction generator is complex, and it is difficult to regulate the excitation effectively. The permanent magnet materials are also used in brushless DC generator, so its cost is also high. The switched reluctance (SR) motor drive had been applied with high reliability for many years [1–9]. It can also be used as generator system [10–12].

The switched reluctance (SR) generator system consists of an SR generator body, power converter, and controller [1–6]. The generator rotor is only laminated by electrical steel, and there are brushless, no winding, no permanent magnets on the rotor and concentrated windings on the stator. It is easy to manufacture the waterproof structure. It has advantages like its firm and durable structure, low manufacture cost, and easy maintenance. It is suitable for harsh outdoor environment operation, and other types of generators cannot match its long-life operation. The independence of each phase can be done on the magnetic paths and the circuit, and the system can ensure the continued safe operation by removing the fault phase when a phase fails. It has high operational reliability and fault tolerance. The SR generator system developed for ocean current generator system has a good prospect.

This paper presents for the first time the nonlinear simulation model of the developed switched reluctance ocean current generator system by MATLAB platform, which is

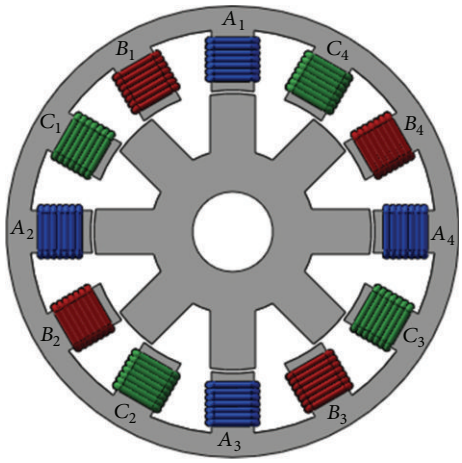

Figure 1: Sketch map of the three-phase 12/8 structure switched reluctance generator.

integrated with the magnetization curves of switched reluctance generator calculated by the two-dimensional finite-element electromagnetic field calculation, the nonlinear electrical network model of the power converter, and the excitation/commutation control algorithms. The simulation results in phase current waveforms and the output voltage curves are compared with the measured waveforms and curves for the developed prototype. The developed prototype consists of the three-phase 12/8 structure doubly salient poles reluctance generator, the three-phase asymmetric bridge power converter, and the controller, which could be applied to ocean current energy systems.

2. Structure of Generator System

The developed SR ocean current generator adopts three-phase 12/8 structure doubly salient poles reluctance generator. The sketch map of the three-phase 12/8 structure SR generator is shown in Figure 1. There are 12 poles on the stator and 8 poles on the rotor. The concentrated windings are wound on each stator pole, and four diametrically opposite windings can be connected to make up a phase winding, such as A_1, A_2, A_3, and A_4 for A phase, B_1, B_2, B_3, and B_4 for B phase, and C_1, C_2, C_3, and C_4 for C phase.

The SR generator works in separately excited mode, and the main circuit of the power converter adopts three-phase asymmetrical bridge structure as shown in Figure 2. MOSFETs are used as main switches, S_1, S_2, S_3, S_4, S_5, and S_6, and fast recovery diodes are adopted as freewheeling diodes, D_1, D_2, D_3, D_4, D_5, and D_6. The voltage rating of main switches and freewheeling diodes are 80 V; the current rating of main switches and freewheeling diodes are 80 A. Though the circuit seems to be complicated, it is convenient to control the generator system since the excited loop and the power generation loop are independent of each other, the excitation is supplied by the external DC power supply during the whole operation period, and the excited voltage, and the output voltage can be adjusted independently. As shown in Figure 2, i_e is excited current, i_g is generated current, i_a is A phase current, i_b is B phase current, i_c is C phase current, R is load, Us is the excited voltage and U is the output voltage. The triggering signals of the down main switches, S_2, S_4, and S_6, are modulated by the PWM signal. The phase winding average excited voltage could be adjusted by regulating the duty ratio of the PWM signal. So the output voltage and the output power are adjustable by regulating the duty ratio of the PWM signal. The excited voltage Us is DC 24 V, and the frequency of the PWM signal is set to 5 kHz.

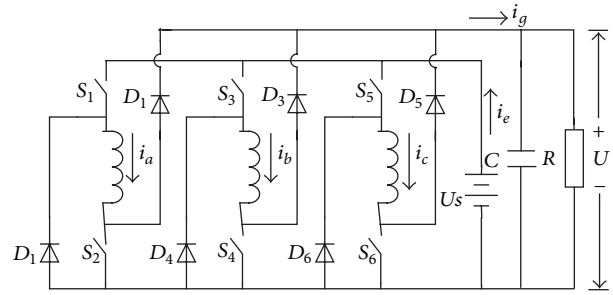

Figure 2: Power converter main circuit.

The operating status of SR generator can be divided into the excitation stage and the power generation stage when the main switches are closed and opened, respectively, which are shown in Figure 3, according to the circuit-theoretic equations as follows.

In the excitation stage when $\theta_{on} \le \theta \le \theta_{off}$,

$$u_k = i_k r_k - e = i_k r_k + \frac{d\psi_k}{dt}, \tag{1}$$

where θ is real-time rotor angle, θ_{on} is turn-on angle, θ_{off} is turn-off angle, u_k is phase voltage, i_k is phase current, r_k is phase resistance, and Ψ_k is flux linkage of phase k.

In the power generation stage when $\theta_{off} \le \theta \le 2\theta_{off} - \theta_{on}$,

$$u_k = -i_k r_k + e = -i_k r_k - \frac{d\psi_k}{dt}. \tag{2}$$

By Merging (1) and (2),

$$\pm u_k = i_k r_k + \frac{d\psi_k}{dt}. \tag{3}$$

3. Simulation Models

In the paper, two-dimensional finite-element electromagnetic field calculation method is used to obtain the magnetization curves of SR generator and the magnetization curves are stored in the "Lookup Table" module on MATLAB/SIMULINK. While the rotor angle and the phase current are input to the "Lookup Table" module, the flux linkage at any instantaneous rotor angle and current can be obtained. Figure 4 shows the three-dimensional graphics of the obtained flux linkage at different rotor angles and phase current and its specific variations are shown in Figures 5 and 6. Figure 5 shows that the flux linkage varies with different phase currents at different rotor angles, and it can be

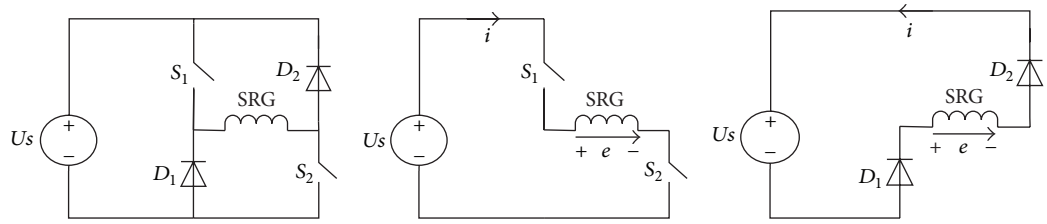

(a) Topology of one-phase circuit (b) Excitation stage (c) Power generation stage

FIGURE 3: Sketch map of one-phase circuit.

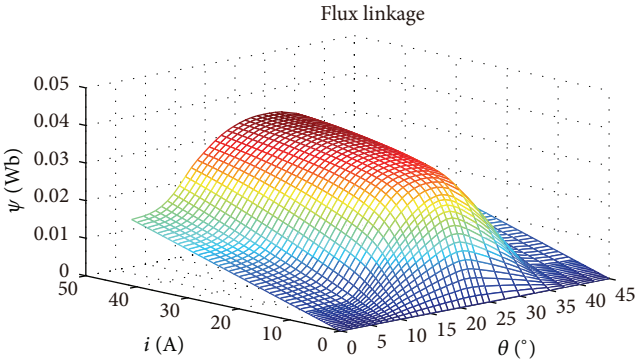

FIGURE 4: Three-dimensional graphics of flux linkage.

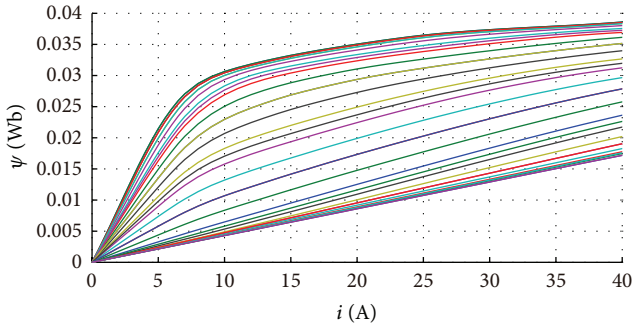

FIGURE 5: Flux linkage varies with phase current at different rotor angles.

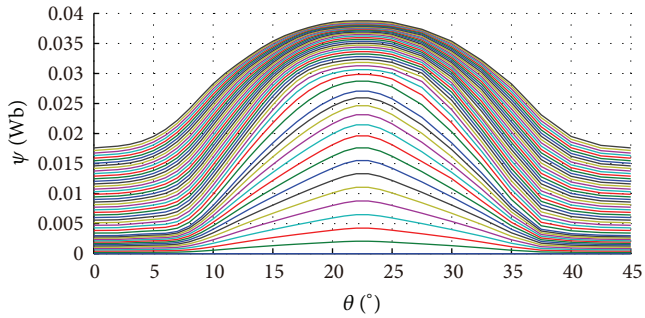

FIGURE 6: Flux linkage varies with rotor angle at different phase currents.

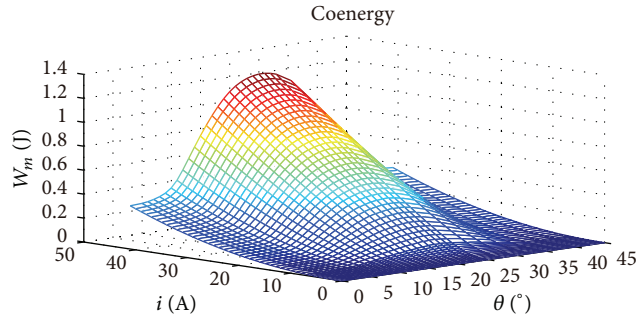

FIGURE 7: Three-dimensional graphics of conjugated magnetic energy.

seen that the flux linkage varies linearly with different phase currents when the rotor angles are close to the minimum phase inductance position 0°; the flux linkage saturation increases with the increase of the rotor angle, and the larger the phase current is, the larger the flux linkage is at a constant rotor angle. Figure 6 shows that the flux linkage varies with different rotor angle at different phase currents. It is shown that the flux linkage increases with the increase of the rotor angle at a constant phase current in the first half period. The three-dimensional graphics of the conjugated magnetic energy vary with different rotor angles and phase current can be obtained from the three-dimensional graphics of flux linkage which is shown in Figure 7.

3.1. Main Model. Figure 8 shows the main simulation model of SR generator system, including the rotor position calculation module, the controller module, the power converter module, the phase winding module, the power calculation module, the excited current, and the generated current calculation module. The rotor position calculation module "Rotor_position" simulates the rotor angle relative to the stator, "w" is the generator angular velocity, the controller module "Controller" simulates the controller, the power converter module "Converter" simulates the power converter, and the phase winding modules "A phase", "B phase", and "C phase" simulate SR generator body. The power calculation module "Sum", the excited current calculation module "Sum1", and the generated current calculation module "Sum2" in the bottom

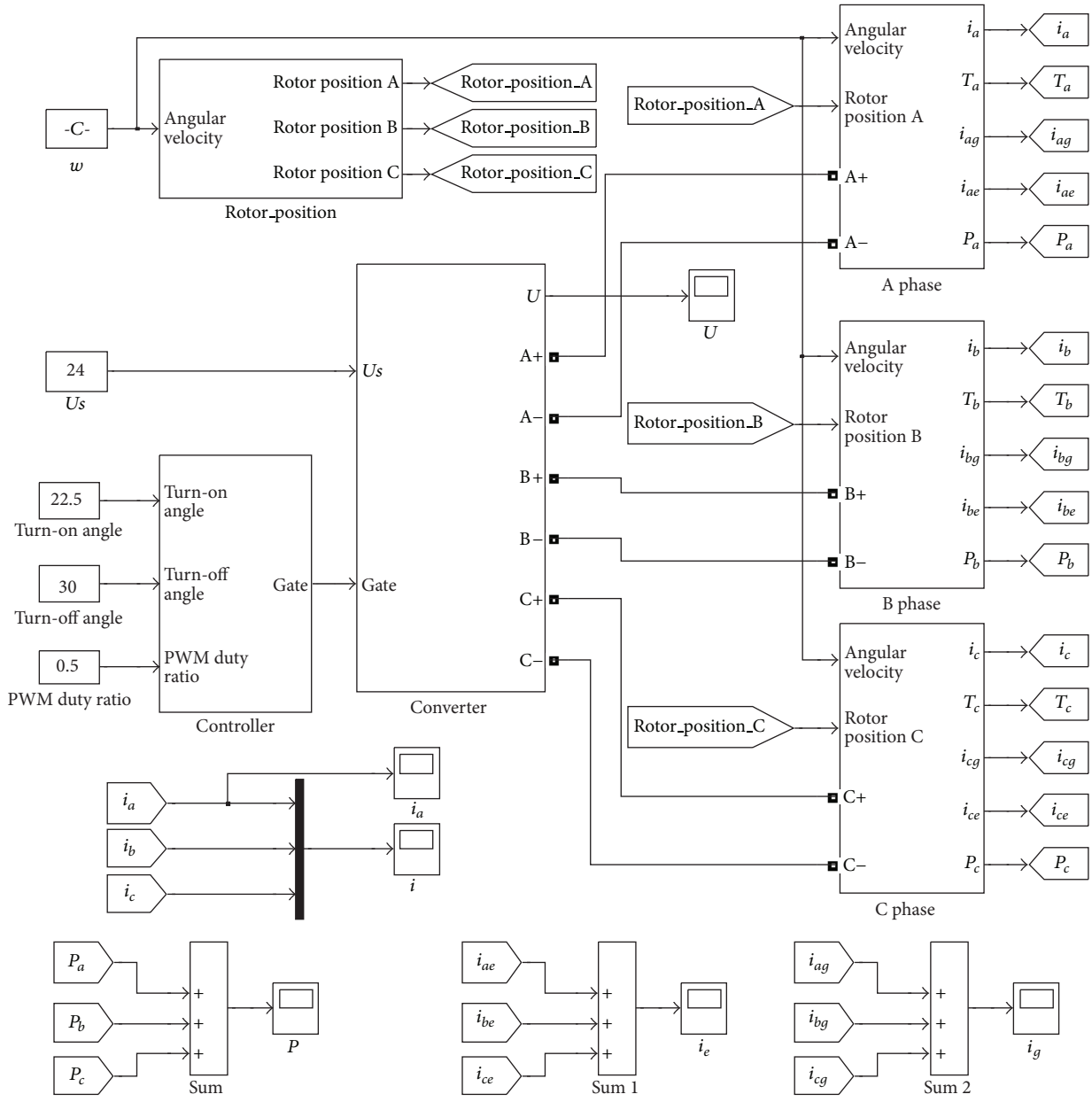

Figure 8: Main model.

of Figure 8 calculate the output power, the excited current, and the generated current of the system, respectively. The system output power P is obtained by adding A phase output power P_a, B phase output power P_b, and C phase output power P_c as follows:

$$P = P_a + P_b + P_c. \tag{4}$$

The sum of A phase excited current i_{ae}, B phase excited current i_{be}, and C phase excited current i_{ce} is the total excited current i_e in the excited loop as follows:

$$i_e = i_{ae} + i_{be} + i_{ce}. \tag{5}$$

The sum of A phase generated current i_{ag}, B phase generated current i_{bg}, and C phase generated current i_{cg} is the total generated current i_g in the power generation loop as follows:

$$i_g = i_{ag} + i_{bg} + i_{cg}. \tag{6}$$

The module between "Controller" and "Sum" is used to calculate and display A phase current "i_a" and three-phase current "i".

3.2. Rotor Position Calculation Module. As shown in Figure 9, the rotor position calculation module is used to calculate the rotor salient pole angle relative to each phase stator. While the rotor "Angular velocity" is input to the module, the relative angle of each phase "Rotor position A," "Rotor position B," and "Rotor position C" can be output. The total turning angle

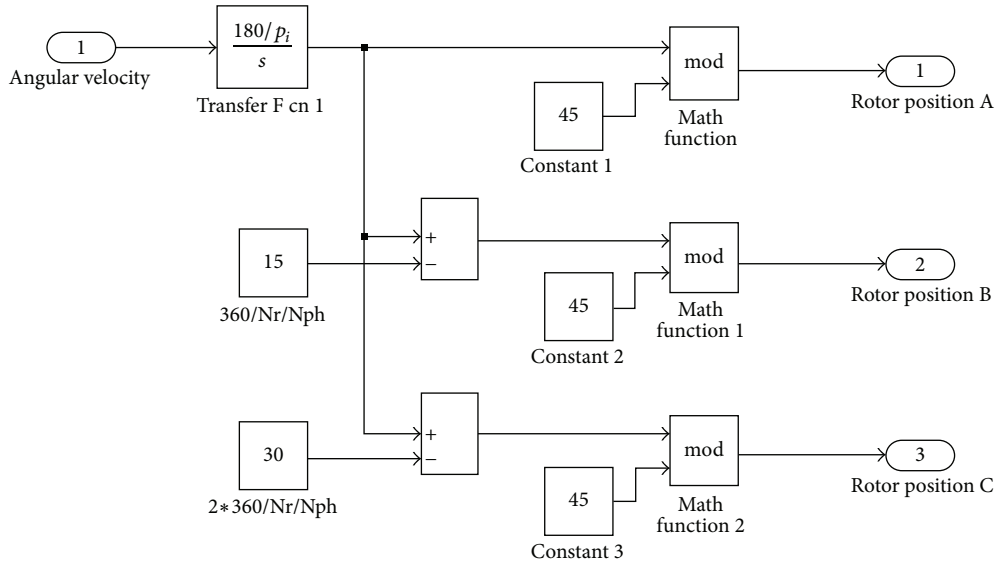

Figure 9: Internal structure of rotor position calculation module.

of the rotor can be converted by the turning radius which is calculated through integrating the angular velocity "Transfer Fcn1", subtracting the relative phase angle difference, and calculating the remainder through "mod" which limits the rotor angle between 0° and the cycle turning angle of the rotor θ_r, so that the rotor relative angle of each phase can be obtained. In the paper, the θ_r of three-phase 12/8 motor is 45° that "Constant 1," "Constant 2," and "Constant 3" are "45". Since A, B, and C phase must be electrified, respectively, in one period, the phase angle difference θ_p between two adjacent phases can be calculated by

$$\theta_p = \frac{\theta_r}{m}, \tag{7}$$

where m is the number of phase, which is three in the paper. So the phase angle differences between A phase and B phase, A phase and C phase are 15° and 30°, which are set to "15" and "30", respectively.

3.3. Controller Module. The controller module with the three-phase main switches logic is shown in Figure 10. The controller module consists of the PWM signal module and the gate drive signal module of the power converter main switches which has three submodules "Gate A," "Gate B," and "Gate C". The PWM signal "Duty" can be obtained by inputting "PWM duty ratio" in the PWM signal module. "Repeating sequence" module is used to generate periodic ramp signal, and the signal cycle should be the same as the PWM signal cycle whose frequency is set to 5 kHz. While the output of "Repeating sequence" is smaller than the "PWM duty ratio," the "Switch" output is "1." While the output of "Repeating sequence" is larger than the "PWM duty ratio," the "Switch" output is "0." Those can meet the requirements of the PWM signal "Duty". PWM signal can control one or two main switches of each phase, which is the so-called single switch chopping mode or double switches chopping mode, and the single switch chopping mode is adopted in the paper. In the gate drive signal module, "Rotor_position_A," "Rotor_position_B," and "Rotor_position_C" are the rotor angles relative to the stator of each phase that are connected to the outputs of "Rotor_position" in main model. "Turn-on angle" and "Turn-off angle" denote the turn-on angle and the turn-off angle of the power converter main switches. "Duty" is the PWM signal obtained from the PWM signal module. "i_a," "i_b," and "i_c" are the phase currents, and "i_{rf}" is the current protection limit. The gate drive signals of three-phase main switches "Gate" can be gained through logical judgment and operation, which consist of "Gate A+," "Gate A−," "Gate B+," "Gate B−," "Gate C+," and "Gate C−".

3.4. Gate A Module. The submodule describes the internal logical operation of the gate drive signals module of each phase. Take "Gate A" as an example, it contains three components: the position logical judgment part, the current hysteresis part, and the combinational logical judgment part as shown in Figure 11. In the position logical judgment part, while the input value of "Rotor position A" is between the set values of "turn-on angle" and "turn-off angle," which means that the rotor angle of phase A is in the opening angle range, the "Interval test dynamic" outputs 1, otherwise the "Interval test dynamic" outputs 0. In the current hysteresis part, the compared results of the phase current "i_a" and the current protection limit "i_{rf}" is input to the hysteresis "Relay", the width of hysteresis can be regulated through "Relay". While A phase current "i_a" exceeds current protection limit "i_{rf}" and "i_a"-"i_{rf}" is greater than the width of the hysteresis, the output "Relay" is 0. While "i_a" is less than "i_{rf}" and "i_{rf}"-"i_a" is greater than the width of the hysteresis, the output "Relay" is 1. Finally, the gate drive signals of the main switches in each phase can be obtained through the combinational logical judgment parts "Logical operator" and "Logical operator1" with combining the position logical operation output, the

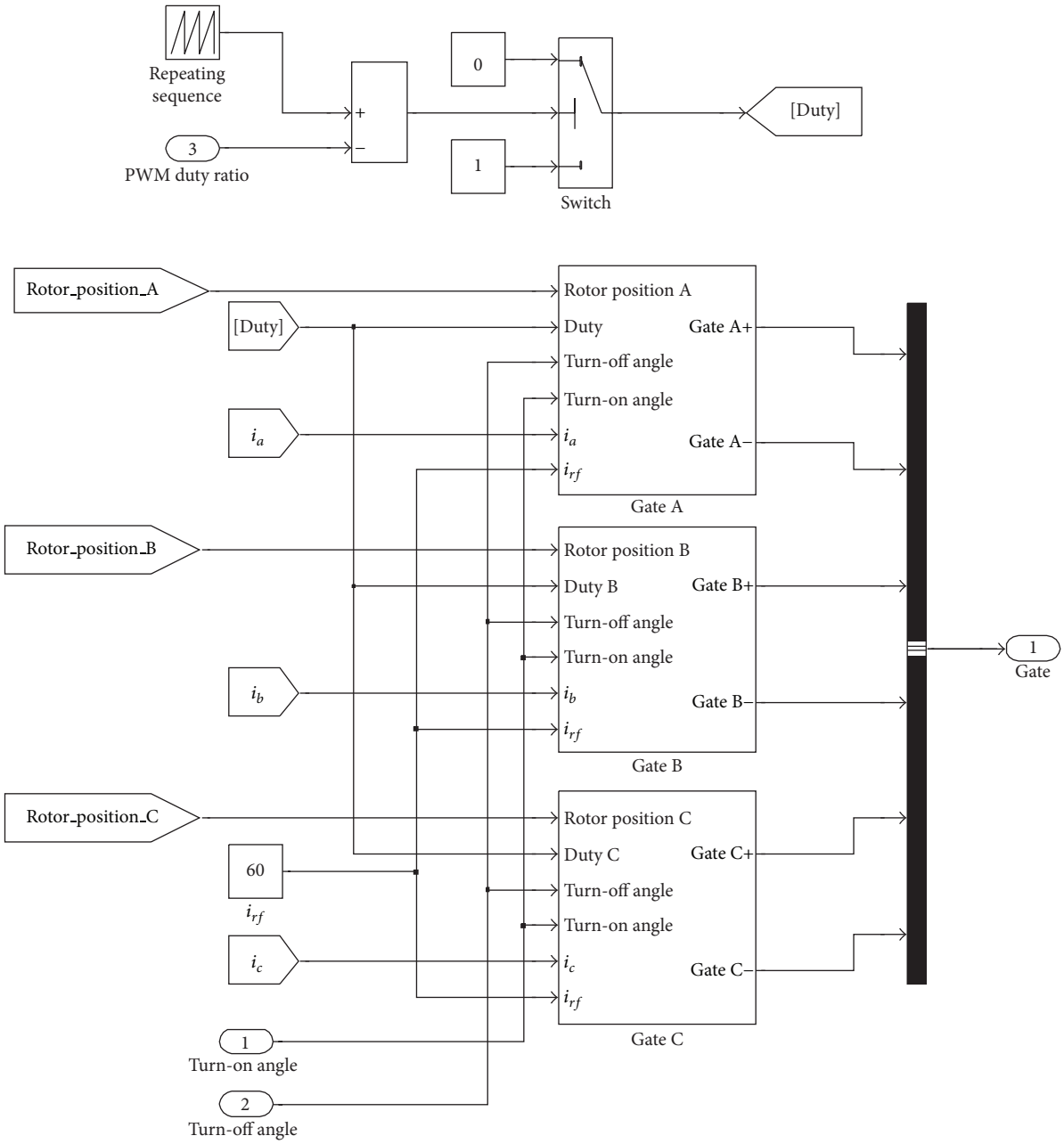

Figure 10: The internal structure of controller.

PWM signal "Duty," and the current hysteresis result as the down gate drive signal "Gate A−," and the upper gate drive signal "Gate A+" is the output of position logical judgment part.

3.5. Power Converter Module. The internal structure of power converter is shown in Figure 12, which is set up according to the power converter topology structure shown in Figure 2. The inputs are DC excited power voltage "*Us*", the three-phase gate drive signals "Gate" which are connected to the output of the controller "Gate." The outputs are the output voltage "*U*" and three-phase voltages "A+" and "A−," "B+," and "B−", "C+" and "C−" which are connected to "Phase A," "Phase B," and "Phase C" main model, respectively. "M_1–M_6" denote the main switches, "D_1–D_6" denote the fast recovery diodes, and "T_1–T_6" are used to present fault information in the simulation process connected to the output ports of "M_1–M_6." In the system, the excited voltage "*Us*" is set to 24 V, the "*RC*" of the excitation circuit are set to 0.0001 Ω and 2200 μF to stabilize the voltage, the capacitor "*C*" is set to 2200 μF and the resistance "*r*" is set to 0.0001 Ω. The current flows through the freewheeling diodes "D_1," "D_3," and "D_5" to the charge capacitor "*C*" and supplies power to the load "*R*" when the main switches are opened, where the capacitor "*C*" plays the dual role of storage and voltage-stabilizing in the circuit.

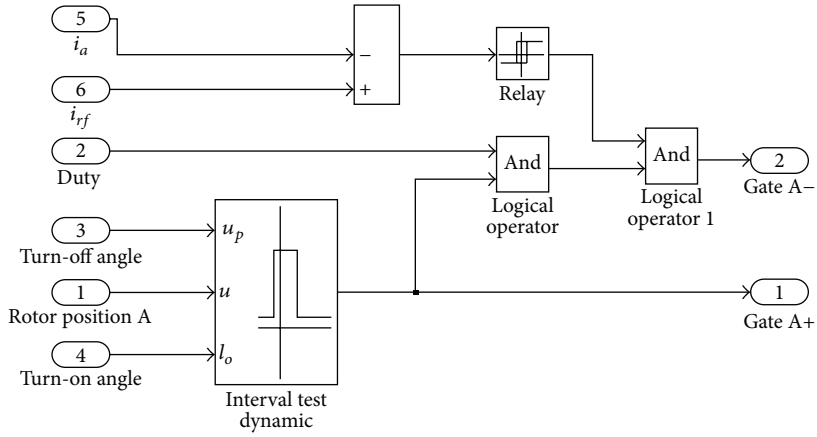

Figure 11: Internal structure of submodule "gate A."

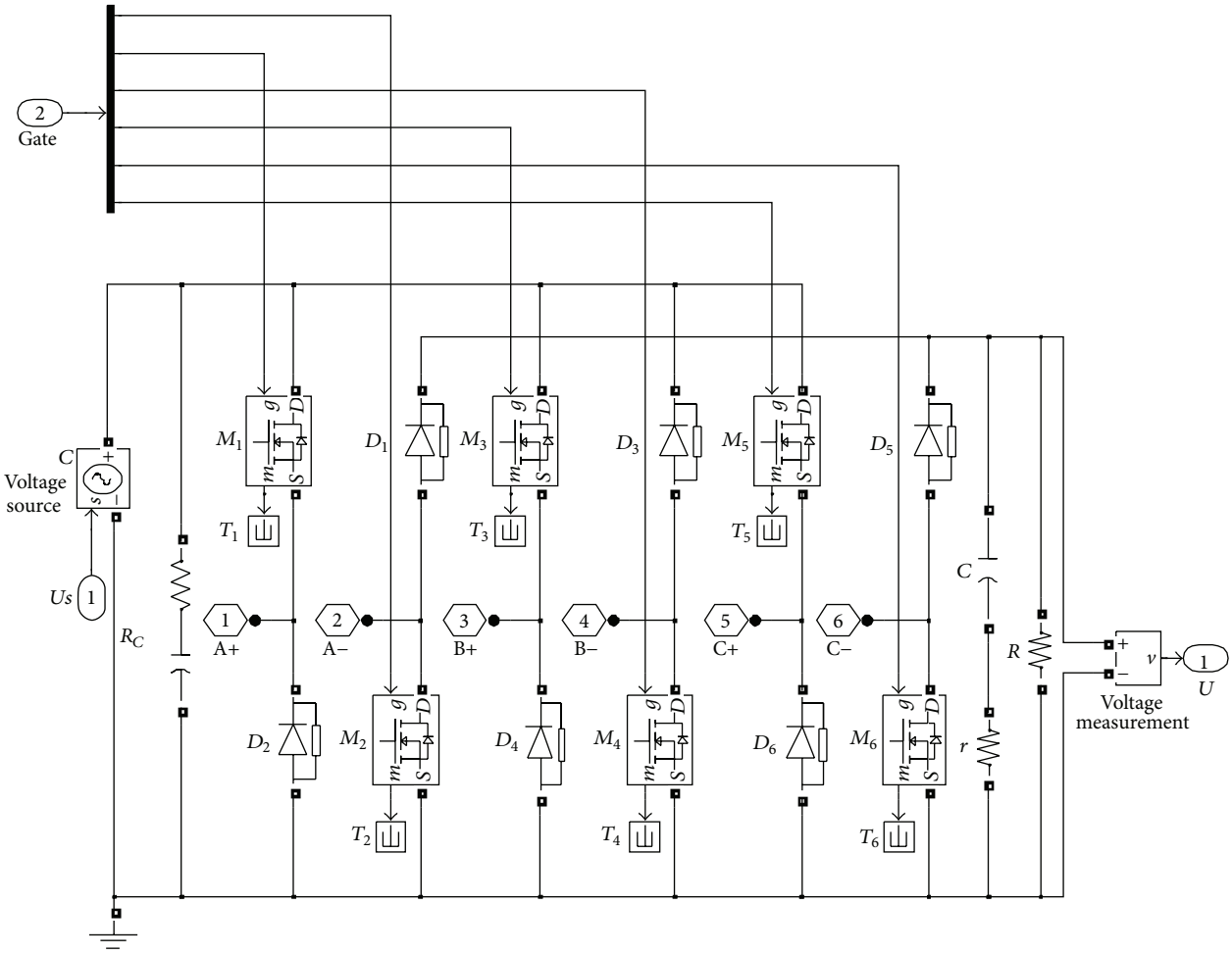

Figure 12: Internal structure of power converter main circuit.

3.6. Phase Windings Module. By taking A phase as an example, the internal structure of "A phase" module in main model consists of the current calculation module, the torque calculation module, and the power calculation module as shown in Figure 13. Submodule "B phase" and submodule "C phase" are similar to submodule "A phase".

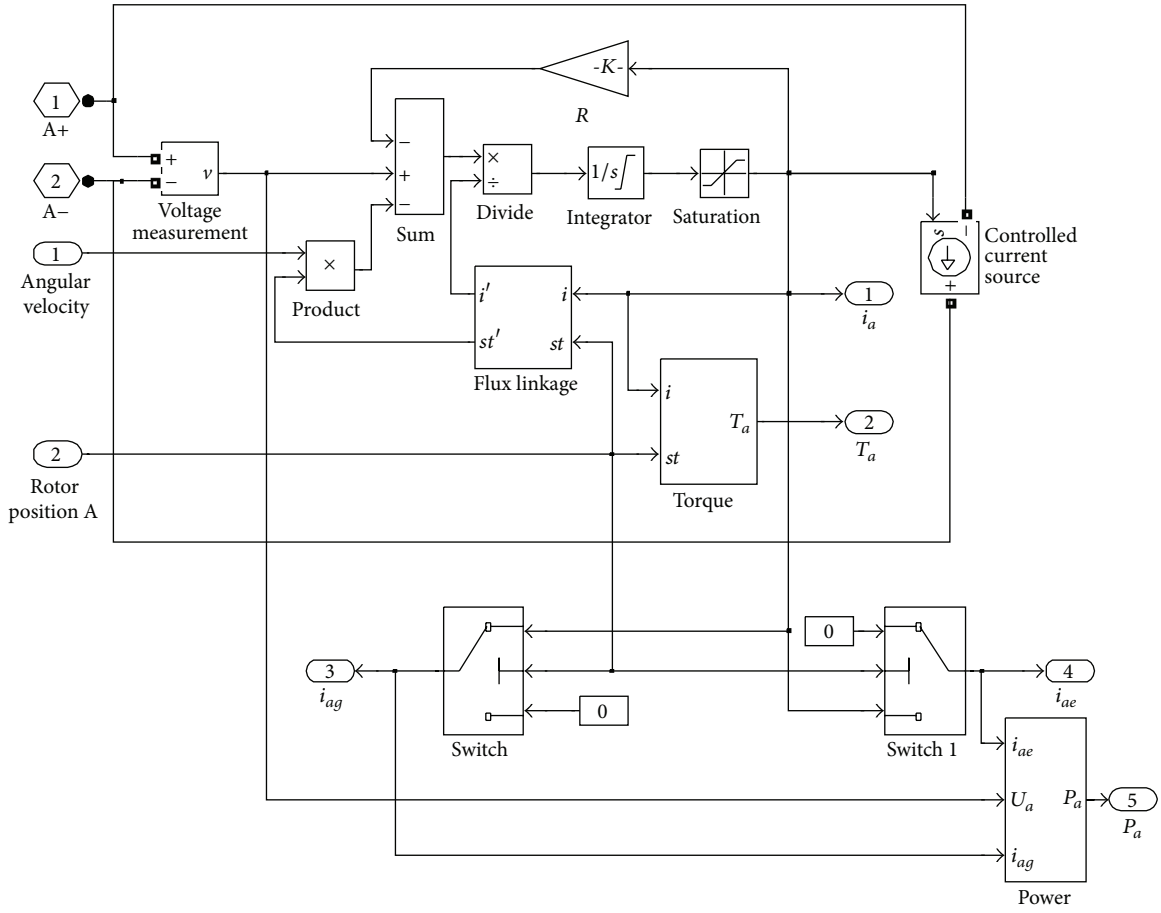

Figure 13: Internal structure of phase A module.

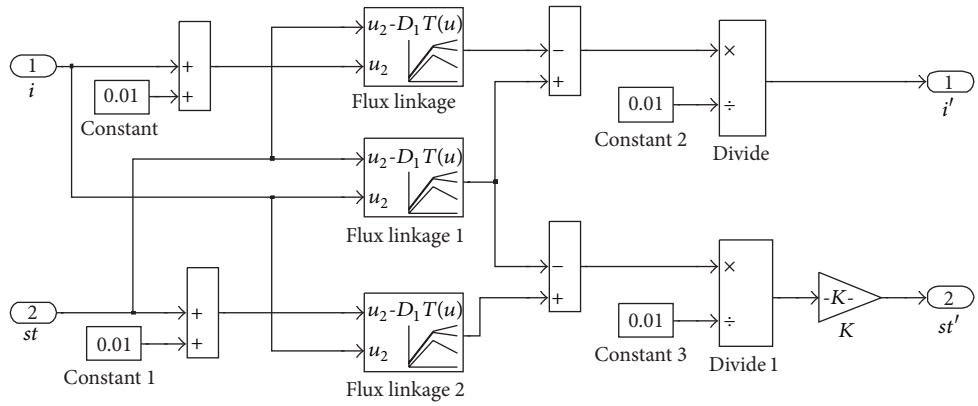

Figure 14: Internal structure of "flux linkage" submodule.

Ignoring mutual inductance between phase windings, the voltage balance equation of k-phase is as follows:

$$u_k = r_k i_k + \frac{d\psi_k}{dt}, \quad k = a. \tag{8}$$

The flux linkage Ψ_k is the function of the phase current i_k and the rotor position angle θ of k-phase as follows:

$$\psi_k = \psi_k(i_k, \theta), \quad k = a. \tag{9}$$

Thus,

$$u_k = r_k i_k + \frac{\partial \psi_k}{\partial i_k}\frac{di_k}{dt} + \frac{\partial \psi_k}{\partial \theta}\frac{d\theta}{dt}, \quad k = a. \tag{10}$$

Transforming the above equation is as follows:

$$\frac{di_k}{dt} = \frac{u_k - r_k i_k - (\partial \psi_k/\partial \theta)\,\omega}{\partial \psi_k/\partial i_k}, \quad k = a, \tag{11}$$

where ω is the generator angular velocity.

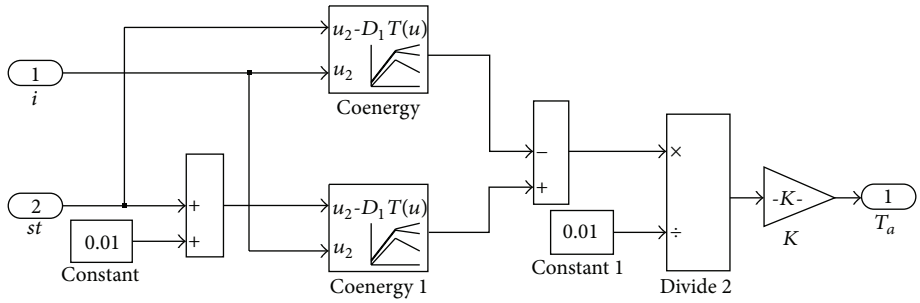

Figure 15: Internal structure of torque calculation module.

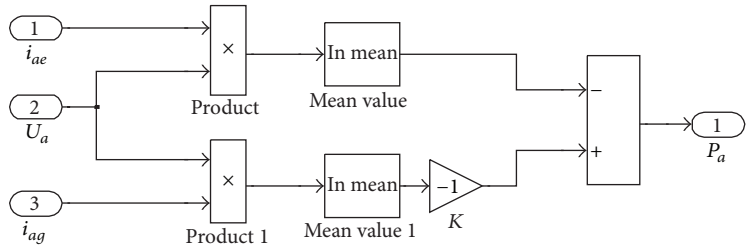

Figure 16: Internal structure of power calculation module.

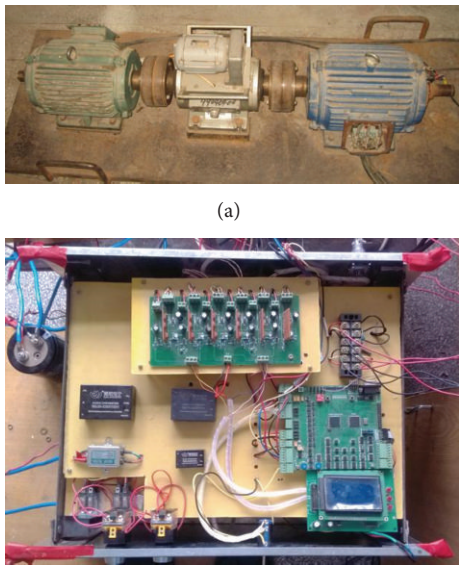

(a)

(b)

Figure 17: Photograph of prototype.

The current calculation module of "A phase" is built according to (11) as shown in Figure 13. The inputs are the A phase voltage signals "A+" and "A−" which are connected to the outputs of the power converter, the rotor angular velocity "Angular velocity," and the rotor angle relative to A phase "Rotor position A." The outputs are the phase current "i_a", the instantaneous torque of A phase "T_a", the excited current "i_{ae}", the generated current "i_{ag}," and the A phase output power "P_a." Combine A phase voltage signals "A+" and "A−" to A phase voltage U_a through "Voltage measurement" module, multiply the feedback phase current "i_a" and the phase winding resistance "R" to obtain the winding resistance voltage drop, calculate results of "di_a/dt" through "Sum" and "Divide" module, and then get A phase current through "Integrator" as the input of "Controlled current source," which is used to connect the electrical ports and the signal ports to transport the A phase current "i_a." The "Switch 1" module and "Switch" are used to separate the phase current to the excited current "i_{ae}" and the generated current "i_{ag}" by setting the value of turn-off angle as boundary, which means the threshold of "Switch 1" and "Switch" is set to the same value with "turn-off angle." While the "Rotor position A" is smaller than the threshold, the generator enters into the excitation stage, $i_{ae} = i_a$, $i_{ag} = 0$. Otherwise while the "Rotor position A" is larger than the threshold, the generator enters into the power generation stage, $i_{ae} = 0$, $i_{ag} = i_a$. The last submodules "Flux linkage," "Torque," and "Power" included in phase winding modules are used to calculate the partial derivatives of the flux linkage to phase current $\partial\psi_k/\partial i_k$ and to rotor angle $\partial\psi_k/\partial\theta$, the instantaneous torque of A phase T_a, and the A phase output power P_a. The following will introduce them, respectively.

3.7. Flux Linkage Module. The partial derivatives are calculated by:

$$\frac{\partial\psi_k}{\partial i_k} = \frac{\psi(i+\Delta i,\theta) - \psi(i,\theta)}{\Delta i},$$
$$\frac{\partial\psi_k}{\partial\theta} = \frac{\psi(i,\theta+\Delta\theta) - \psi(i,\theta)}{\Delta\theta}, \quad (12)$$
$$k = a,$$

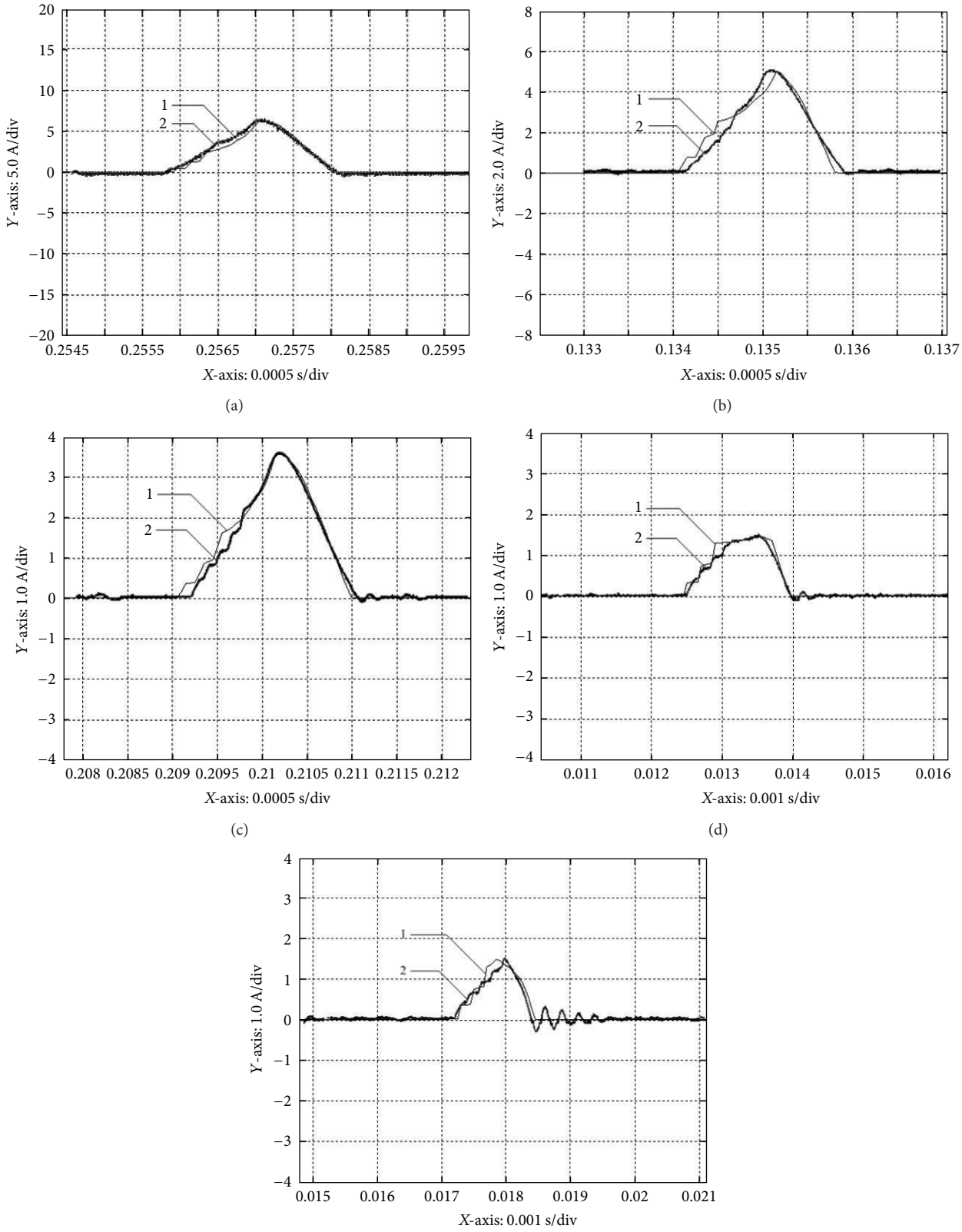

Figure 18: Phase current waveforms I.

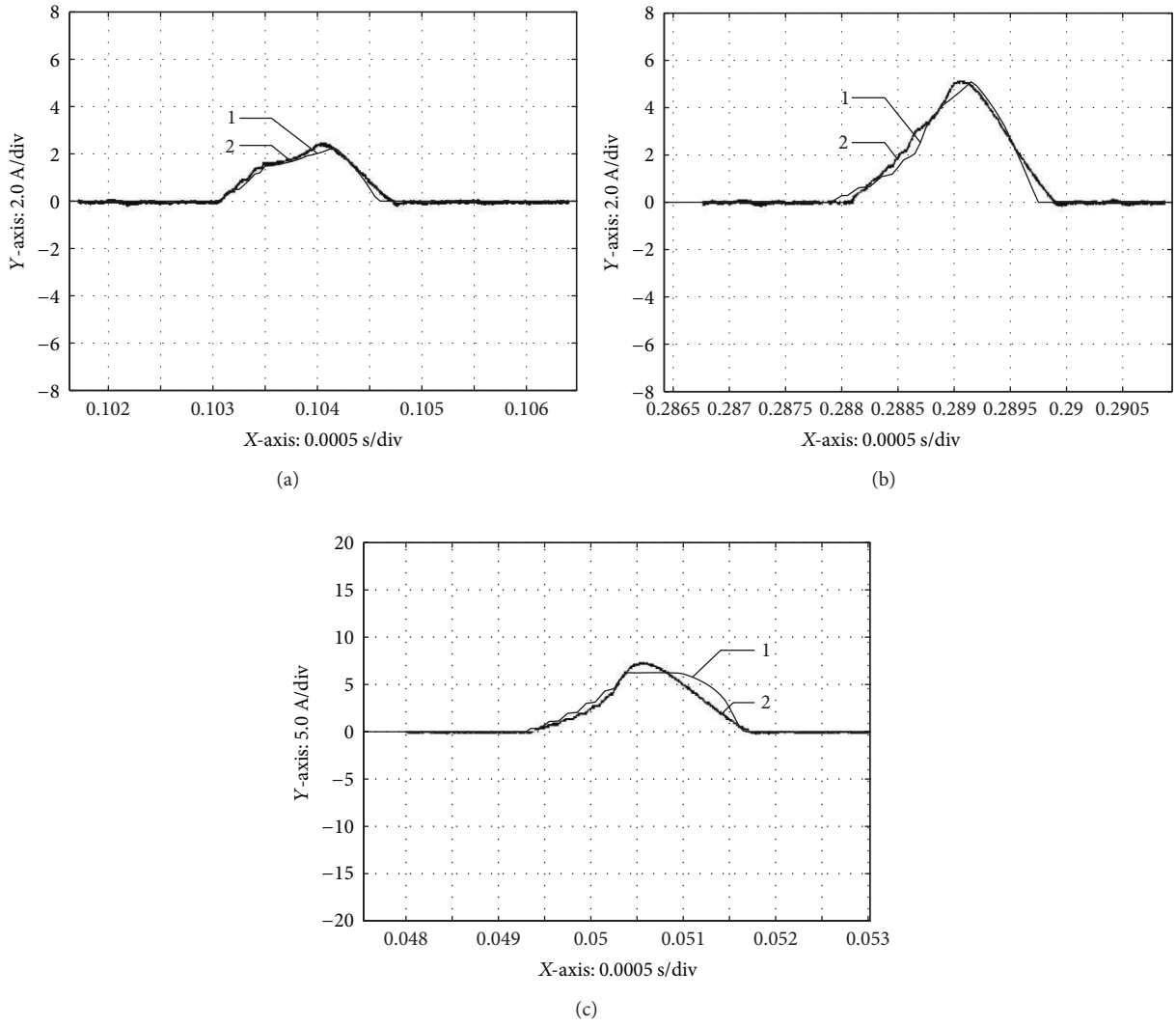

Figure 19: Phase current waveforms II.

where i and θ are the instantaneous values of phase current and rotor angle; Δi and $\Delta\theta$ are the increments of phase current and rotor angle.

As shown in Figure 14, the submodule "Flux linkage" in Figure 13 is built according to (12). The inputs are the instantaneous values of phase current "i" and rotor relative angle "st", and $\partial\psi_k/\partial i_k$ and $\partial\psi_k/\partial\theta$ can be calculated which are denoted by "i'" and "st'". The data of magnetization curves shown in Figure 4 are stored in "flux linkage," "flux linkage 1," and "flux linkage 2," and the two-dimension sample insert method is adopted for calculating the flux linkage at the certain phase current and the certain rotor angle based on the magnetization curve data. "Constant" and "Constant2" which denote the current increment "Δi" are both set to 0.01, "Constant1" and "Constant3" which denote the rotor angle increment "$\Delta\theta$" are both set to 0.01. In addition, the proportion coefficient "K" is used to unify the units of the rotor relative angle and the value in the lookup table of the flux linkage and conjugated magnetic energy, which is set to "$\pi/180$."

3.8. Torque Module. The instantaneous torque of one phase is given by

$$T_k = \left.\frac{\partial W'}{\partial\theta}\right|_{i_k=\text{const}}, \quad k = a,$$
$$\frac{\partial W'}{\partial\theta} = \frac{W'(i,\theta+\Delta\theta) - W'(i,\theta)}{\Delta\theta}, \quad k = a, \tag{13}$$

where "W'" is conjugated magnetic energy of SR generator.

The conjugated magnetic energy at different phase currents and rotor angles can be calculated by the following equation with its three-dimension graphics shown in Figure 7:

$$W' = \int_0^{i_k} \psi_k di, \quad k = a. \tag{14}$$

The "Torque" submodule can be built as shown in Figure 15 according to the previous equations. The conjugated magnetic energy data are stored in "Coenergy" and

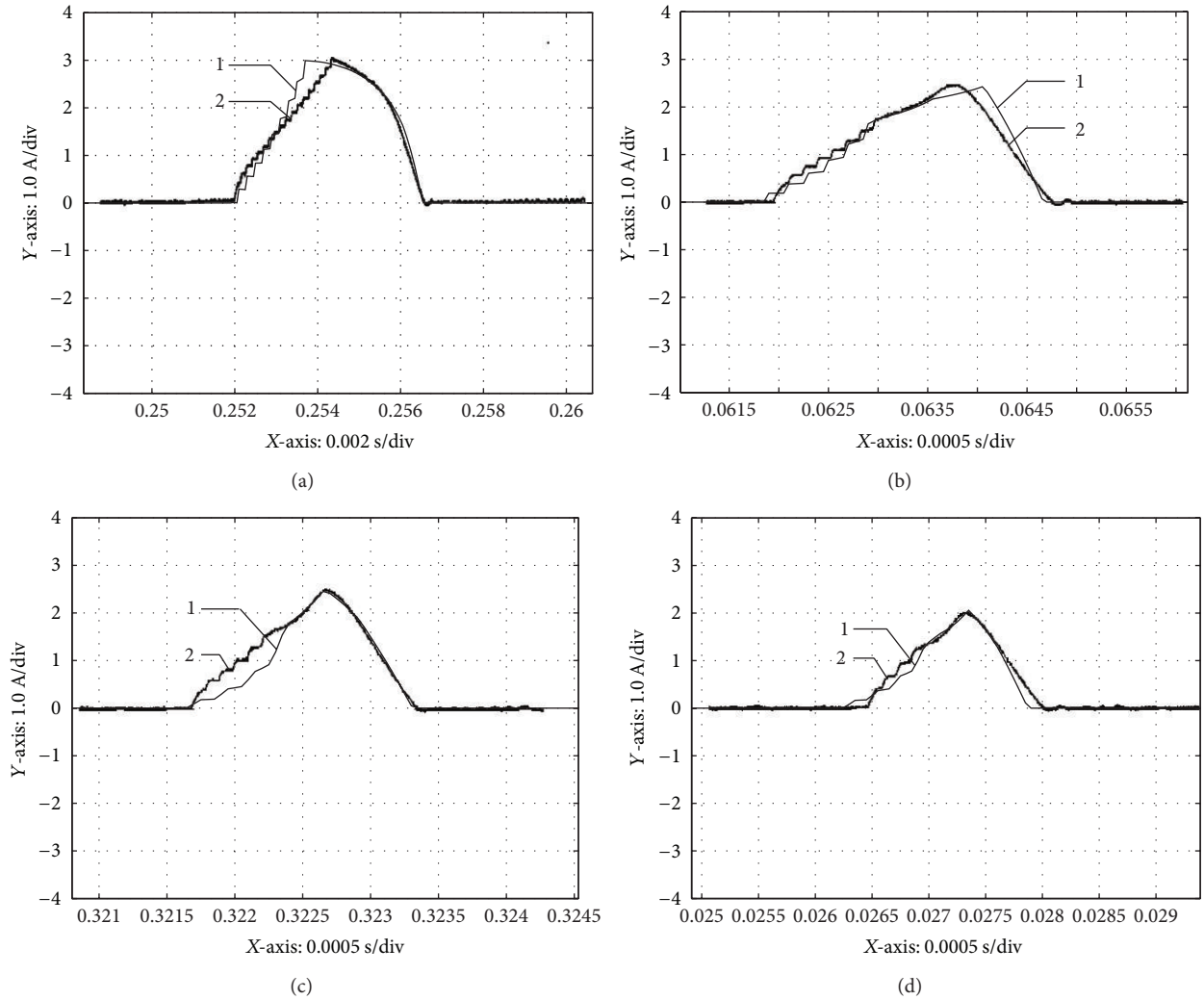

Figure 20: Phase current waveforms III.

"Coenergy1." Inputs are the instantaneous values of the phase current "i" and the rotor relative angle "st," and output is the A phase torque "T_a." "Constant" and "Constant1" which denote the rotor angle increment are both set to 0.01. The proportion coefficient "K" is set to "$\pi/180$", which plays the same role with the "K" in Figure 14.

3.9. Power Calculation Module. The "Power" module is shown in Figure 16. The inputs are the generated current "i_{ag}," the phase voltage "U_a," and the excited current "i_{ae}." The output is the output power of phase A "P_a." The generated power "P_{ag}" and the excited power "P_{ae}" can be obtained by the generated current "i_{ag}" and the excited current "i_{ae}" multiplied by the phase voltage "U_a," respectively, and then through the "Mean Value" and "Mean Value 1" to get the mean value. In addition, the generated power value is negative that can be transformed as positive value by setting "K" as "–1." Then the result of the generated power "P_{ag}" minus the excited power "P_{ae}" to get the value of the output power of A phase is as follows:

$$P_a = P_{ag} - P_{ae}. \tag{15}$$

4. Simulation and Experimental Results

The simulation of the prototype is performed by the developed models on MATLAB. According to the designed hardware and software of the SR generator system prototype, the experiments have been carried out. The photograph of the three-phase 12/8 structure SR ocean current generator system prototype is shown in Figure 17 with SR generator and power converter-controller. The hardware experimental platform consists of the SR generator body, the power converter, the controller, the prime mover, and the torque/rotor speed instrument. The excited voltage is 24 V, the frequency of the PWM signal is set to 5 kHz, and the rotor cycle turning angle is 45°, while the maximum inductance position is at 22.5° and

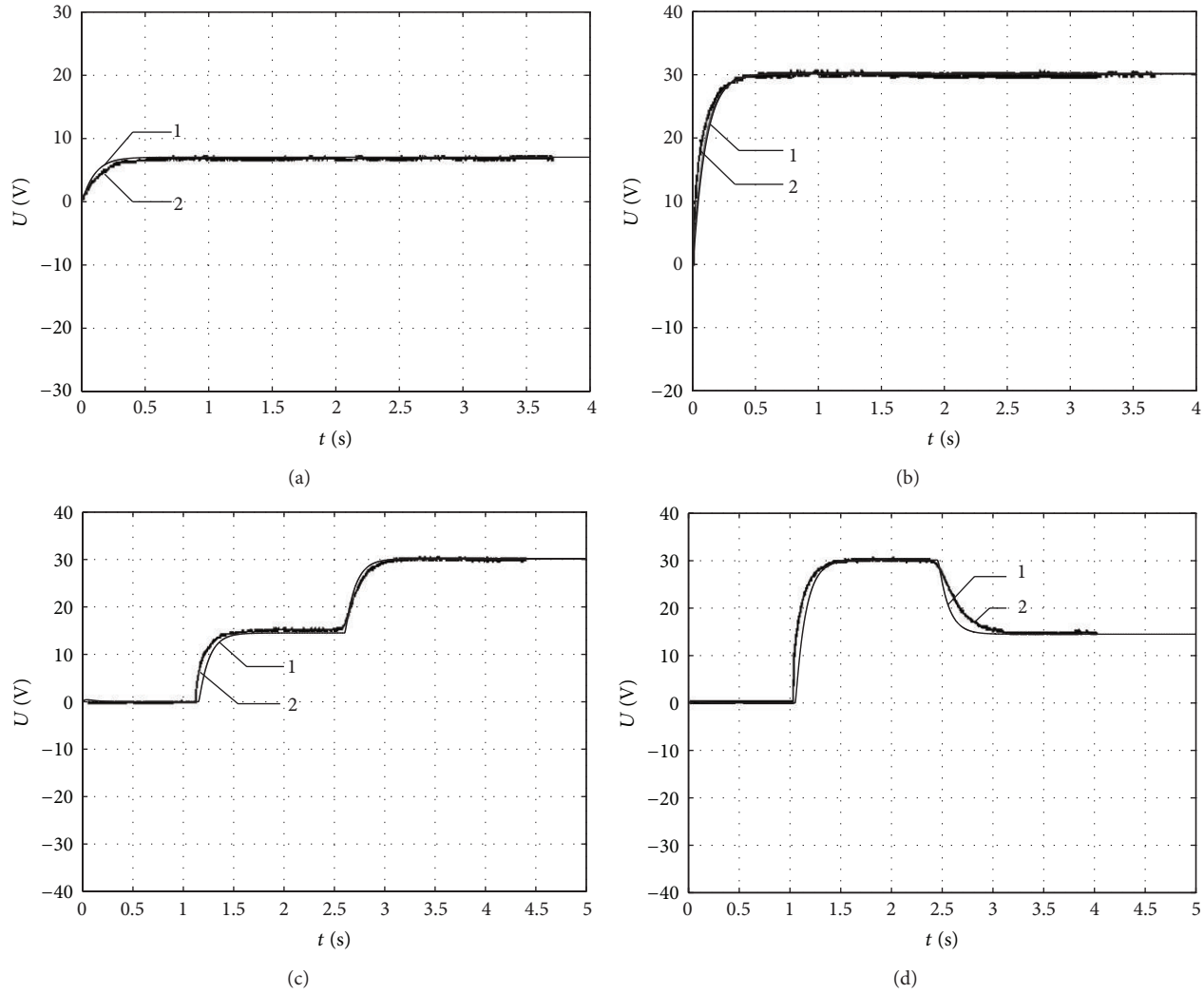

Figure 21: Output voltage curves.

the minimum inductance position is at 0°. The turn-on angle is fixed at the maximum inductance position of 22.5°.

The tested phase current waveforms are shown as "2" lines, and the simulated phase current waveforms are shown as "1" lines. While the rotor speed is 1000 r/min and the turn-off angle is 30°, the phase current waveforms are shown in Figure 18 as follows: (a) the output power is 30.27 W, the efficiency is 81.66%, the abscissa is 0.0005 s/div, and the ordinate is 5.0 A/div, (b) the output power is 18.51 W, the efficiency is 79.34%, the abscissa is 0.0005 s/div, and the ordinate is 2.0 A/div, (c) the output power is 8.55 W, the efficiency is 68.12%, the abscissa is 0.0005 s/div, the ordinate is 1.0 A/div, (d) the output power is 1.63 W, the efficiency is 55.25%, the abscissa is 0.001 s/div, and the ordinate is 1.0 A/div, and (e) the output power is 0.6 W, the efficiency is 29.13%, the abscissa is 0.001 s/div, the ordinate is 1.0 A/div. It is shown that the phase current decreases with the decrease of the load.

While the rotor speed is 1000 r/min, the phase current waveforms are shown in Figure 19 as follows: (a) the turn-off angle is 28°, the output power is 4.98 W, the efficiency is 74.77%, the ordinate is 2.0 A/div, and the abscissa is 0.0005 s/div, (b) the turn-off angle is 30°, the output power is 15.38 W, the efficiency is 73.30%, the ordinate is 2.0 A/div, and the abscissa is 0.0005 s/div, and (c) the turn-off angle is 33.75°, the output power is 22.56 W, the efficiency is 60.43%, the ordinate is 5.0 A/div, and the abscissa is 0.0010 s/div. The maximum of phase current increases significantly with the increase of the turn-off angle and the increase of the output power.

While the turn-off angle is 30°, the ordinate is 1.0 A/div, the phase current waveforms are shown in Figure 20 as follows: (a) the rotor speed is 250 r/min, the output power is 2.47 W, the efficiency is 21.04%, and the abscissa is 0.0020 s/div, (b) the rotor speed is 500 r/min, the output power is 2.63 W, the efficiency is 46.55%, and the abscissa is 0.0010 s/div, (c) the rotor speed is 750 r/min, the output power is 2.47 W, the efficiency is 42.27%, the abscissa is 0.0005 s/div, and (d) the rotor speed is 1000 r/min, the output power is 2.36 W, the efficiency is 63.10%, and the abscissa is

0.0005 s/div. The phase current decreases with the increase of the rotor speed and the decrease of the output power.

While the turn-on angle is 22.5°, the turn-off angle is 30°, the rotor speed is 1000 r/min, the abscissa is 0.5 s/div, and the ordinate is 10.0 V/div, the output voltage curves in establishing voltage process are shown in Figure 21 as follows: (a) the given output voltage is 7.0 V, the output power is 4.50 W, (b) the given output voltage is 30.0 V, the output power is 82.57 W, (c) the given output voltage is from 14.5 V to 30.0 V and the output power is from 19.29 W to 82.57 W, and (d) the given output voltage is from 30.0 V to 14.5 V and the output power is from 82.57 W to 19.29 W.

It is shown that the simulated phase current waveforms are consistent with the experimental results. The simulated output voltage curves agree well with the tested output voltage curves experimentally. The nonlinear simulation model of the developed SR ocean current generator system by MATLAB platform is validated.

5. Conclusions

The SR generator system has a good prospect for ocean current generator system with high operational reliability and fault tolerance. The simulated phase current waveforms agree well with the tested phase current waveforms experimentally. The simulated output voltage curves agree well with the tested output voltage curves experimentally. The proposed nonlinear simulation model of the three-phase 12/8 structure SR generator system on MATLAB/SIMULINK is valid. The method of developed nonlinear simulation models can be adopted to set up the nonlinear simulation models of the other SR generator system with other structure switched reluctance generators, other topologies of the power converter, and other generator control schemes on MATLAB/SIMULINK. The developed nonlinear simulation model contributes to optimized control strategies and parameters of the SR ocean current generator system with saving developed period.

Acknowledgments

This work was supported in part by the National Natural Science Foundation of China under Grant no. 51277174, International S&T Cooperation Program of China under Grant no. 2011DFA61150, and the Specialized Research Fund for the Doctoral Program of Higher Education of China under Grant no. 20120095110019.

References

[1] C. Lee and R. Krishnan, "New designs of a two-phase e-core switched reluctance machine by optimizing the magnetic structure for a specific application: concept, design, and analysis," *IEEE Transactions on Industry Applications*, vol. 45, no. 3, pp. 1804–1814, 2009.

[2] H. Hayashi, K. Nakamura, A. Chiba, T. Fukao, K. Tungpimolrut, and D. G. Dorrell, "Efficiency improvements of switched reluctance motors with high-quality iron steel and enhanced conductor slot fill," *IEEE Transactions on Energy Conversion*, vol. 24, no. 4, pp. 819–825, 2009.

[3] O. Ustun, "Measurement and real-time modeling of inductance and flux linkage in switched reluctance motors," *IEEE Transactions on Magnetics*, vol. 45, no. 12, pp. 5376–5382, 2009.

[4] P. C. Desai, M. Krishnamurthy, N. Schofield, and A. Emadi, "Novel switched reluctance machine configuration with higher number of rotor poles than stator poles: concept to implementation," *IEEE Transactions on Industrial Electronics*, vol. 57, no. 2, pp. 649–659, 2010.

[5] Y. Hasegawa, K. Nakamura, and O. Ichinokura, "Optimization of a switched reluctance motor made of permendur," *IEEE Transactions on Magnetics*, vol. 46, no. 6, pp. 1311–1314, 2010.

[6] J. De Santiago, H. Bernhoff, B. Ekergård et al., "Electrical motor drivelines in commercial all-electric vehicles: a review," *IEEE Transactions on Vehicular Technology*, vol. 61, no. 2, pp. 475–484, 2012.

[7] H. Torkaman, E. Afjei, and M. S. Toulabi, "New double-layer-per-phase isolated switched reluctance motor: concept, numerical analysis, and experimental confirmation," *IEEE Transactions on Industrial Electronics*, vol. 59, no. 2, pp. 830–838, 2012.

[8] C. Li and W. Hofmann, "Speed regulation technique of one bearingless 8/6 switched reluctance motor with simpler single winding structure," *IEEE Transactions on Industrial Electronics*, vol. 59, no. 6, pp. 2592–2600, 2012.

[9] H. Chen, Q. Wang, and H. H. C. Iu, "Acceleration closed-loop control on switched reluctance linear launcher," *IEEE Transactions on Plasma Science*, vol. 41, no. 5, pp. 1131–1137, 2013.

[10] H. Chen and J. J. Gu, "Implementation of the three-phase switched reluctance machine system for motors and generators," *IEEE/ASME Transactions on Mechatronics*, vol. 15, no. 3, pp. 421–432, 2010.

[11] Y. J. Bao, K. W. E. Cheng, N. C. Cheung, and S. L. Ho, "Experimental examination on a new switched reluctance wind power generator system for electric vehicles," *IET Power Electronics*, vol. 5, no. 8, pp. 1262–1269, 2012.

[12] Y.-C. Chang and C.-M. Liaw, "Establishment of a switched-reluctance generator-based common dc microgrid system," *IEEE Transactions on Power Electronics*, vol. 26, no. 9, pp. 2512–2527, 2011.

Hindawi Publishing Corporation
Advances in Mechanical Engineering
Volume 2013, Article ID 941781, 6 pages
http://dx.doi.org/10.1155/2013/941781

Review Article

Development of Ocean Energy Technologies: A Case Study of China

Qin Guodong, Lou Ping, and Wu Xianglian

College of Jiaxing Vocational Technology, Jiaxing 314036, China

Correspondence should be addressed to Qin Guodong; qinguodong123@sina.cn

Received 28 June 2013; Revised 5 September 2013; Accepted 27 September 2013

Academic Editor: Haitao Yu

Copyright © 2013 Qin Guodong et al. This is an open access article distributed under the Creative Commons Attribution License, which permits unrestricted use, distribution, and reproduction in any medium, provided the original work is properly cited.

For the energy shortage in China's coastal areas, which has exerted severe impact on economy development, a growing number of attentions have been paid to ocean energy utilization. In this paper, a review of related researches as well as development of ocean energy in China is given. The main part of this paper is the investigation into ocean energy distribution and technology status of tidal energy, wave energy, and thermal energy, especially that of the tidal energy and wave energy. Finally, some recommendations for the future development of ocean energy in China are also provided. For further research in this field and development of ocean energy utilization in China, this review can be taken as reference.

1. Introduction

China's economy has kept a rapid growth for over 30 years, which, in most cases, means a large amount of energy demands and consumption. In 2001, China accounted for 10% of global energy demand but met 96% of those needs with domestic energy supplies. Nowadays, China's share of global energy use has swelled to over 15% [1, 2]. According to preliminary estimation of 2009, the total electricity consumption reached 3.697 trillion kWh, with an increase of 6.2% from 2008. In addition, before 2020, China's annual GDP will continue to increase at an average rate of 8%. Therefore, China's energy requirement will be rising in the near future with its economy development [3, 4].

China's modern tidal energy development and utilization have experienced three periods so far. The fact is that tidal energy stations growing up in Fujian and Guangzhou in 1955 mark the beginning of development of tidal energy technology, then it gradually turns to the construction period, and now it is the period of improvement and consolidation. China wave energy research rose from Shanghai in 1978, was originally learned from Japan pneumatic principle, and developed a 1 kW air turbine wave energy buoy [5–7]. The 1 kW air turbine wave energy buoy was tested and put into operation in the area of Zhoushan Islands in Zhejiang province, but due to the lack of testing means the exact data was not measured.

In addition, thermal energy and salinity are also discussed in this paper, and some recommendations for the future development of China are provided.

2. Tidal Energy Technology

The long coastline of China contains a large quantity of tidal energy, which is estimated to be 110 MW. Tidal energy is caused by flood and ebb tide, principle of which is similar to that of hydroelectric generation. Tidal energy can be extracted by building a dam (barrage) across an estuary or coastal inlet, with the dam containing turbines to generate electricity.

As has been mentioned above, China's modern tidal energy development and utilization have experienced three periods. The first period started around the year 1958. It is in Shun De County, Guangdong province, that small tidal energy station first appeared, and it soon spread across Zhejiang, Shandong, Jiangsu, Shanghai, Fujian, Liaoning, and other provinces [8]. Up to 1958's national tidal energy conference held by the Chinese Academy of Sciences and the Ministry of Electricity and Water in Shanghai, there had been 44 small tidal energy stations built, such as Da Liang

Figure 1: Jiangxia pilot tidal plant.

tidal energy station in Guangdong province, but most of the stations were with a small capacity ranging from 5 KW to 144 KW. Besides, there are only two energy stations keeping long-term operation for energy generation, including Sand Hill Energy Station which is in Wen-ling County in Zhejiang province and Chou dong Energy Station located in Chang-le County in Hunan province [9].

In 1970s, came the second period. Construction of tidal energy stations appeared in the coastal area of China, with a total number of more than 20, such as Jin-gang in Shandong province Chen-gang Station [10, 11]. The tidal energy stations in the second period were greatly improved: larger in scale, more standard, and more rigorous in design, operation, and equipments. Most stations possessed an installed capacity ranging from 100 kW to 200 kW, for example, Jiang-xia Tidal Yest Station in Zhejiang province and Bai-Shakou Station in Shandong province, which were constructed by the state and had a larger scale and more regular operation, with a total installed capacity of 320 kW and 960 kW, respectively. During this period, researches on tide resource were conducted in Yue-qing Bay, Zhejiang province, for planning programming, and, finally, four development plans were proposed. Jiang-xia Tidal Test Station is the implementation of the scheme of minimum [12, 13]. Apart from Jiang-xia Station and Bai-Shakou Station, there are other stations keeping long-term running, such as Hai-Shan Station, Yue-pu Station of Zhejiang province, Liu-he Station of Jiangsu province, Ganzhu Beach Station of Guangdong province, and Guo-Zishan of Guangxi.

Jiangxia pilot tidal power plant (see Figure 1), located in the north end of Yueqing Bay, is the most remarkable one of the three plants, and the other two are La Rance tidal power plant in France and Annapolis tidal generating station in Canada. Jiangxia pilot tidal power plant's construction was started in the year 1974 and completed in 1985, and the plant was installed with one set generator of 500 kW, one set of 600 kW, and three sets of 700 kW, with a total capacity of 3.2 MW [14]. The engineering staff of Jiangxia plant were investigated into industrialization research of tidal generating for many years; remarkable achievements in reliability of the generator sets were gained, such as reservoir sediments reducing, erosion protecting, floating method, operating automation, and optimal scheduling.

The third period is from the late 1970s to the 1990s. This period is to improve, consolidate, and steadily move forward. Main focus is on the following aspects [14, 15].

(1) Carrying out the investigation and evaluation of tidal energy resources. In the early 1980s, under the leadership of the Ministry of Water, the second national coastal tidal energy resources survey was completed by the water conservancy departments in coastal provinces and cities. In the late 1980s, under the leadership of the State Oceanic Administration and the Ministry of Electricity and Water, the relevant units of the two systems completed the planning of ocean energy resources in the coastal rural areas and regional planning, including the development of installed capacity from 200 to 1000 kW.

(2) The energy plants such as River Tidal test energy stations, Baishakou, and Haishan tidal energy stations have been built.

(3) Building of new energy plants. In 1989, on the basis of Pingtan County tideland reclamation project, Xingfuyang tidal test energy plant with a capacity of 320 kW was built in Fujian province.

(4) Preparation for medium-sized tidal energy plant construction. From the beginning of the 1980s, under the circumstance of rapid national economy construction, the obvious conflicts between energy supply and demand and the great situation of the national call to vigorously develop new energy, leading departments and coastal provinces, especially Zhejiang and Fujian province, to carry out many preliminary surveys on the tidal energy plant construction and plan feasibility. For example, Zhejiang province did an examination on Yueqing Bay, Xiangshan Port, Jiantiaogang tidal energy station dam; the marine group of the State Science and Technology Commission did an examination on the million-kW tidal energy plant in coastal areas of Zhejiang and Fujian; and feasibility study of Bachimen, Dagongban, Jiantiaogang tidal energy plant, and so forth.

Since June 2009, the automation and safety of plant have been improved after technology upgrading. In the National Nature Development and Reform Commission (NDRC) of Medium and Long-Term Development Plan for Renewable Energy in China, there was a target that 100,000 kW tidal power stations would be built by 2020 [16–18]. For the realization of this goal, a series of preliminary work has been completed. The feasibility study of a 10 MW intermediate experimental tidal power station in Jiantiao Port of Zhejiang province and Daguanban Port of Fujian province has been conducted. And the planning of the Maluanwan Tidal Power Plant is under way [19].

3. Wave Energy Technology

Wave energy, that is, the kinetic energy and potential energy in waves, is proportional to square of wave's height and period of motion and is unstable. Wave energy can be used in

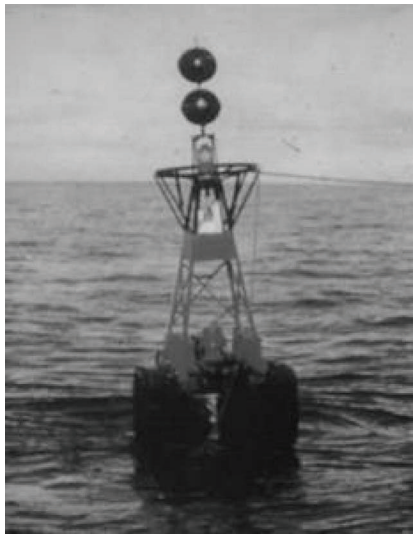

Figure 2: 1 kW wave energy buoy in Shengshan Island, Zhejiang.

water drawing, heat supply, seawater desalination hydrogen production, and so forth.

At the beginning of 1970s, the wave energy research activities expanded from Shanghai to Guangzhou, Beijing, Dalian, Qingdao, Tianjin, and Nanjing [9, 12]. There were a dozen units engaged in wave energy research. 1 kW wave energy buoy was successfully developed in 1975 and the test was completed in Shengshan Island, Zhejiang (as shown in Figure 2).

After nearly 30 year's research and development, the wave energy technology has gained rapid development. Pneumatic beacon lights floating microwave energy device was the first achievement and already put into commercial production. Now there are more than 600 aids to navigation in the north and south coast, and electricity supply was solved by floating microwave energy devices. Elbow buoy wave energy device, developed in cooperation with Japan, has been exported to foreign countries, and the technology is in the international leading level. In 1990, the Institute of Energy in Guangzhou did a research on successful generation test of a 3 kW shore wave energy plant in the Pearl River Estuary Dawanshan Island [20]. In 1996, the successful construction of 20 kW shore-type wave energy experimental energy station, 5 kW wave energy boat, and then the 100 kW shore wave force experimental energy station were accomplished in Shanwei, Guangdong province.

During the 10th Five-Year Plan period, with the support of the national "863" project and the Chinese Academy of Sciences Innovation directional project, the Chinese Academy of Sciences in Guangzhou Institute of Energy did a study on the independence and stability of the wave energy generation system. On January 9, 2005, the first low-energy test under real sea condition in Shanwei wave energy station proved wave energy generation system to be good in independence [21]. According to the test results, expected results of impact resistance, stability, and energy generation have been achieved by the wave energy generation system, which consists of three parts: independent energy system, fresh water, and floating charging system. An independent wave energy supply system, with a total installed capacity of 50 kW and the maximum wave peak energy of 400 kW, was developed in Zhelang Town, Shanwei City. However, after a 29 h typhoon, the device was wrecked by giant waves.

China's wave energy generation system still remains in 10–10^2 kW level, and the long-term goal by 2020 is 10^2–10^3 kW level. According to the current technology development, China's wave energy development can step into the demonstration operation stage, but commercializing is difficult to be realized in the near future. For the next stage, building of 10^2 kW devices and problems of costs, efficiency, and reliability are of priorities. By 2020, an MW level wave power plant farm will be constructed and connected to the grid [22].

In short, research on wave energy in China has a short history, but with the support of the "863" planning and the development of science and technology, it develops rapidly [20, 23, 24]. Microwave energy generation technology has gained maturation and commercialization. The small-shore wave energy technology has gone forward to the international market. However, the scale of the wave energy device demonstration test in China is much smaller than that in Norway and the United Kingdom, and the type of test development approach is far less than that of Japan. The small device is far from being put into practice, and its running stability and reliability remain to be further improved.

4. Thermal Energy Generation Technology

The temperature difference between warm surface ocean water and cold deep ocean water leads to the formation of thermal energy. As a result of heating effect of solar radiation, temperature difference in most tropical and subtropical oceans can reach 20°C or more. For utilizing the temperature difference, the Ocean Thermal Energy Conversion (OTEC) technique is adopted to make a thermodynamic cycle through heat engine to produce power.

In China, thermal energy generation technology began in the early 1980s, and the research was carried out in Guangzhou, Qingdao, Tianjin, and so forth [14]. In 1986, the thermal energy conversion test analog devices were completed in Guangzhou. In 1985, Guangzhou Institute of Energy Conversion made a study on open-cycle ocean thermal energy conversion by using a method called droplet elevating cycle, which increased potential energy of the seawater and density of thermal energy and reduced the size of the system. It is estimated that seawater will be elevated to a height of 125 m by releasing heat and driving the turbine when its temperature decreases from 20°C to 7°C [24].

Since 1980, Taiwan has carried out a research on the ocean thermal energy resources in the east coast of Taiwan island and an evaluation and program design of the natural environmental conditions of Hualien County Heping river, Shihtiping, and Taitung County Zhangyuan and also gave a plan of constructing a 40,000 kW demonstration energy plant in 1995 [25].

Another promising way to utilize thermal energy is Seawater-source Heat Pump (SWHP) technology. The first

plant adopting SWHP system in China is Qingdao Power Plant in November, 2004 [26]. It is proved that the cost of winter heating by using SWHP is much lower than that of coal heating, which are 15 CNY/m^2 and 25 CNY/m^2, respectively. Therefore, air conditioning in Olympic Sailing Venue in Qingdao adopts this system.

5. Marine Salinity Gradient Energy Technology

Salinity gradient energy, the potential chemical electrical energy caused by difference in salt concentration between seawater and fresh water or between seawaters with different salt concentrations, mainly exists in the area where river meets the sea. Usually the potential chemical electrical between seawater (35% salinity) and fresh water has an energy density of 240 m water head, which can directly drive the turbine to produce power [13].

It is calculated that the total amount of salinity gradient energy resource along China's coast can reach 3.58×10^{15} kJ, but the distribution is uneven. It is relatively scarce in northern China, while that in the southern region of Yangtze River accounts for 92.5% of the total amount [14, 27], especially in the estuaries of Yangtze River and Pearl River. Shanghai and Guangzhou are located in the estuaries of Yangtze River and Pearl River respectively, and those two areas are the most developed in economy and with large energy consumption.

In 1980s, research on salinity gradient energy generation and semipermeable membrane in China began, and laboratory device of Salt Lake concentration energy generation was successfully developed in 1985 in Xi'an. In the test, the solvent (water) to the solution (brine), penetrating the water column of the solution increased to 10 m hydrogenerating unit generating energy from 0.9 to 1.2 W. Obviously, salinity gradient energy generation research in China is still at the preliminary stage of the laboratory principle.

Xi'an University of Architecture and Technology made an experimental research on elevated tank system in 1985. The upper tank in the experiment was about 10 m above the permeator and 30 kg dry salt was used for a work of 8–14 h and to generate 0.9–1.2 W electricity. Unless the permeation flux was improved by one order of magnitude and the seawater could be used without pretreatment, the technology of osmotic energy development would be commercialized [14].

Although marine salinity gradient energy exploitation is simple in principle, lots of difficulties remain to be solved to achieve commercialization and industrialization. Some experts reckon that commercial exploitation of salinity gradient energy is difficult to realize, investment would be unadvisable, and the environment impact should also be taken into consideration under present conditions of technology and process. Therefore, after some theoretical researches and putting forward of energy conversion devices, few further research on it are made in China [28].

6. Ocean Current Energy Technology

Ocean current energy is the kinetic energy of flowing seawater, mainly caused by the relatively steady ocean flow in strait or channel and the regular tides current flow. The power of current is in proportion to velocity cubed and flux. Therefore, the higher the speed, the more powerful the current.

Figure 3: The tidal current pilot plant in Guishan channel.

From the Bohai Sea to the South China Sea, distribution of ocean current energy resources is uneven. Current velocity in most areas of Bohai Sea is less than 0.77 m/s, except for water channels in Bohai Strait, among which the highest speed can reach 2.5 m/s. Current velocity in the Yellow Sea coast is larger than that of 0.5–1.0 m/s in Bohai Sea.

Ocean current energy technology in China can be traced back to 1978. At the year of 1987, He Shijun, from Dinghai, Zhejiang, made a tidal current conversion testing device and harnessed 5.7 kW electricity at a velocity of 3 m/s in Xihoumen channel. In January 2002, the first floating moored tidal current turbine in China was built by Harbin Engineering University, and installed (WanXiang I) in Guishan channel (Daishan, Zhejiang), as shown in Figure 3. The "WanXiang I" consists of two vertical axis rotors, driven systems, control mechanism, and floating platform, and every 2.2 m diameter rotor is composed of four vertical blades with variable pitches.

In 2009, a project of National Key Technology R&D Program (NKTRDP), research and demonstration of 150 kW tidal current power station technology was launched, which aims to test the prototype turbine and to demonstrate technology and will be finished in 2014.

7. Suggestions

With years of development, ocean energy harnessing technology has gained maturity. In terms of technical maturity, tidal power generation technology is the most mature one, but it may cause possible environmental impacts. Therefore, careful consideration should be taken in its development. For the short term, China's ocean energy development mainly focuses on tidal power generation and construction of 10 MW-level tidal power plant. At present, technical problems of reducing costs in devices and improvement of reliability should be the point disscussed. In the near future, construction of hundreds of kW level demonstration generation devices and accumulating experience for commercialization should be the task. For this, the following measures should be taken.

(1) Increasing financial support in science and technology. Social forces and nongovernment capital must

be introduced into researches on ocean energy development as well as investment in national science and technology development planning.

(2) Establishing a strategic position for ocean renewable energy, incorporating it into national planning and improving its development by preferential policies and economic means of tax cuts, feed-in tariff, and so forth.

(3) Making efforts to its industrialization and commercialization, seeking a combination of low cost and large-scale development to improve economic returns and market competitiveness.

It is predicted that China's energy demands will increase year by year, and the total energy consumption in 2050 will be 3 times as much as that in 2000. Such a huge demand cannot be satisfied by conventional energy and we must make full use of ocean energy, and gradually reverse the energy structure and the structure of electricity supply. Only in this way coordination of China's energy, economy, and environment can be accomplished.

8. Conclusions

In this review, different types of ocean energy and related technologies in China are introduced and evaluated. Ocean renewable energy faces a good opportunity for development and China has offered a favorable environment, especially for the tidal energy and wave energy, so there is much reason to believe that ocean energy will get greater development in the future and contribute more to national economy.

However, to realize the commercialization of ocean energy is not an easy work. Many inventions still need to be made, and many challenging problems remain to be solved. In general, cooperation of research institutions in ocean energy technology and collaboration between governments should be strengthened to remove difficulties, reduce cost, and improve ocean energy utilization rate.

Acknowledgment

This research was supported by Science Technology Department of Jinxing State (no. 2013AY21034).

References

[1] H. Gao and A. Zhang, *Technology and Application of Renewable Energy*, National Defense Industry Press, Beijing, China, 2007.

[2] M. Huang, Y. He, and H. Cen, "Predictive analysis on electric-power supply and demand in China," *Renewable Energy*, vol. 32, no. 7, pp. 1165–1174, 2007.

[3] C. K. Wang and S. W. Yong, "The ocean resources and reserves evaluation in China," in *Proceedings of the 1st National Symposium on Ocean Energy*, pp. 169–179, Hangzhou, China, 2008.

[4] Y. Yu, H. Tang, and J. Guo, "Developing prospect analysis of renewable energy resources in China," *East China Electric Energy*, vol. 37, no. 8, pp. 1306–1308, 2009.

[5] T. J. Zhu, *The Utilities and Development of Ocean Energy Resources*, Chemical Industry Press, Beijing, China, 2005.

[6] Y. Mao, H. Sheng, and F. Yang, "The true cost of coal," in *The China Sustainable Energy Program, World Wide Fund for Nature*, Greenpeace, Beijing, China, 2008.

[7] J. Chang, D. Y. C. Leung, C. Z. Wu, and Z. H. Yuan, "A review on the energy production, consumption, and prospect of renewable energy in China," *Renewable and Sustainable Energy Reviews*, vol. 7, no. 5, pp. 453–468, 2003.

[8] Y.-G. You, Y.-H. Zheng, Y.-M. Shen, B.-J. Wu, and R. Liu, "Wave energy study in China: advancements and perspectives," *China Ocean Engineering*, vol. 17, no. 1, pp. 101–109, 2003.

[9] J. Zhu, "Status of new and renewable energy development in China," *Renewable Energy*, vol. 21, no. 2, pp. 3–8, 2003.

[10] Y. G. You, B. Wu, and S. Sheng, "Proposals on the development of wave energy technologies in China," in *Proceedings of the 1st National Symposium on Ocean Energy*, pp. 17–29, Hangzhou, China, 2008.

[11] L. Yan and K. Li, "The present status and the future development of renewable energy in China," *Renewable Energy*, vol. 10, no. 213, pp. 319–322, 1997.

[12] Y. Su, Y. You, and Y. Zheng, "Investigation on the oscillating buoy wave power device," *China Ocean Engineering*, vol. 16, no. 1, pp. 141–149, 2002.

[13] P. Zhang, Y. Yang, J. Shi, Y. Zheng, L. Wang, and X. Li, "Opportunities and challenges for renewable energy policy in China," *Renewable and Sustainable Energy Reviews*, vol. 13, no. 2, pp. 439–449, 2009.

[14] Y.-G. You, Y.-H. Zheng, Y.-J. Ma, Z. Yu, and N.-D. Jiang, "Structural design andprotective methods for the 100 kW shoreline wave power station," *China Ocean Engineering*, vol. 17, no. 3, pp. 439–448, 2003.

[15] J. Li and G. Hu, *China Wind Energy Report 2007*, China Environmental Science Press, Beijing, China, 2008.

[16] National Development and Reform Commission (NDRC), *The National Eleventh Five-Year Plan for Renewable Energy Development*, 2007.

[17] National Development and Reform Commission (NDRC), *Medium and Long-Term Development Plan for Renewable Energy in China*, 2007.

[18] F. Liu, Z. Zhang, H. Xu, J. Meng, and R. Zhang, "Evaluation method of fuzzy integrated estimate for potential impacts on the environment of tide power stations," *Ocean Technology*, vol. 26, no. 3, pp. 110–113, 2007.

[19] J. Chang, D. Y. C. Leung, C. Z. Wu, and Z. H. Yuan, "A review on the energy production, consumption, and prospect of renewable energy in China," *Renewable and Sustainable Energy Reviews*, vol. 7, no. 5, pp. 453–468, 2003.

[20] L.-Q. Liu, Z.-X. Wang, H.-Q. Zhang, and Y.-C. Xue, "Solar energy development in China—a review," *Renewable and Sustainable Energy Reviews*, vol. 14, no. 1, pp. 301–311, 2010.

[21] S. Li and Z. Xu, "Analysis of causes of different regional energy intensities in China," *Sino-Global Energy*, vol. 14, no. 8, pp. 1–10, 2009.

[22] Experts in Advanced Energy Technology Field of National High-Tech R&D Program of China (863 Program), *Introduction of Development of Advanced Energy Technology in China*, SINOPEC Press, 2010.

[23] C. K. Wang and W. Y. Shi, "The ocean resources and reserves evaluation in China," in *Proceedings of the 1st National Symposium on Ocean Energy*, pp. 169–179, Hangzhou, China, 2008.

[24] Q. J. Xie, X. Q. Liao, B. Lu, and X. H. Chen, "Summary of tidal energy utilization at home and abroad," *Water Conservancy*

Science and Technology and Economy, vol. 15, no. 8, pp. 670–671, 2009.

[25] J. S. Chen, D. H. Wang, and C. Y. Lv, "Tidal energy generation and its application prospect," *Ocean Development and Management*, vol. 25, no. 11, pp. 84–86, 2008.

[26] Seawater-source Heat Pump Technology (SWHP) widely used in Olympic Sailing Center, Qingdao, China, http://scitech.people.com.cn/GB/25509/58105/118897/7059125.html.

[27] F. Y. Liu, Z. H. Zhang, H. R. Xu, J. Meng, and R. Zhang, "Evaluation method of fuzzy integrated estimate for potential impacts on the environment of tide energy stations," *Ocean Technology*, vol. 26, no. 3, pp. 110–113, 2007.

[28] Y. W. Li, *Ocean Energy Resources Development*, Ocean Press, Beijing, China, 2008.

Hindawi Publishing Corporation
Advances in Mechanical Engineering
Volume 2013, Article ID 963093, 11 pages
http://dx.doi.org/10.1155/2013/963093

Research Article

Design and Analysis of a Linear Hybrid Excitation Flux-Switching Generator for Direct Drive Wave Energy Converters

Lei Huang,[1] Minqiang Hu,[1] Jing Liu,[2] Chunyuan Liu,[1] and Weibo Zhong[1]

[1] *Engineering Research Center for Motion Control of MOE, School of Electrical Engineering, Southeast University, Nanjing 210096, China*
[2] *College of Mechanical and Electronic Engineering, China University of Petroleum (Huadong), Qingdao 266580, China*

Correspondence should be addressed to Minqiang Hu; mqhu@seu.edu.cn

Received 28 June 2013; Revised 31 August 2013; Accepted 31 August 2013

Academic Editor: Fabrizio Marignetti

Copyright © 2013 Lei Huang et al. This is an open access article distributed under the Creative Commons Attribution License, which permits unrestricted use, distribution, and reproduction in any medium, provided the original work is properly cited.

Linear generators have the advantage of a simple structure of the secondary, which is suitable for the application of wave energy conversion. Based on the vernier hybrid machines (VHMs), widely used for direct drive wave energy converters, this paper proposes a novel hybrid excitation flux-switching generator (LHEFSG), which can effectively improve the performance of this kind of generators. DC hybrid excitation windings and multitooth structure were used in the proposed generator to increase the magnetic energy and overcome the disadvantages of easily irreversible demagnetization of VHMs. Firstly, the operation principle and structure of the proposed generator are introduced. Secondly, by using the finite element method, the no-load performance of the proposed generator is analyzed and composed with ones of conventional VHM. In addition, the on-load performance of the proposed generator is obtained by finite element analysis (FEA). A dislocation of pole alignments method is implemented to reduce the cogging force. Lastly, a prototype of the linear flux-switching generator is used to verify the correctness of FEA results. All the results validate that the proposed generator has better performance than its counterparts.

1. Introduction

Sea wave energy, originating from sun, is huge, clean, and renewable [1]. Wave energy is a widely distributed, highest-grade energy density, most easily directly used, clean, and renewable ocean energy [2]. Wave energy generation system, using electrical machines to convert energy from wave motion to electricity, is the main form of the development and utilization of wave energy. Since 1970s, there have been many different wave energy generation systems to be proposed. Direct drive power take-off systems have been proposed and widely concerned. Linear generators have directly been implemented to the drive of wave motion without using medium devices, such as air turbines, so that the generation system is simplified. A typical direct drive power take-off system is shown in Figure 1.

This system consists of two buoys, inner and outer buoys, a damper plate, and a linear generator. Because of the special design of inner buoy and damper plate, the inner buoy is not up and down with the wave undulating. Therefore, the stator (primary) of linear generator is seen as static suspended in water. The mover (secondary) of the generator is connected with the outer buoy and moved with the motion of a sea wave.

The linear generators are the core of direct drive wave power systems. The performances of linear generators directly determine the performances of the systems, such as the efficiency, power density, and quality of electric energy. At present, the major linear generators used for direct drive wave energy extraction are linear synchronous permanent magnet motor, which have permanent magnets (PMs) on the mover (secondary) [2–5]. This kind of linear permanent magnet machines has disadvantages of complex structure of the secondary, which might cause unexpected temperature rise and higher costs. In addition, these generators, evolved from conventional rotating generator, cannot obtain a high power density at a low speed motion environment. This is

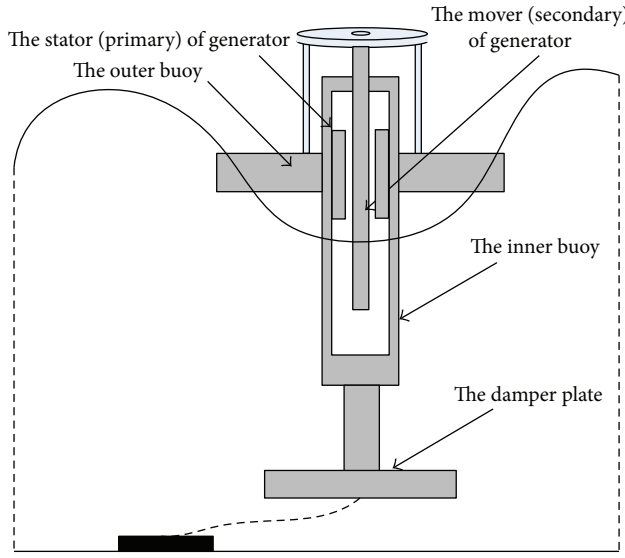

Figure 1: The typical direct drive power take-off system.

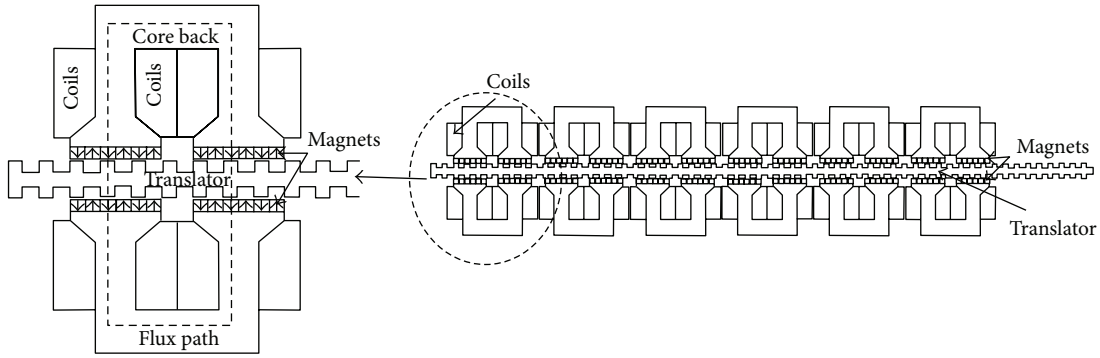

Figure 2: The typical topology of VHM.

not suitable for direct drive wave energy converters. In order to obtain a high rate of change of energy in the air gap and a higher power density, based on the rotating stator-permanent magnet machines [6–8], some researches were focused on the primary permanent magnet linear generator, whose permanent magnets are assembled in the primary, such as vernier hybrid machine (VHM) [9–11] and switched reluctance generator [12, 13]. Compared with the primary permanent magnet linear generators, secondary permanent magnet linear generators cannot be designed as small pole pitch, because of the limitation of the machining dimension [14]. For VHMs and switched reluctance generators, by using the secondary slotted surface, the reluctance variation produces a rapid flux changing, resulting in shear stresses orders of magnitude increased. However, in order to increase the rate of flux changing, the size of permanent magnet of the VHMs must be designed very small. It suffers from the disadvantages of easily irreversible demagnetization. Therefore, to overcome shortcomings of the VHMs and increase the controllability of air gap flux, a novel linear hybrid excitation flux-switching generator is proposed for wave energy extraction in this paper.

Firstly, the operation principle and structure of the proposed generator were introduced. Secondly, by using the finite element method, the power density, cogging force, efficiency of energy transfer, and output voltage regulation of the proposed generator were optimized and analyzed. Lastly, a prototype of linear permanent magnet flux-switching machine was used to verify the correctness of the finite element analysis results.

2. The Structure and Operation Principle of the Proposed Generator

Based on the magnetic gear effect, the pole pitch of VHM is smaller than conventional PM machine. Thus, these modulate the magnetic field produced by PMs to the high-speed traveling magnetic field. Therefore, the VHM has advantages of high shear stresses, high rate of change of flux. These make it attractive in cases where a conventional machine would be very large and heavy in low speed environment, such as direct drive wave energy converters. Figure 2 shows the typical topology of VHM.

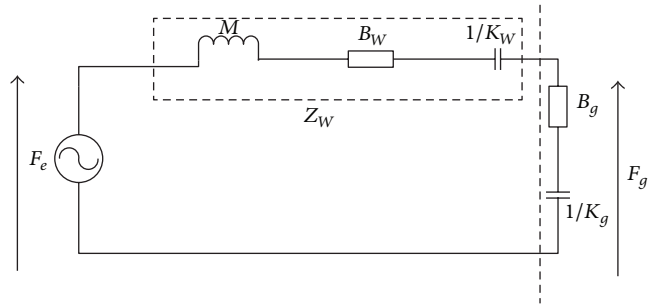

Figure 3: Electrical analogue of the direct drive power take-off system.

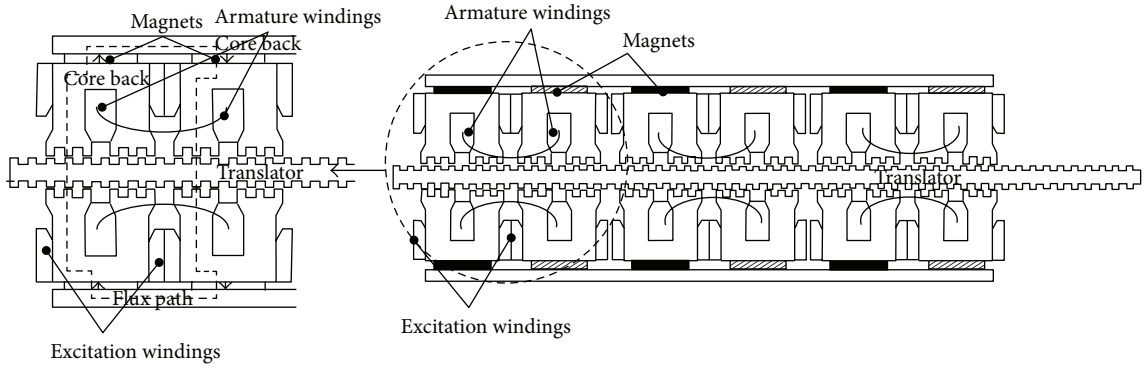

Figure 4: The topology of the proposed generator.

However, because of smaller pole pitch of PMs, the VHMs inevitably suffer from easily irreversible demagnetization and severe flux leakage.

In order to obtain maximizing power extraction, the force generated by the directly coupled linear generator should be controlled. The electrical analogue of the direct drive power take-off system is shown in Figure 3 [6].

As shown in Figure 3, the EMF source F_e represents the wave excitations force, the inductance M represents the mass of the device, and the resistance B_W and the capacitance K_W represent the mechanical damping and the spring stiffness force, respectively. The generator is represented by the load B_g and K_g. When the sum of the imaginary components of the total impedance adds up to zero, maximum power will be obtained. Consider

$$\begin{aligned} B_g &= B_W, \\ K_g &= \omega^2 M - K_W. \end{aligned} \tag{1}$$

Therefore,

$$f_g = B_W \dot{x} + \left(\omega^2 M - K_W\right) x. \tag{2}$$

According to the principle of PM machine, the reaction force of the linear generator can be expressed as [15]

$$\begin{aligned} f_g &= \frac{3}{2} k_f I_{\mathrm{PM}} \widehat{I} \cos\left(\omega t + \varphi_g\right) \\ &= \frac{3}{2} k_f I_{\mathrm{PM}} \left(\widehat{I} \cos \omega t \cos \varphi_g - \widehat{I} \sin \omega t \sin \varphi_g\right) \\ &= \frac{3}{2} k_f I_{\mathrm{PM}} \left(i_{\dot{x}} + i_x\right), \end{aligned} \tag{3}$$

where, I_{PM} is the equivalent current of the magnetics in the primary. Therefore, to obtain the maximum power, the current of the generator should be controlled according to (4) and (5). Consider

$$i_x = -\left(\frac{\omega^2 M - K_W}{(3/2)\, k_f I_{\mathrm{PM}}}\right) x, \tag{4}$$

$$i_{\dot{x}} = \frac{B_W}{(3/2)\, k_f I_{\mathrm{PM}}} \dot{x}. \tag{5}$$

From (4), it can be seen, with the changing of the frequency ω, that the RMS phase current should have a large scope of working. However, the current of the linear generator is limited by the rated current value of armature and cannot increase unrestrictedly. Therefore, the working range during maximum energy output is very small and limited.

For the shortcomings of VHMs, such as easily irreversible demagnetization, severe flux leakage, and small working range, a novel linear hybrid excitation flux-switching generator (LHEFSG), shown in Figure 4, is proposed in this paper.

By using hybrid excitation, the I_{PM} can be controlled to change with the ω, and the RMS phase current is optimized. The multitooth structure which is used to increase the rate of change of magnetic flux will not change the pole pitch of PMs.

As shown in Figure 5, when the translator moves, the fundamental of PM flux linkage in one-phase coil changes with magnetic reluctance at different positions and induces electromotive force (EMF).

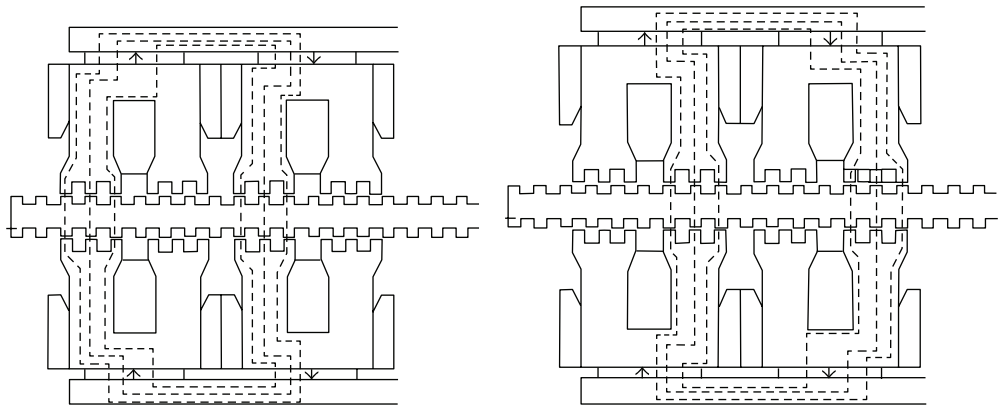

(a) (b)

Figure 5: The operational principle of the proposed generator. (a) Typical position one. (b) Typical position two.

3. Performance Analysis

To investigate the characteristics of the proposed generator, a typical VHM, used for wave energy conversion, is employed to compare with the proposed generator. The 2-D FEM combined with an equivalent circuit is employed to analyze electromagnetic characteristics of the two generators.

The basic parameters and materials of the respective member of the TPPMLG and the TSPMLG are listed in Tables 1 and 2, respectively.

3.1. The No-Load Performance. Firstly, the no-load performances of the two generators are analyzed. The voltage of one phase can be expressed as

$$V = \frac{d\left(\psi_e + \psi_{\mathrm{PM}}\right)}{dt}, \tag{6}$$

where ψ_e and ψ_{PM} are flux linkage due to DC exciting winding and PM excitation, respectively.

When the speed of mover is 0.5 m/s, the flux linkage and the no-load voltage are obtained by FEA and shown in Figure 6.

As can be seen, compared with the VHM, the proposed generator has advantages of higher voltage and magnetic energy density. The harmonic component of the proposed is smaller. In addition, output voltage has a greater range of adjustment.

The field distribution of two generators obtained by FEM is shown in Figure 7.

It can be seen that the flux leakage of the VHM is more severe than the one of the proposed generators.

The cogging force, which is produced by slot effect and end effect and may cause the mechanical vibration, is unexpected. The cogging forces of two generators are obtained by static finite element analysis and shown in Figure 8.

Obviously, because there is no PM at the end sides of primary and secondary, the major component of cogging force of the proposed generator is caused by slot effect and is far less than the one of VHM, even with the maximum excitation current 15 A.

Table 1: Basic parameters of two generators.

	Items	Value
The typical VHM	Primary depth (mm)	100 mm
	Primary length (mm)	478 mm
	PM width (mm)	4.5 mm
	PM thickness (mm)	4 mm
	Pole pitch of PMs	10 mm
	Total turns from one phase	400
	Secondary tooth width	4.5
	Secondary tooth pitch	10 mm
The proposed generator	Primary depth (mm)	100 mm
	Primary length (mm)	426 mm
	Distance between phases	73.33 mm
	Primary tooth width (mm)	4.5 mm
	PM width (mm)	40 mm
	PM thickness (mm)	4 mm
	Pole pitch of PMs	70 mm
	Total turns from one phase	400
	Secondary tooth width	4.5
	Secondary tooth pitch	10 mm
	Air gap (mm)	1 mm

In addition, the inductance performance is studied. By moving the mover, when the coil phase B coincides with the axis of d, the coil phase B is effectively axis coil d; thus,

$$L_d = \frac{\psi_b - \psi_{\mathrm{PM}}}{i_b}. \tag{7}$$

When the coil phase B coincides with the axis of q, the coil q is equivalent to axis coil d; thus,

$$L_q = \frac{\psi_b}{i_b}. \tag{8}$$

The d-axis inductance and q-axis inductance are obtained and shown in Figure 9.

The inductance performance of the proposed generator is similar to the one of the permanent magnet synchronous machines.

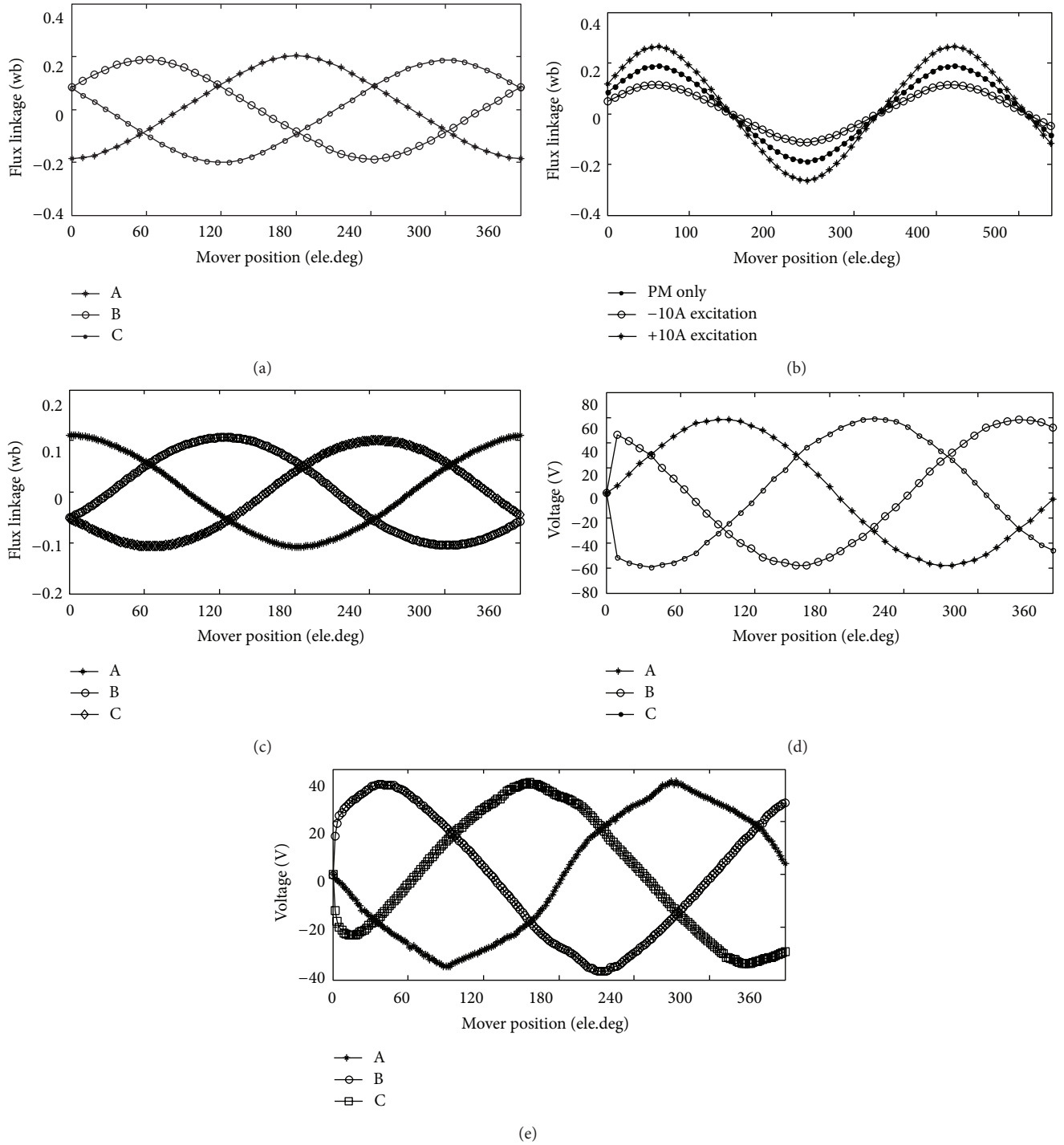

FIGURE 6: The flux linkage and EMF. (a) The flux linkage of the proposed generator with only PM excitation. (b) The flux linkage of the proposed generator with different excitation current. (c) The flux linkage of the VHM. (d) The no-load voltage of the proposed generator. (e) The no-load voltage of the VHM.

3.2. The Load Performance. Considering copper loss and core loss, the output power and the efficiency are calculated by the next equations:

$$P_{\text{Out}} = 3I^2 R_o,$$

$$P_{\text{In}} = P_{\text{Out}} + P_{\text{Loss-Copper}} + P_{\text{Loss-Fe}},$$

$$P_{\text{Loss-Fe}} = P_h + P_e = k_h f\left(a_h + b_h B_{\max}\right) + k_e f^2 B_{\max}^2,$$

$$\eta = \frac{P_{\text{Out}}}{P_{\text{In}}}, \tag{9}$$

where $P_{\text{Loss-Fe}}$ is the core loss, P_{Out} is the output power, P_{In} is the total input power, R_o is the load resistance per

Table 2: Material types and magnetic properties of two generators.

	Material name	Performance	
		Parameter	Value
Core of primary and secondary	Steel_10	Conductivity (S/m)	$2e + 6$
		Permeability	Nonlinear[a]
Primary windings	Copper	Conductivity (S/m)	$5.8e + 7$
		Relative permeability	0.99991
PM	$Nd_2Fe_{14}B$	Remanence (T)	1.23
		Coercivity (A/m)	$9.07e + 5$

[a]Importing the B-H curve of steel grade 10 (GB/T 711-2008).

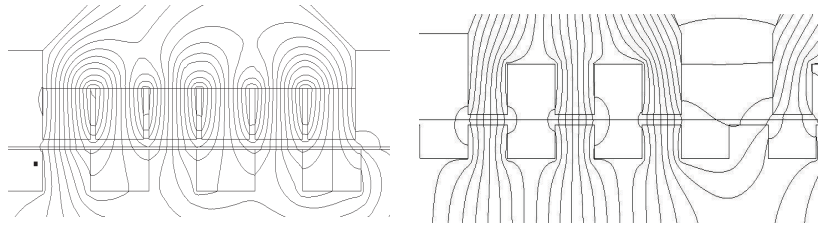

(a) (b)

Figure 7: The field distribution of two generators. (a) VHM. (b) The proposed generator.

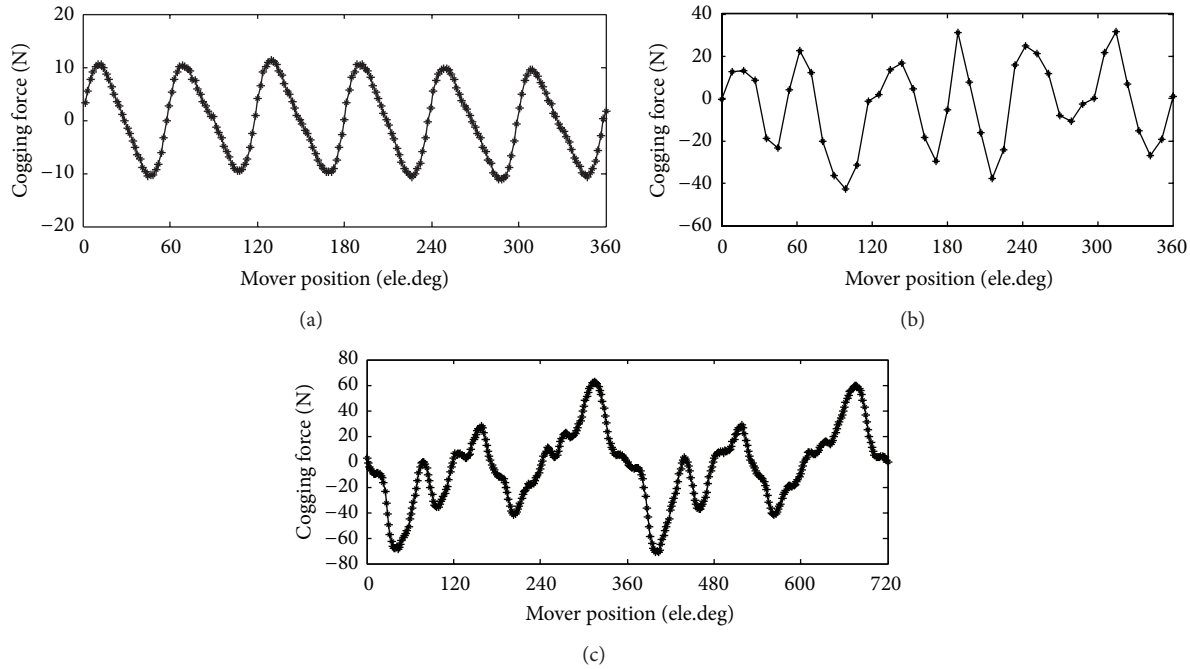

Figure 8: The cogging force of two generators. (a) The cogging force of the proposed generator only PM excitation. (b) The cogging force of the proposed generator under 15 A excitation. (c) The cogging force of the VHM.

phase, f and B_{max} are the frequency and the peak value of magnetic flux density, respectively, and k_h, k_e, a_h, and b_h are the loss coefficients of steel sheet provided by the supplier.

The performances of output power, output voltage, and efficiency of the proposed generator with different resistance are shown in Figure 8.

From Figure 10, it can be seen that the proposed generator has acceptable voltage regulation and high energy conversion efficiency.

Under the DC excitation, the DC filed loss can be calculated by

$$P_{\text{loss-DC}} = i_{\text{DC}}^2 R_{\text{DC}},$$
$$\eta = \frac{P_{\text{Out}}}{\left(P_{\text{In}} + P_{\text{loss-DC}}\right)}. \tag{10}$$

Therefore, under 15 A excitation, the performances of output power and efficiency of the proposed generator, considering the exciting loss, are shown in Figure 11.

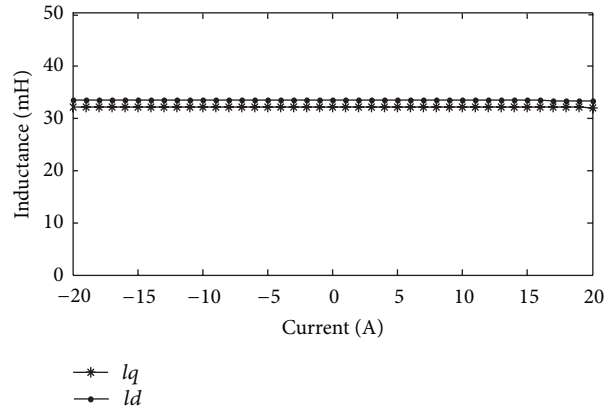

Figure 9: The inductance performance of the proposed generator.

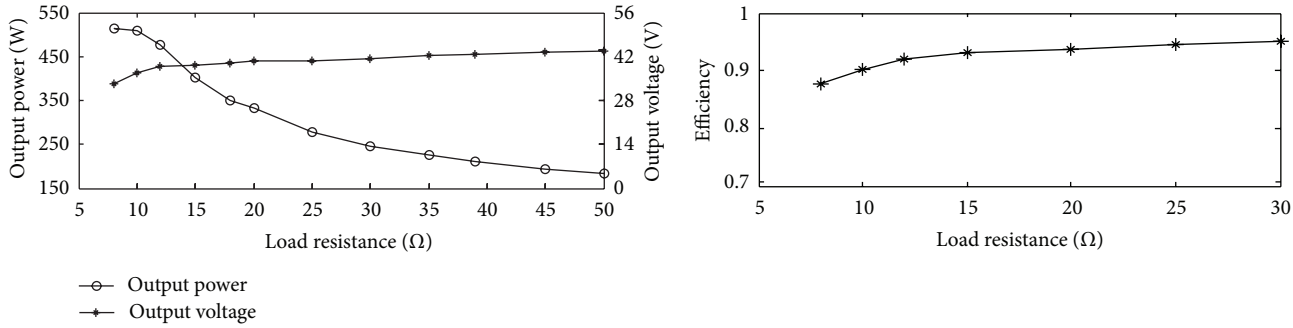

Figure 10: The on-load performance of the proposed generator only PM excitation.

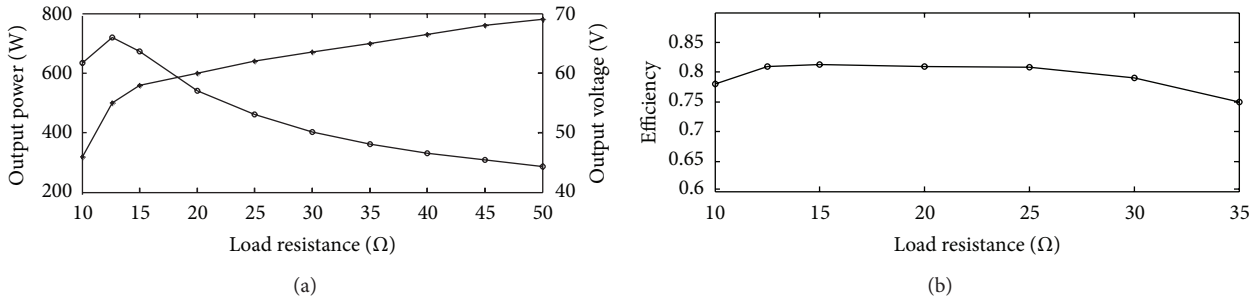

Figure 11: The on-load performance of the proposed generator under 15 A excitation.

The flux density distribution of the proposed generator, under the maximizing power output, is shown in Figure 12.

Because of the use of hybrid excitation, the output power, obtained by FEA, can reach to 720 W. It is far greater than the output power of the typical VHM. At this moment, the phase current is 4.23 A and the current density is 4.3 A/mm^2. These are reasonable values. As we can see, under the maximizing power output condition, local magnetic saturation is appearance. The saturation level is still within the acceptable range. However, because of the excitation loss, the output efficiency is slightly lower than the ones of the VHM.

4. The Optimization of Cogging Force

The cogging force, which may cause the mechanical vibration, is unexpected and unavoidable for linear generator. Therefore, minimized cogging force is the goal of PM generator design. To further reduce the cogging force, a dislocation of pole alignments method is implemented to suppress the fluctuations caused by cogging force. Figure 13 shows the structure dislocation of stator and pole alignments.

According to the cogging force shown in Figure 7, the major harmonic component of the cogging force is six-order harmonics. Therefore, the distance of dislocation l is

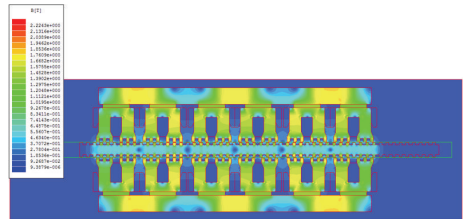

Figure 12: The flux density distribution under the maximizing power output.

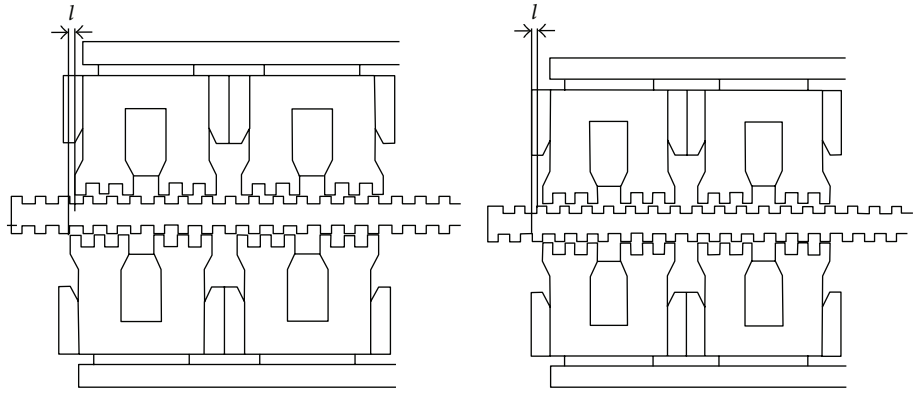

Figure 13: The structures dislocation of stator and pole alignments of mover. (a) Dislocation of stator alignment. (b) Dislocation of pole alignment.

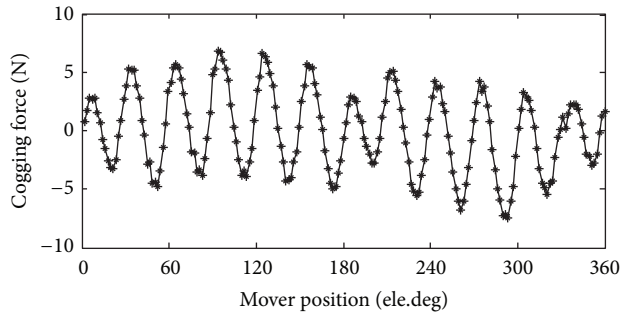

Figure 14: The cogging force with dislocation of pole alignments.

$\tau/12$. The optimal cogging force is obtained and shown in Figure 14.

It can be seen that the cogging force is reduced significantly, by using the method of dislocation of pole alignments. The electromagnetic force under the same load, with the dislocation of pole alignment and not, is obtained and shown in Figure 15.

The thrust ripple is reduced significantly, by using the method of dislocation of pole alignments. Because the output voltage is reduced at the same speed, the output power has a slight decrease.

5. Experimental Results

To investigate the performance of this kind of generator, a linear permanent magnet flux-switching machine, shown in Figure 16, is studied. The electromagnetic parameters of the machine are listed in Table 3.

Table 3: Basic parameters of the experimental prototype.

Items	Value
Primary tooth width (mm)	6.3
Primary slot width (mm)	14.7
PM pole pitch (mm)	70
PM thickness (mm)	5
Total turns from one phase	280
Secondary tooth width (mm)	6.3
Secondary tooth pitch (mm)	14
Air gap (mm)	1

To verify proposed methods using dislocation of stator and pole alignments, the double sides secondaries were staggered 1.2 mm (about $\tau/12$) distance. The cogging force and voltage are measured and shown in Figures 17 and 18.

As shown in Figure 18, the results of FEA, by using dislocation of stator and pole alignments, the cogging force and the harmonic component of voltage are both reduced effectively. The output voltage under different speed obtained and load resistance by FEA and the experiment were shown in Figure 19.

The results of FEA value agree with the experimental ones. As shown in the experiment results, the proposed

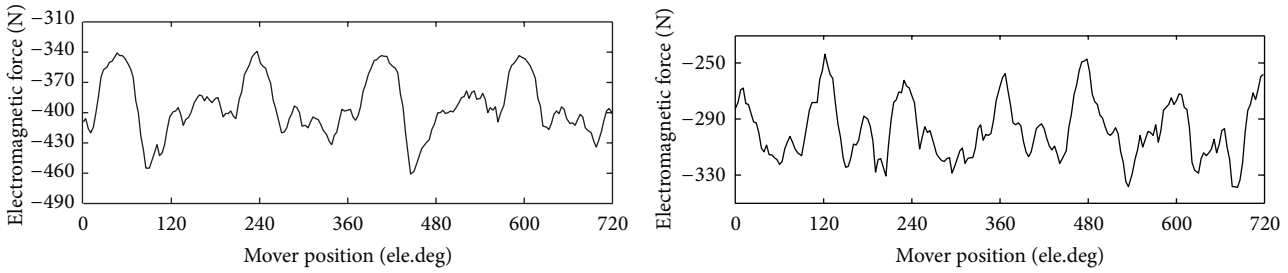

Figure 15: The electromagnetic force under the same load and same speed. (a) The electromagnetic force without dislocation of pole alignments. (b) The electromagnetic force with dislocation of pole alignments.

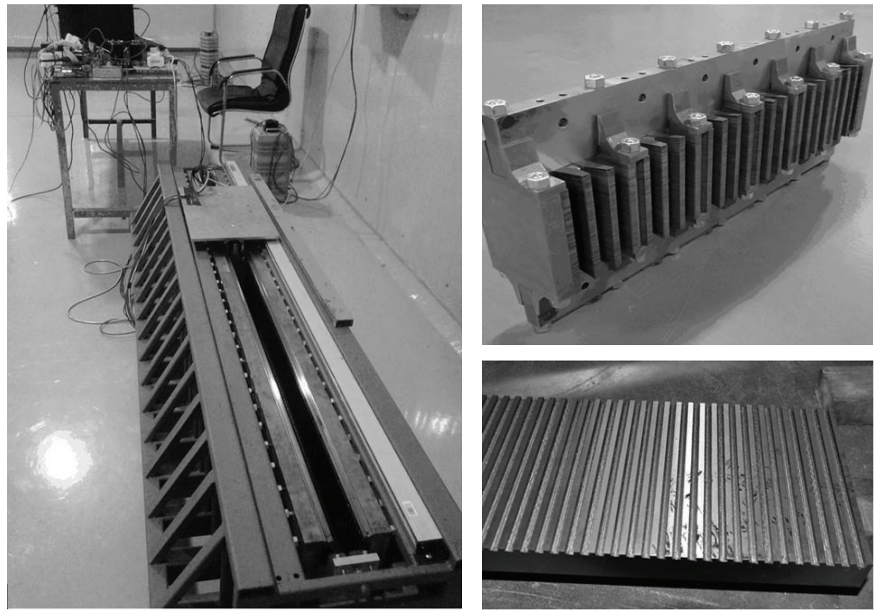

Figure 16: The experimental prototype.

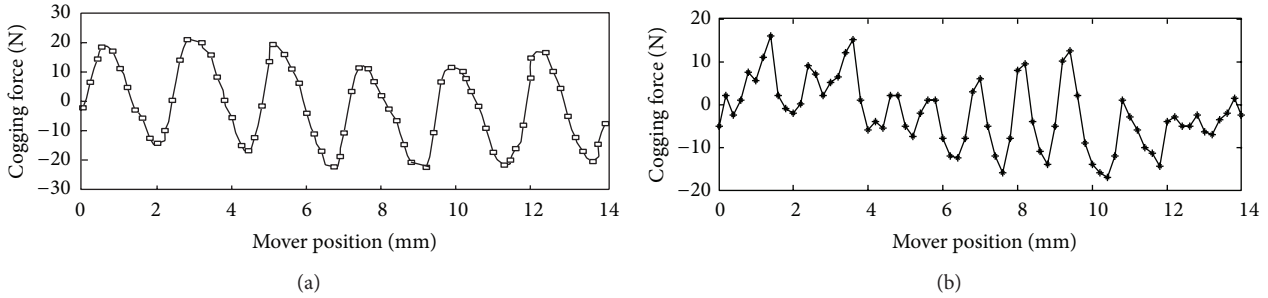

Figure 17: The experimental results of cogging force. (a) Without dislocation of pole alignments. (b) With dislocation of pole alignments.

generator has advantages of higher frequency, higher power density, and minor cogging force.

6. Conclusions

In this paper, a novel linear hybrid excitation flux-switching generator is proposed for direct drive wave energy converters. The operation principle has been analyzed. The proposed generator is compared with the typical VHM. The no-load and on-load performances are obtained and analyzed by using FEM. In addition, a dislocation of pole alignments method is implemented to suppress the cogging force. Lastly, a prototype of linear permanent magnet flux-switching machine has been employed to validate the results of FEA. All the results indicate that the proposed linear generator, with simple structure, minor cogging force, higher power density,

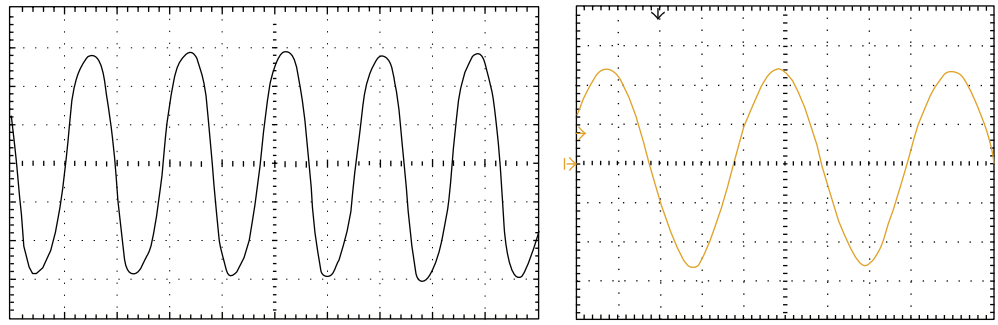

(a) (b)

Figure 18: The experimental results of no-load voltage. (a) Without dislocation of pole alignments (10 ms/div, 10 v/div). (b) With dislocation of pole alignments (5 ms/div, 10 v/div).

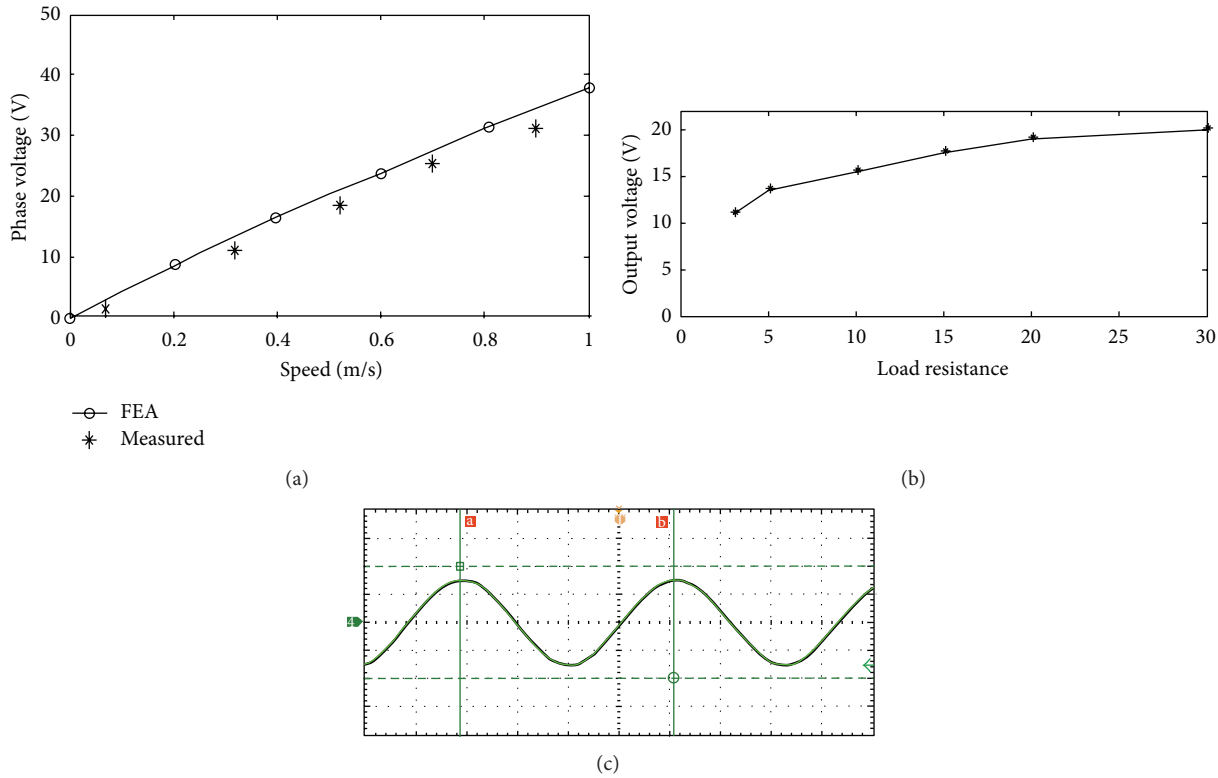

(a) (b)

(c)

Figure 19: The voltage obtained under different speed obtained and load resistance. (a) The no-load voltage obtained by FEA and experiment. (b) The on-load voltage obtained by experiment. (c) The voltage under 5 Ω resistance, at speed of 0.5 m/s, obtained by experiment (5 ms/div, 10 v/div).

higher output frequency, and larger range of output power, is suitable for the application of wave energy conversion.

Acknowledgments

This work was supported by the Special Foundation for State Oceanic Administration of China (GHME2011GD02) and by the National Natural Science Foundation of China under Grant no. 41076054.

References

[1] J. Falnes, *Ocean Waves and Oscillating Systems*, Cambridge University Press, Cambridge, UK, 2002.

[2] T. W. Thorpe and M. J. Picken, "Wave energy devices and the marine environment," *IEE Proceedings A*, vol. 140, no. 1, pp. 63–70, 1993.

[3] H. Polinder, M. E. C. Damen, and F. Gardner, "Linear PM generator system for wave energy conversion in the AWS," *IEEE Transactions on Energy Conversion*, vol. 19, no. 3, pp. 583–589, 2004.

[4] O. Danielsson, M. Leijon, and E. Sjöstedt, "Detailed study of the magnetic circuit in a longitudinal flux permanent-magnet synchronous linear generator," *IEEE Transactions on Magnetics*, vol. 41, no. 9, pp. 2490–2495, 2005.

[5] N. M. Kimoulakis, A. G. Kladas, and J. A. Tegopoulos, "Power generation optimization from sea waves by using a permanent

magnet linear generator drive," *IEEE Transactions on Magnetics*, vol. 44, no. 6, pp. 1530–1533, 2008.

[6] I. Boldea, C. Wang, B. Yang, and S. A. Nasar, "Analysis and design of flux-reversal linear permanent magnet oscillating machine," in *Proceedings of the IEEE Industry Applications Conference*, vol. 1, pp. 136–143, October 1998.

[7] Z. Q. Zhu, X. Liu, and Z. P. Pan, "Analytical model for predicting maximum reduction levels of vibration and noise in switched reluctance machine by active vibration cancellation," *IEEE Transactions on Energy Conversion*, vol. 26, no. 1, pp. 36–45, 2011.

[8] I. Boldea, *Variable Speed Electric Generators*, CRC Press, Boca Raton, Fla, USA, 2006.

[9] M. A. Mueller and N. J. Baker, "Modelling the performance of the vernier hybrid machine," *IEE Proceedings: Electric Power Applications*, vol. 150, no. 6, pp. 647–654, 2003.

[10] Y. Du, K. T. Chau, M. Cheng et al., "Design and analysis of linear stator permanent magnet vernier machines," *IEEE Transactions on Magnetics*, vol. 47, no. 10, pp. 4219–4222, 2011.

[11] J. K. H. Shek, D. E. Macpherson, M. A. Mueller, and J. Xiang, "Reaction force control of a linear electrical generator for direct drive wave energy conversion," *IET Renewable Power Generation*, vol. 1, no. 1, pp. 17–24, 2007.

[12] M. Blanco, G. Navarro, and M. Lafoz, "Control of power electronics driving a switched reluctance linear generator in wave energy applications," in *Proceedings of the 13th European Conference on Power Electronics and Applications (EPE '09)*, pp. 1–9, September 2009.

[13] J. H. Du, D. L. Liang, L. Y. Xu, and Q. F. Li, "Modeling of a linear switched reluctance machine and drive for wave energy conversion using matrix and tensor approach," *IEEE Transactions on Magnetics*, vol. 46, no. 6, pp. 1334–1337, 2010.

[14] L. Huang, H. T. Yu, M. Q. Hu, J. Zhao, and Z. Cheng, "A novel flux-switching permanent-magnet linear generator for wave energy extraction application," *IEEE Transactions on Magnetics*, vol. 47, no. 5, pp. 1034–1037, 2011.

[15] P. R. M. Brooking and M. A. Mueller, "Power conditioning of the output from a linear vernier hybrid permanent magnet generator for use in direct drive wave energy converters," *IEE Proceedings: Generation, Transmission and Distribution*, vol. 152, no. 5, pp. 673–681, 2005.

Hindawi Publishing Corporation
Advances in Mechanical Engineering
Volume 2013, Article ID 297803, 6 pages
http://dx.doi.org/10.1155/2013/297803

Research Article

Performance Analysis of a Completely Sealed Double Oscillating Structure Applied in Wave Energy Extraction

Zhenchuan Shi,[1] Haitao Yu,[1] and Fabrizio Marignetti[2]

[1] *School of Electrical Engineering, Southeast University, Si Pai Lou 2, Nanjing 210096, China*
[2] *Department of Electrical and Information Engineering, University of Cassino and Southern Latium, Via G. Di Biasio 43, 03043 Cassino, Italy*

Correspondence should be addressed to Zhenchuan Shi; szcshi@gmail.com

Received 28 June 2013; Accepted 17 September 2013

Academic Editor: Luigi Cappelli

Copyright © 2013 Zhenchuan Shi et al. This is an open access article distributed under the Creative Commons Attribution License, which permits unrestricted use, distribution, and reproduction in any medium, provided the original work is properly cited.

Most of the traditional wave energy converters are of a single oscillation structure, which leads to difficulties in sealing and installation. Based on the technological status of disc-type permanent magnetic coreless generator (DPMCLG) and long-stroke tape-type spring, a small scale wave energy extracting structure which can be completely sealed and work under the principle of double oscillation is proposed in this paper. By building a double oscillating model of the structure, the time domain differential equations and an equivalent circuit scheme are drawn, from which a phase-space solution by phase method is derived. Based on the solution, the performance of the structure is compared with that of single oscillating structure. The conclusion is that the double oscillating structure has a wider period range and higher power response for wave extraction, as well as the protection of power generator from damage in storm conditions.

1. Introduction

The enthusiasm towards the exploitation of renewable energies has prompted a significant interest in wave power so that various structures have been invented, among which the point absorber is an excellent approach for its simple mechanism, easy fabrication, and point absorption effect. The point absorption method usually aims for large capacity power systems, so such components are adopted as permanent magnets, linear generator, and buoy and anchor [1–8]. Anchored or stationary components work with floating components to extract as much power as possible. However, there are some problems for this type of structure. (1) It is difficult to encapsulate electric devices with relatively moving parts in ocean conditions. (2) Because of a large rating power, conventional linear generators often have considerable cogging force, and thus they are incapable of working in small waves. (3) To meet the requirements of buoy stroke, many permanent magnets should be used in linear generator. (4) Buoy's direct driving generator can enhance wave conversion ability, but it is vulnerable to rough weather conditions. For small-capacity wave power systems, these drawbacks are unacceptable. In this paper, one wave power structure completely encapsulating the relatively moving parts is proposed to overcome these defects. The structure is a vibration pick-up device or double oscillating structure which has been applied in micropower harvesting system. For example, there are vibration generators based on piezoelectric effect and voice coil generators based on Faraday's law [9, 10]. Both generators harvest vibration energy for sensors. There is a similar device used to collect shaking energy of vehicle, which works well in high frequency conditions [11]. For low frequency conditions such as marine gravity waves, particular study is required. Lancaster's project FROG and PS FROG had played a pioneer role here by their two reactionless ocean wave energy converters, along with many materials about the design and performance evaluation [1, 8, 12, 13]. Project called ISWEC from Politecnico di Torino employs gyroscopic principle to achieve the similar goal [14, 15]. Being different, the paper tries to propose another realization and emphasis on performance comparison in various periods for double oscillating and single oscillating structures.

2. Structure

For analysis convenience, stoppers are neglected, though they are indispensable in reality. Therefore, the structure analyzed consists of three major parts (Figure 1).

(1) Outer body: taking a form of vertical cylinder and working as a floater in water.

(2) Inner body: working as oscillator moving vertically within the structure.

(3) Tape spring for generator: tape spring connects outer body and inner body with an appropriate stiffness and concentrically couples a disc-type permanent-magnet coreless generator (DPMCLG) [16]. Both spring and generator rotate synchronously. The tape spring supports the inner body against gravity when the structure is at rest.

The operation principles of the structure are as follows.

(1) When excited by waves, the outer body moves vertically.

(2) Because of inertia, the inner body lags behind the outer body. Hence there is relative motion.

(3) The relative motion revolves the tape spring, and the energy is absorbed by the coaxial generator.

Advantages of the structure are as follows.

(1) The motion of generator and oscillator is within the chamber, so a totally sealed structure is available.

(2) The tape spring is characterized by long stroke and small elastic coefficient, which enables inner body to work in a state of near weightlessness maximizing the absorption of vibration energy [17].

(3) Compared with most other types of PM generators, DPMCLG suffers little cogging force and is suitable for small wave.

(4) The tape spring with long stroke and small elastic coefficient finds mature application in lifting gear and DPMCLG in wind power generation.

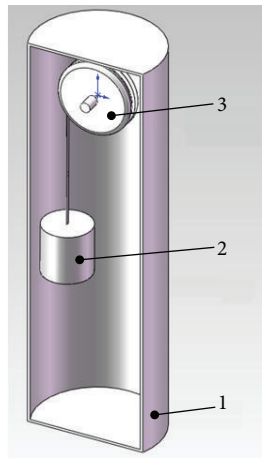

Figure 1: Double oscillating structure.

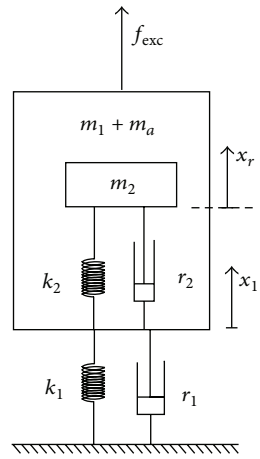

Figure 2: Simplified model of double oscillating structure.

3. Assumptions and Physical Model

For analysis convenience, the following assumptions are made. (1) There is full space for the inner body to move. (2) Friction between mechanical components is small enough. The system can be simplified to a double oscillating model as shown in Figure 2.

4. Mathematical Model

4.1. Differential Equations. The resultant force acting upon the inner body is a summation of spring force, gravity, friction, and electromagnetic force, and that upon outer body is a summation of buoyancy, gravity, spring force, friction, and generator electromagnetic force. According to Newton's second law, the dynamic differential equations for the oscillating model can be written as

$$\begin{aligned} m_t \frac{d^2x_1}{dt^2} + r_1 \frac{dx_1}{dt} + k_1 x_1 + m_2 \frac{d^2x_r}{dt^2} &= f_{exc}, \\ m_2 \frac{d^2x_1}{dt^2} + m_2 \frac{d^2x_r}{dt^2} + r_2 \frac{dx_r}{dt} + k_2 x_r &= 0, \end{aligned} \tag{1}$$

where $m_t = (m_1 + m_2 + m_a)$, and f_{exc} is the wave excitation force. In reality, hydrodynamic parameters r_1 and m_a depend on wave frequency.

4.2. Equivalent Scheme. The dynamic equations of double oscillating system can be expressed in circuit scheme just as Figure 3 demonstrates. To make a comparison, the equivalent scheme for single oscillating structure is shown in Figure 4 [18]. It is clear that both structures have a topology like a band-pass circuit. Compared with single oscillating structure, the double oscillating structure is more complicated; hence there is a wider range for regulation.

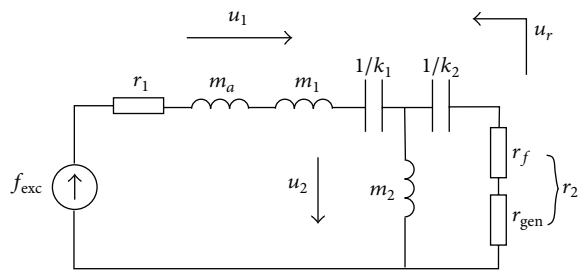

Figure 3: Equivalent scheme of dynamic equations for double oscillating system.

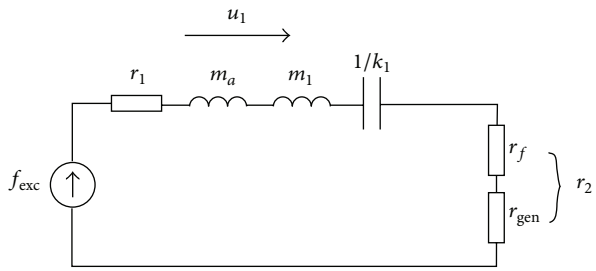

Figure 4: Equivalent circuit of dynamic equations for single oscillating system.

4.3. Phase Equations and Solution. For a monochromatic wave, water surface levitation can be expressed as follows:

$$\eta = A_w \sin(\omega t). \tag{2}$$

When the size of the structure is small enough compared with the wavelength, the wave excitation force f_{exc} can be approximately expressed according to linear wave theory as follows:

$$f_{\text{exc}} \approx k_1 \eta = \rho g \pi a^2 A_w \sin(\omega t). \tag{3}$$

The excitation force can be transformed into phase form by adding hat to variables; that is,

$$\widehat{F}_1 = k_1 \widehat{\eta}. \tag{4}$$

Based on research from [18–20], the heave hydrodynamic damping and added mass for vertical cylinder can be expressed as $r_1 = 2\pi\omega\rho a^3 \varepsilon_{33}/3$, $m_a = 2\pi\rho a^3 \mu_{33}/3$, where ε_{33} and μ_{33} are corresponding nondimensionalised coefficients, and if concentrating only on difference with single oscillating structure, constant values would bring benefits, so pick values with $\varepsilon_{33} = 0.08$, $\mu_{33} = 1.125$ for both structures. Thus, like the excitation force, the equations for system can be written as phase form accordingly:

$$\left(i\omega \begin{bmatrix} m_t & m_2 \\ m_2 & m_2 \end{bmatrix} + \begin{bmatrix} r_1 & 0 \\ 0 & r_2 \end{bmatrix} + \frac{1}{i\omega} \begin{bmatrix} k_1 & 0 \\ 0 & k_2 \end{bmatrix}\right) \begin{Bmatrix} \widehat{u}_1 \\ \widehat{u}_r \end{Bmatrix} = \begin{Bmatrix} \widehat{F}_1 \\ 0 \end{Bmatrix}, \tag{5}$$

Table 1: Parameters of double oscillating model.

Parameter	Value	Parameter	Value
k_1 (N/m)	1963.5	k_2 (N/s)	1400
r_1 (kg/s)	8.22	r_2 (kg/s)	500
m_1 (kg)	10	m_2 (kg)	150
m_a (kg)	36.82		

Table 2: Parameters of single oscillating model.

Parameter	Value	Parameter	Value
k_1 (N/m)	1963.5		
r_1 (kg/s)	8.22	r_2 (kg/s)	500
m_1 (kg)	160		
m_a (kg)	36.82		

where i = SQRT(−1). The solution for the linear phase equations can be easily deduced as follows:

$$\widehat{u}_1 = \frac{\widehat{\eta} k_1 \left(i\omega m_2 - (ik_2/\omega) + r_2\right)}{\omega^2 m_2^2 + \left[i\omega m_t - (ik_1/\omega) + r_1\right]\left(i\omega m_2 - (ik_2/\omega) + r_2\right)},$$
$$\widehat{u}_r = \frac{-i\omega\widehat{\eta} k_1 m_2}{\omega^2 m_2^2 + \left[i\omega m_t - (\mathrm{i}k_1/\omega) + r_1\right]\left(i\omega m_2 - (ik_2/\omega) + r_2\right)}. \tag{6}$$

For comparison, the phase solution for single oscillating structure is as follows:

$$\widehat{u}_1 = \frac{k_1 \widehat{\eta}}{i\omega\left(m_1 + m_a\right) - (ik_1/\omega) + r_1 + r_2}. \tag{7}$$

The corresponding displacement and power can be calculated as follows:

$$\widehat{x}_1 = \frac{\widehat{u}_1}{i\omega}, \qquad \widehat{x}_r = \frac{\widehat{u}_r}{i\omega},$$
$$P_{\text{gen}} = \frac{1}{2}\left|\widehat{u}_r\right|^2 r_{\text{gen}}. \tag{8}$$

5. Computation and Discussion

5.1. Model Parameters. The system is designed under the condition that the resonating period $T_w = 2$ s, wave height $H_w = 0.4$ m, generator power $P_{\text{gen}} = 150$ W, and damping $r_2 = 500$ kg/s. The radius of the structure a is equal to 0.25 m. The parameters for double and single oscillating structure are listed in Tables 1 and 2, respectively. The k_2 and m_2 are absent in Table 2, and the m_1 equals the total mass of Table 1.

5.2. Performance with Different Wave Period. The power absorption, max. velocity amplitude, and max. displacement amplitude of two structures under different wave periods are compared by computation according to expressions (8~12). The curves are in Figures 5, 6, and 7. First, the max. absorption power is about 150 W which is close to the designation for the single oscillating structure, while the double oscillating structure has a value of 220 W, which is about 1.5 times of the

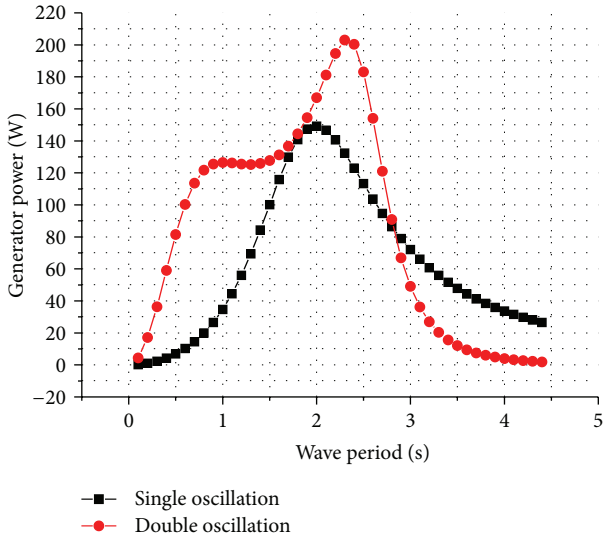

Figure 5: Generator power-wave period for two systems.

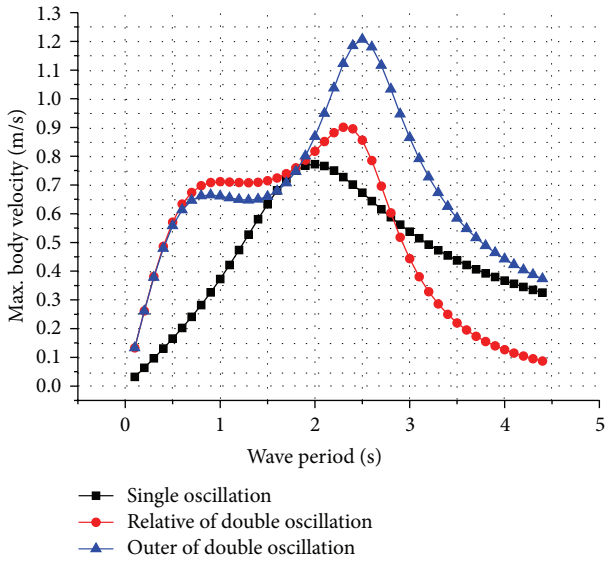

Figure 6: Speed amplitude-wave period for two systems.

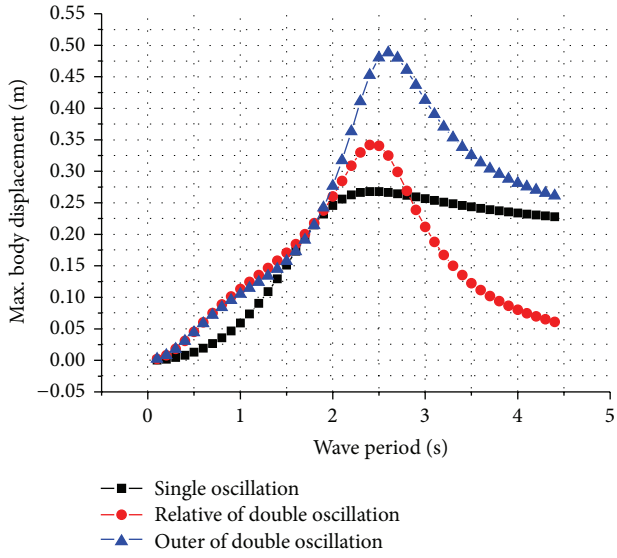

Figure 7: Displacement amplitude-wave period for two systems.

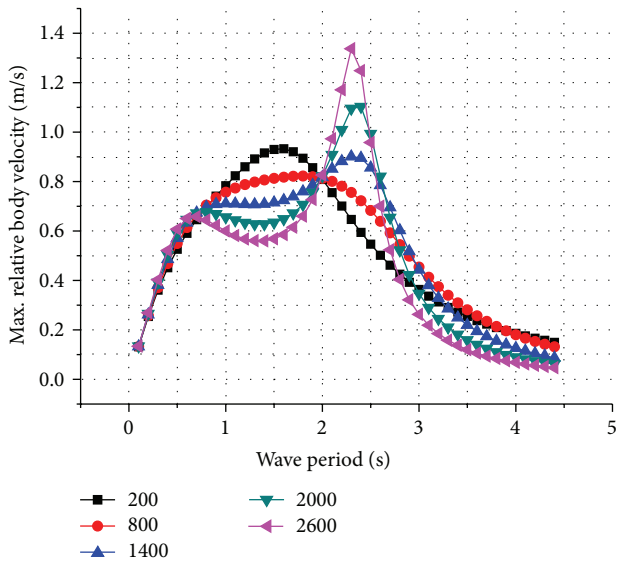

Figure 8: Relative speed amplitude-wave period for double oscillating system with different k_2.

designation. Secondly, the period when max. power absorption happens is about 2 s for single oscillating structure, with a value of 2.4 s for double oscillating structure. Thirdly, suppose that there is a goal of contributing power of at least 100 W; the structure with single oscillation can only work in a range from 1.5 s to 2.6 s, while the double oscillating system can work in a wider range that is from 0.6 s to 2.7 s. All of these illustrate that the double oscillating structure can be smaller, lighter, and easier for control than single oscillating system with the same designing wave period scope and power demand. Finally, the response of the double oscillating system decays more quickly than that of the single one, which is useful in the protection of generator under extreme weather conditions because large wave period means high wave in general.

5.3. Performance with Different k_2. The special performance of double oscillating system derives from the parameter k_2. The calculation results concerning performance of the double oscillating system with different value of k_2 are shown in Figures 8 and 9. It can be seen that the double oscillating system keeps its band-pass feature well. The period for max. response increases from 1.5 s to 2.3 s as k_2 increases from 200 N/m to 2600 N/m. When k_2 is larger than 2000 N/m, there is a saddle point at 1.5 s, and the max. response at 2.3 s increases rapidly. As k_2 increases, the scope of response narrows and max. value increases sharply.

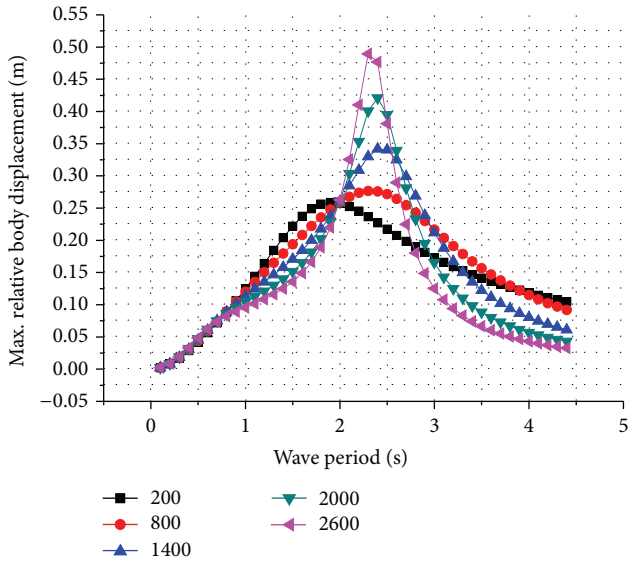

FIGURE 9: Relative displacement amplitude-wave period for double oscillating system with different k_2.

6. Conclusions

The double oscillating structure is proposed to solve the main problems of the single oscillating structure. The structure is modeled and analyzed by mathematical equations. According to the case given in the paper, the double oscillating structure has shown an advantage in wider wave range and rougher wave conditions. Furthermore, the double oscillating structure may reduce sealing and installation cost comparing with the single oscillating structure. However, to bring the structure into practice, there are many problems remaining to be solved. Firstly, the structure needs a more accurate model to explore its behavior more exactly by taking into account the nonlinear parameters that were simplified for comparison convenience here. Moreover, the design of the structure needs proper tape spring and generator, and the mechanical support needs further research.

Nomenclature

x_1: Displacement of outer body from the equilibrium (m)
x_r: Relative displacement of inner body from equilibrium to outer body (m)
u_1: Velocity of outer body (m/s)
u_2: Velocity of inner body (m/s)
u_r: Relative velocity of inner body to outer body (m/s)
m_1: Mass about parts moving with outer body (kg)
m_2: A mass summation of components moving with inner body, including inner body and equivalent mass from control method for generator (kg)
m_a: Added mass for system in the water (kg)
r_1: Hydrodynamic damping (kg/s)
r_f: Mechanical damping (kg/s)
r_{gen}: Damping from generator, which indicates the power absorption ability (kg/s)
r_2: An equivalent resistance that indicates the power absorption of structure, including damping from mechanical action and generator (kg/s)
k_1: Stiffness in the water of outer body (kg/s^2), for vertical cylinder $k_1 = \rho g \pi a^2$
k_2: Total stiffness between inner body and outer body, including stiffness of spring and equivalent stiffness of generator (kg/s^2)
a: Outer radius of the cylinder (m)
ρ: Density of water (kg/m^3)
ω: Angle frequency of wave (rad/s)
ε_{33}: Nondimensionalised hydrodynamic heave coefficient of damping
μ_{33}: Nondimensionalised hydrodynamic heave coefficient of added mass
g: Acceleration of gravity (m/s^2)
η: Water surface levitation for wave (m)
f_{exc}: Wave excitation force (N)
A_w: Amplitude of wave levitation that is half of the height from though to crest (m)
t: Time variable (s)
P_{gen}: Power generated by generator (W).

References

[1] A. F. D. O. Falcão, "Wave energy utilization: a review of the technologies," *Renewable and Sustainable Energy Reviews*, vol. 14, no. 3, pp. 899–918, 2010.

[2] U. A. Korde, "On providing a reaction for efficient wave energy absorption by floating devices," *Applied Ocean Research*, vol. 21, no. 5, pp. 235–248, 1999.

[3] M. Vantorre, R. Banasiak, and R. Verhoeven, "Modelling of hydraulic performance and wave energy extraction by a point absorber in heave," *Applied Ocean Research*, vol. 26, no. 1-2, pp. 61–72, 2004.

[4] P. Li, *Investigation on the performance of the oscillating buoy wave power device [M.S. thesis]*, Dialian University of Technology, 2005.

[5] M. Yang, *Design of float-type wave energy device and research of power characteristics [M.S. thesis]*, College of Shipbuilding Engineering, Harbin Engineering University, 2010.

[6] F. Zabihian and A. S. Fung, "Review of marine renewable energies: case study of Iran," *Renewable and Sustainable Energy Reviews*, vol. 15, no. 5, pp. 2461–2474, 2011.

[7] G. Nunes, D. Valério, P. Beirão, J. S. da Costa, and D. ValÃĺrio, "Modelling and control of a wave energy converter," *Renewable Energy*, vol. 36, pp. 1913–1921, 2011.

[8] I. López, J. Andreu, S. Ceballos et al., "Review of wave energy technologies and the necessary power-equipment," *Renewable and Sustainable Energy Reviews*, vol. 27, pp. 413–434, 2013.

[9] L. Haodong and P. Pillay, "A linear generator powered from bridge vibrations for wireless sensors," in *Proceedings of the 2007 IEEE Industry Applications Conference 42nd Annual Meeting (IAS '07)*, pp. 523–529, September 2007.

[10] X. Tang and L. Zuo, "Simulation and experiment validation of simultaneous vibration control and energy harvesting from

buildings using tuned mass dampers," in *Proceedings of the 2011 American Control Conference (ACC '11)*, pp. 3134–3139, July 2011.

[11] Z. Yuanyuan, *Research on some key technique problems of the equipment for harvesting energy from car-vibration [M.S. thesis]*, Hebei University of Technology, 2009.

[12] R. H. Bracewell, *FROG and PS FROG: a study of two reactionless ocean wave energy converters [Ph.D. thesis]*, Lancaster University, 1990.

[13] A. P. McCabe, A. Bradshaw, J. A. C. Meadowcroft, and G. Aggidis, "Developments in the design of the PS Frog Mk 5 wave energy converter," *Renewable Energy*, vol. 31, no. 2, pp. 141–151, 2006.

[14] G. Bracco, E. Giorcelli, and G. Mattiazzo, "ISWEC: a gyroscopic mechanism for wave power exploitation," *Mechanism and Machine Theory*, vol. 46, no. 10, pp. 1411–1424, 2011.

[15] G. Bracco, E. Giorcelli, G. Mattiazzo, and M. Pastorelli, "Design of a gyroscopic wave energy system," in *Proceedings of the 37th Annual Conference of the IEEE Industrial Electronics Society (IECON '11)*, pp. 3134–3139, November 2011.

[16] X. Wang, J. Yan, and G. Wang, "Study of disk type corelss permanent magnet synchronous generator applied in ocean current energy system," in *Proceedings of the 15th International Conference on Electrical Machines and Systems (ICEMS '12)*, pp. 1–9, October 2012.

[17] J. Guo and Y. Jing, "Design of a spring device with approximately constant elasticity," *Journal of Tianjin Iinstitute of Technology*, vol. 16, pp. 46–48.

[18] J. Falnes, *Ocean Waves and Oscillating Systems: Linear Interactions Including Wave-Energy Extraction*, Cambridge University Press, Cambridge, UK, 2002.

[19] D. R. F. Harleman, W. C. Nolan, and V. C. Honsinger, "Dynamic analysis of offshore structures," in *Proceedings of the International Conference on Coastal Engineering*, 1962.

[20] Z. Zhili, *Water Wave Thories and Their Applications*, Peking Science Press, 2005.

Hindawi Publishing Corporation
Advances in Mechanical Engineering
Volume 2013, Article ID 978140, 8 pages
http://dx.doi.org/10.1155/2013/978140

Research Article

Efficiency of a Directly Driven Generator for Hydrokinetic Energy Conversion

Mårten Grabbe, Katarina Yuen, Senad Apelfröjd, and Mats Leijon

Division of Electricity, The Ångström Laboratory, The Swedish Centre for Renewable Electric Energy Conversion, Uppsala University, P.O. Box 534, 751 21 Uppsala, Sweden

Correspondence should be addressed to Mårten Grabbe; marten.grabbe@angstrom.uu.se

Received 23 May 2013; Revised 6 September 2013; Accepted 6 September 2013

Academic Editor: Fabrizio Marignetti

Copyright © 2013 Mårten Grabbe et al. This is an open access article distributed under the Creative Commons Attribution License, which permits unrestricted use, distribution, and reproduction in any medium, provided the original work is properly cited.

An experimental setup for hydrokinetic energy conversion comprising a vertical axis turbine, a directly driven permanent magnet generator, and a control system has been designed and constructed for deployment in the river Dalälven in Sweden. This paper is devoted to discussing the mechanical and electrical design of the generator used in the experimental setup. The generator housing is designed to be water tight, and it also acts as a support structure for the turbine shaft. The generator efficiency has been measured in the range of 5–16.7 rpm, showing that operation in the low velocity range up to 1.5 m/s is possible with a directly driven generator.

1. Introduction

Research activities in the area of energy conversion from freely flowing water have increased over the last couple of years, and much has been published regarding tidal currents [1–4] as a promising renewable resource. Furthermore, a handful of rather large tidal turbines have been going through initial tests recently at test sites such as EMEC (http://www.emec.org.uk/about-us/emec-history/, 2013-01-07) or at individual sites such as the 1.2 MW Seagen in Strangford Lough (http://www.marineturbines.com/, 2013-01-07). Less has been published regarding energy conversion from the freely flowing water in rivers, however, but it should be noted that Khan et al. have reviewed the technology [5, 6] and that Toniolo et al. recently have performed interesting work regarding the river resource in Alaska [7–11]. Here, the term *hydrokinetic energy conversion* is used to emphasize that any kind of water current can be of interest, be it tidal currents, rivers, or other ocean currents.

Turbines for tidal currents and turbines for rivers may in many instances have a lot in common. At the same time, however, other technical solutions might be preferable in a river setting, for instance, regarding foundation design and deployment procedure, as well as the fact that smaller turbines might be required due to the limited water depth. Some examples of turbines for hydrokinetic energy conversion in rivers include Verdant Power's turbines in East River, New York (http://verdantpower.com/, 2013-01-07) and a floating Darrieus turbine by New Energy Corporation (http://newenergycorp.ca/, 2013-01-07) deployed in Winnipeg River at Pointe du Bois, Manitoba [12].

The concept presented in this paper comprises a fixed pitch, vertical axis turbine connected to a directly driven permanent magnet generator. The generator and control system is designed to electrically start, control, and brake the turbine to exclude the use of a blade pitch mechanism and a mechanical brake. An experimental station has recently been finalized, and the concept is set to be tested in a river setting in river Dalälven at Söderfors, Sweden. This paper presents experimental results pertaining to the generator performance in the full range of operation expected at the river site. To the best of the author's knowledge, this is the first time a direct drive generator will be used in the low velocity range presented by a river. The results are important for evaluating the turbine performance in the prototype energy converter, and the mechanical design and the generator performance may be of interest for other research projects looking to utilize the hydrokinetic resource.

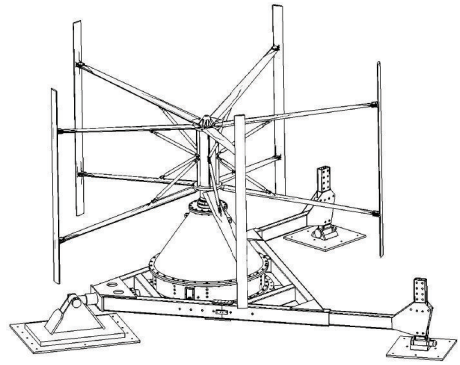

Figure 1: Overview of the whole unit with turbine and generator mounted on a tripod foundation. As a reference of scale, the turbine blades are 3.5 m long and the turbine radius is 3 m. Design by Anders Nilsson.

2. The Söderfors Project

A brief overview of the Söderfors project is included to give the context in which the generator has been designed and under what conditions it will be operated. As mentioned in [13], the experimental station at Söderfors is primarily intended for proof of concept, validation of simulation tools, and experience.

The site was chosen as it was deemed suitable from a practicable viewpoint: it is less than an hour's drive from the university, the unit can be deployed from a bridge, and close cooperation with the owner of the upstream hydropower plant will allow for control of the flow to a certain extent during experiments. The water velocity at the site is mostly in the range of up to 1.5 m/s [14], well suited for studying system performance at the comparatively low velocities presented by rivers.

As with many early prototypes, several design choices have been made with simplicity in mind. For instance, the turbine is a straight bladed Darrieus turbine with non-tapered blades, and a tripod gravity foundation (see Figure 1) is used to allow for deployment with no underwater construction work. A sea cable connects the generator to a measuring station on shore, housing the control system and electrical load as the experimental station is not grid connected initially.

3. Theory

The amount of kinetic energy extracted by a turbine from a flowing fluid can be expressed in terms of its power coefficient C_P as

$$P_t = \frac{1}{2} C_P \rho A v^3, \tag{1}$$

where v is the water velocity and A is the turbine cross sectional area. The value of C_P depends on the relative velocity between the turbine blades and the water, usually called tip speed ratio λ and defined as

$$\lambda = \frac{\omega r}{v}, \tag{2}$$

where ω is the angular velocity of the turbine and r is the turbine radius. For a certain tip speed ratio, λ_{opt}, the turbine will give the highest power coefficient, $C_P^{\max}$. It is preferable to operate the turbine near its optimal tip speed ratio from the cut in velocity up to the nominal velocity. In order to maintain maximum power capture while the water velocity changes, the generator and turbine rotational speed should be controlled so that

$$\omega = \frac{v \lambda_{\text{opt}}}{r}. \tag{3}$$

The mechanical power on the generator shaft will thus be proportional to the rotational speed cubed, or ω^3, during fixed tip speed operation according to (1). The mechanical system can be described as

$$\frac{d}{dt}\omega = \frac{P_t - P_g - P_{\text{floss}} - P_{\text{eloss}}}{J\omega}, \tag{4}$$

where P_g is the electrical power output of the generator, P_{floss} is the frictional loss in bearings and sealing, P_{eloss} is the total electrical losses in the generator, and J is the total angular inertia of turbine, shaft, and rotor. At the same time, the terminal voltage of the generator is roughly proportional to the rotational speed ω. It is thus of interest to choose the nominal current carefully, in order to allow for electrical control and braking of the turbine at higher water velocities. Knowledge of the velocity distribution is therefore an important piece in the generator design procedure.

The generator has been designed with the aid of an in-house developed design tool where the combined set of field and circuit equations are solved in the finite element environment ACE [15]. The magnetic field inside the core of the generator is assumed to be axisymmetrical and modelled in two dimensions. The displacement field is neglected and the permanent magnets are modelled using the current sheet approach [16]. Furthermore, coil end impedances are introduced in the circuit equations, the laminated stator core is modelled using a single valued magnetization curve, and a correction factor of 1.5 is used for all iron losses.

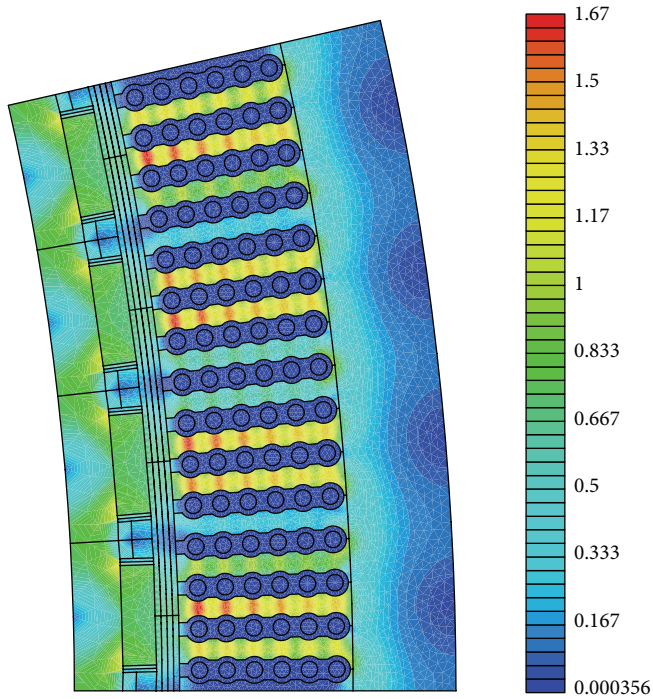

Figure 2: The simulated field distribution in a symmetrical section of the generator under nominal load conditions.

The complete generator model is described by a combined set of field and circuit equations. The magnetic vector potential inside the generator is described by

$$\sigma \frac{\partial A_z}{\partial t} + \nabla \cdot \left(\frac{1}{\mu_0 \mu r \nabla A_z} \right) = -\sigma \frac{\partial V}{\partial z}, \tag{5}$$

where σ is the conductivity, μ is the permeability, A_z is the axial component of the magnetic vector potential, and V is the applied potential.

The circuit equations are described by

$$\begin{aligned} I_a + I_b + I_c &= 0, \\ U_{ab} &= U_a + R_s I_a + L_s^{\text{end}} \frac{\partial I_a}{\partial t} - U_b - R_s I_b - L_s^{\text{end}} \frac{\partial I_b}{\partial t}, \\ U_{cb} &= U_c + R_s I_c + L_s^{\text{end}} \frac{\partial I_c}{\partial t} - U_b - R_s I_b - L_s^{\text{end}} \frac{\partial I_b}{\partial t}, \end{aligned} \tag{6}$$

where I_a, I_b, and I_c are the conductor currents in the three phases a, b, and c, respectively. U_{ab} and U_{cb} are the terminal line voltages, and U_a, U_b, and U_c are the phase voltages obtained from solving the field equation. R_s is the winding resistance, and L_{end} describes the coil end inductance. Furthermore, it should be noted that frictional losses in the bearings and windage losses are neglected in the simulation model while evaluating the efficiency due to the low rotational speed and high torque.

4. Experimental Setup

The main goal with the experimental setup is to test the system under realistic conditions in a river setting, and therefore, several design choices have been made with simplicity in mind rather than optimizing for energy production. The depth at the site is around 7 m, and in order to leave ample room for the foundation and generator, as well as avoiding floating debris and ice near the surface, it was decided to use turbine blades of 3.5 m in height. The simple NACA0021 chord was used for the blades as there are measurements available, and five blades were used to limit the torque oscillations. Simulations suggest that the 21 m^2 turbine should have a C_P of 0.35 at a tip speed ratio of 3.5 (see [14] for more information), resulting in the nominal electrical power of 7.5 kW at a velocity of 1.4 m/s. The system was designed to operate the turbine at a lower tip speed ratio in the range 1.4–1.7 m/s so as to limit the power captured by the turbine. At higher velocities, the generator will be connected to a dump load to brake and stop the turbine. The highest expected velocity at the site is 2 m/s.

4.1. Generator. The electrical design of the generator is based on a laboratory prototype [17], adjusted to the turbine characteristics and the flow velocities at the site. It is essentially a cable wound permanent magnet generator rated at 7.5 kW, 128 V at unity power factor, and a nominal speed of 15 rpm. It has 112 poles and six cables per slot and is wound with a 5/4 fractional wave winding. No slot wedges are used, as the cables are put in axially in each slot rather than radially from the air gap. The nominal design values are given in Table 1, and the FE model of the generator is shown in Figure 2.

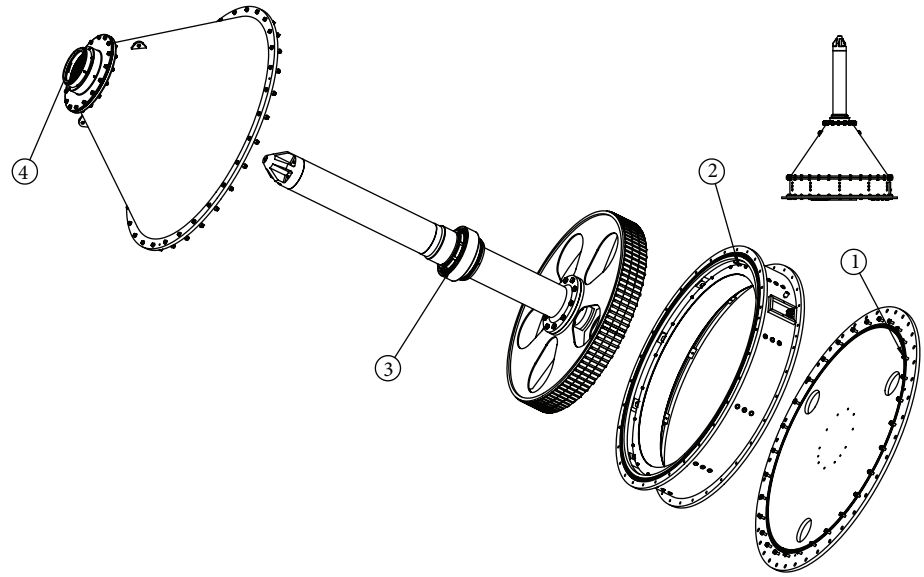

Figure 3: Overview of stator support structure and the generator housing. 1: the flat bottom flange with holes used for mounting magnets, 2: stator support, 3: rotor and shaft with bearings, and 4: lid and turbine support with sealing and bearing housing.

Table 1: Generator design data and measured values.

Parameter	Design	Experiment
Dimensions		
Axial length	197 mm	197 mm
Stator outer diameter	1800 mm	1 800 mm
Stator inner diameter	1635 mm	1 635 mm
Air gap	7 mm	6.5–7.1 mm
Number of poles	112	112
Magnet thickness	10 mm	10 mm
Magnet width	30 mm	30 mm
Nominal performance		
Speed	15 r.p.m.	15 r.p.m.
Armature voltage	128 V	109.7 V
Frequency	14 Hz	14 Hz
Apparent power	7.5 kW	7.5 kW
Power factor	1	1
B in air gap	0.69 T	0.66–0.68 T
B in tooth	1.74 T	—
Nominal torque	5.6 kNm	5.93 kNm
Efficiency	84.4%	80.5%
Load angle	10°	—

Most of the work concerned integration of the mechanical design with the turbine and the foundation, as well as sealing of the generator housing and inclusion of equipment for control and monitoring. All of the parts were designed at the university, machined at a local work shop, and assembled by hand at the university before being transported to the test site.

The housing supports both the turbine and the generator and is designed to be water tight. The stator frame is basically a thin metal ring, or steel tube, reinforced with beams and flanges (see Figure 3, item 2). Firstly, the laser cut stator sheets (M800-100A) were stacked and secured, and the stator was wound with a standard 16 mm^2 cable (RK 16 450/750 V); see Figures 4 and 5.

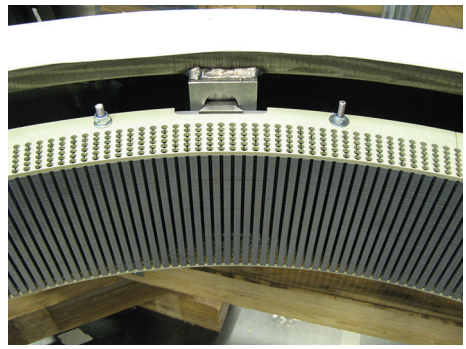

Figure 4: The stator before winding.

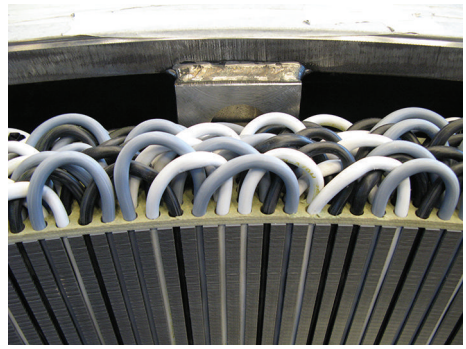

Figure 5: The stator winding with white, grey, and black cables used for the three phases.

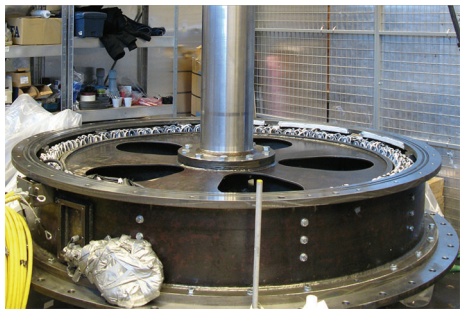

Figure 6: The un-magnetized rotor in position resting on the thrust bearing.

After winding, the stator section was fastened to the flat flanged bottom with standard O-rings for sealing. The un-magnetized rotor was then lowered into the stator, resting on a spherical roller bearing (SKF 23940 CC/W33); see Figure 6. The conically shaped lid was mounted onto the upper stator flange, and the rotor was thus secured with the toroidal roller bearing (SKF C 3056 K) in the top of the cone. The forces on the turbine bearing are thus transmitted through the conical lid and stator frame down to the foundation. The conical lid allows for just one bearing and one seal for turbine support and generator housing. The seal (Trelleborg Turcon Roto VL Seal) was, however, not used in the laboratory experiments as it is supposed to operate in water.

In order to facilitate the laboratory experiments, the generator was tilted on its side and fastened in a provisional support structure. The rotor could then be magnetized with three NdFeB magnets per pole inserted through the holes in the flat flanged bottom and into the milled grooves in the rotor. In order to drive the generator in a laboratory setting, it was connected to a 22 kW induction motor with a gearbox (gear ratio 89.89) and a 30 kW frequency inverter, allowing operation up to 16.7 rpm and 12 kNm. After testing was completed, the sealing was mounted and filled with biodegradable grease (SKF LGGB 2) before a short test run. The holes in the flat flanged bottom were then permanently sealed, and the generator was painted before being transported to Söderfors to be mounted on the foundation.

4.2. Measurement System. The control and measurement system of the Söderfors station is based on LabVIEW and a CompactRIO (http://www.ni.com/, 2013-01-07). This interface is used to control the electrical system of the Söderfors station, as described in [18], so as to operate the turbine at a designated tip speed ratio and to handle start and brake procedures. The control system also includes current and voltage measurements which are used during these laboratory experiments with the generator. Aside from the current and voltage measurements that are incorporated in the Söderfors station, the laboratory experiments have allowed the measurement of frictional losses, torque, and B-fields as described below.

Currents are measured for each generator phase and to and from the capacitor bank using HAL 100 and 200 current transducers from LEM (http://www.lem.com/, 2013-01-07). They have an accuracy of 1% and give a voltage signal proportional to the current within a specified range. Voltages from the generator and over the load have been measured after voltage division. Three line-to-line voltages and one phase-to-neutral voltage are measured.

Measurement signals are acquired using a C-series module NI9205 in the CompactRIO, and a sampling rate of 2 kHz was used. The voltage signals were calibrated using an APPA 207 True RMS meter, which gave a scale factor for each voltage division. The offset of the current transducers was set to be within ±0.018 A.

In the laboratory setup, torque on the generator shaft was measured with a DF-30 torque sensor from Lorenz Messtechnik, and the signal was transmitted to the NI 9205 module via a 2.4 GHz SG-link from MicroStrain.

Before magnetizing the rotor, retardation tests were performed. The rotational speed of the rotor was then measured using an IR-sensor (Photologic OPB715) which detected the milled grooves in the rotor. After magnetization, a handheld gaussmeter (Lakeshore Model 410) with an accuracy of ±2% of reading and ±0.1% of full scale (±2 T) was used to measure the B-field in the air gap.

5. Experiments

Frictional losses prior to magnetization were measured by accelerating the rotor manually and recording its deceleration. The retardation from over 20 rpm to standstill was recorded, capturing the expected range of operation.

The B-field in the air gap was measured both during standstill and at nominal speed.

Two sets of experiments were performed using the motor-drive system described in Section 5. In the first, the generator was operated at variable speed (2–16.7 rpm) against a purely resistive, Y-connected balanced three-phase load. Different loads were used to cover the expected range of power for fixed tip speed ratio operation of the vertical axis turbine. In the second set of experiments, the generator was operated against an uncontrolled diode rectifier bridge connected to a resistive load in parallel with a capacitor bank of 26.4 mF to more closely resemble the intended operation in Söderfors. In both cases, the resistive load was a set of 1 Ω resistors (Vishay RPS 500 series) mounted on heat sinks.

6. Results and Discussion

Three retardation tests were analysed, suggesting that the frictional torque is close to 32 Nm in the operating range. However, once in operation, the bearings will operate under much higher radial loads, likely increasing the frictional losses somewhat.

The B-field was measured at the surface of several stator teeth positioned in front of a pole. The field varied slightly, 0.66–0.68 T, measured with an accuracy of ±0.02, perhaps slightly lower than the simulated field; see Table 1. Part of the variation may be explained due to differences between individual magnets, specified to have a typical remanence of 1.22 T and a minimum remanence of 1.17 T.

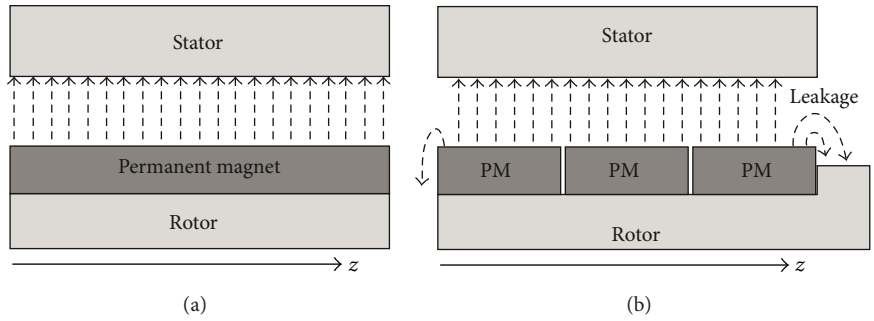

Figure 7: Artistic impression of the flux components created by the permanent magnets in a radial cross section of the machine. (a) The simulated case with no leakage flux. (b) The actual machine with significant leakage at the top of the rotor. The effective length is thus shorter than the stator stack length.

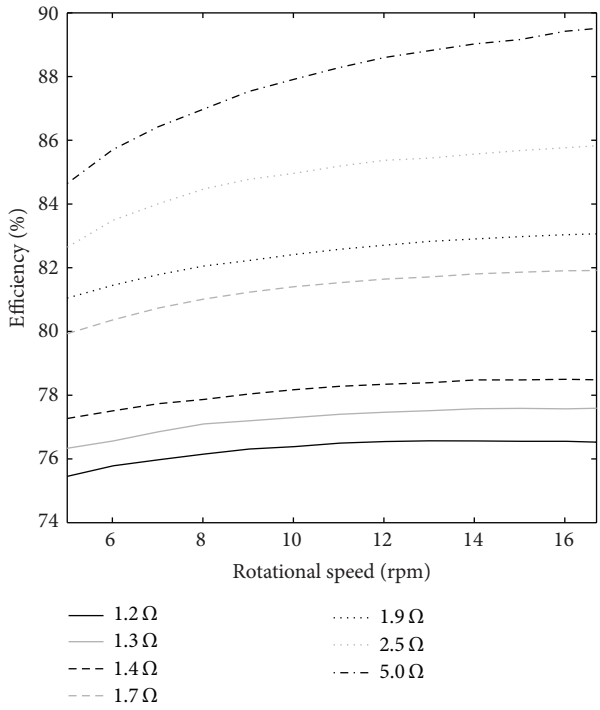

Figure 8: Measured efficiency during variable speed operation with different resistive loads.

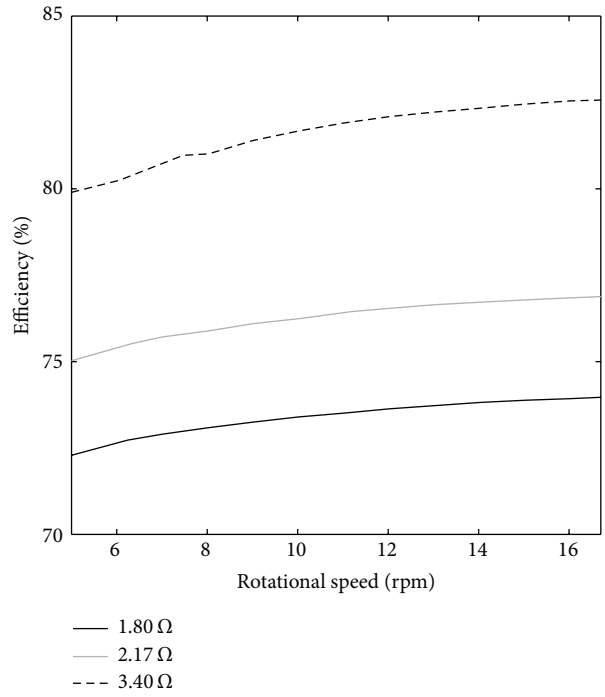

Figure 9: Measured efficiency during variable speed operation with rectifier and different resistive loads.

During magnetization, it was noticed that a part of the rotor was not machined properly, resulting in unexpected leakage flux. At that point in time, it was decided not to delay the project by dismantling the machine.

The machine worked well during operation, although at a lower voltage level due to the mentioned leakage flux, in turn resulting in higher copper losses and lower efficiency at the intended design point (7.5 kW at 15 rpm; see Table 1). Simulations predict the same no-load voltage as the experiments (138 V) with an effective length of 177 mm, 20 mm shorter than the stator stack length. This can to a large extent be explained by the leakage flux at the top of the rotor; see Figure 7 for a graphical illustration of the situation. Furthermore, the simulations do not account for leakage due to each pole being made of three separate magnets or leakage due to equal rotor and stator stack length as discussed in [19].

The measured efficiency in the range 5–16.7 rpm with a resistive load and with a rectifier is shown in Figures 8 and 9, respectively. The generator is expected to operate in the presented range during fixed tip speed ratio operation of the turbine. It will operate at higher efficiency at low speed and low load, while to handle the quickly increasing power from the turbine at higher velocities, the efficiency will drop at higher rotational speed during fixed tip speed operation as discussed in [20]. To illustrate this, the measured voltage drop at constant rotational speed (15 rpm) and increasing power is shown in Figure 10. As expected, the voltage drops quicker as the generator output is rectified.

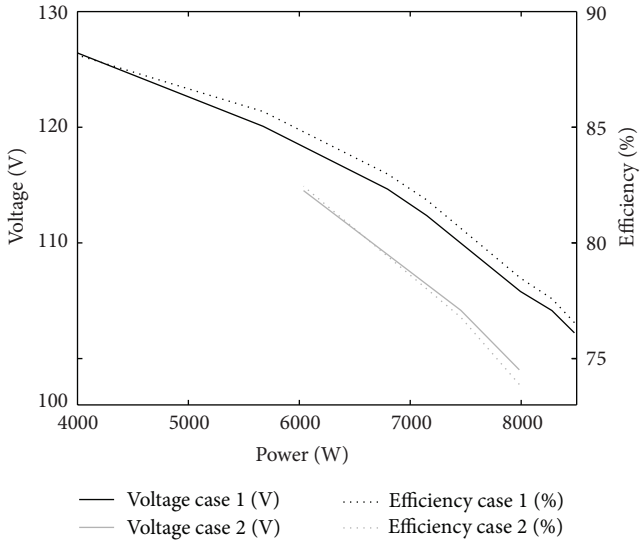

Figure 10: Comparison of the measured voltage drop and efficiency at nominal speed as a function of power output for the two cases, that is, operation with increasing resistive load (1) and with rectifier and increasing resistive load (2).

7. Conclusions

A cable wound PM generator for hydrokinetic energy conversion has been finalized. Laboratory experiments show that the generator efficiency is above 80% with a resistive load in the expected range of water velocities up to the rated velocity of 1.4 m/s. In operation with a diode rectifier and a resistive load, the efficiency remains above 75% in the same range of operation. The efficiency is lower than expected, mainly due to axial leakage flux. In conclusion, the results show that the generator is suitable for operation with a vertical axis turbine in the range of velocities expected at the site at hand.

Conflict of Interests

The authors have no direct relation, financial or otherwise, with the commercial identities mentioned in the paper that might lead to a conflict of interests for any of the authors.

Acknowledgments

The work reported was financially supported by the Swedish Centre for Renewable Electric Energy Conversion, STandUP for Energy, Ångpanneföreningen's Foundation for Research and Development (ÅForsk), the J. Gust. Richert Foundation, Vattenfall, AB, and the Swedish Research Council (Grant no. 621-2009-4946). The mechanical design of the generator performed by Anders Nilsson is deeply appreciated. Anders Karlsson, Johanna Lundqvist, Daniel Käller, and Erika Schweitz are acknowledged for assembly work.

References

[1] L. S. Blunden and A. S. Bahaj, "Tidal energy resource assessment for tidal stream generators," *Journal of Power and Energy*, vol. 221, no. 2, pp. 137–146, 2007.

[2] M. Grabbe, E. Lalander, S. Lundin, and M. Leijon, "A review of the tidal current energy resource in Norway," *Renewable and Sustainable Energy Reviews*, vol. 13, no. 8, pp. 1898–1909, 2009.

[3] A. S. Bahaj, "Generating electricity from the oceans," *Renewable and Sustainable Energy Reviews*, vol. 15, no. 7, pp. 3399–3416, 2011.

[4] F. O'Rourke, F. Boyle, and A. Reynolds, "Tidal current energy resource assessment in Ireland: current status and future update," *Renewable and Sustainable Energy Reviews*, vol. 14, no. 9, pp. 3206–3212, 2010.

[5] M. J. Khan, M. T. Iqbal, and J. E. Quaicoe, "River current energy conversion systems: progress, prospects and challenges," *Renewable and Sustainable Energy Reviews*, vol. 12, no. 8, pp. 2177–2193, 2008.

[6] M. J. Khan, G. Bhuyan, M. T. Iqbal, and J. E. Quaicoe, "Hydrokinetic energy conversion systems and assessment of horizontal and vertical axis turbines for river and tidal applications: a technology status review," *Applied Energy*, vol. 86, no. 10, pp. 1823–1835, 2009.

[7] H. Toniolo, P. Duvoy, S. V. Anlesberg, and J. Johnson, "Modelling and field measurements in support of the hydrokinetic resource assessment for the Tanana river at Nenana, Alaska," *Journal of Power and Energy*, vol. 224, no. 8, pp. 1127–1139, 2010.

[8] C. Walsh, J. Fochesatto, and H. Toniolo, "The importance of flow and turbulence characteristics for hydrokinetic energy development on the Tanana River at Nenana, Alaska," *Journal of Power and Energy*, vol. 226, no. 2, pp. 283–299, 2012.

[9] H. Toniolo, "Hydrokinetic assessment of the Kvichak River near Igiugig, Alaska, using a two-dimensional hydrodynamic model," *Energy and Power Engineering*, vol. 4, no. 6, pp. 422–431, 2012.

[10] P. Duvoy and H. Toniolo, "HYDROKAL: a module for in-stream hydrokinetic resource assessment," *Computers and Geosciences*, vol. 39, pp. 171–181, 2012.

[11] H. Toniolo, "Bed forms and sediment characteristics along the thalweg on the Tanana River near Nenana, Alaska, USA," *Natural Resources*, vol. 4, no. 1, pp. 20–30, 2013.

[12] E. Bibeau, S. Kassam, J. Woods, T. Molinski, and C. Bear, "Operating a 5-kW grid-connected hydrokinetic turbine in a river in cold climates," *Journal of Ocean Technology*, vol. 4, no. 4, pp. 71–82, 2009.

[13] K. Yuen, S. Lundin, M. Grabbe, E. Lalander, A. Goude, and M. Leijon, "The Söderfors project: construction of an experimental hydrokinetic power station," in *Proceedings of the 9th European Wave and Tidal Energy Conference (EWTEC '11)*, pp. 1–5, Southampton, UK, September 2011.

[14] M. Grabbe, K. Yuen, A. Goude, E. Lalander, and M. Leijon, "Design of an experimental setup for hydro-kinetic energy conversion," *International Journal on Hydropower and Dams*, vol. 16, no. 5, pp. 112–116, 2009.

[15] *ACE User Manual, Modified Version 3.1, ABB Common Platform for Field Analysis and Simulations*, ABB Corporate Research Centre, Västerås, Sweden, 2001.

[16] R. Gupta, T. Yoshino, and Y. Saito, "Finite element solution of permanent magnetic field," *IEEE Transactions on Magnetics*, vol. 26, no. 2, pp. 383–386, 1990.

[17] K. Thomas, M. Grabbe, K. Yuen, and M. Leijon, "A low-speed generator for energy conversion from marine currents—experimental validation of simulations," *Journal of Power and Energy*, vol. 222, no. 4, pp. 381–388, 2008.

[18] K. Yuen, *System perspectives on hydro-kinetic energy conversion [Ph.D. thesis]*, Uppsala University, Uppsala, Sweden, 2012.

[19] J. Pyrhönen, V. Ruuskanen, J. Nerg, J. Puranen, and H. Jussila, "Permanent-magnet length effects in AC machines," *IEEE Transactions on Magnetics*, vol. 46, no. 10, pp. 3783–3789, 2010.

[20] K. Yuen, K. Thomas, M. Grabbe et al., "Matching a permanent magnet synchronous generator to a fixed pitch vertical axis turbine for marine current energy conversion," *IEEE Journal of Oceanic Engineering*, vol. 34, no. 1, pp. 24–31, 2009.

Hindawi Publishing Corporation
Advances in Mechanical Engineering
Volume 2013, Article ID 835051, 11 pages
http://dx.doi.org/10.1155/2013/835051

Research Article

Bidirectional Power Performance of a Tidal Unit with Unilateral and Double Guide Vanes

Chunxia Yang,[1] Yuan Zheng,[2] Daqing Zhou,[3] Xinfeng Ge,[1] and Lingyu Li[3]

[1] *College of Water Conservancy and Hydropower Engineering, Hohai University, Nanjing 210098, China*
[2] *National Engineering Research Center of Water Resources Efficient Utilization and Engineering Safety, Nanjing 210098, China*
[3] *College of Energy and Electrical Engineering, Hohai University, Nanjing 210098, China*

Correspondence should be addressed to Chunxia Yang; yangchunxia@hhu.edu.cn

Received 16 June 2013; Revised 22 August 2013; Accepted 29 August 2013

Academic Editor: Fabrizio Marignetti

Copyright © 2013 Chunxia Yang et al. This is an open access article distributed under the Creative Commons Attribution License, which permits unrestricted use, distribution, and reproduction in any medium, provided the original work is properly cited.

To improve the bidirectional power performance of a tidal unit, two designs were investigated. The use of unilateral or double guide vanes in a tubular tidal unit influences the performance of the hydraulic unit. Based on the N-S equations and the RNG k-ε turbulence model, the SIMPLEC algorithm was used for 3D steady-state numerical simulation of the entire turbine flow passage with unilateral and double guide vanes. The internal flow condition under positive and reverse power generation conditions was also analyzed. At the same time, the turbine, with a runner 1.6 m in diameter, was scaled down to 0.35 m diameter for model tests. The model tests were based on a multifunction hydromechanical test bench at Hohai University. The water head, discharge, and torque of the tubular turbine were, respectively, tested using a pressure difference sensor, electromagnetic flow meter, and torque meter under different guide-vane openings. The results show that turbine efficiency in the model test is slightly lower than that predicted by numerical simulation under the same conditions. However, the difference is not large. With double side guide vanes, although the efficiency of positive power generation decreased, the efficiency of reverse power generation is greatly improved.

1. Introduction

Acknowledging the looming energy crisis and global climate warming, more and more countries around the world start to invest much time and money on the clean and renewable energy [1–3]. Oceans cover approximately 71% of Earth's surface and hold a large amount of energy more than 2×10^3 TW [4–6], which is the largest untapped renewable energy resource on the planet. The development and utilization of the usable capacity, 800 million kilowatts, would provide one-fifth the capacity of all the hydropower stations which can be developed. Therefore, the development potential of tidal power is tremendous. As renewable energy, tidal power is clean and generates no pollution. Compared with conventional hydropower stations, tidal power causes no flood losses or soil erosion, as hydroelectric power does. Construction of a tidal power station does not require immigrant workers or occupy much land. The development of tidal power shows obvious advantages, combined with comprehensive utilization projects such as enclosing tideland, aquatic breeding, and marine chemical production. At present, countries with rich tidal energy resources perform almost all the research into their development and use, including Cook's Cove in Alaska (United States), Bay of Fundy (Canada), Severn River (United Kingdom), Inchon Harbor (Korea), and others.

The tubular turbine is one of the most economical and appropriate turbine types to develop a water resource with low head, such as the tidal resource, because of its advantages of large discharge, high speed, high efficiency, wide area of high efficiency, compact structure, and simple arrangement. In the head range of $H > 4$ m the tubular or bulb turbines are used as commercially based type. Even in the range of about $H > 1.5$–2 m, the same type of turbine is applied as the extension [7]. The tubular turbine developed by Wang Zhengwei of Tsinghua University was the bulb tubular type installed in the Jiang Xia tidal power station [8, 9]. Shuhong et al. [10] modified the runner of the tubular turbine of FuJian DaGan water power station. Amelioration of the turbine was taken from the point of increasing the discharge, which increased the output of the power station.

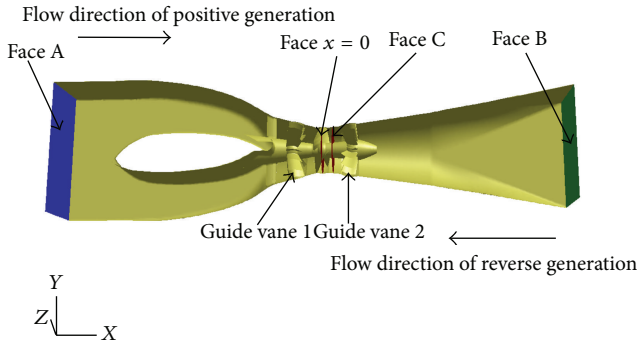

FIGURE 1: Schematic diagram of the entire flow passage of a pit turbine with double guide vanes.

Li et al. [11] used the boundary vorticity dynamics (BVD) method to optimize the runner blade shape of a tubular turbine. The distribution of the boundary vorticity flux (BVF) [12, 13] on the runner blade surfaces was then analyzed to find where the flow behavior was defective. Compared with the bulb tubular turbine, the pit turbine shows advantages such as simple structure, convenient maintenance, and less investment. Therefore, research into new bidirectional tidal unit-pit turbines with low head, large discharge, and high efficiency is of great significance.

This paper describes the development of a new bidirectional pit turbine installed in a tidal power station with low head and large discharge. The required output is 150 kW per unit under a head of 2.5 m. The main working parameters of the prototype turbine are runner diameter 1.6 m, 3 runner blades, 15 guide-vane blades, rated head 2.5 m, highest head 3.65 m, lowest head 2.0 m, average head 2.5 m, and design flow rate 8.0 m^3/s.

The flow field was calculated by CFD theory [14–16] to analyze the influence on turbine performance of unilateral and double guide vanes. Using a 1 : 8 ratio, the prototype turbine was scaled down to build a model turbine for model tests. The head, discharge, and torque of the tubular turbine were tested under different guide-vane openings. Then the efficiency and output of the turbine were calculated. The results of the model tests were compared with those from numerical simulation.

2. Numerical Simulation

2.1. Geometric Model. Figure 1 shows a schematic diagram of the entire flow passage of the pit turbine with low head, large discharge, and double guide vanes. Guide vanes 1 and 2 are located on either side of the runner. Guide vane 2 was fully open in the positive power condition, and the opening of guide vane 1 was controlled to regulate the flow through the turbine. Face A was the inlet, and face B was the outlet. In the reverse power condition, guide vane 1 was fully open, and the opening of guide vane 2 was controlled to regulate the flow through the turbine. Face B was the inlet, and face A was the outlet. The calculation region for numerical simulation was the entire flow passage of the turbine, as shown in Figure 1.

2.2. Turbulence Model. Assuming three-dimensional viscous flow through the turbine, the continuity equation and the Navier-Stokes [17–19] equations were used for numerical simulation as follows:

$$\frac{\partial U_i}{\partial x_i} = 0,$$

$$\frac{\partial \left(U_i U_j\right)}{\partial x_j} = -\frac{1}{\rho}\frac{\partial P}{\partial x_i} + \frac{\partial}{\partial x_j}\left[\nu\left(\frac{\partial U_i}{\partial x_j} + \frac{\partial U_j}{\partial x_i}\right)\right] - \frac{\partial \left(\overline{u_i' u_j'}\right)}{\partial x_j}, \tag{1}$$

where U, p, ν, and ρ are velocity, pressure, kinematic viscosity, and density, respectively. Numerical predictions were carried out using a RNG k-ε model for turbulence [20–22]. The simulation type was steady state.

Turbulent kinetic energy equation is:

$$\rho\frac{Dk}{dt} = \frac{\partial}{\partial x_j}\left[\left(\mu + \frac{\mu_t}{\sigma_k}\right)\frac{\partial k}{\partial x_j}\right] + P_k - \rho\varepsilon. \tag{2}$$

Dissipation equation is:

$$\rho\frac{D\varepsilon}{dt} = \frac{\partial}{\partial x_j}\left[\left(\mu + \frac{\mu_t}{\sigma_\varepsilon}\right)\frac{\partial \varepsilon}{\partial x_j}\right] + \frac{\varepsilon}{k}C_{\varepsilon 1}P_k - C_{\varepsilon 2}^*\rho\frac{\varepsilon^2}{k}. \tag{3}$$

Eddy viscosity coefficient is:

$$\mu_t = C_\mu \rho \frac{k^2}{\varepsilon}, \tag{4}$$

where P_k is the pressure generated caused by velocity gradient as follows:

$$P_k = -\rho\overline{u_i' u_j'}\frac{\partial \overline{U}_i}{\partial x_j}. \tag{5}$$

After modeling for incompressible turbulent flow we have:

$$P_k = \mu_t\left(\frac{\partial \overline{U}_i}{\partial x_j} + \frac{\partial \overline{U}_j}{\partial x_i}\right)\frac{\partial \overline{U}_i}{\partial x_j}. \tag{6}$$

The main difference between RNG k-ε model and standard k-ε model is the correction of $C_{\varepsilon 2}$ of dissipation equation as follows:

$$C_{\varepsilon 2}^* = C_{\varepsilon 2} + \frac{C_\mu \rho \eta^3 \left(1 - \left(\eta/\eta_0\right)\right)}{1 + \beta\eta^3}, \tag{7}$$

where

$$\eta = S\frac{k}{\varepsilon}, \qquad \eta_0 = 4.38, \qquad \beta = 0.012,$$
$$S = \sqrt{\left(\frac{\partial \overline{U}_i}{\partial x_j} + \frac{\partial \overline{U}_j}{\partial x_i}\right)\frac{\partial \overline{U}_i}{\partial x_j}}. \tag{8}$$

Empirical constant values of the above formula are $\sigma_k = 0.72$, $\sigma_e = 0.75$, $C_{\varepsilon 1} = 1.42$, $C_{\varepsilon 2} = 1.68$, and $C_{\mu 1} = 0.0845$.

The RNG k-ε turbulence model can obtain a more accurate description of turbulent transfer relationships with

Table 1: Elements' number of three grids scales.

Scales	Elements				Total
	Inlet passage	Guide vane	Runner part	Outlet passage	
Scale 1	690965	142049	837636	711479	2382129
Scale 2	550673	120997	514561	602503	1788734
Scale 3	475762	80525	356926	448109	1361322

Reynolds number or vortex scale changes. Such a model can better deal with the low Reynolds-number zone near the wall.

2.3. Algorithm and Boundary Conditions. The calculation region contains the inlet passage, the guide vane parts, the runner part, and the outlet passage, in which runner is rotating domain and others are stationary domains. In this study, three-dimensional discretization was used with the finite volume method (FVM) provided by the FLUENT6.3 software. The finite volume method argued by some scientists to be the preferred numerical approach in CFD involves complex geometries [23]. For the computational domain, unstructured 3D tetrahedral meshing was employed, due to its flexibility when solving complex geometries. In order to accurately simulate the flow in a turbine passage, further mesh refinement around the blades' edges was required.

Grid-independency studies were done to prove that results do not change any further with different sizes of grids. Three sizes of grids were used for calculation as shown in Table 1. The smaller the grid size is, the larger the number of grid is. Figures 2(a), 2(b), and 2(c) show the velocity contours of face $x = 0$ with three different grid scales. It can be seen that velocities were almost the same at a physical location $x = 0$ as predicted by 3 different grids. The grid-independency was verified. The grid scale 2 was chosen here. Typical CPU time required to reach the steady state for the above grid system scale 2 is about 3 hours on a 4 GB RAM, 1.6 GHz machine.

The numerical calculations used the segregated method with the SIMPLEC [24–26] pressure-velocity coupling algorithm. The velocity correction is entirely due to the pressure differential item of SIMPLE method. The corrected SIMPLEC algorithm shows better accuracy.

A second-order upwind [27, 28] scheme for momentum and a second-order scheme for pressure were used. For the interface unknowns, first-order upwind scheme takes values of upstream node, meaning that the ϕ of interface is considered equal to the ϕ value of a node upstream because of convection. This discrete scheme takes into account the impact of the flow direction. From the physical sense, always having a reasonable solution under any conditions will not cause oscillation solution. The discrete scheme is not limited by Pe $<$ 2, long been widely used. A single second-order upwind equation contains not only unknown of neighbouring nodes, but also includes the unknown of other nodes next to the neighbouring nodes. Discrete equations are no longer the original tridiagonal equations. Second-order upwind scheme can be seen as a first-order upwind scheme, based on the consideration of the physical distribution curve between

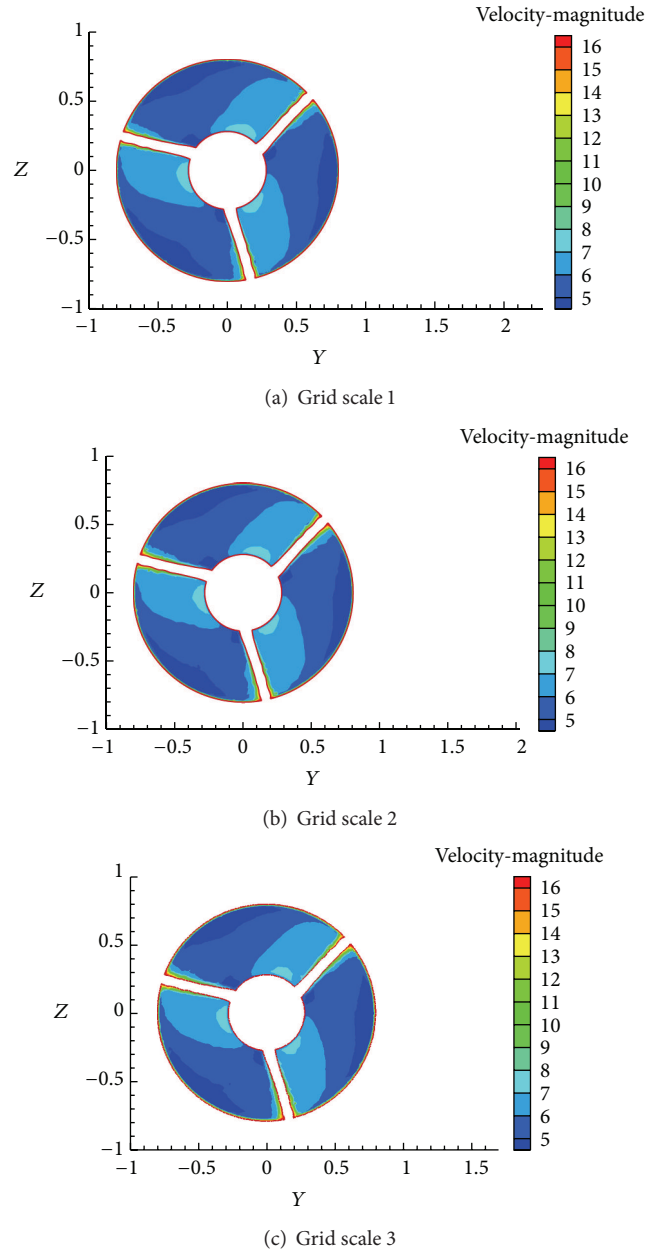

(a) Grid scale 1

(b) Grid scale 2

(c) Grid scale 3

Figure 2: Velocity contours of face $x = 0$.

nodes curvature effects. In the second-order upwind scheme, in fact, just the convection term uses a second-order upwind format, while the diffusion term still uses central difference scheme. Second-order upwind scheme shows second-order accuracy. When the flow is aligned with the grid the first-order upwind discretization may be acceptable. For triangular and tetrahedral grids, since the flow is never aligned with the grid, generally more accurate results will be obtained by using the second-order discretization.

The relaxation factor was reduced for the calculation process. The relaxation factors were pressure 0.2, momentum 0.5, and turbulent viscosity 0.8. Other relaxation factors keep unchanged.

On the inlet boundary, the total pressure was specified according to the averaged water head.

Consider

$$P_o = P_s + 0.5\rho V^2, \tag{9}$$

in which P_o is the total pressure, P_s is the static pressure, ρ is the density, and V is the averaged velocity of the turbulent flow.

For turbulent flow, based on the empirical formulae,

$$k = 0.003V^2,$$
$$\varepsilon = \frac{C_\mu k^{1.5}}{0.5D} \tag{10}$$

hold in which D is the inlet hydraulic diameter.

Assuming that the flow field was fully developed at the outlet of calculation domain, there is no backflow on the outlet boundary. The boundary flow parameters do not influence the upstream. The outlet velocity was obtained according to continuous conditions. Turbulent kinetic energy and dissipation rate were obtained by the node's linear extrapolation as

$$(\text{grad}\,\varphi)\cdot n = 0, \quad (\varphi = k, \varepsilon), \tag{11}$$

in which n is the tangential direction of the main streamline on the outlet boundary.

The average static pressure was specified on the outlet boundary, assuming it to be zero. The nonslip wall boundary condition was applied, and standard wall functions for the near-wall region. If the wall was rotating then the circumferential velocity was considered to be the boundary velocity [29, 30].

3. Numerical Simulation of Bidirectional Performance

Figure 3 shows the relative velocity distribution on the front and back of runner with unilateral and double guide vanes. Seen from the figures, water flows in from inlet of blade, flowing along the blade's surface and the flowing out from the outlet of blade. The water flows smoothly. There is no vortex, and the flow pattern is good.

3.1. Positive Power Performance of Unilateral and Double Guide Vanes. Figure 4 shows the schematic diagram of the entire flow passage of a pit turbine with a unilateral guide vane. The guide mechanism is one of the most important parts of a turbine. The guide vane is a main component of the flow parts. Circulation is formed after water flows through the guide vane and distributes itself uniformly at the same time. Finally, the water flows axisymmetrically into the runner. Table 2 gives the calculation results for positive power performance with unilateral and double guide vanes. It is apparent that positive power generation with a unilateral guide vane located at the end of the shaft shows higher efficiency and better performance than that with double guide vanes. With double side guide vanes, discharge through the turbine is reduced, and efficiency and output are decreased. With adding guide vane 2, because of the increased amount of crowding water, the discharge through the turbine is decreased. With the turbine's spatial oblique guide vanes, the water is blocked from the outlet of runner under the positive power generation, even though guide vane 2 is fully open. Using the unilateral guide vane 1, the head loss from face C to face B is 0.085 m, and the head loss is 0.195 m with double guide vanes. The head loss is obviously increased, and it has influence on the decreased efficiency of turbine. This means that the turbine with unilateral guide vane shows good performance for positive power generation.

Figures 5 and 6 show the velocity profile for positive power generation on the axial plane with unilateral and double guide vanes. The inlet flow pattern can be seen to be symmetrically distributed along the shaft under both conditions. The water is not affected by the disturbance and circulation generated by the guide vanes and runner, but it maintains a steady flow. The velocity distribution is uniform on the runner, and the streamlines are smooth. No undesirable flow patterns such as partial vortices are observed.

3.2. Reverse Power Generation Performance of Unilateral and Double Guide Vanes. Under the reverse-generation condition, the passage with shaft is the outlet conduit. Table 3 gives the reverse-generation calculation results for turbines with unilateral and double guide vanes. The efficiency of reverse generation is low (only 71.55%) with a unilateral guide vane located at the end of the shaft. The discharge through the turbine is slightly reduced with double guide vanes, but the efficiency of reverse power generation is greatly improved, reaching 80.66%, and the output is also improved. With adding guide vane 2, the amount of crowding water increased and the discharge through the turbine is decreased. But at the same time, under the reverse power generation, certain circulation is formed before entering the runner with guide vane 2. So, the efficiency of runner is improved, leading to the improvement of turbine's efficiency. This means that, for reverse power generation, the turbine with double guide vanes shows better performance.

Figures 7 and 8 show the velocity profile of reverse power generation on the axial plane with unilateral and double guide vanes. The streamlines are smooth under the reverse power-generation condition with unilateral and double guide vanes. The flow pattern is generally good, but there are vortices at the outlet and the end of the shaft, where the flow pattern is undesirable. The hydraulic losses are large, leading to low efficiency in reverse power generation.

3.3. Static Pressure Distribution and Vector Profile on Near Outer Edge of the Guide Vane Blade. Figure 9 shows the static pressure distribution on the near outer edge of guide vane blade under the four modes above. At the positive condition, the static pressure of guide vane 1 is almost the same with unilateral guide vane and double guide vanes. That means, adding guide vane 2 almost has no influence on the passage

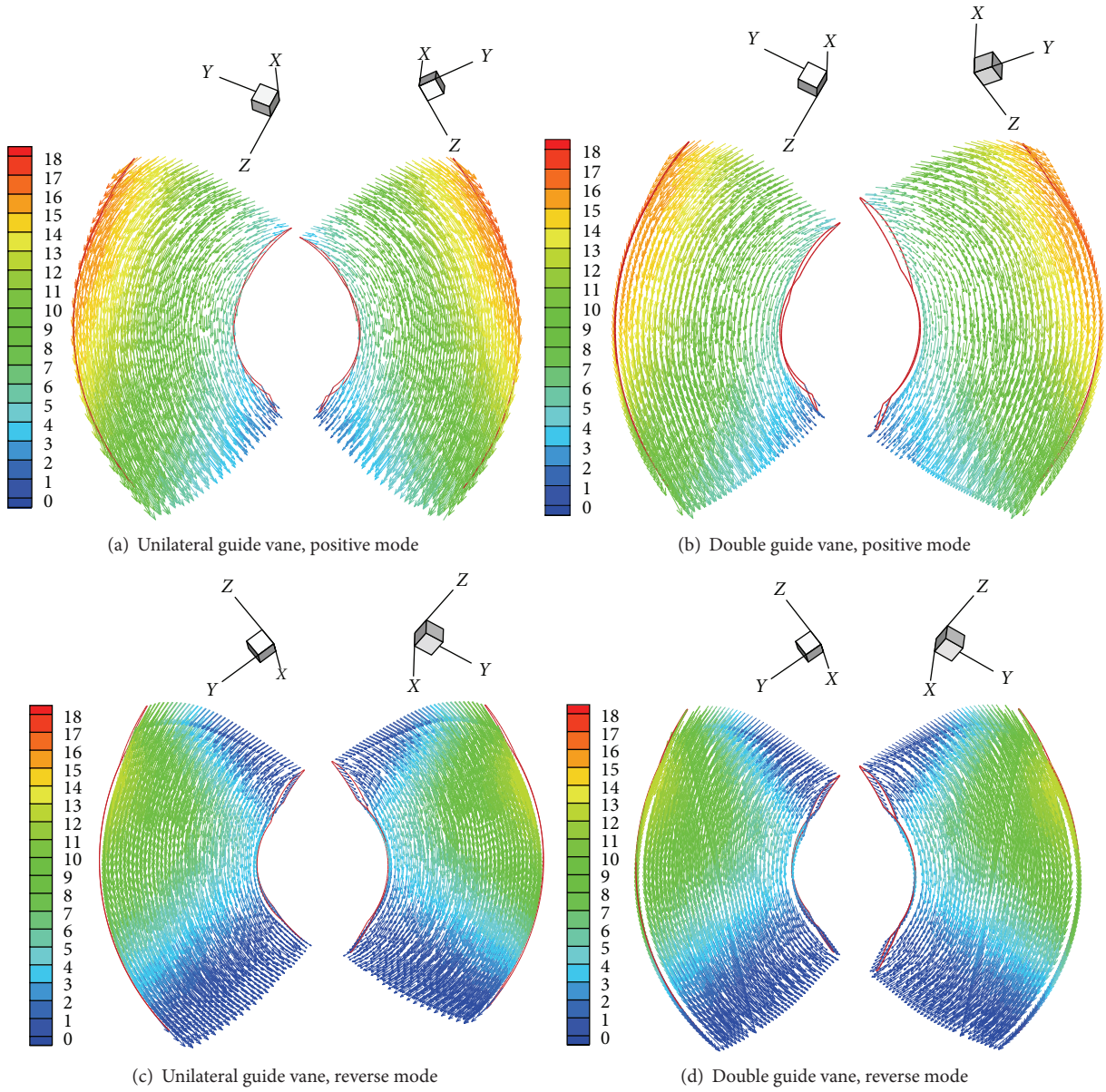

(a) Unilateral guide vane, positive mode

(b) Double guide vane, positive mode

(c) Unilateral guide vane, reverse mode

(d) Double guide vane, reverse mode

Figure 3: Relative velocity distribution on the front and back of blade.

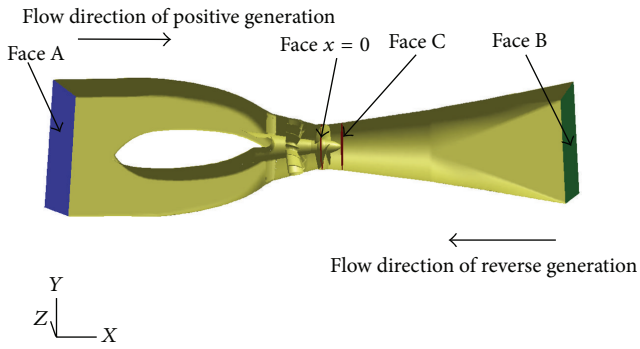

Figure 4: Schematic diagram of the entire flow passage of a pit turbine with unilateral guide vane.

Table 2: Numerical simulation results for positive power generation with unilateral and double guide vanes.

Guide vane	Speed (r/min)	Head (m)	Discharge (m^3/s)	Efficiency (%)	Moment (nm)	Output (kW)
Unilateral	200	2.5	8.45	90.49	8952.33	187.46
Double	200	2.5	7.98	85.81	8019.98	167.94

before water flows into guide vane 1. The pressure of guide vane 2 greatly reduces after the working runner. At the reverse condition, the local pressure on the back of the guide vane 1 with unilateral guide vane is lower than that with double guide vanes. Comparing Figures 9(a) and 9(f), the static

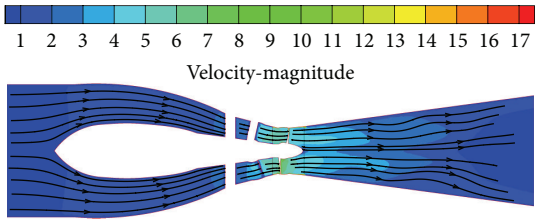

Figure 5: Velocity profile of positive power generation for a turbine with unilateral guide vane.

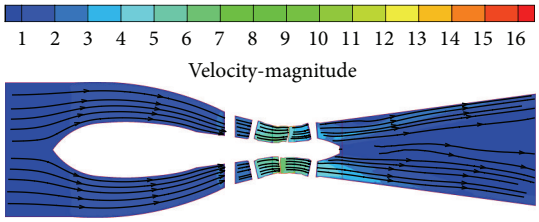

Figure 6: Velocity profile of positive power generation for a turbine with double guide vanes.

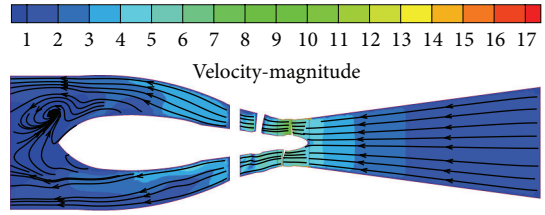

Figure 7: Velocity profile of reverse power generation for a turbine with unilateral guide vane.

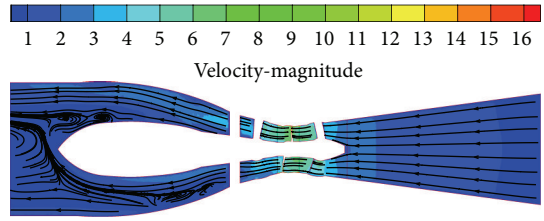

Figure 8: Velocity profile of reverse power generation for a turbine with double guide vanes.

Table 3: Numerical simulation results for reverse power generation with unilateral and double guide vanes.

Guide vane	Speed (r/min)	Head (m)	Discharge (m^3/s)	Efficiency (%)	Moment (nm)	Output (kW)
Unilateral	200	2.5	8.94	71.55	7492.02	156.88
Double	200	2.5	8.19	80.66	7737.03	162.01

pressure of guide vane 2 is lower at the reverse-double mode than that of guide vane 1 at the positive-unilateral mode. The difference is mainly caused by different inlet passage. And local high pressure occurred on the head of both guide vanes above, because of the water flow impaction.

Figure 10 shows the vector profile of the near outer edge of guide vane blade. The water flows along the wall of guide vane at every mode. And the velocity is small near the guide vane wall because of the viscosity. The guide vane 1 at reverse-unilateral mode shows the largest velocity, which leads to the high local loss of guide vane.

4. Model Test

4.1. Parameters of Model Turbine and Test Instrument. The prototype turbine was scaled down to a model turbine with a 0.35 m diameter runner for the model test. The performances of positive and reverse power generation were tested using unilateral and double guide vanes. The main working parameters were rated head 2.5 m, highest head 4.2 m, lowest head 1.0 m, rated discharge 0.383 m^3/s, and rated speed 914.29 r/min.

The model test was based on a multifunction hydromechanical experimental bench at Hohai University. The measuring instruments were (1) head measurement: EJA110A pressure difference sensor made by CYS, precision of ±0.1%; (2) discharge measurement: RFM4110-500 electromagnetic flow meter made by SGAIC, precision of ±0.2%; (3) torque and speed measurement: JCZ-200 torque meter made by XYDC, precision of ±0.1%; (4) vacuum, atmospheric pressure, and temperature measurement: EJA430A pressure transmitter made by CYS for measuring vacuum, precision of ±0.075%; level 0.5 aneroid barometer for measuring atmospheric pressure; and mercury thermometer for measuring temperature.

4.2. Results of Model Test. Table 4 presents the bidirectional power generation data from the model test and the data for the switched prototype turbine with unilateral and double guide vanes under the design conditions, head 2.5 m and speed 200 r/min. These results reveal that positive power generation shows high efficiency and large output with a unilateral guide vane. The efficiency and output of positive power generation slightly decreases with double guide vanes. However, the efficiency of reverse power generation is improved greatly with double guide vanes. The efficiency of reverse power generation is improved from 69.64% to 80.12% when converted into prototype turbine data. The output is improved from 148.42 kW to 156.80 kW, which meets the design requirements.

5. Comparison of Numerical Simulation with Model Test

Figure 11 presents a comparison of numerical simulation and model test results for positive power generation with unilateral and double guide vanes. The efficiency-discharge curve reveals that, both in the numerical simulation and in the model test, the efficiency varies with discharge for the unilateral guide vane. The highest efficiency for positive power generation, both in the model test and in the numerical simulation, is greater than 85%. With double

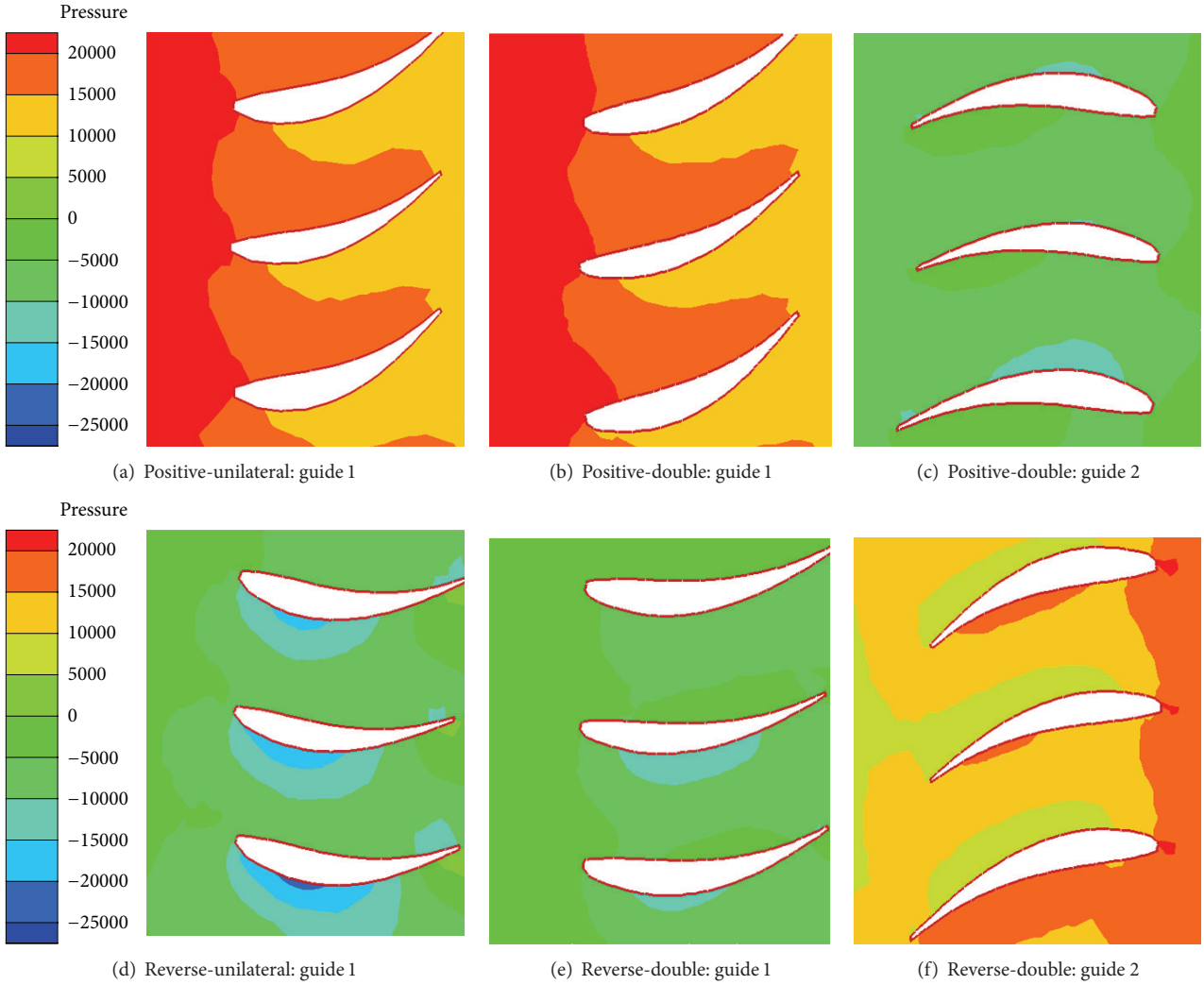

Figure 9: Static pressure distribution on the near outer edge of guide vane blade.

guide vanes, the efficiency, according to both numerical simulation and model test, also varies with discharge. The highest efficiency for positive power generation, according to both the model test and the numerical simulation, is greater than 80%. As the output-discharge curve shows, the output curve follows the discharge trends with a unilateral guide vane. The largest output is greater than 150 kW. The output curve also follows the discharge trends with double guide vanes. The largest output for positive generation is greater than 150 kW according to both the model test and the numerical simulation. The error between the model test and the numerical simulation is small for both unilateral and double guide vanes at the optimum operating condition. The large difference between test data and numerical data at large flow rate was caused by the more complex flow deviation from the optimum operating condition. The difference also increased of numerical simulation without considering the clearance and frictional force between the runner and runner chamber. The clearance between the guide vane and stay ring was not taken into account either.

Figure 12 presents a comparison of numerical simulation and model test results for reverse power generation with unilateral and double guide vanes. The efficiency-discharge curve shows that efficiency, according to both the numerical simulation and the model test, follows the trends in discharge with a unilateral guide vane. The highest efficiency for reverse power generation, according to both the model test and the numerical simulation, is less than 75%. Efficiency also follows discharge trends with double guide vanes, according to both the numerical simulation and the model test. The highest efficiency for reverse power generation in both the model test and the numerical simulation is greater than 80%. The output-discharge curve shows that the output curve follows discharge trends with a unilateral guide vane. The output from the model test is lower than that from the numerical simulation, and the largest output is less than 150 kW. The output curve also follows discharge trends with double guide vanes. The largest output from reverse generation is greater than 150 kW according to both the model test and the numerical simulation. The error between the model test and

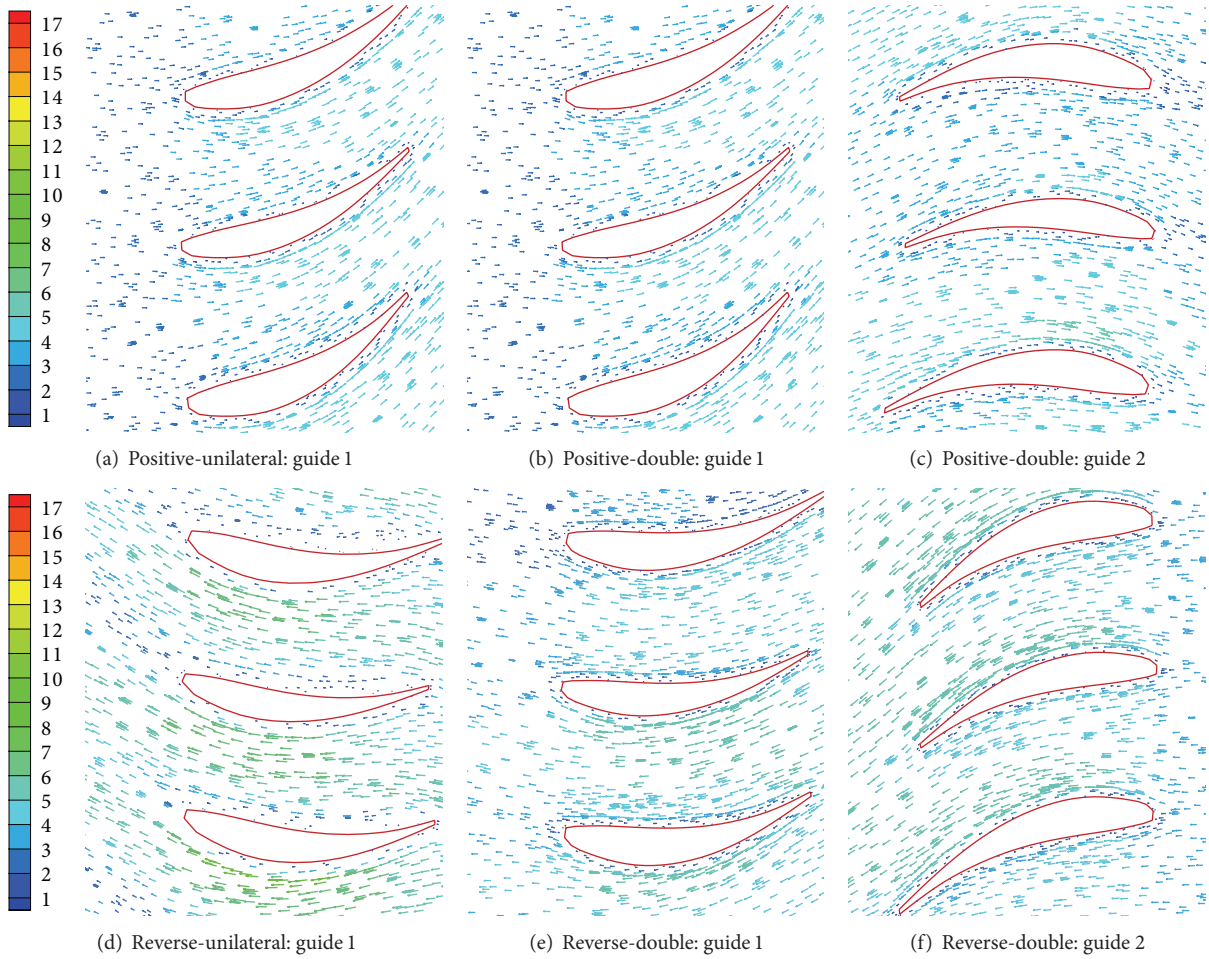

(a) Positive-unilateral: guide 1 (b) Positive-double: guide 1 (c) Positive-double: guide 2

(d) Reverse-unilateral: guide 1 (e) Reverse-double: guide 1 (f) Reverse-double: guide 2

Figure 10: Vector profile of the near outer edge of guide vane blade.

Table 4: Bidirectional power generation data from the model test and data from the switched prototype turbine with unilateral and double guide vanes under design conditions.

Guide vane and generation condition	Discharge (m^3/s)		Efficiency (%)		Output (kW)	
	Model	Prototype	Model	Prototype	Model	Prototype
Unilateral, positive	0.394	8.23	86.97	89.36	8.40	180.36
Double, positive	0.375	7.84	81.64	84.03	7.51	161.57
Unilateral, reverse	0.416	8.69	67.25	69.64	6.86	148.42
Double, reverse	0.382	7.96	77.73	80.12	7.28	156.80

the numerical simulation is small for both unilateral and double guide vanes. In the model test results, the points of maximum efficiency and maximum output move to the bottom left compared to the simulation results. However, the difference becomes relatively large in the small-discharge and large-discharge parts of the curve. This is mainly because, as conditions deviate from the optimum, the turbine flow movement becomes more complex. The difference also increased of numerical simulation without considering the clearance and frictional force between the runner and runner chamber. The clearance between the guide vane and stay ring was not taken into account either.

6. Conclusions

Numerical simulations and model tests were done of a new bidirectional pit turbine for tidal power stations with low head and large discharge under different guide-vane openings, especially with unilateral or double guide vanes.

(1) The results of numerical simulation show that under positive power generation, the unit exhibits high efficiency, 90.49%, with a unilateral guide vane and a discharge of 8.45 m^3/s. The output, 187.46 kW, is large. However, the unit's reverse power-generation

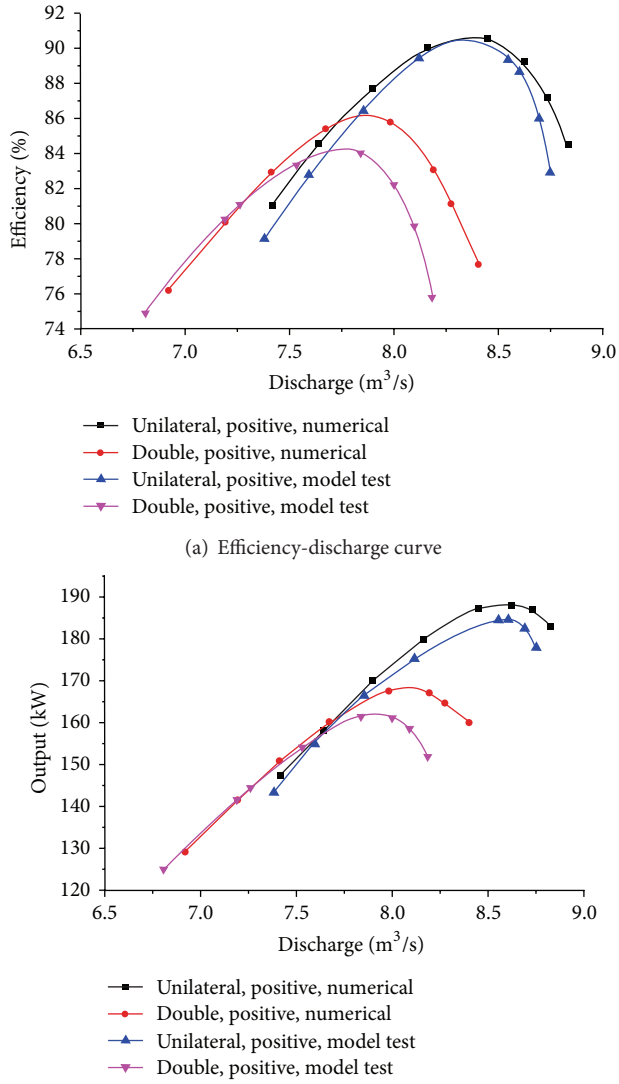

Figure 11: Comparison of numerical simulation and model test results for positive power generation with unilateral and double guide vanes.

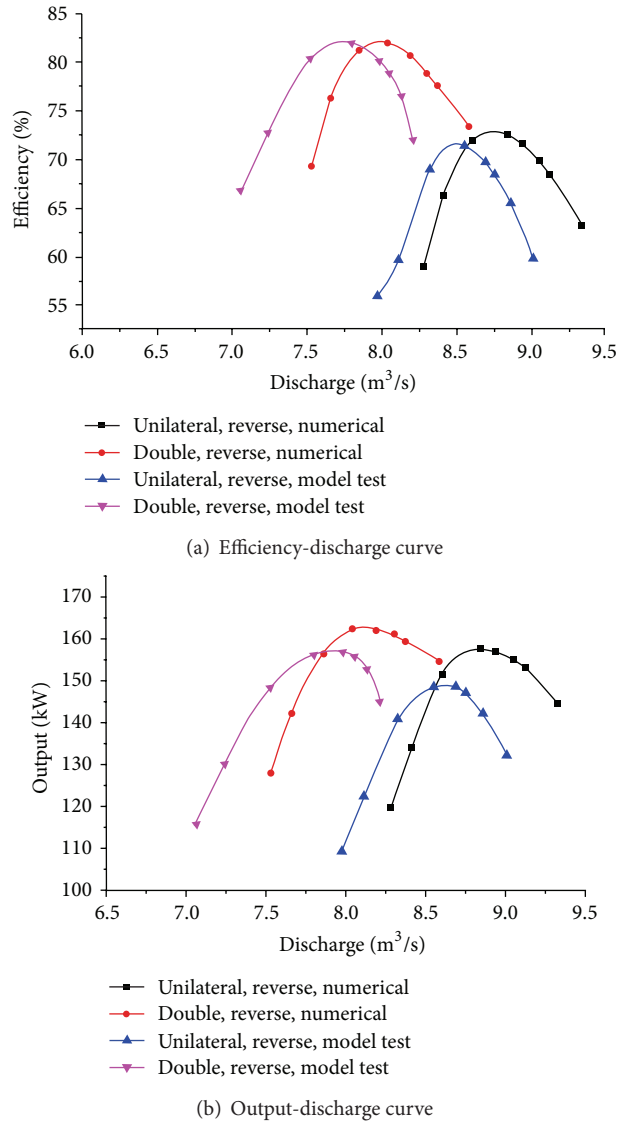

Figure 12: Comparison of numerical simulation and model test results for reverse power generation with unilateral and double guide vanes.

efficiency is low. The highest efficiency is only 71.55%, and the output is 156.88 kW. The unit's highest efficiency was reduced to 85.81% in positive generation with double guide vanes, with a discharge of 7.98 m^3/s and an output of 167.94 kW. However, the efficiency of reverse generation is significantly improved with double guide vanes, with a highest efficiency of 80.66%, a discharge of 8.19 m^3/s, and an output of 162.01 kW.

(2) The model test results under corresponding conditions converted to prototype data show that the unit's highest efficiency in positive power generation is 89.36% with a unilateral guide vane, with a discharge of 8.40 m^3/s and an output of 180.36 kW. The unit's highest efficiency in reverse power generation is 69.64%, with a discharge of 8.69 m^3/s and an output of 148.42 kW. The unit's highest efficiency in positive power generation with double guide vanes is 84.03%, with a discharge of 7.84 m^3/s and an output of 161.57 kW. The unit's highest efficiency in reverse power generation is 80.12%, with a discharge of 7.96 m^3/s and an output of 156.80 kW.

(3) Considering the positive and reverse power-generation performance, the turbine with double guide vanes shows better performance. The efficiency of reverse-double mode is greatly improved mainly because of the formed circulation before water flows into the runner. The results for discharge,

output, and efficiency for the model test were lower than those from the numerical simulation under the same conditions, but the deviation was small. The difference was caused by numerical simulation without considering the clearance and frictional force between the runner and runner chamber and the clearance between the guide vane and stay ring. On the whole, the results of the model test thus verified the reliability of the numerical calculation.

Conflict of Interests

All the authors declare that there is no conflict of interests regarding the publication of this paper. All the authors do not have a direct financial relation with the commercial identities mentioned in their paper that might lead to a conflict of interests for any of the authors.

Acknowledgments

The work is financially supported by the project Special Founds for MRE: GHME2011CX02.

References

[1] R. Pelc and R. M. Fujita, "Renewable energy from the ocean," *Marine Policy*, vol. 26, no. 6, pp. 471–479, 2002.

[2] M. Islam, A. Fartaj, and D. S.-K. Ting, "Current utilization and future prospects of emerging renewable energy applications in Canada," *Renewable and Sustainable Energy Reviews*, vol. 8, no. 6, pp. 493–519, 2004.

[3] H.-W. Liu, S. Ma, W. Li, H.-G. Gu, Y.-G. Lin, and X.-J. Sun, "A review on the development of tidal current energy in China," *Renewable and Sustainable Energy Reviews*, vol. 15, no. 2, pp. 1141–1146, 2011.

[4] T. Kanemoto, "Dream of marine-topia: new technologies to utilize effectively renewable energies at offshore," *Current Applied Physics*, vol. 10, no. 2, pp. S4–S8, 2010.

[5] D. Li, S. Wang, and P. Yuan, "An overview of development of tidal current in China: energy resource, conversion technology and opportunities," *Renewable and Sustainable Energy Reviews*, vol. 14, no. 9, pp. 2896–2905, 2010.

[6] C. Lins and M. Laguna, "Development of hydro power," *Renewable Energy*, vol. 2004, pp. 46–49, 2004.

[7] A. Furukawa, S. Watanabe, D. Matsushita, and K. Okuma, "Development of ducted Darrieus turbine for low head hydropower utilization," *Current Applied Physics*, vol. 10, no. 2, pp. S128–S132, 2010.

[8] Z. Wang, X. Yang, and Y. Xiao, "Hydraulic performance optimization of bidirectional tidal power turbine," *Journal of Drainage and Irrigation Machinery Engineering*, vol. 28, no. 5, pp. 417–421, 2010.

[9] X. Zhongqiang, "Chen Kangming Design of new tidal power turbine," *Hongshui River*, vol. 27, no. 4, pp. 26–28, 2008.

[10] L. Shuhong, Y. Wei, and W. Yulin, "3-D steady turbulent simulation and modification of the tubular turbine," *Journal of Hydroelectric Engineering*, vol. 26, no. 1, pp. 110–118, 2007.

[11] F. Li, H. Fan, Z. Wang, and N. Chen, "Optimum design of runner blades of a tubular turbine based on vorticity dynamics," *Journal of Tsinghua University*, vol. 51, no. 6, pp. 836–839, 2011.

[12] J. Z. Wu and J. M. Wu, "Vorticity dynamics on boundaries," *Advances in Applied Mechanics*, vol. 32, pp. 119–275, 1996.

[13] J. Z. Wu and J. M. Wu, "Boundary vorticity dynamics since Lighthill's 1963 article: review and development," *Theoretical and Computational Fluid Dynamics*, vol. 10, no. 1–4, pp. 459–474, 1998.

[14] N. C. Markatos, "Computational fluid flow capabilities and software," *Ironmaking and Steelmaking*, vol. 16, no. 4, pp. 266–273, 1989.

[15] V. Prasad, "Numerical simulaiton for flow characteristics of axial flow hydraulic turbine runner," *Energy Procedia*, vol. 14, pp. 2060–2065, 2012.

[16] J. G. I. Hellström, B. D. Marjavaara, and T. S. Lundström, "Parallel CFD simulations of an original and redesigned hydraulic turbine draft tube," *Advances in Engineering Software*, vol. 38, no. 5, pp. 338–344, 2007.

[17] D. Shirokoff and R. R. Rosales, "An efficient method for the incompressible Navier-Stokes equations on irregular domains with no-slip boundary conditions, high order up to the boundary," *Journal of Computational Physics*, vol. 230, no. 23, pp. 8619–8646, 2011.

[18] R. A. Saeed and A. N. Galybin, "Simplified model of the turbine runner blade," *Engineering Failure Analysis*, vol. 16, no. 7, pp. 2473–2484, 2009.

[19] M. Coroneo, G. Montante, A. Paglianti, and F. Magelli, "CFD prediction of fluid flow and mixing in stirred tanks: numerical issues about the RANS simulations," *Computers and Chemical Engineering*, vol. 35, no. 10, pp. 1959–1968, 2011.

[20] V. Yakhot and S. A. Orszag, "Renormalization group analysis of turbulence. I. Basic theory," *Journal of Scientific Computing*, vol. 1, no. 1, pp. 3–51, 1986.

[21] F. Z. Sierra, Z. Mazur, J. Kubiak et al., "Modelling of the flow at the last stage blade tenon in a geothermal turbine using renormalization group theory turbulence model," *Applied Thermal Engineering*, vol. 20, no. 1, pp. 81–101, 2000.

[22] V. V. Ranade, M. Perrard, N. le Sauze, C. Xuereb, and J. Bertrand, "Trailing vortices of Rushton turbine: PIV measurements and CFD simulations with snapshots approach," *Chemical Engineering Research and Design*, vol. 79, no. 1, pp. 3–12, 2001.

[23] C. Hirsch, *Numerical Computation of Internal and External Flows*, John Wiley and Sons, Oxford, UK, 2007.

[24] J. P. Van Doormaal and G. D. Raithby, "Enhancement of the SIMPLE method for predicting incompress-ible fluid flow," *Numerical Heat Transfer*, vol. 7, no. 2, pp. 147–163, 1984.

[25] W. Feng, L. Song, L. Zuo, and B. Yuan, "3D numerical simulation on unsteady turbulence flow in axial flow pump system," *Journal of Drainage and Irrigation Machinery Engineering*, vol. 28, no. 6, pp. 531–536, 2010.

[26] S. V. Patankar and D. B. Spalding, "A calculation procedure for heat, mass and momentum transfer in three-dimensional parabolic flows," *International Journal of Heat and Mass Transfer*, vol. 15, no. 10, pp. 1787–1806, 1972.

[27] M. K. Patel, M. Cross, and N. C. Markatos, "An assessment of flow-oriented schemes for reducing False Diffusion," *International Journal for Numerical Methods in Engineering*, vol. 26, no. 10, pp. 2279–2304, 1988.

[28] M. Kobayashi, J. M. C. Pereira, and J. C. F. Pereira, "A second-order upwind least-squares scheme for incompressible flows on unstructured hybrid grids," *Numerical Heat Transfer B*, vol. 34, no. 1, pp. 39–60, 1998.

[29] R. A. Saeed, A. N. Galybin, and V. Popov, "Modelling of flow-induced stresses in a Francis turbine runner," *Advances in Engineering Software*, vol. 41, no. 12, pp. 1245–1255, 2010.

[30] R. Xiao, Z. Wang, and Y. Luo, "Dynamic stresses in a francis turbine runner based on fluid-structure interaction analysis," *Tsinghua Science and Technology*, vol. 25, no. 5, pp. 587–592, 2008.

Hindawi Publishing Corporation
Advances in Mechanical Engineering
Volume 2013, Article ID 623020, 9 pages
http://dx.doi.org/10.1155/2013/623020

Review Article

A Review of Offshore Wave Energy Extraction System

Zhongxian Chen, Haitao Yu, Minqiang Hu, Gaojun Meng, and Cheng Wen

Engineering Research Center of Motion Control of Ministry of Education, Southeast University, Nanjing 210096, China

Correspondence should be addressed to Haitao Yu; htyu@seu.edu.cn

Received 28 June 2013; Accepted 30 August 2013

Academic Editor: Fabrizio Marignetti

Copyright © 2013 Zhongxian Chen et al. This is an open access article distributed under the Creative Commons Attribution License, which permits unrestricted use, distribution, and reproduction in any medium, provided the original work is properly cited.

Offshore wave energy can be easily predicted and is proved to be much better than other forms of ocean energy such as shoreline wave, near-shore wave, and tides. Research on offshore wave energy extraction has been carried out in many countries to meet the growing demand for clean energy and reduce the impact on natural environment. This paper reviews the development of offshore wave energy extraction systems in the recent decade. Several aspects are introduced, including a global wave energy resource assessment, offshore wave energy extraction technologies, and the interaction between wave and floating buoy as well as linear generators. Although various offshore wave energy extraction systems have been proposed and even tested, it is difficult to decide which is the best one. In fact, design of floating buoy and linear generators plays an important role in the operational efficiency of offshore wave energy extraction system. This review provides some useful guidelines for future studies in this field.

1. Introduction

Currently petroleum and coal resources count the majority of world energy supply. However, consumption of petroleum and coal resource is the main cause of serious environmental problems such as acid rain and global warming. Thereby the Kyoto protocol has been approved in 1997. In addition, the use of nuclear energy may also lead to environmental problems and safety issues. For example, one of the most disastrous earthquakes on record hit Japan and brought about radiation leakage from Fukushima Daiichi Nuclear Power Plant in 2011. Therefore, clean and renewable energy is increasingly needed to meet the economy development and reduce the impact on natural environment in the near future.

Wave energy, a source of renewable energy, has the advantages of a high energy density and persistence and, therefore, is a competitive candidate for energy supply. It is estimated that the total amount of ocean wave energy is 2000 TWh/year, which amounts to about 10 percent of the total electricity generated worldwide in 2005 [1, 2]. Ocean wave energy along European west coast is estimated to be able to meet the electricity demand in Western European countries [3]. There are various methods of wave energy extraction to realize the application by human beings [4–6]. Research and development (R&D) programmes on wave energy extraction are conducted in a number of countries, such as Norway, Denmark, Portugal, Sweden, USA, and Australia [7–10]. Following the targets for greenhouse gas emissions reduction and the growing consumption of energy, many researchers from electrical engineering, mechanical engineering, and hydrodynamics are going into this research field.

Despite a wide variety of technologies and more than one thousand patents for wave energy extraction system, which are generally classified according to working principle (attenuator, point absorber, and terminator) and location (shoreline, near-shore, and offshore), wave energy extraction is a hydrodynamic and mechanical process including complex wave phenomena (radiation and diffraction) and nonlinear oscillations, especially for the offshore wave energy extraction systems. This explains why many wave energy extraction systems are at the R&D or theoretical stage [11], with only very few of which have been installed and tested in waves. The point absorber PowerBuoy Prototype, designed by Ocean Power Technologies (OPT) Inc. and installed off the Hawaii coast, USA, represents one of the leading offshore wave energy extraction systems that are currently operating [12]. Another example for the leading offshore wave energy extraction system is Pelamis, installed at Agučadoura Wave Park, Portugal, and represents one of the technologies for

wave energy extraction with a high power capture rate [13]. Provided that suitable methods are applied in the design, construction, operation, and maintenance, offshore wave energy would be a promising renewable energy.

Electrical generators are the conception of power takeoff (PTO) of wave energy extraction systems which should allow conversion of wave energy into usable electrical power. The method of PTO depends on the location of wave energy extraction station, but the general method of obtaining electrical power is through conventional rotary generators or linear generators [14]. However, the characteristics of wave such as wave period, wave height, and seasonal variation cause the variability of energy absorption [15, 16]. Accordingly, designing a suitable generator for wave energy extraction system in certain sea site is very necessary. In addition, the survivability of electrical generators in extreme conditions (e.g., typhoon or hurricane) is another issue that should be considered.

The layout of the rest of the paper is as follows. The second section is about wave energy resource in the world. The third part is about technologies for offshore wave energy extraction system, and the forth part is theoretical analysis of interaction between wave and floating buoy. Before the last section of conclusions, some linear generators of wave energy extraction systems are discussed in the fifth section.

2. Wave Energy Resource

Wave energy is produced by the effect of wind on surface water and is, therefore, indirectly considered as one type of solar energy. In fact, the time-averaged energy flow is concentrated when solar energy is converted into wind energy, and wave energy is even more concentrated when wind blows [17, 18]. Therefore, the availability of wave energy is much higher than that of wind energy and solar energy [19]. Wave energy consists of kinetic energy and potential energy, which arise from the motion of waves. The total amount of wave energy mainly depends on the characteristics of wave such as wave height, wave period, location, and seasonal variation. In general, the stored energy per unit wave surface in deep water (approximately a depth exceeding half of the wavelength) is proportional to the wave height squared, which can be described by the following equation [15, 18]:

$$E = \rho g \frac{H_s^2}{8}, \tag{1}$$

where E is the stored energy per unit wave surface (J/m^2), ρ is the mass density of wave (1030 kg/m^3), g is the acceleration of gravity (kg/m^3), and H_s is the progressive harmonic plan wave height (m). According to linear theory and superposition principle [20, 21], a real sea wave may be characterized as energy spectrum and the stored energy can be equally divided between kinetic energy and potential energy.

Assessment of wave energy resource is one of the important prerequisite work for wave energy extraction system designing and prototype testing. Actually, (1) is not enough for the assessment of wave energy resource. The assessment should include the characteristics of wave (e.g., wave height, wave period, water depth, and seasonal variation) and the location of wave energy extraction system (e.g., channel, reefs, harbor, and coast). In 1991, European Commission started a project to investigate the characteristics of wave energy and produced some recommendations for prototype testing [22]. The WERATLAS, funded by European Commission and considered as a reference for wave energy extraction system construction, proposed a proper numerical wind-wave modeling to describe the detailed characteristics of waves at 85 points off the Atlantic and Mediterranean coast of Europe [23].

Generally, the annual mean wave energy in offshore (20~100 kW/m in the areas of moderate-to-high latitudes) is much more than that in shoreline and near shore. Figure 1 shows the global distribution of annual mean wave energy density [24–27]. A large seasonal variation makes southern hemisphere (e.g., southern coasts of South America, western coasts of Europe, Africa, Australia, and New Zealand) a competitive candidate for the location of wave energy extraction station.

3. Offshore Wave Energy Extraction Technologies

The advantage of offshore wave energy extraction system lies in that a great deal of wave energy and economic benefits can be obtained through a high energy density in deep water [28, 29]. However, construction and maintenance of offshore wave energy extraction system are expensive and difficult due to the complex sea condition. The system may be subject to strong wave impulsive load (e.g., typhoon or hurricane) and thereby damaged by peak pressures. Since 95% of energy in offshore wave is between water surface and 7 m under water surface [28, 29], the objective of this section is to briefly review the technologies in offshore wave energy extraction system.

Offshore wave energy extraction systems are basically oscillating floating bodies, and the horizontal dimensions of these floating bodies are usually smaller than one wavelength. The idea of converting offshore wave energy into electrical energy has witnessed a significant development in recent years. Some important examples of offshore wave energy extraction systems are given below.

3.1. Single-Body Floating Systems. An early example of single-body floating system is a floating buoy connected to a linear permanent magnet generator of seabed-fixed device through a rope, and the rope is kept tight by a spring under the linear permanent magnet generator, as shown in Figure 2 [30–32]. Spring obtains wave energy during half a wave cycle (wave from trough to crest) and drives linear permanent magnet generator to produce electrical energy in another half of the wave cycle (wave from crest to trough). One advantage of this system is that the floating buoy's nature angular frequency in heave can be matched with the incident wave angular frequency. A full-scale single-body floating system (the radius of floating buoy is equal to 3 m) was constructed at a depth of 25 m, 2 km off the Swedish west coast, and tested in 2007 [30]. In the years to come, an array of single-body

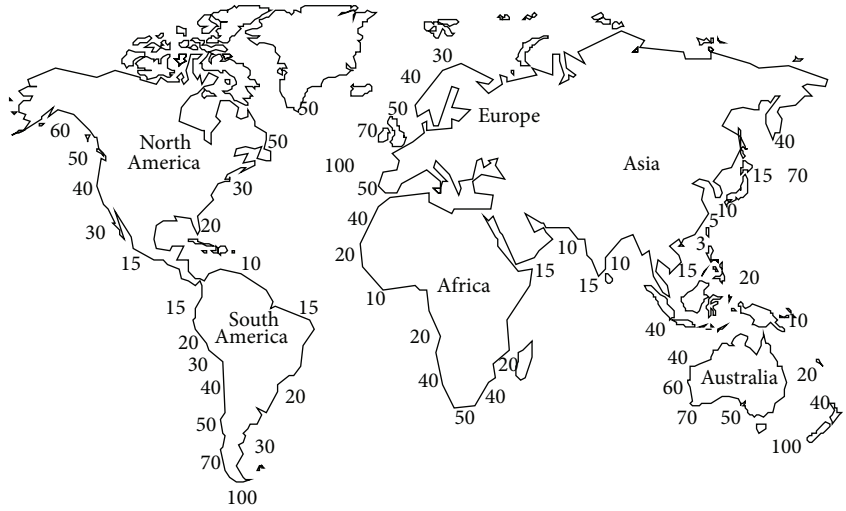

Figure 1: Approximate global distribution of annual mean wave energy density (kW/m) [24–27].

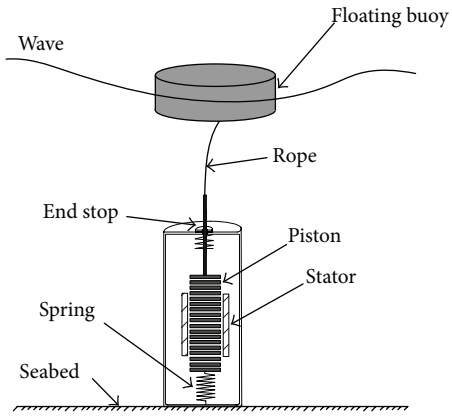

Figure 2: Cross-sectional view of a wave energy extraction system with single-body floating [30–32].

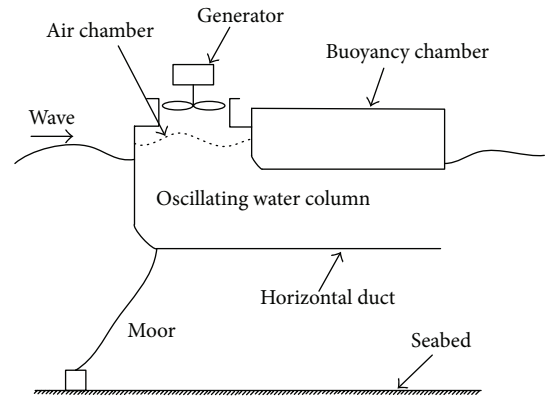

Figure 3: Sketch of a backward bent duct buoy [33].

floating systems will be deployed at the same site to evaluate the concepts of technology, ecology, and economy.

The backward bent duct buoy, another single-body floating system (also known as an oscillating water column converter), was designed in Japan under the leadership of Yoshio Masuda. Figure 3 shows the sketch of a backward bent duct buoy [33]. In comparison with the frontward facing duct buoy, the advantages of backward bent duct buoy are that the oscillating water column could be designed to resonance with incident waves, and a high energy conversion rate with low mooring force could be achieved [34]. The backward bent duct buoy has been investigated in several countries (Japan, Korea, China, and so on) and installed in Japan and China. In the second half of 2006, a 12 m long prototype with a novel Walls turbine was installed off Ireland western coast [35].

3.2. Two-Body Floating Systems. The single-body floating systems may cause some problems because of the unstable distance between water surface and seabed-fixed device, especially under the condition of typhoon or hurricane. In addition, installation of the device on seabed is expensive and difficult. Two-body floating systems may be utilized instead, where wave energy can be obtained through the relative motion between two floating bodies. The characteristics of oscillating of floating body are analyzed theoretically in papers [31, 32]. One famous example of two-body floating systems is PowerBuoy (shown in Figure 4) designed by Ocean Power Technologies Inc. (an American company in Pennington, NJ, USA), and installed off the Spain's northern coast with a capacity of 40 kW, in September 2008 [12]. The PowerBuoy consists of two floating bodies, the outer one acts as a resonating body with incident waves and the inner one as a fixed reference. The resultant mechanical stroking between two floating bodies drives a generator to produce electrical energy via a hydroelectric turbine, and the produced electrical energy is delivered ashore by an underwater cable.

Besides, PowerBuoy can be designed for strong wave impulsive load (e.g., typhoon or hurricane). PowerBuoy's sensors monitor the relative motion of two floating bodies

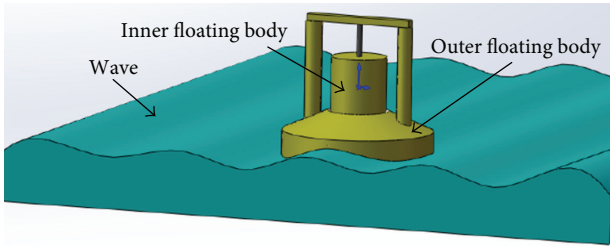

Figure 4: Sketch of a PowerBuoy by Ocean Power Technologies Inc. [12].

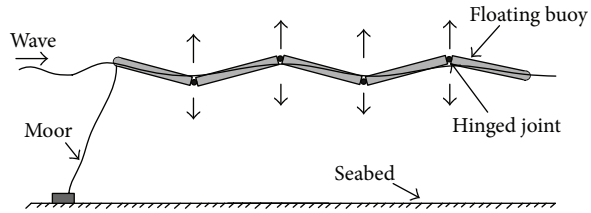

Figure 5: Sketch of the Pelamis [13].

and surrounding ocean waves continuously. In the case of strong wave impulsive load, the PowerBuoy will shut off and cease electrical energy production. The PowerBuoy will continue to produce electrical energy when the strong wave impulsive load has passed.

3.3. Multibody Floating Systems. The most successful wave energy extraction system based on multibody floating systems is Pelamis (shown in Figure 5), which represents one of the most widely-used offshore wave energy extraction systems with a high power capture/unit weight [13]. This system is a semisubmerged articulated structure consisting of several floating buoys linked through hinged joints. The relative vertical and horizontal motions of floating buoys are resisted by hinged joints which are used to drive electrical generators via high pressure oil and hydraulic motors. A set of three Pelamis has been installed at the European Marine Energy Centre of Orkney (a capacity of 750 kW) to establish the first grid-connected offshore wave energy extraction system for commercial purposes between 2004 and 2007. The Aegir wave farm of Shetland is expected to increase its capacity (10 MW) by installing 13 Pelamis [36, 37].

4. Interaction between Wave and Floating Buoy

Study of the interaction between wave and floating body could benefit from previous investigations on the motion of ship in waves. This section will review the motion of floating buoy based on vertical wave force.

4.1. Added Mass and Damping of Floating Buoy. The hydrodynamic parameters such as added mass and damping play an important role in the study of motion of floating buoy, there exist a lot of numerical methods for calculating the two hydrodynamic parameters of floating buoy, for example, traditional wave source distribution method, finite element variation formulations, and integrovariational method [38]. However, the above numerical methods are time consuming and complicated. In fact, the two hydrodynamic parameters of floating buoy can be simply calculated by the use of eigenfunctions, especially for the low-frequency motion [39]. Therefore, a quick calculation method consists of parameters (e.g., water depth, radius of floating buoy, and its draft) and summary formulas for the two hydrodynamic parameters are proposed, and the calculation results are verified by some available experimental results [40].

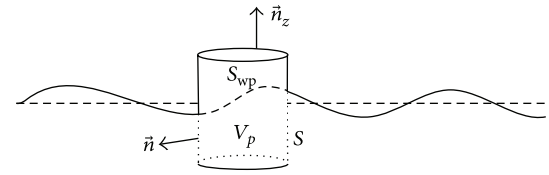

Figure 6: Floating buoy with water plane area S_{wp}, submerged volume V_p (volume of displaced water), and wet surface S with unit normal $\vec{n}$.

It is expected that calculation of the two hydrodynamic parameters will optimize the dynamic performance of floating buoy design and increase the efficiency of offshore wave energy extraction system.

4.2. Vertical Wave Force on Floating Buoy. It is assumed that the dimensions of heaving buoy are smaller than incident wavelength, and the fluid is irrotational and incompressible and experiences variation in sinusoidal curve as time goes on. Then the linearized theory and potential energy theory are applied. Generally, the velocity potential of wave [43] can be expressed as

$$\hat{\phi} = \hat{\phi}_0 + \hat{\phi}_d + \hat{\phi}_r, \tag{2}$$

where $\hat{\phi}_0$ is incident potential, $\hat{\phi}_d$ is diffracted potential, and $\hat{\phi}_r$ is radiated potential.

From potential theory the vertical wave force $\hat{F}_z$ on the wet surface S (see Figure 6) can be written as

$$\hat{F}_z = -\iint_S p\vec{n}_z dS = \hat{F}_{\mathrm{FK}} + \hat{F}_d, \tag{3}$$

where p is hydrodynamic pressure, $\vec{n}_z$ is vertical unit vector, $\hat{F}_{\mathrm{FK}}$ is Froude-Krylov force vector, and $\hat{F}_d$ is diffraction force vector [15]. Consider

$$\hat{F}_{\mathrm{FK}} = i\omega\rho \iint_S \hat{\phi}_0 \vec{n}_z dS, \tag{4}$$

$$\hat{F}_d = i\omega\rho \iint_S \hat{\phi}_d \vec{n}_z dS. \tag{5}$$

In (4) and (5), $\rho = 1030\,\mathrm{kg/m^3}$ is the mass density of sea water, and ω is the angular frequency of sea wave. Equation (4) may be divided into one integral over the area $S + S_{wp}$ and

one integral over the area S_{wp} by area integral method [44], as shown in

$$\widehat{F}_{\mathrm{FK}} = i\omega\rho \iint_{S+S_{wp}} \widehat{\phi}_0 \vec{n}_z dS - i\omega\rho \iint_{S_{wp}} \widehat{\phi}_0 \vec{n}_z dS. \quad (6)$$

In addition, the integral over the area $S + S_{wp}$ can be transformed into one triple integral over the displaced water volume V_p by divergence $\nabla \cdot (\widehat{\phi}_0 \vec{n}_z)$ and Gauss' theorem [15, 44]

$$\begin{aligned} i\omega\rho \iint_{S+S_{wp}} \widehat{\phi}_0 \vec{n}_z dS &= i\omega\rho \iiint_{V_p} \left(\nabla \widehat{\phi}_z\right) \cdot \vec{n}_z dV \\ &= i\omega\rho \iiint_{V_p} \frac{\partial \widehat{\phi}_z}{\partial z} dV. \end{aligned} \quad (7)$$

Therefore,

$$\begin{aligned} \widehat{F}_{\mathrm{FK}} &= i\omega\rho \iiint_{V_p} \frac{\partial \widehat{\phi}_z}{\partial z} dV - i\omega\rho \iint_{S_{wp}} \widehat{\phi}_0 \vec{n}_z dS \\ &= \rho \iiint_{V_p} \widehat{a}_z dV + \vec{n}_z \rho g \iint_{S_{wp}} \widehat{\eta}_0 dS, \end{aligned} \quad (8)$$

where $\widehat{a}_z = i\omega(\partial \widehat{\phi}_z / \partial z)$ and $\widehat{\eta}_0 = -i(\omega/g)\widehat{\phi}_0$ are the acceleration and amplitude of floating buoy in terms of complex, respectively.

In order to calculate the diffraction force vector $\widehat{F}_d$, it is not necessary to calculate the diffracted potential $\widehat{\phi}_d$ but the proportional coefficient φ_z of radiated velocity potential $\widehat{\phi}_r$. From the Green's theorem [3, 15], the diffraction force vector $\widehat{F}_d$ can be expressed as

$$\begin{aligned} \widehat{F}_d &= i\omega\rho \iint_S \widehat{\phi}_d \vec{n}_z dS \\ &= -i\omega\rho \iint_S \varphi_z \frac{\partial \widehat{\phi}_0}{\partial n_z} dS = -\rho \iint_S \varphi_z \widehat{a}_z dS. \end{aligned} \quad (9)$$

4.3. Motion Equation of Floating Buoy. As shown in Figure 6, the floating buoy is subject to three forces, namely, the vertical wave force $\widehat{F}_z$, the radiation force $\widehat{F}_r$, and the hydrostatic buoyancy force $\widehat{F}_b$. According to Newton's law, the motion equation of floating buoy in heave may be written as

$$m_m \widehat{a}_z = \widehat{F}_z + \widehat{F}_r + \widehat{F}_b, \quad (10)$$

where m_m is the weight of floating buoy. According to linear theory, the radiation force $\widehat{F}_r$ is proportional to the so-called radiation impedance $Z_z = im_z + R_z$ of floating buoy, and the hydrostatic buoyancy force $\widehat{F}_b$ is proportional to the excursion $\widehat{S}_z$ of floating buoy from its equilibrium position, both of which can be written as

$$\begin{aligned} \widehat{F}_r &= -Z_z \widehat{v}_z, \\ \widehat{F}_b &\approx -\rho g S_{wp} \widehat{S}_z, \end{aligned} \quad (11)$$

where $\widehat{v}_z$ is the speed of floating buoy in heave [15]. In terms of complex amplitude ($\widehat{a}_z = i\omega\widehat{v}_z = -\omega^2 \widehat{S}_z$) and small-body approximation the speed of floating buoy in heave may be written as

$$\widehat{v}_z = \frac{\widehat{F}_z}{i\omega\left[m_m + m_z\right] + R_z + i\left(\rho g S_{wp}/\omega\right)}, \quad (12)$$

where m_z and R_z are added mass and damping of floating buoy, respectively.

Figure 7(a) shows a two-body floating system oscillating in heave. The wave propagates in sinusoidal trace, at the wave height of 1.4 meters and wave period of 5 seconds. Both of the diameters of outer floating buoy and damper plate (at the bottom of inner floating buoy) are equal to 2.4 m. The function of damper plate is to increase the damping effect on inner floating buoy by the surrounding water. The depths of submergence of outer and inner floating buoys are shown in Figure 7(a). From the above theory of interaction between wave and floating buoy, the speed curves of outer and inner floating buoys in heave are shown in Figure 7(b). Based on this concept of relative motion between outer and inner floating buoys, a two-body floating system with a novel permanent magnet tubular linear generator rated at 5 kW will be installed off the eastern coast of China, in the second half of 2013.

5. Linear Generators

The ultimate product of wave energy extraction system is electrical energy, which is produced from various kinds of electrical generators (e.g., conventional rotating generators or linear generators) and delivered into a grid [45–49]. Electrical generator is one of most important devices determining the operation efficiency of wave energy extraction system. In the case of conventional rotating generators, a linear-to-rotary conversion device (e.g., air turbine, water turbine, or hydraulic motor) is needed to convert the linear motion of wave into a uniform rotary motion [50, 51]. Although the first linear generator has been proposed since over 100 years ago in the USA [52], and linear generators have been designed for wave energy extraction systems since the late 1970s [4], there are still very few kinds of linear generators that have been tested in sea waves. In recent years, the term "direct-drive wave energy extraction system" emerges, which indicates coupling the wave's speed and linear generator directly without any pneumatics or complex linear-to-rotary conversion systems. Thus, the complex conversion device is avoided and the mechanical loss is, therefore, decreased.

5.1. Two-Sided Permanent Magnet Linear Generator. Archimedes Wave Swing [41] is a fully submerged wave energy extraction system and consists of three parts: a two-sided permanent magnet linear generator, a basement (bottom part), and a floater (upper part), as shown in Figure 8. When a wave crest is above the AWS, the floater is pushed down by the added pressure of water, and when a wave trough is above it, the floater is moved up by the reduced pressure of water. The motion of floater is resisted by a two-sided permanent magnet

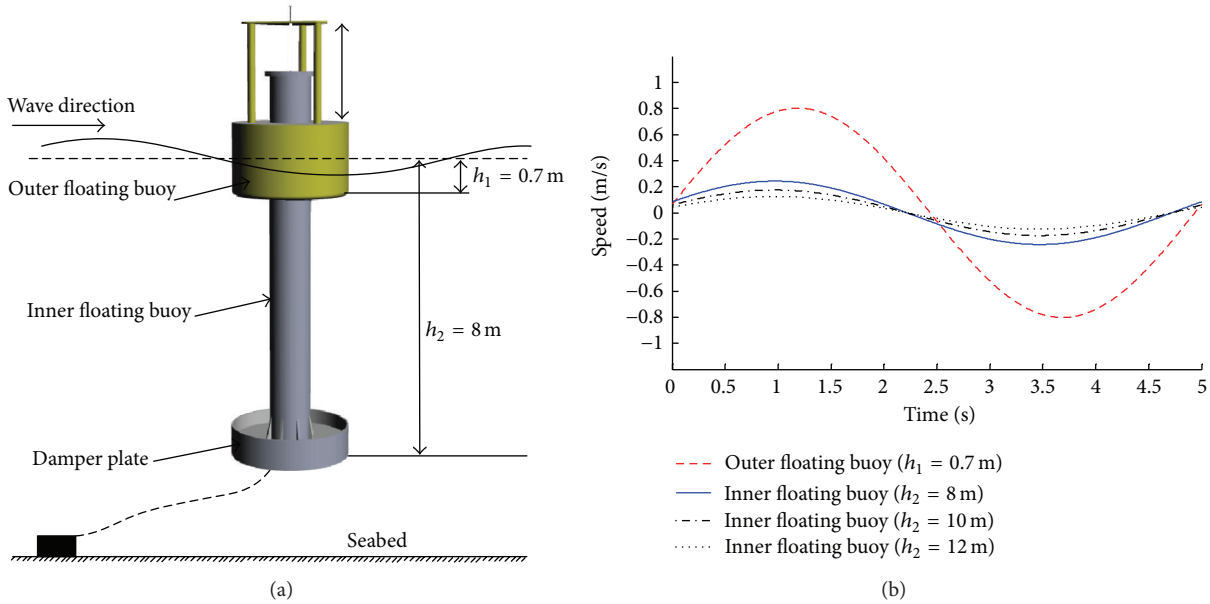

Figure 7: (a) A two-body floating system and (b) speed curves of outer and inner floating buoy in heave.

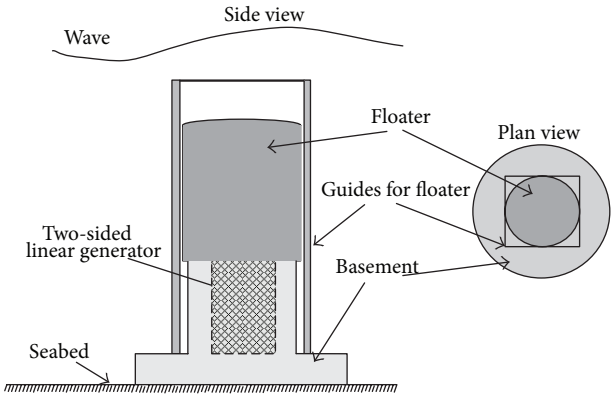

Figure 8: Sketch of the AWS [41].

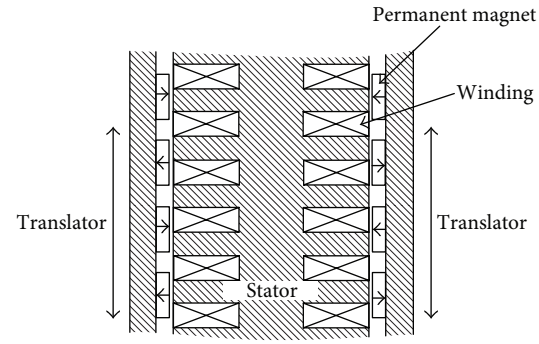

Figure 9: Sketch of a section of the two-sided permanent magnet linear generator, where the arrows in permanent magnet represent the magnetization direction [42].

linear generator, and the sketch of this two-sided permanent magnet linear generator is shown in Figure 9 [42]. There are several advantages of a two-sided permanent magnet linear generator:

(i) high force density,

(ii) reasonable work efficiency,

(iii) permanent magnet material is cheap,

(iv) the electricity is only restricted in stator.

The AWS is the first wave energy extraction system, which is equipped with a permanent magnet linear generator, installed and tested in sea waves.

5.2. Permanent Magnet Tubular Linear Generator. A novel three-phase permanent magnet tubular linear generator (PMTLG) with Halbach array was proposed for wave energy extraction system by Southeast University, China, in 2010 [53]. One significant advantage of PMTLG is that assistant teeth are adopted to minimize the detent force and optimize the dynamic performance of wave energy extraction system. Figure 10 shows the structure of PMTLG. With the assistant teeth, up to 70% of detent force is reduced. A wave energy extraction system equipped with a PMTLG has been designed and tested in China under the supporting of National Natural Science Foundation of China (NSFC), as shown in Figure 11. The test results indicate that a large amount of wave energy (3–5 KW/m) can be obtained from the East China Sea and the South China Sea, which is quite considerable because China possesses a long coastline of over 18,000 km.

Besides, a new linear switched reluctance generator was proposed for wave energy conversion by University of Beira Interior, Portugal, in 2012 [54]. The numerical analysis and optimization results showed that the proposed linear switched reluctance generator was high force density, robustness, and easy design and installation.

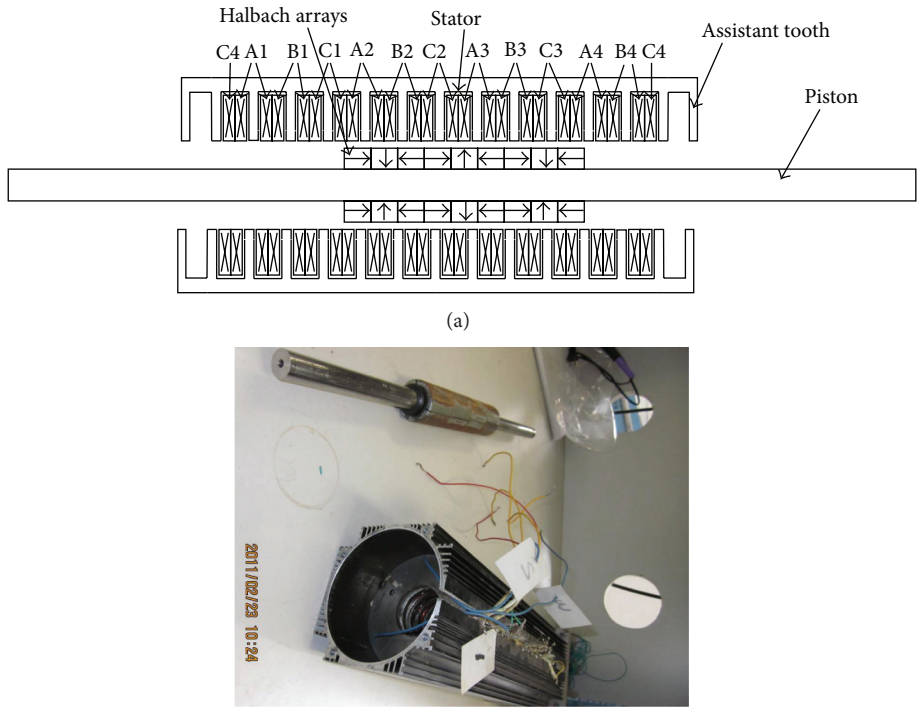

Figure 10: (a) Cross-sectional view of the PMTLG; and (b) prototype of the PMTLG.

Figure 11: A wave energy extraction system was installed in Xuanwu Lake, China (in trial phase).

6. Discussions and Conclusions

Although many studies have analyzed offshore wave energy extraction systems theoretically and a few kinds of prototype have been tested in wave tank or real sea, some R&D financial supports from governments are still necessary for the construction and maintenance of the extraction system in harsh environment. In order to ensure a full-scale offshore wave energy extraction system absorbing wave energy maximally, the geometry and size of certain floating buoy should be designed to resonance with incident waves. For this reason, a larger size and capacity of linear generators are needed in design and construct (D&C).

Offshore wave energy extraction systems are still far from maturity. To develop a grid-connected and commercial offshore wave energy extraction system is not an easy task. Many difficulties and issues are still to be solved. Researchers in related fields should cooperate to promote technological development and avoid repetitive mistakes. It is believed that high quality research results would lead to a better working efficiency and economic benefit for the offshore wave energy extraction system.

This review shows the current status of offshore wave energy extraction technologies. The interaction between wave and floating body, as well as linear generators, is also illustrated.

Conflict of Interests

The authors declared that they have no conflict of interests to this paper.

Acknowledgments

This work was financially supported by the National Natural Science Foundation of China (Grant no. 41076054), Special Foundation for State Oceanic Administration of China (GHME2011GD02), and the Support of Science and Technology project from Jiangsu Provincial (BE2012138).

References

[1] B. Drew, A. R. Plummer, and M. N. Sahinkaya, "A review of wave energy converter technology," *Proceedings of the Institution of Mechanical Engineers A*, vol. 223, no. 8, pp. 887–902, 2009.

[2] V. C. Tai, P. C. See, S. Merle, and M. Molinas, "Sizing and control of the electric power take off for a buoy type Point absorber wave energy converter," in *Proceedings of the International Conference on Renewable Energies and Power Quality*, Granada, Spain, March 2012.

[3] J. Brooke, *Wave Energy Conversion*, Elsevier, New York, NY, USA, 2003.

[4] M. E. McCormick, *Ocean Wave Energy Conversion*, Wiley, New York, NY, USA, 1981.

[5] Engineering Committee on Oceanic Resources and Working Group on Wave Energy Conversion, *Wave Energy Conversion*, Elsevier, New York, NY, USA, 2003.

[6] S. Petroncini, *Introducing wave energy into the renewable energy marketplace [M.S. thesis]*, University of Edinburgh, Edinburgh, UK, 2000.

[7] L. Bergdahl, "Review of research in Sweden," in *Proceedings of the Wave Energy Workshop*, Cork, Ireland, October 1992.

[8] G. Fredrikson, "IPS wave power Buoy Mark IV," in *Proceedings of the Wave Energy Workshop*, Cork, Ireland, October 1992.

[9] K. Nielsen and N. I. Meyer, *The Danish Wave Energy Programme*, EWEC, Patras, Greece, 3rd edition, 1998.

[10] Officers of World Energy Council, *Survey of Energy Resources, Interim Update 2009*, London, UK, 2009.

[11] M. Previsic, "E21 EPRI assessment offshore wave energy conversion devices," Report E21 EPRI WP-004-US-Rev 1, Electric Power Research Institute, Palo Alto, Calif, USA, 2004.

[12] Ocean Power Technologies (OPT) Inc, Recent News, http://www.oceanpowertechnologies.com.

[13] L. Lin and H. T. Yu, "Offshore wave energy generation devices: impacts on ocean bio-environment," *Acta Ecologica Sinica*, vol. 32, pp. 117–122, 2012.

[14] M. A. Mueller, "Electrical generators for direct drive wave energy converters," *IEE Proceedings*, vol. 149, no. 4, pp. 446–456, 2002.

[15] J. Falnes, *Ocean Waves and Oscillating Systems*, Cambridge University Press, Cambridge, 2002.

[16] M. Lucia, M. H. Anne, and F. Peter, "A method for EIA scoping of wave energy converters-based on classification of the used technology," *Environmental Impact Assessment Review*, vol. 32, no. 1, pp. 33–44, 2012.

[17] N. N. Panicker, "Power resource estimate of ocean surface waves," *Ocean Engineering*, vol. 3, no. 6, pp. 429–439, 1976.

[18] J. Falnes, "A review of wave-energy extraction," *Marine Structures*, vol. 20, no. 4, pp. 185–201, 2007.

[19] R. Pelc and R. M. Fujita, "Renewable energy from the ocean," *Marine Policy*, vol. 26, no. 6, pp. 471–479, 2002.

[20] Y. Goda, *Random Seas and Design of Maritime Structure*, University of Tokyo Press, Tokyo, Japan, 1985.

[21] M. J. Tucker, *Waves in Ocean Engineering: Measurement, Analysis, Interpretation*, Ellis Horwood, New York, NY, USA, 1991.

[22] T. Pontes, D. Mollison, J. C. Borge, L. Cavaleri, and G. A. Athanassoulis, "Evaluation of the wave energy resource," in *Proceedings of the Workshop on Wave Energy R&D*, Cork, Ireland, 1993.

[23] M. T. Pontes, "Assessing the European wave energy resource," *Journal of Offshore Mechanics and Arctic Engineering*, vol. 120, no. 4, pp. 226–231, 1998.

[24] J. R. Joubert, *An investigation of the wave energy resource on the South African coast, focusing on the spatial distribution of the south west coast [M.S. thesis]*, University of Stellenbosch, Stellenbosch, South Africa, 2008.

[25] S. Barstow, M. Gunnar, D. Mollison, and J. Cruz, *The Wave Energy Resource*, Springer, Berlin, Germany, 2008.

[26] M. T. Pontes, L. Cavaleri, and D. Mollison, "Ocean waves: energy resource assessment," *Marine Technology Society Journal*, vol. 36, no. 4, pp. 42–52, 2002.

[27] S. F. Barstow, O. Haug, and H. E. Krogstad, "Satellite altimeter data in wave energy studies," in *Proceedings of the 3rd International Symposium on Ocean Wave Measurement and Analysis (WAVES '97)*, vol. 2, pp. 339–354, November 1997.

[28] L. Duckers, "Wave energy," in *Renewable Energy*, Oxford University Press, Oxford, UK, 2nd edition, 2004.

[29] U. A. Korde, "Control system applications in wave energy conversion," in *Proceedings of the MTS/IEEE Conference and Exhibition (OCEANS '00)*, vol. 3, pp. 1817–1824, September 2000.

[30] R. Waters, M. Stålberg, O. Danielsson et al., "Experimental results from sea trials of an offshore wave energy system," *Applied Physics Letters*, vol. 90, no. 3, Article ID 034105, 3 pages, 2007.

[31] V. Ferdinande and M. Vantorre, "hydrodynamics of ocean wave energy utilization," in *The Concept of A Bipartite Point Absorber*, Springer, Berlin, Germany, 1986.

[32] J. Falnes, "Wave-energy conversion through relative motion between two single-mode oscillating bodies," *Journal of Offshore Mechanics and Arctic Engineering*, vol. 121, no. 1, pp. 32–38, 1999.

[33] Y. Masuda, L. Xianguang, and G. Xiangfan, "High performance of cylinder float backward bent duct buoy (BBDB) and its use in European seas," in *Proceedings of the 1st European Wave Energy Symposium*, pp. 323–337, 1993.

[34] Y. Masuda and T. Kuboki, "Prospect of economical wave power electric generator by the terminator backward bent duct buoy (BBDB)," in *Proceedings of the 12th International Offshore and Polar Engineering Conference*, pp. 26–31, May 2002.

[35] Ocean Energy Inc, Recent News, http://www.oceanenergy.ie/.

[36] F. Zabihian and A. S. Fung, "Review of marine renewable energies: case study of Iran," *Renewable and Sustainable Energy Reviews*, vol. 15, no. 5, pp. 2461–2474, 2011.

[37] A. F. D. O. Falcão, "Wave energy utilization: a review of the technologies," *Renewable and Sustainable Energy Reviews*, vol. 14, no. 3, pp. 899–918, 2010.

[38] R. W. Yeung, "Added mass and damping of a vertical cylinder in finite-depth waters," *Applied Ocean Research*, vol. 3, no. 3, pp. 119–133, 1981.

[39] C. J. R. Garrett, "Wave forces on a circular dock," *Journal of Fluid Mechanics*, vol. 46, no. 1, pp. 129–139, 1971.

[40] T. Sabuncu and S. Calisal, "Hydrodynamic coefficients for vertical circular cylinders at finite depth," *Ocean Engineering*, vol. 8, no. 1, pp. 25–63, 1981.

[41] N. J. Baker, *Linear generators for direct drive marine renewable energy converters [Ph.D. thesis]*, University of Durham, Durham, UK, 2003.

[42] F. E. Gardner, "Learning experience of AWS pilot plants test offshore Portugal," in *Proceedings of the 6th European Wave Energy Conference*, pp. 149–154, 2005.

[43] L. H. Holthuijsen, *Waves in Oceanic and Coastal Waters*, Cambridge University Press, Cambridge, UK, 2007.

[44] R. Haberman, *Applied Partial Differential Equation: With Fourier Series and Boundary Value Problems*, Addison Wesley, Upper Saddle River, NJ, USA, 4th edition, 2004.

[45] J. Ribeiro and I. Martins, "Development of a low speed linear generator for use in a wave energy converter," in *Proceedings of the International Conference on Renewable Energies and Power Quality*, Granada, Spain, 2010.

[46] N. J. Baker, M. A. Mueller, and P. R. M. Brooking, "Electrical power conversion in direct drive wave energy converters," in *Proceedings of the 5th European Wave Energy Conference*, Cork, Ireland, 2003.

[47] N. J. Baker, M. A. Mueller, and E. Spooner, "Permanent magnet air-cored tubular linear generator for marine energy converters," in *Proceedings of the 2nd IEE International Conference on Power Electronics, Machines and Drives (PEMD '04)*, pp. 862–867, Edinburgh, UK, April 2004.

[48] M. Eriksson, J. Isberg, and M. Leijon, "Hydrodynamic modelling of a direct drive wave energy converter," *International Journal of Engineering Science*, vol. 43, no. 17-18, pp. 1377–1387, 2005.

[49] V. D. Colli, P. Cancelliere, F. Marignetti, R. Di Stefano, and M. Scarano, "A tubular-generator drive for wave energy conversion," *IEEE Transactions on Industrial Electronics*, vol. 53, no. 4, pp. 1152–1159, 2006.

[50] S. Raghunathan, "The wells air turbine for wave energy conversion," *Progress in Aerospace Sciences*, vol. 31, no. 4, pp. 334–386, 1995.

[51] L. C. Rome, L. Flynn, E. M. Goldman, and T. D. Yoo, "Biophysics: generating electricity while walking with loads," *Science*, vol. 309, no. 5741, pp. 1725–1728, 2005.

[52] M. Eriksson, *Modelling and experimental verification of direct drive wave energy conversion-Buoy-generator dynamics [Ph.D. thesis]*, Uppsala University, Uppsala, Sweden, 2007.

[53] H. Yu, C. Liu, B. Yuan, M. Hu, L. Huang, and S. Zhou, "A permanent magnet tubular linear generator for wave energy conversion," *Journal of Applied Physics*, vol. 111, no. 7, Article ID 07A741, 3 pages, 2012.

[54] M. R. A. Calado, P. M. C. Godinho, and S. J. P. S. Mariano, "Design of a new linear generator for wave energy conversion based on analytical and numerical analyses," *Journal of Renewable and Sustainable Energy*, vol. 4, no. 3, Article ID 033117, 11 pages, 2012.

Hindawi Publishing Corporation
Advances in Mechanical Engineering
Volume 2013, Article ID 416109, 11 pages
http://dx.doi.org/10.1155/2013/416109

Research Article

Numerical Analysis of Impulse Turbine for Isolated Pilot OWC System

Zhen Liu,[1,2,3] Jiyuan Jin,[4] Ying Cui,[2] and Haiwen Fan[2]

[1] *Shandong Provincial Key Laboratory of Ocean Engineering, Ocean University of China, Qingdao 2661-00, China*
[2] *College of Engineering, Ocean University of China, Qingdao 266-100, China*
[3] *Qingdao Municipal Key Laboratory of Ocean Renewable Energy, Ocean University of China, Qingdao 266-100, China*
[4] *Research Institute Korea Institute of Ocean Science and Technology, Daejon 305-343, Republic of Korea*

Correspondence should be addressed to Jiyuan Jin; kimkilwon@gmail.com

Received 9 June 2013; Revised 16 July 2013; Accepted 26 July 2013

Academic Editor: Haitao Yu

Copyright © 2013 Zhen Liu et al. This is an open access article distributed under the Creative Commons Attribution License, which permits unrestricted use, distribution, and reproduction in any medium, provided the original work is properly cited.

Oscillating water column (OWC) is the most widely used wave energy converting technology in the world. The impulse turbine is recently been employed as the radial turbine in OWC facilities to convert bidirectional mechanical air power into electricity power. 3D numerical model for the impulse turbine is established in this paper to investigate its operating performance of the designed impulse turbine for the pilot OWC system which is under the construction on Jeju Island, Republic of Korea. The proper mesh style, turbulence model, and numerical solutions are employed to study the velocity and air pressure distribution especially around the rotor blade. The operating coefficients obtained from the numerical simulation are compared with corresponding experimental data, which demonstrates that the 3D numerical model proposed here can be applied to the research of impulse turbines for OWC system. Effects of tip clearances on flow field distribution characteristics and operating performances are also studied.

1. Introduction

Oscillating water column (OWC) is the most widely used wave energy technology in the world. It is utilized to convert wave energy into low pressure pneumatic energy in the form of a bidirectional air flow. Capable of rotating in one-way under above flow conditions, Wells turbine or impulse turbines linked to the electric generator in the air duct is generally used to convert the dynamic air pressure into mechanical energy.

A number of efforts have been made to study the operating performance of air turbines for OWC wave energy converters. Maeda et al. [1] presented experimental research reports on the impulse turbine within fixed guide vanes for the OWC wave energy converter. Iffects of guide vanes on Wells turbines in the reciprocating air flows are experimentally investigated in [2], demonstrating better performance than turbines without guide vanes. The self-starting characteristics and operating performance of the Wells turbine in irregular waves are studied by experimental and numerical methods in [3]. Huang et al. [4] proposed a simple method for dealing with effects of pressure drops induced by the Wells turbine on the operating performance of air chambers. The fitting formula is used, which is derived from laboratory research on the flat plate as the Wells turbine's pressure drop substitute.

It was first investigated for the tip clearance of impulse turbine by 3D numerical model, which has been reported by Thakker and Dhanasekaran [5] that the turbine with 0.25 tip clearance performed almost similar to the case of without tip clearance for entire flow coefficients. An accurate description of the steady three-dimensional flow field in a high solidity Wells turbine was provided in [6]. The analysis has been performed by numerically solving incompressible NS equations in a noninertial reference frame rotating with the turbine. A design method combining two powerful design tools (Pugh concept analysis and 3D CAD environment) is used in [7] in order to create an improved impulse turbine using a systematic method. An investigation on the performance of a Wells turbine for wave energy conversion using the CFD method was reported by Taha et al. [8]. The study utilized several numerical models and NACA0020 blade profiles with various

uniform tip clearances under steady flow conditions, and it was validated with corresponding experimental data. The automatic optimization procedure for a monoplane Wells turbine using symmetric airfoil blades was carried out by coupling an optimization algorithm with an industrial CFD code in [9]. Pereiras et al. [10] proposed an improved radial impulse turbine with newly designed blades and vane profiles using CFD method. The initial results of experimental validation for twin unidirectional impulse turbine topology were presented in [11]. In the experiment, a concept scale model was built and tested using simulated bidirectional flow. The model consisted of two 165 mm impulse turbines each individually coupled to 375 W grid connected induction machines.

Recent research and reports have pointed out that impulse turbines could overcome shortcomings of Wells turbines, such as poor self-starting characteristics and narrow operating flow rate domains to keep high operating efficiencies. Furthermore, most previous studies focused on experimental investigation and were limited by laboratory conditions and expenses. The incident air velocity distribution details in the whole flow domain, which are important for investigation on effects of bi-directional air flows on the efficiency of impulse turbines, were rarely obtained by the experiments.

Although the impulse turbine rotates in a bi-directional air flow, it is still valuable to analyze its performance in a steady flow for design and optimization purposes. The impulse turbine is planned to be utilized in the 500 kW pilot OWC system on Jeju Island of Korea because of its advantages on self-starting and stable power output. The research team from Korea Maritime University has put efforts on the numerical analysis and improvement for the impulse turbine practical utilization [12–14]. The present paper focused on the numerical simulation of optimized impulse turbine performance, which has been validated by the corresponding experimental data. The multiple reference frame and mixing plane models are utilized for setting up of numerical rotating machines, and RNG k-ε turbulence model is applied to deal with turbulent effects. 3D air velocity and pressure distributions along the flow path are simulated numerically and operating coefficients for various tip clearances are compared for the purpose to improve and optimize the design of impulse turbines.

2. Impulse Turbine for Wave Energy Conversion

The typical three-dimensional impulse turbine model including rotor blades and guide vanes [15] within the outline utilized in the OWC pilot plant is shown in Figure 1. For the rotor blade, the profile is elliptical in shape on the suction side and has a circular arc shape on the pressure side. There are two rows of symmetrically placed plate-type fixed guide vanes on both sides of the rotor. The camber line of the guide vanes consists of a straight line and a circular arc.

The design profile and parameters of impulse turbines used in the present paper are derived from corresponding experiments in [1]. There are 30 rotor blades and 26 fixed guide vanes. The rotor blade pitch S_r is 26.7 mm, the width of flow path t_a is 10.6 mm, the spacing G between the blade and the guide vane represents 20 mm, and the guide vane pitch S_g is 30.8 mm. The rotor blade inlet angle is 60°, the radius of the circular arc is 30.2 mm, and the lengths of the major and minor axes of the elliptic arc on the suction side are 125.8 mm and 41.4 mm, respectively. The hub diameter is 210 mm, and the tip diameter is 298 mm.

The chord length of guide vanes is fixed at 70 mm, and the length of camber's straight line is 34.8 mm. The radius of the circular arc of guide vane R_a and the camber angle of guide vane δ vary with setting angles of the guide vane θ.

Typical characteristics of the performance of an impulse turbine in steady unidirectional flow are presented in terms of input coefficient C_A, torque coefficient C_T, turbine efficiency η, and flow coefficient ϕ. The definitions are given as follows [16]:

$$
\begin{aligned}
C_A &= \frac{2\Delta pQ}{\rho_a \left(v_a^2 + U_R^2\right) bl_r z v_a}, \\
C_T &= \frac{2T_0}{\rho_a \left(v_a^2 + U_R^2\right) bl_r z r_R}, \\
\eta &= \frac{T_0 \omega}{\Delta pQ} = \frac{C_T}{C_A \varphi}, \\
\phi &= \frac{v_a}{U_R},
\end{aligned}
\tag{1}
$$

where Δp, Q, ρ_a, T_0 represent total pressure drop between setting camber and atmosphere, air flow rate, air density, and turbine output torque; v_a, r_R, ω, U_R, b, and z represent mean axial flow velocity, mean radius, angular velocity of the turbine, circumferential velocity at r_R, blade height, and number of rotor blades, respectively.

3. Numerical Model

3.1. Governing Equations. In this study, the Reynolds-averaged Navier-Stokes equations and continuity equations are used as the governing equations. The Renormalization Group (RNG) turbulence model is taken into account for enclosing equations:

$$
\begin{aligned}
&\frac{\partial \rho}{\partial t} + \frac{\partial}{\partial x_i}\left(\rho u_i\right) = 0, \\
&\frac{\partial \rho u_i}{\partial t} + \frac{\partial \rho u_i u_j}{\partial x_j} = -\frac{\partial p}{\partial x_i} + \rho f_{x_i} + \frac{\partial}{\partial x_j}\left(\mu \frac{\partial u_i}{\partial x_j} - \rho \overline{u_i' u_j'}\right),
\end{aligned}
\tag{2}
$$

where ρ, u, P, μ are the air density, the velocity, body force, and dynamic turbulent viscosity. Each of subscripts i, j, k denotes one of the components corresponding to the spatial axes of x, y, z. δ_{ij} represents the Kronecher Delta, and $-\rho \overline{u_i' u_j'}$ is defined as Reynolds Stress.

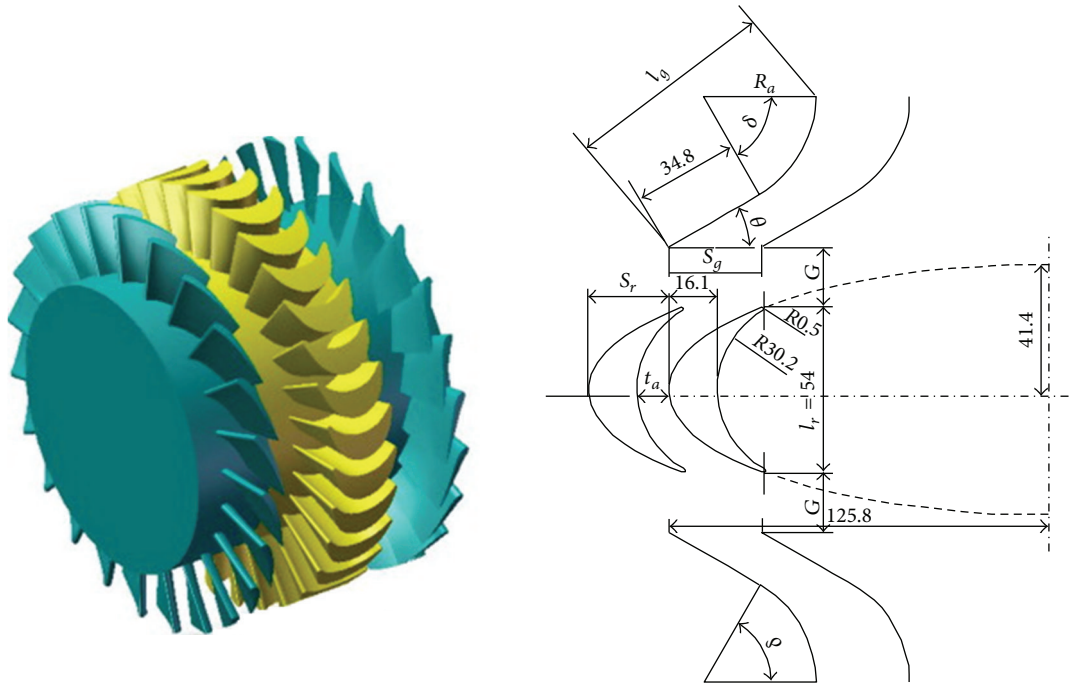

FIGURE 1: Impulse turbine with fixed guide vane.

RNG turbulence model induces the functions of turbulent kinetic energy k and turbulent dissipation rate ε to deal with Reynolds Stress:

$$\frac{\partial \rho k}{\partial t} + \frac{\partial (\rho k u_i)}{\partial x_i} = \frac{\partial}{\partial x_j}\left[a_k \mu_{\text{eff}} \frac{\partial k}{\partial x_j}\right] + G_k + \rho\varepsilon,$$
$$\frac{\partial \rho \varepsilon}{\partial t} + \frac{\partial (\rho \varepsilon u_i)}{\partial x_i} = \frac{\partial}{\partial x_j}\left[a_k \mu_{\text{eff}} \frac{\partial \varepsilon}{\partial x_j}\right] + \frac{C_{1\varepsilon}^*}{k} G_k - C_{2\varepsilon}\rho\frac{\varepsilon^2}{k}, \tag{3}$$

where

$$\mu_{\text{eff}} = \mu + \mu_i, \qquad \mu_i = \rho C_u \left(\frac{k^2}{\varepsilon}\right), \qquad C_\mu = 0.0845,$$
$$a_k = a_\varepsilon = 1.39, \qquad C_{1\varepsilon}^* = C_{1\varepsilon} - \frac{\eta\,(1 - \eta_E/\eta_0)}{1 + \beta\eta_E^3},$$
$$C_{1\varepsilon} = 1.42, \qquad C_{2\varepsilon} = 1.68, \qquad \eta_0 = 4.377, \tag{4}$$
$$\beta = 0.012,$$
$$\eta_E = \left(2E_{ij} \cdot E_{ij}\right)^{1/2} \frac{k}{\varepsilon}, \qquad E_{ij} = \frac{1}{2}\left(\frac{\partial u_i}{\partial x_j} + \frac{\partial u_j}{\partial x_i}\right).$$

3.2. Numerical Solutions. The computational domain is divided into three parts: the up-stream guide vane domain, the rotor blade domain, and the down-stream guide vane domain, which is shown in Figure 2. The guide vane domains are stationary, and the rotor blade domain rotates at different RPMs (Revolutions Per Minute) and is defined using the Moving Reference Frame (MRF) model to aid in the integration of rotating blades and stationary guide vanes.

As a consequence, the periodic angles for the rotor and guide vanes are different. The mixing plane model has been utilized to allow the modeling of one rotor blade/guide vane combination in order to make the calculation practical. In the mixing plane model, each fluid zone is solved as a steady-state problem. After each iteration, the area-weighted averages of flow data at the mixing plane interface are taken in the circumferential direction on both the upstream and downstream boundaries. The above process is used to create profiles of flow properties, which are employed to update boundary conditions along two zones of the mixing plane interface.

The main boundaries of the computation domain are also given in Figure 2. Rotational periodic boundaries were defined at each side of rotor and guide vane regions. The impermeable condition was employed for the cover and bottom of computational domains. A velocity inlet was defined at the inlet of the upstream guide vane region, and pressure outlet boundaries were defined at the outlet of downstream guide vane region, where the static pressure was set as the gauge pressure and the default value in Fluent is utilized. The detailed definitions of above boundary conditions are described in the Fluent User's Guide [17].

Governing equations are solved by using the Finite Volume Method (FVM). The Quick discretization is considered for convection terms. The pressure-velocity coupling is calculated using the SIMPLEC algorithm. In the present study, the rotation speed has been kept unchanged while the incident velocity was varied to produce a range of flow coefficient. Numerical frames and Cooper type meshes of the impulse turbine are generated by the Grid-preprocess Software Gambit 2.2 (Figure 3). The number of grids is around 2–2.5 $\times$ 10^4 and Reynolds number is approximately 0.92×10^5, where

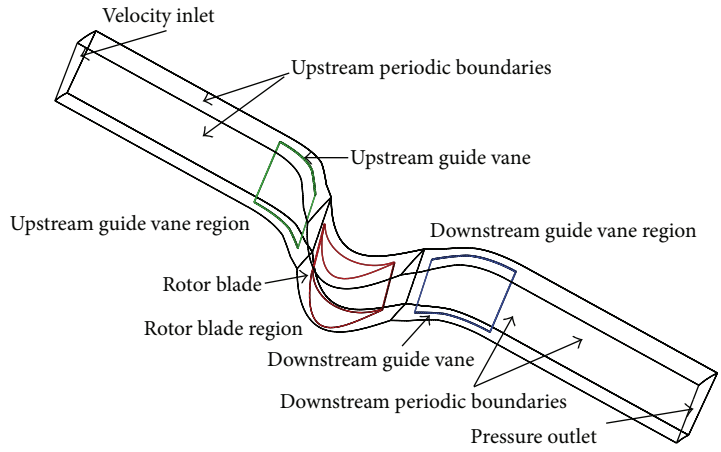

Figure 2: 3D schematic of computational fluid domains.

the characteristic length is defined as the rotor blade pitch S_r. Meshes near the surface are refined using the boundary layer regular grids in Fluent. Mesh independence effects and $Y+$ calculation have been performed in previous studies [18]. Nonequilibrium wall functions were employed as the near wall modeling, which were preferred to standard wall functions due to their better capability to deal with complex flows involving separation, reattachment, and strong pressure gradients [17].

4. Results and Discussion

4.1. Experimental Validation. Operating performance of the impulse turbine within various setting angles of guide vanes is calculated and compared with experimental data in [1] using the 3D numerical method proposed in the present paper. As shown in Table 1, the radius of circular arc of guide vane R_a and the camber angle of guide vane δ vary with the setting angles of the guide vane θ. The tip clearance employed in this section is $T_C = 1$ mm. Comparisons between experimental and numerical results for input coefficients, torque coefficients, and turbine efficiencies are shown in Figures 4–6, respectively. For the flow coefficient ϕ, the values defined at the incident velocity inlet are considered as mean axial velocities v_a in the numerical model.

From Figure 4, it can be seen that 3D input coefficients C_A from the numerical simulation are overpredicted for 15° setting angle because of the overprediction of pressure difference, which is induced by overestimation of air flows hitting on the pressure side of rotor blades in the numerical model. Within setting angles increasing, the overestimation effects will reduce. Idealized conditions including smooth blade surfaces and flow paths cause less pressure drops along the air flow traveling, consequently the input coefficients are underestimated comparing with experimental results at larger setting angles. For the torque coefficient C_T in Figure 5, the computed values generally agreed well with measured values. Since turbine output torque is derived from normal vectors of surface forces, the underprediction of pressure difference between blade two sides as described above has caused driving torques decreasing. Therefore, torque coefficients will be underpredicted comparing with experimental results.

Table 1: Variation of guide vane profiles.

θ (°)	R_a (mm)	δ (°)
15	32	75
22.5	34.6	67.5
30	37.2	60
37.5	41.7	52.5
45	47.5	45

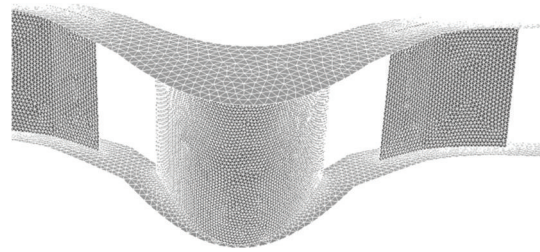

Figure 3: Schematics of 3D computational meshes for impulse turbine.

The computational prediction for turbine efficiencies η as shown in Figure 6 matches well with experimental results especially at high flow coefficients except 15° setting angle. The smaller values for 15° setting angle are generated by numerical overestimating for input coefficients. The above comparisons imply that the present 3D numerical model has shown its ability to predict the operating performance of the impulse turbine and RNG turbulent model produces good results in the higher rotational speed of the turbine, comparing with the prediction using standard k-ε turbulent model in lower flow coefficients in [5].

4.2. Effects of Tip Clearance. The tip clearance of the impulse turbine is defined as the distance between the outside diameter and the tip of rotor blade. In the present study, the outside diameter is fixed and the tip clearance changes with

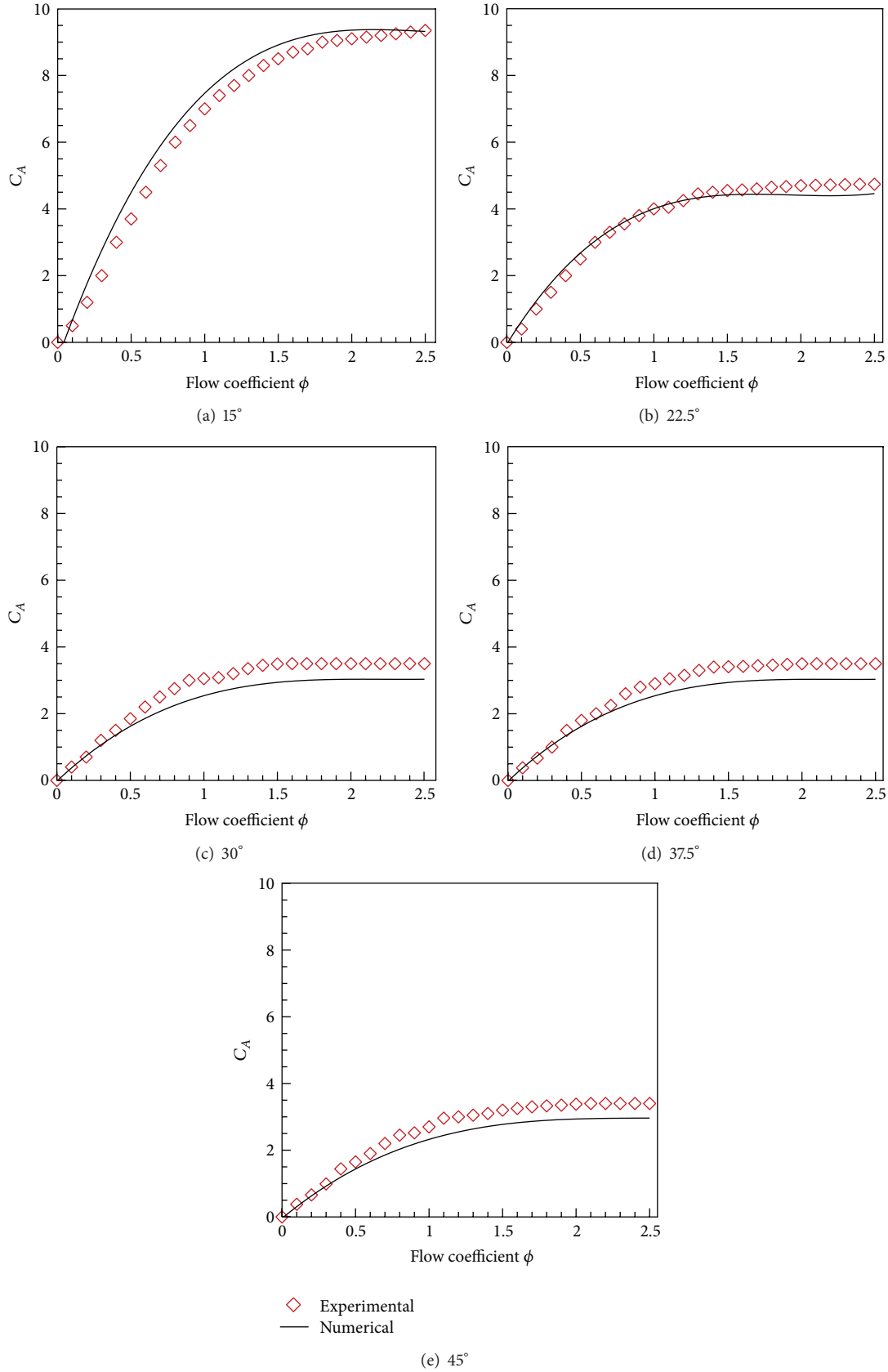

Figure 4: Comparison between numerical and experimental results on input coefficients.

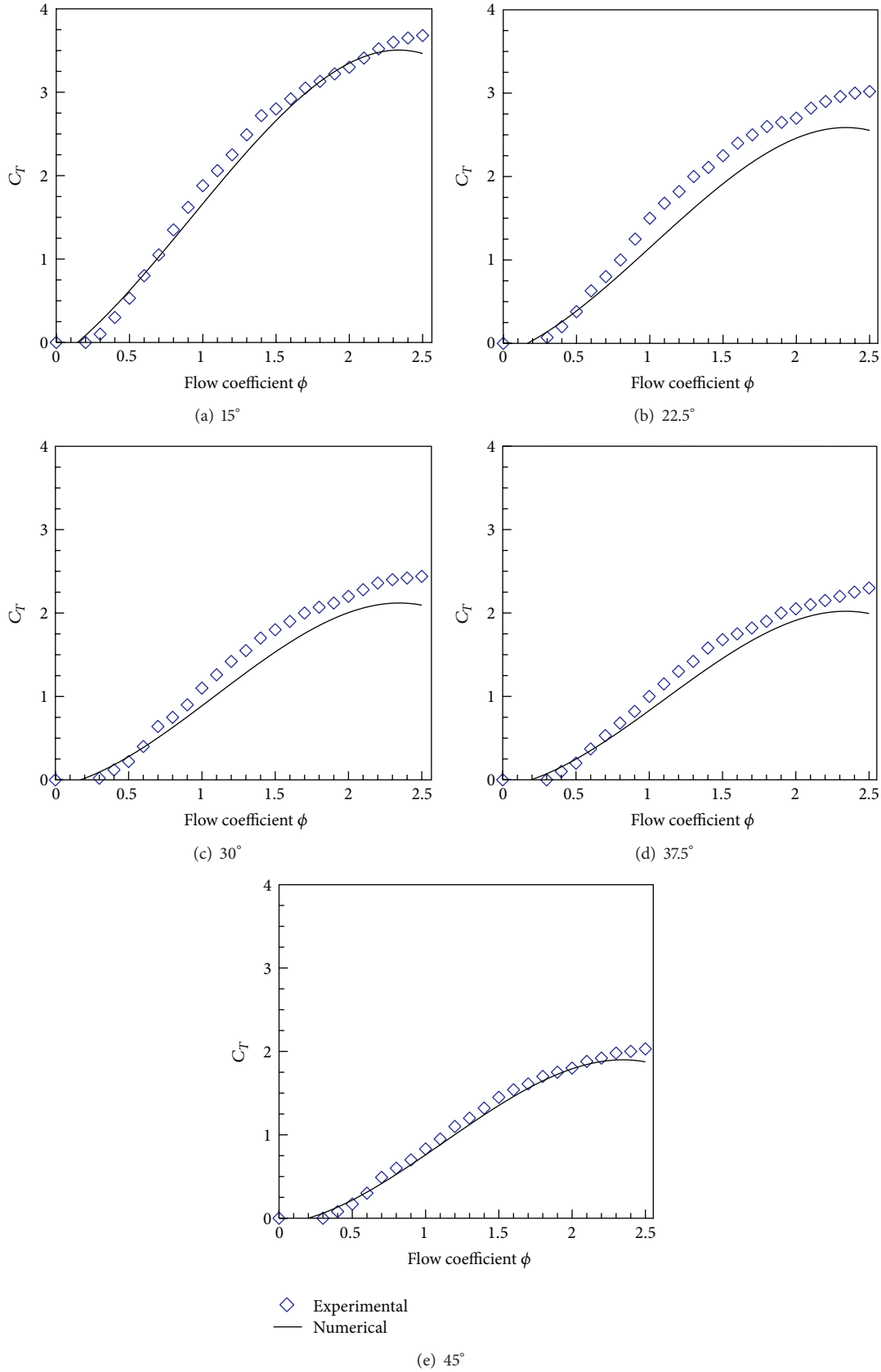

Figure 5: Comparison between numerical and experimental results on torque coefficients.

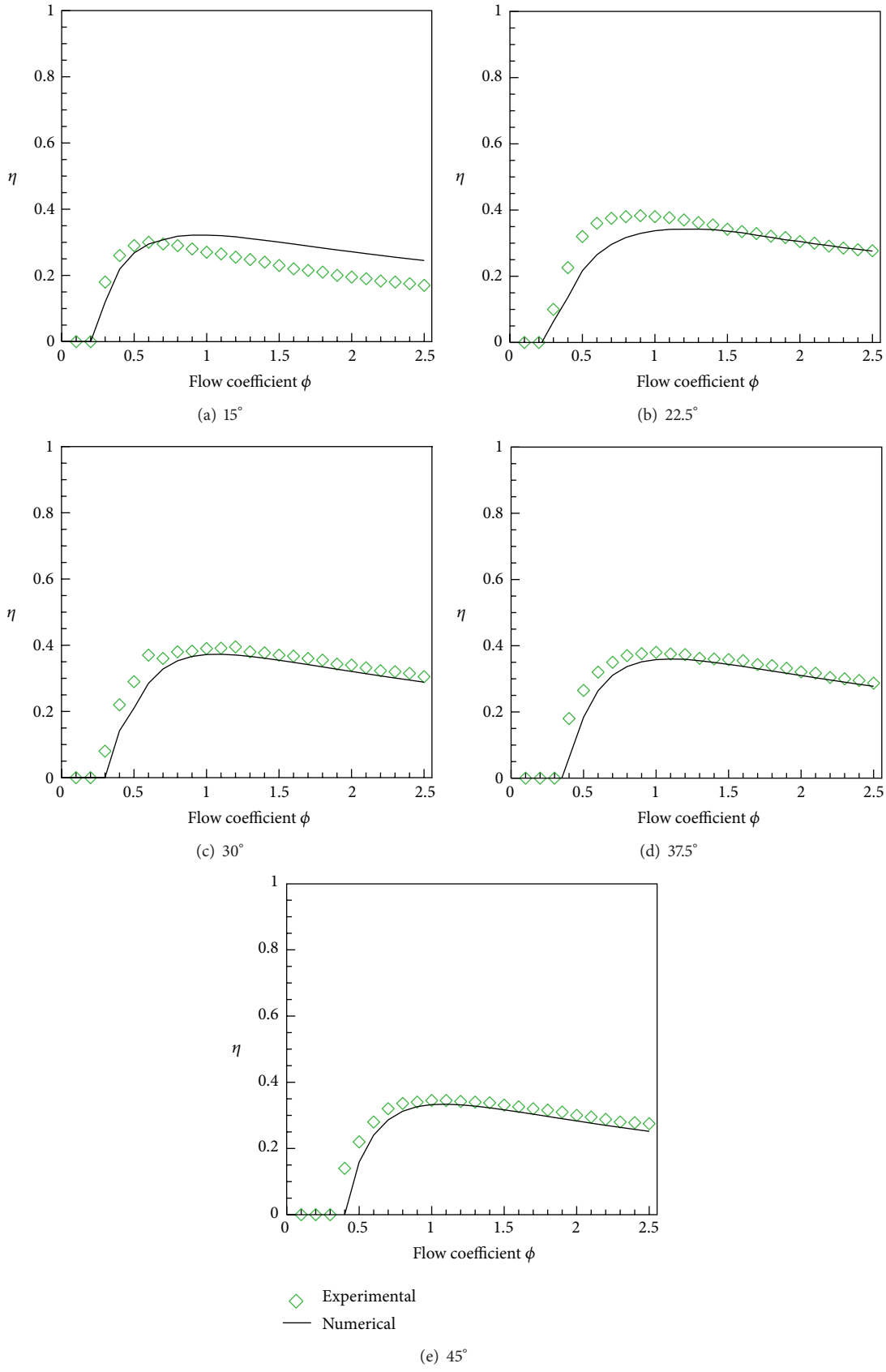

Figure 6: Comparison between numerical and experimental results on turbine efficiencies.

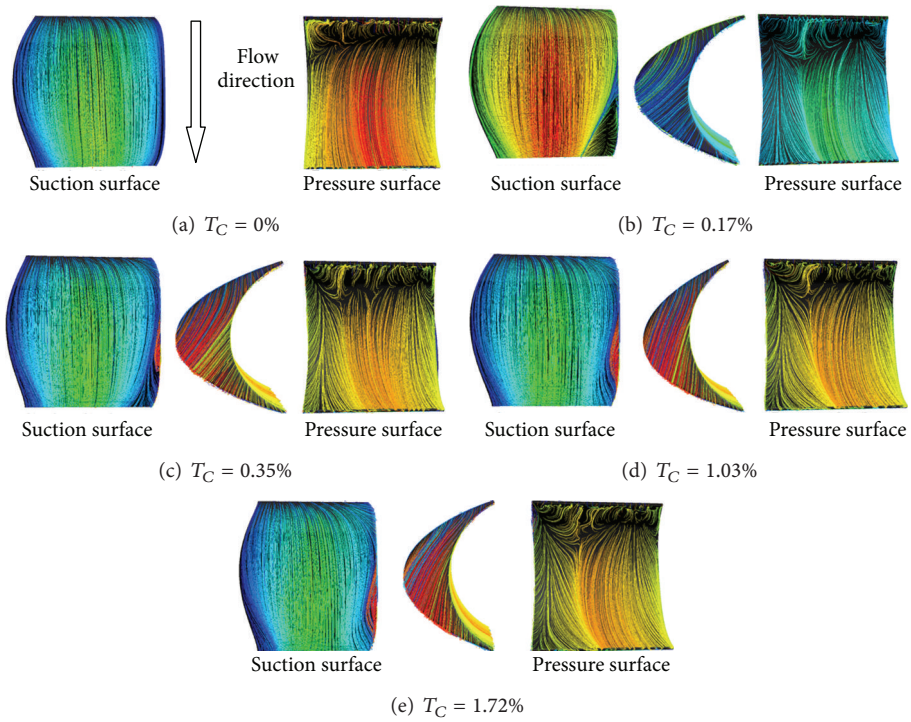

FIGURE 7: Flow path line distributions for various tip clearance ratio (ϕ = 1.5).

the variation of rotor blade heights. The setting angle of the guide vane in this section is fixed as 30°. Tip clearance ratio T_C is employed to demonstrate the effects of the tip clearance on impulse turbines, defined as follows:

$$T_C = \frac{t}{r_t}, \tag{5}$$

where t is the tip clearance and r_t is the tip radius. Five ratios (T_C = 0, 0.17%, 0.35%, 1.03%, 1.72%) are utilized, where the tip radius is fixed and tip clearance varies as 0, 0.5 mm, 1.0 mm, 3.0 mm, and 5.0 mm according to the variation in the rotor blade height (45 mm, 44.5 mm, 44 mm, 42 mm, and 40 mm). Although T_C = 0 is difficult to achieve in the arena of practical engineering, it is necessary to show its influence on flow distribution and turbine efficiency, which is helpful for design and further optimization.

Flow path lines on the rotor blade surface within different tip clearance ratios are given in Figure 7. It can be seen that path line distribution on the suction surface is uniform as T_C is zero. Vortexes are generated at the leading edge of blade along the blade passage and make the flow structure more complex. It also should be noted that no air flows on the pressure surface can overtop and affect the flow field around the suction side because of the structure characteristics. When the tip clearance ratio occurs, air flows not only generate vortexes at the leading edges but also overtop the rotor blade tip from pressure surface and generate vortex rolling-up around suction surface. Once above phenomena occurs, this part of air flows cannot contribute to the toque generation on pressure surface and induce energy loss to cause a decrease in efficiency. It can be imaged that more energy will be lost when the tip clearance increases.

Figure 8 illustrates the gauge pressure distributions on rotor blade surfaces for various tip clearances under certain flow coefficients. On the suction side, the vortex occurs near 40% of blade passage width for all the tip clearance ratios. The size of the vortex keeps growing as the tip clearance decreases. On the other hand, the tip leakage vortex occurs at the trailing edges on the pressure surface especially for all nonzero tip clearance ratios and there is no visible vortex generated on the pressure surface for T_C = 0. From Figure 8, it can be interpreted that the tip leakage flow induces a significant area of low-momentum fluid.

Effects of the tip clearance ratio on turbine efficiency are illustrated in Figure 9. As shown in Figure 9(a), the difference of input coefficients with different T_C is minor when the flow coefficient is small ($\phi \leqslant 0.5$). At higher flow coefficients, input coefficients become larger with flow coefficients increasing. On the other hand, it can be concluded from Figure 9(b) that torque coefficients will decrease as the tip clearance ratio grows. In Figure 9(c), turbine efficiency will get larger together with flow coefficients as $\phi < 1$. After the peak of flow coefficients, the turbine efficiency will get smaller. Impulse turbines with smaller tip clearances show better operating performance because of its lower energy loss over the tip of its rotor blades.

Generally, it can be concluded that tip clearance has significant effects on turbine efficiency. Although turbines with smaller T_C possess better operating performance, the complex structure of impulse turbines leads to difficulty in manufacturing. Therefore, it is necessary to consider all the

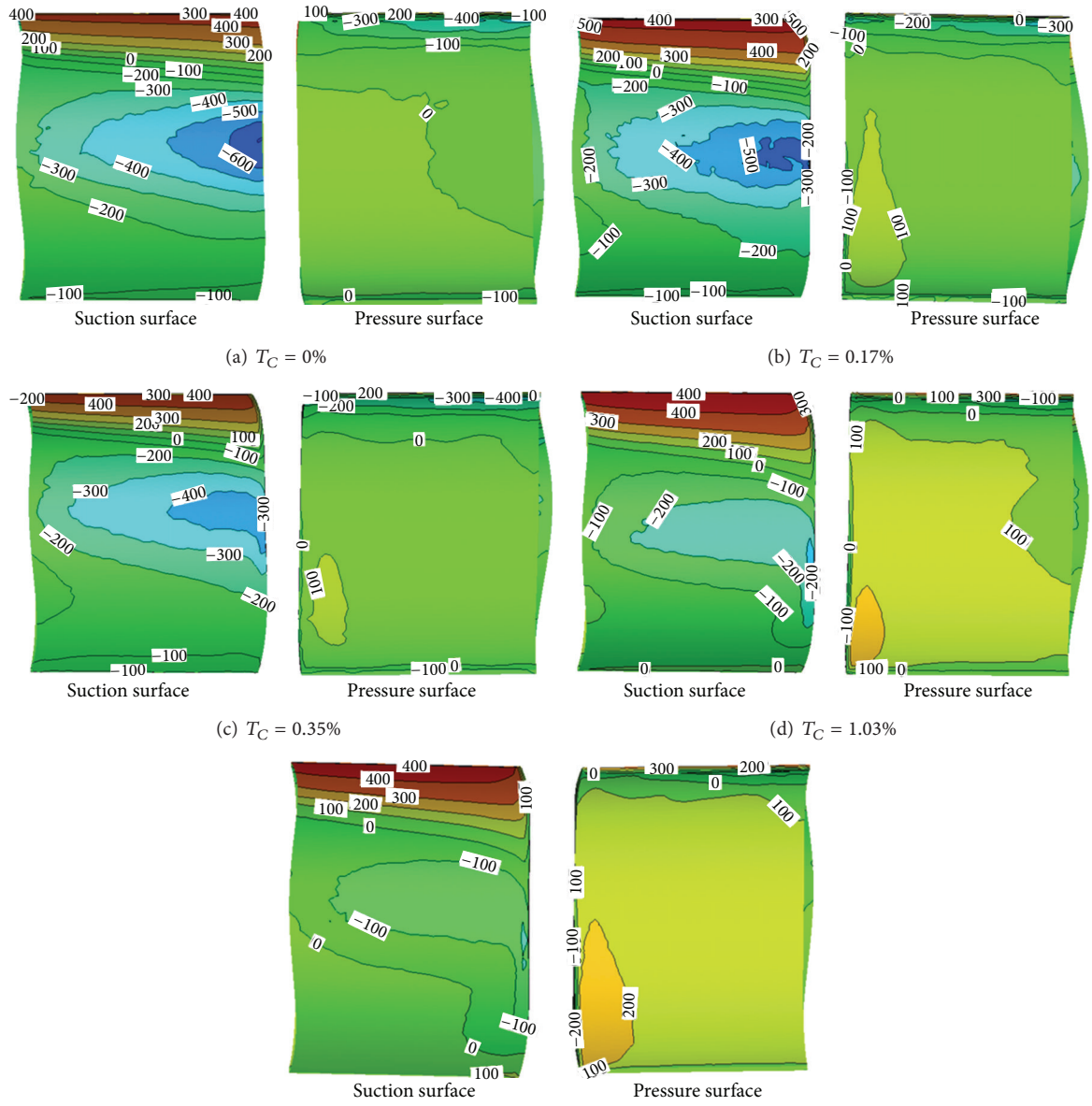

(a) $T_C = 0\%$ (b) $T_C = 0.17\%$

(c) $T_C = 0.35\%$ (d) $T_C = 1.03\%$

(e) $T_C = 1.72\%$

FIGURE 8: Pressure distribution on blade surfaces for various tip clearances ($\phi = 1.5$).

influential factors and the tip clearance ratio $0.35\% \leqslant T_C \leqslant 1.03\%$ is optimal in the selected domain of tip clearance values. According to the above analysis, optimization of rotor blades to reduce vortex rolling-up will also improve the turbine efficiency.

5. Conclusions

In this paper, a 3D numerical predicting model was established to investigate the operating performance characteristics of the impulse turbine, which has been improved from the basic design and is planned to be utilized in the 500 kW pilot OWC system on Jeju Island, Republic of Korea. The 3D numerical model was compared and validated with the experimental data for various setting angles of guide vanes. The close agreement of computational and experimental data shows the capability of the present numerical methodology on predicting flow distribution and turbine operating performance. RNG turbulent model shows better capability especially for higher flow coefficients within large rotating velocities.

Effects of tip clearance on turbine efficiency for the designed impulse turbine presented in this paper were studied numerically. It can be seen that larger tip clearance will cause more air flows from the pressure surface overtopping the tip of rotor blade and vortex rolling-up. Although smaller tip clearance generates better operating performance of impulse turbine, manufacturing and assembling difficulties

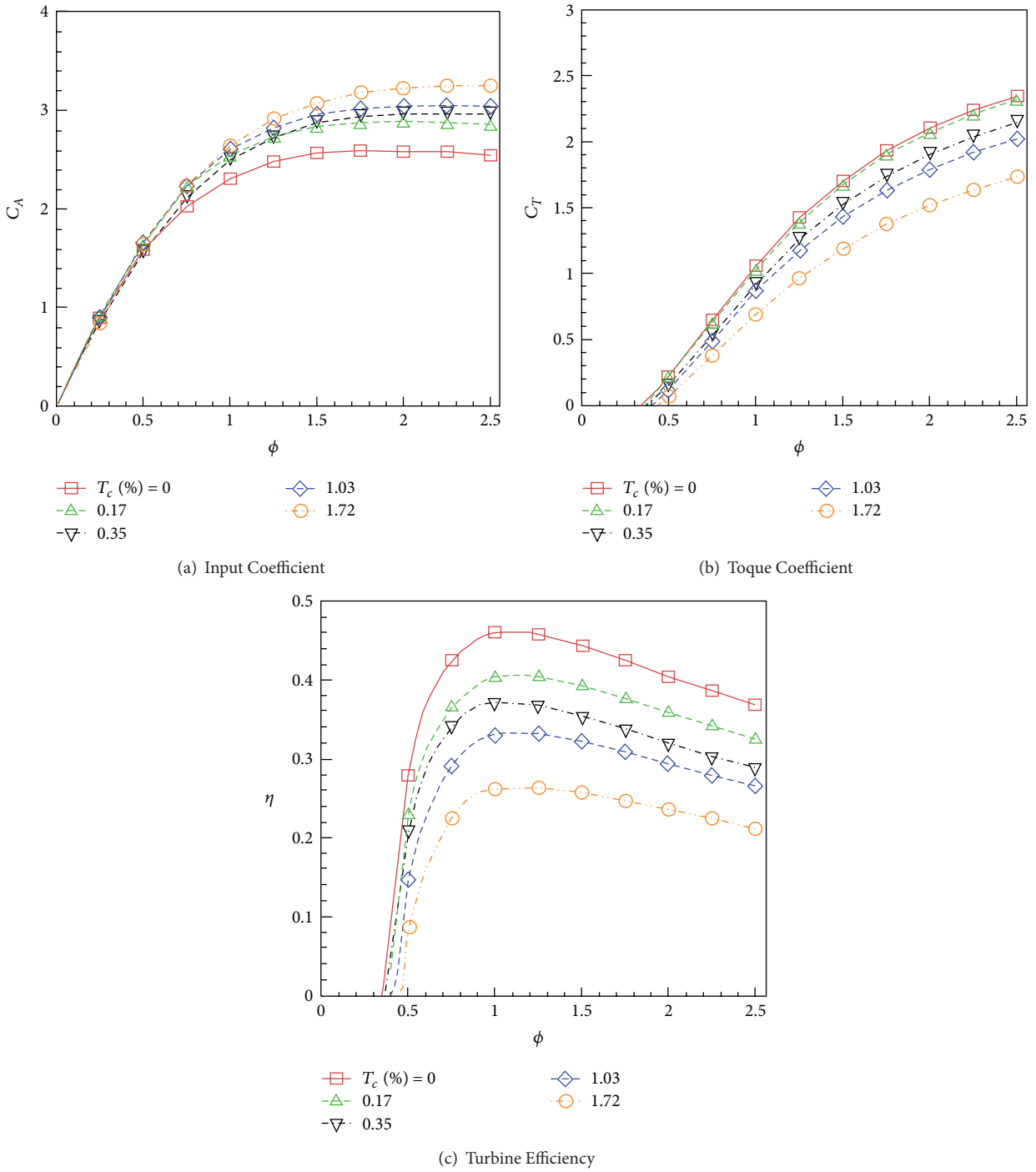

FIGURE 9: Numerical results of turbine performance for various tip clearance ratios.

will restrict the application of small tip clearance. Overall considering of operating performance and turbine fabrication, the value of tip clearance is recommended to be around 0.3 for better torque output and wave energy conversion.

Acknowledgments

This Project is supported by NSFC (Grant No.: 51279190 and 51311140259), Research Fund for the Doctoral Program of Higher Education (20100132110012) of China and Project "Development of Ocean Energy Utilization System" funded by Ministry of Land, Transport and Maritime affairs of Korea.

References

[1] H. Maeda, S. Santhakumar, T. Setoguchi, M. Takao, Y. Kinoue, and K. Kaneko, "Performance of an impulse turbine with fixed guide vanes for wave power conversion," *Renewable Energy*, vol. 17, no. 4, pp. 533–547, 1999.

[2] X. G. Liang, P. Y. Sun, W. Wang, and N. D. Jiang, "Experiment study of 2-direction guide-vane turbine in to-and-fro air-flow," *The Ocean Engineering*, vol. 19, no. 4, pp. 84–93, 2001 (Chinese).

[3] Z. Huang, Z. Yu, and N. Jiang, "Numerical simulation and experimental investigation on performance of the Wells turbine in irregular oscillating flow," *China Ocean Engineering*, vol. 15, no. 3, pp. 407–416, 2001.

[4] Z. Huang, Z. Yu, and Y. Zheng, "Simple method for predicting drag characteristics of the wells turbine," *China Ocean Engineering*, vol. 20, no. 3, pp. 473–482, 2006.

[5] A. Thakker and T. S. Dhanasekaran, "Computed effects of tip clearance on performance of impulse turbine for wave energy conversion," *Renewable Energy*, vol. 29, no. 4, pp. 529–547, 2004.

[6] M. Torresi, S. M. Camporeale, P. D. Strippoli, and G. Pascazio, "Accurate numerical simulation of a high solidity Wells turbine," *Renewable Energy*, vol. 33, no. 4, pp. 735–747, 2008.

[7] A. Thakker, J. Jarvis, M. Buggy, and A. Sahed, "3DCAD conceptual design of the next-generation impulse turbine using the Pugh decision-matrix," *Materials and Design*, vol. 30, no. 7, pp. 2676–2684, 2009.

[8] Z. Taha, S. Sugiyono, and T. Sawada, "A comparison of computational and experimental results of Wells turbine performance for wave energy conversion," *Applied Ocean Research*, vol. 32, no. 1, pp. 83–90, 2010.

[9] M. H. Mohamed, G. Janiga, E. Pap, and D. Thévenin, "Multi-objective optimization of the airfoil shape of Wells turbine used for wave energy conversion," *Energy*, vol. 36, no. 1, pp. 438–446, 2011.

[10] B. Pereiras, F. Castro, A. E. Marjani, and M. A. Rodríguez, "An improved radial impulse turbine for OWC," *Renewable Energy*, vol. 36, no. 5, pp. 1477–1484, 2011.

[11] K. Mala, J. Jayaraj, V. Jayashankar et al., "A twin unidirectional impulse turbine topology for OWC based wave energy plants-experimental validation and scaling," *Renewable Energy*, vol. 36, no. 1, pp. 307–314, 2011.

[12] B. S. Hyun, J. S. Moon, S. W. Hong, and Y. Y. Lee, "Practical numerical analysis of impulse turbine for OWC-type wave energy conversion using a commercial CFD code," in *Proceedings of the 14th International Offshore and Polar Engineering Conference (ISOPE '04)*, vol. 1, no 1, pp. 253–259, Toulon, France, May 2004.

[13] B. S. Hyun, J. S. Moon, S. W. Hong, and K. S. Kim, "Design of impulse turbine with an end plate for wave energy conversion," in *Proceedings of the 15th International Offshore and Polar Engineering Conference (ISOPE '05)*, vol. 1, no 1, pp. 507–511, Seoul, Republic of Korea, 2005.

[14] B. S. Hyun, J. S. Moon, S. W. Hong, and K. S. Kim, "Analysis of ring-type impulse turbine for wave energy conversion," in *Proceedings of the Korea Society of Ocean Engineering*, vol. 1, pp. 1552–1557, 2005.

[15] A. F. D. O. Falcão, "Wave energy utilization: a review of the technologies," *Renewable and Sustainable Energy Reviews*, vol. 14, no. 3, pp. 899–918, 2010.

[16] T. Setoguchi, S. Santhakumar, H. Maeda, M. Takao, and K. Kaneko, "A review of impulse turbines for wave energy conversion," *Renewable Energy*, vol. 23, no. 2, pp. 261–292, 2001.

[17] Fluent Inc, *User's Guide for Fluent 6.3*, Fluent Inc, New York, NY, USA, 2006.

[18] B. S. Hyun and J. S. Moon, "Analysis of impulse turbine for wave energy conversion using CFD method," *Journal of Ocean Engineering and Technology*, vol. 18, no. 5, pp. 1–6, 2004.